SINGLE CRYSTALS GROWTH AND PHYSICAL PROPERTIES CHARACTERIZATION OF $NbSe_2$ SUPERCONDUCTOR

Ph.D. Thesis

By

RUKSHANA PERVIN

DISCIPLINE OF METALLURGY ENGINEERING AND MATERIALS SCIENCE (MEMS)

INDIAN INSTITUTE OF TECHNOLOGY INDORE

MARCH-2020

SINGLE CRYSTALS GROWTH AND PHYSICAL PROPERTIES CHARACTERIZATION OF $NbSe_2$ SUPERCONDUCTOR

A THESIS

Submitted in Partial Fulfilment of the Requirements for the Award of the Degree of

DOCTOR OF PHILOSOPHY

By

RUKSHANA PERVIN
Roll No. **PHD1501181001**

DISCIPLINE OF MATELLURGY ENGINEERING AND MATERIAL SCIENCE (MEMS)
INDIAN INSTITUTE OF TECHNOLOGY INDORE
MARCH-2020

“The most beautiful thing we can experience is the mysterious. It is the source of all true art and science”

- Albert Einstein

INDIAN INSTITUTE OF TECHNOLOGY INDORE

CANDIDATE'S DECLARATION

I hereby certify that the work which is being presented in the thesis entitled **SINGLE CRYSTALS GROWTH AND PHYSICAL PROPERTIES CHARACTERIZATION OF $NbSe_2$ SUPERCONDUCTOR** in the partial fulfilment of the requirements for the award of the degree of **DOCTOR OF PHILOSOPHY** and submitted in the **DISCIPLINE OF METALLURGY ENGINEERING AND MATERIALS SCIENCE, INDIAN INSTITUTE OF TECHNOLOGY INDORE**, is an authentic record of my own work carried out during the time period from March-2015 to March-2020 under the supervision of Dr. Parasharam M. Shirage, Associate Professor, Discipline of Metallurgy Engineering and Materials Science.

The matter presented in this thesis has not been submitted by me for the award of any other degree of this or any other institute.

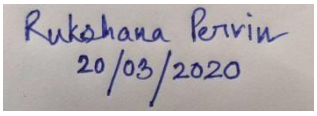

Signature of the student with date
(RUKSHANA PERVIN)

This is to certify that the above statement made by the candidate is correct to the best of my knowledge.

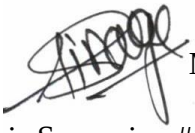

March 20, 2020

Signature of Thesis Supervisor#1 with date
(Dr. PARASHARAM M. SHIRAGE)

RUKSHANA PERVIN has successfully given his Ph.D. Oral Examination held on **18/09/2020.**

Signature of Chairperson (OEB)
Date: 18/09/2020

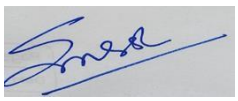

Signature of External Examiner
Date: 18/09/2020

Signature of Thesis Supervisor
Date: 18/09/2020

Signature of PSPC Member #1
Date: 18/09/2020

Signature of PSPC Member #2
Date: 18/09/2020

Signature of Convener, DPGC
Date: 18/09/2020

Signature of Head of Discipline
Date: 18/09/2020

ACKNOWLEDGEMENTS

First and foremost, I would like to express my profound and genuine gratefulness to my supervisor Associate Professor Dr. Parasharam M. Shirage, IIT Indore, for providing me the prospect to do research and helped me with fruitful remarks and guidance during my Ph.D. study. His enthusiasms towards work have intensely cheered me to work more actively and fervently.

I would like to extend my sincere gratitude to my PSPC member Dr. Rupesh S. Devan, MEMS, IITI and Dr. Santosh Hoshmani, MEMS, IITI for their encouragement and invaluable suggestions.

During my Ph.D. years, I was fortunate enough to receive the financial support from INSIPRE, DST, Govt. of India for providing me the fellowship as a inspire fellow under grant no. DST/INSPIRE Fellowship/2015/IF150330. I also owe my genuine obligations to Discipline of Matellurgy Engineering and Material Science, IITI for providing the laboratory facilities and rich environment to explore new ideas. I am also grateful to all the academic and administrative staff of IITI for providing practical support with friendly enthusiasm and grace. I thank Nitin Upadhyay for helping me in the technical works at SIC Indore.

I am extremely thankful to Sachin Kumar Dabaral and Dr. Rajiv Rawat, IUC Indore for permitting me to use the characterization facilities at their institute. I am also thankful to my friends and lab mates for their co-operation and support during my Ph.D. work.

I appreciatively acknowledge Manikandan Krishnan, M. Kannan, and Prof. S. Arumugam from Bharathidasan University for giving the magnetization measurement data of all samples used in this research work. Their intense supports help me to complete my research work.

My sincere thanks to Abyay Ghosh and Prof. Haranath Ghosh, Raja Ramanna Centre for Advanced Technology, Indore for their contributions in my research work and valuable discussions regarding the difficulty facing during the analysis of measurement data. I also have to thank prof. Sulabha K. Kulkarni of Indian Institute of Science Education and Research

(IISER), Pune, India for her helpful and efficient evaluation during the upgradation from JRF to SRF.

Most importantly, I owe my heartfelt gratitude to my family; Mother, Father, and siblings without whom none of this will be possible. My family has been a continuous source of love, concern, care and strength during these years.

On a very special and personal note I extend regards from the core of my heart to Almighty God for his continuous blessing. It is his love and trust which give me the strength to complete this beautiful journey of my life.

Date: **18/09/2020** *Rukshana Perwin*

Dedicated

To Almighty God

&

To my parents and two sisters

LIST OF PUBLICATIONS

PAPER – 1

R. Pervin, M. Krishnan, A. K. Rana, M. Kannan, S. Arumugam, P. M. Shirage, Enhancement of Superconducting Critical Current Density by Fe Impurity Substitution in $NbSe_2$ Single Crystals and the Vortex Pinning Mechanism, *Phys. Chem. Chem. Phys.* **19**, 11230, 2017. (IF = 3.430)

PAPER – 2

R. Pervin, M. Krishnan, A. K. Rana, S. Arumugam, P. M. Shirage, Effect of Cr atoms in vortex dynamics of $NbSe_2$ superconductor and study of second magnetization Peak Effect, *Mater. Res. Express.* **5**, 076001, 2018. (IF = 1.929)

PAPER – 3

R. Pervin, M. Krishnan, S. Arumugam, P. M. Shirage, Coexistence of Superconductivity and Ferromagnetism in Defect-Induced $NbSe_2$ Single Crystals, *J. Mater. Sci.* **54**, 11903-11912, 2019. (IF = 3.553)

PAPER – 4

R. Pervin, A. Ghosh, H. Ghosh, P. M. Shirage, Study of Transport Properties in Se Deficit and Fe Intercalated $NbSe_2$ Single Crystals: Experiment and Theory, *J. Mater. Sci.* **55**, 250-262, 2020. (IF = 3.553)

PAPER – 5

R. Pervin, M. Krishnan, S. Arumugam, P. M. Shirage, Second Magnetization Peak Effect and the Vortex Phase Diagram of $V_{0.0015}NbSe_2$ Single Crystal, *J. Magn. Magn. Mater.* **507**, 166817, 2020. (IF = 2.717)

PAPER – 6

R. Pervin, M. Krishnan, S. Arumugam, P. M. Shirage, Disordering induced second magnetization peak effect and the vortex pinning mechanism in $V_{0.0007}NbSe_2$ single crystal, *J. Supercond. Novel Magn.* **33**, 2679-2689, 2020. (IF = 1.244)

PAPER – 7

R. Pervin, P. M. Shirage, Study of vortex dynamics in $V_{0.001}NbSe_2$ superconductor, *AIP Conference proceedings*, **2100**, 020141, 2019.

LIST OF CONFERENCE/WORKSHOP ATTENDED

1. Oral presentation at "*11th International Conference on Magnetic and Superconducting materials (MSM19)*", Seoul National University, South Korea, 17th-24th August 2019.

2. Poster Presentation at "*27th National Symposium on Cryogenics and Superconductivity (NSCS-27)*", Indian Institute of Technology Bombay (IITB), Mumbai, India, 16th-18th January 2019.

3. Poster presentation at "*National conference on physics and chemistry of materials*", Devi Ahilya University, Indore 27th-28th December 2018.

4. GIAN workshop on "*High-Pressure Synthesized Materials: A Chest of Treasure and Hints*", at IIT Indore, 11th to 19th July 2016.

5. GIAN workshop on "*Chemical Sensors: Principles, Technologies and Applications",* at IIT Indore, 1st to 9th July 2016.

6. Poster presentation at *"2nd International Conference on Materials Science and Technology (ICMST)",* St. Thomas college Palai, Kerala, 05th-08th June 2016.

7. Poster presentation at "*PRL conference on Condensed matter Physics-2016 (PRLCCMP-2016)*", Physical Research Laboratory (PRL), Ahmedabad, India 11th-13th April 2016.

8. Poster presentation at "*Ramanujan Conclave*", 22nd-23rd December, 2015 at IIT Indore.

TABLE OF CONTENTS

LIST OF FIGURES

CHAPTER – 1

CHAPTER – 2

CHAPTER – 3

CHAPTER - 4

CHAPTER - 5

CHAPTER – 6

CHAPTER - 7

LIST OF TABLES

CHAPTER – 1

CHAPTER – 4

CHAPTER - 5

CHAPTER – 6

CHAPTER – 7

NOMENCLATURE

A

A	Ampere

B

BCS	Bardeen, Cooper, and Schrieffer
BL	Bean-Livingstone
BFGS	Broyden-Fletcher-Goldfrab-Shanno

C

CASTEP	Cambridge Sequential Total Energy Package Code
Cr	Chromium
Co	Cobalt
CDW	Charge density wave
CVT	Chemical vapour transport

D

D	Donor
DOS	Density of states
DFT	Density functional theory calculation

E

EDX	Energy dispersive x-ray
E_F	Fermi level
E	Elastic

F

FESEM	Field emission scanning electron microscopy
FE	Fishtail effect
FF	Flux flow
FLL	Flux line lattice
FET	Field-effect-transistor
FS	Fermi surface
FM	Ferromagnetism
Fe	Iron
F_p	Pinning force density

G

GL	Ginzburg Landau
Gi	Ginzburg number

H

H Hexagonal
H_{irr} Irreversible field
H_{c2} Upper critical field
H_{c1} Lower critical field

I

IVT Iodine vapour transport

J

J_c Critical current density

L

L_c Longitudinal coherence length
LO Larkin–Ovchinnikov

M

M Magnetization
MHL Magnetization hysteresis loop

N

$NbSe_2$ Niobium diselenides

P

PC Personal computer
P Plastic
PE Peak effect
PBE Perdew-Burke-Enzerhof

Q

Q Dynamical relaxation rate

R

RT Room temperature
RRR Residual resistance ratio
RE Rare earth element
R Rhombohedral

S

SEM Scanning electron microscopy
SQUID Superconducting quantum interference device
SMP Second magnetization peak effect
STM Scanning tunneling microscopy

SC	Superconductivity
S	Sulphur

T

T	Trigonal
TMDC	Transition metal dichalcogenides
TEM	Transmission electron microscopy
T_c	Critical transition temperature
T_{FM}	Ferromagnetic transition
TAFF	Thermally activated flux flow
TAE	Thermal activation energy

U

U_c	Apparent activation energy

V

V	Vanadium
VSM	Vibrating sample magnetometer
VL	Vortex lattice

W

W	Watt
WHH	Werthamer-Helfend-Hohenberg

X

XPS	X-Ray photoelectron spectroscopy
XRD	X-Ray diffraction

Z

ZC	Field cooled
ZFC	Zero field coole

Physical Constants and Conversion Factors

Flux quantum	$\Phi_0 = 6.02 \times 10^{23}$ Tm^2
Boltzmann's constant	$k = 1.38 \times 10^{-23}$ J/K, 8.62×10^{-5} eV/K
Electronic charge (magnitude)	$q = 1.6 \times 10^{-19}$ C
Electronic rest mass	$m_e = 9.11 \times 10^{-31}$ kg
Planck's constant	$h = 6.63 \times 10^{-34}$ J.s, 4.14×10^{-15} eV.s
Speed of light	$c = 3 \times 10^8$ m/s, 3×10^{10} cm/s

	Prefixes:
1 Å (angstrom) = 10^{-10} m	milli-, m- = 10^{-3}
1 μm (micron) = 10^{-6} m	micro-, μ- = 10^{-6}
1 nm (nano) = 10^{-9} m	nano-, n- = 10^{-9}
	kilo-, k- = 10^3
	mega-, M- = 10^6

CHAPTER 1

Introduction to Superconducting Materials

In this chapter, a brief description of the current research on different superconducting materials is demonstrated. It includes the discoveries from low transition temperature superconductors to high transition temperature superconductors, their properties and the applications associated with them. Also, the previous and the ongoing researches on Niobium Diselenide ($NbSe_2$) superconductor are highlighted. In this section all the significant characteristics of $NbSe_2$ single crystals have been discussed elaborately extracting from different physical properties measurements. Finally, this thesis covers a precise overview of the diverse applications of $NbSe_2$ and the objectives and outline of the thesis work.

1.1. Background and Motivation

1.1.1. Overview of Superconducting Materials

Succeeding the discovery of superconductivity in mercury at 4 K by Prof. Kamerlingh Onnes in 1911, various new superconducting materials have been explored, which led to an incredible growth of higher transition temperature (T_c) superconductors over the decades. This triumph makes a plateau at 23 K with the discovery of superconductivity in Nb_3Ge by Gavaler [**1**]. After 13 more years, the search of high T_c superconductors (*i.e.* ~ 35 K) were accelerated in 1986 after discovering "LBCO" (a mixed oxide of lanthanum, barium, and copper) by Bednorz and Muller [**2**], for which they were awarded the Nobel prize in 1987. Later, in this structure "La" is replaced by another rare earth element "Y" and reported T_c at 90 K in the "123" class of materials by several groups of United States, Japan, and China [**3**]. Shortly thereafter, still higher T_c values were found [**4**] in the "BSCCO" system (mixed oxides of bismuth, strontium, calcium, and copper) and the "TBCCO" [**5**] system (mixed oxides of thallium, barium, calcium, and copper). The discovery of high T_c superconductor enlightened the way to applications which involves only liquid N_2 cooling (77K), rather than liquid helium. Till now, there is no final agreement of the mechanism causing the high T_c in these materials. However, the most important difference in physical properties between a high T_c and conventional BCS type superconductors is the presence of extreme anisotropy which is caused by its layered structure, and from the extremely short coherence length. The layered structured materials show highly anisotropic magnetic behaviour, and in extreme case the two-dimensional behaviour that are resulted from the decoupled superconducting film planes. From this starting point of view, we will focus on the superconducting properties of the anisotropic, layered low T_c superconductors, which are easy to investigate due to moderate upper critical field (H_{c2}) and high critical current density (J_c). We will observe that the practical applicability of the superconducting materials can be improved significantly through controlling different competitive forces (Pinning force density, Lorentz force, *etc.*) acting on flux-line-lattice (FLL), which determines the T_c, J_c and H_c parameters of superconductors.

Among the various type of superconducting materials, quasi two-dimensional transition metal dichalcogenides (TMDCs) superconductors (i.e. 2H-$NbSe_2$, 2H-NbS_2, TaS_2 and so on) emerge as an essential class of materials which shows highly anisotropic nature associated with their layered structures. These materials are characterized by strong bonding within layers and weak (Van der Walls) interaction between the layers and thus exhibit structural anisotropy. From many decades the scientists are endeavouring to understand the vortex dynamics of FLL through rigorous experiments and theoretical approaches. TMDCs are acknowledged to cover different complex vortex phases (*i.e.*, vortex liquid state, Brag glass state, Vortex glass state, Vortex solid state) [**6**], instead of the simple Abrikosov [**7**] vortex lattice of type-II superconductors. Besides, these materials are studied extensively for understanding of fundamental physics among two dimensional materials and showing promising properties in electrical [**8**], mechanical [**9**] and optical devices [**10**]. Rapid and advanced developments have been made in the measurement process of transport and magnetic properties, which make possible to study the details of the transitions between different superconducting phases and anisotropy associated with diverse physical properties.

TMDC materials display a wide range of electronic properties. Depending on these diverse properties, they can be semiconductors ($MoSe_2$, MoS_2, WS_2, *etc*.), semimetals ($MoTe_2$, $PtTe_2$, *etc*.), metals ($NbSe_2$, etc.), superconductors ($NbSe_2$, NbS_2) and topological insulators (Sb_2Se_3, Bi_2Te_3). These materials have been enticing intense research efforts for possible applications in electronic and optoelectronic devices, such as field-effect transistors (FETs) [**11 - 14**], gas sensors [**15-18**], photodetectors [**19-25**], and solar cells [**26-28**]. Layered TMDCs divulge a rich and diverse source of two dimensional (2D) materials. The importance of these 2D materials is associated with their unusual electronic properties and high specific surface areas, which make them useful for applications ranging from electronics to energy storage [**29**]. More specifically, TMDC superconductors are widely investigated due to their layered structure, interplay between charge density wave (CDW) (commensurate, incommensurate) and superconductivity. They can be extracted from their bulk crystals and can be treated as 2D

superconductors [**30, 31**]. The structural and physical properties of these superconductors can be enriched by low doping levels [**32-34**]. Thus, TMDC superconductors take important positions in the materials chemistry.

1.1.2. Niobium Diselenide ($NbSe_2$): The Material of Interest

Literature Survey: Research on $NbSe_2$ is going on for many decades following to a tremendous achievement. $NbSe_2$ has rich literature as it is one of the most studied TMDCs that exhibits metallic behaviour at room temperature but undergoes to charge density wave phase at 33 K and superconductivity at 7.2 K [**35**]. Frindt *et al.* [**36**] first reported on the few molecular layers of 2H-$NbSe_2$ flakes exfoliating mechanically onto various substrates. He observed a decrease in T_c value with decreasing flake thickness in samples estimated to be less than six molecular layers thick. The ongoing researches of $NbSe_2$ superconductor can be categorized into several groups depending on its diverse characteristics. The foremost characteristic is the construction of novel phase diagram of $NbSe_2$ based on transition between different vortex phases and anomalous J_c characteristics through transport, *ac/dc* magnetic measurement and susceptibility study. These studies help improvement of fundamental properties of superconducting materials and open the possibility of discovering the room temperature superconductor. The outcomes of these studies are various novel vortex states like vortex solid state (vortex Bragg glass phase, vortex Bose glass phase), vortex glass phase, and vortex liquid phase (pinned vortex liquid state, unpinned vortex liquid state). On the other hand, the prominent anomalous J_c characteristics have been recognized as peak effect phenomena, fishtail effect (Second magnetization peak effect (SMP effect)) phenomena. Banerjee *et al.* [**37**] reported a generic phase diagram of $NbSe_2$ which is weakly pinned comprising six phases *i.e.*, Bragg glass, plastically deformed vortex glass phase, pinned amorphous phase, unpinned amorphous phase, a low density re-entrant glass phase and a Meissner phase. The boundary separating the re-entrant glass and the Bragg glass phases is referred as a prominent crossover phenomenon. Ravikumar *et al.* [**38**] reported the peak effect phenomena in weakly pinned $NbSe_2$ by metastable vortex states which is characterized by different J_c

characteristics largely influenced by the past thermomagnetic history of the superconductor. They suggested the peak effect phenomena as the occurrence of a first order phase transition from an ordered phase to a disordered vortex phase. Tomy *et al.* [**39**] constructed a generic vortex phase diagram of $NbSe_2$ based on the *ac* and *dc* magnetization measurements of the peak effect phenomena characterizing the phase boundaries of the possible order-disorder transformations in the vortex matter. However, the metastability and hysteretic vortex pinning near the order-disorder transition in $NbSe_2$ were discussed by Bermúdez *et al.* [**40**] that proposes a scenario governed by the interplay between the plastic and elastic energy barriers. Banerjee *et al.* [**41**] demonstrated the peak effect, plateau effect, and the fishtail effect anomaly in 2H-$NbSe_2$ through the magnetic field dependence of J_c characteristics in high-temperature and the low magnetic field region of the (H, T) space. Their experimental results exhibited different pinning regimes like individual pinning region (at low magnetic field), collective pinned quasiordered solid (at intermediate field) and the amorphous state (around the re-entrant peak-effect boundary). Further, Banerjee *et al.* [**42**] reported a generic phase diagram for vortex matter via a study of peak effect phenomenon in 2H-$NbSe_2$. Their experimental details successfully enlighten on the influence of disorder on the peak effect, the revolution of a topologically ordered FLL to a plastically deformed FLL at the onset of the peak effect, and the presence of robust metastability and history dependence of the magnetic response. On the other hand, Okamoto *et al.* [**43**] showed the experimental evidence of the pronounced Bragg glass density wave phase in $NbSe_2$ via scanning tunneling microscopy experiments. They indicated the charge density wave (CDW) is associated with locally strong pinning by non-negligible defects in “Bragg glass” phase having dislocations and antidislocations in bound pairs. Moreover, the glassy dynamics in a heavy ion irradiated $NbSe_2$ crystal was investigated by Eley *et al.* [**44**] with the application of columnar defects tilted ~ 30° from the *c*-axis. They discussed the possibility of competing disorder that introduces a field-orientation-driven transition from a Bose-glass to an anisotropic glass relating to both point and columnar disorder. Contrarily, Ganguli *et al.* [**45**] reported the disordering

of the vortex lattice through successive destruction of positional and orientational order in the weakly pinned $Co_{0.0075}NbSe_2$ single crystal using scanning tunnelling spectroscopy across the peak effect. At the onset of the peak effect, the equilibrium quasi-long range ordered state transforms into an orientational glass through the proliferation of dislocations.

Secondly, $NbSe_2$ is vastly investigated based on the debate of single band superconducting nature and the multi band superconducting nature. BCS (Bardeen, Cooper, and Schrieffer) theory predicts electron-electron pairing to be a direct result of electron-phonon interactions and evaluates the pairing strength as a function of momentum to be constant. This results the isotropic *s*-wave gap in conventional superconductors. This isn't the situation for high-temperature superconductors, where a highly anisotropic gap has been confirmed and unconventional pairing mechanisms other than electron-phonon interaction are actively considered. On the other hand, even for phonon-mediated *s*-wave superconductors, the presence of several Fermi surface (FS) sheets having different electron-phonon coupling constants and differing density of states (DOS) at the Fermi level (E_F) can contribute a momentum dependent superconducting gap in real materials. Several experiments confirmed the two bands or multiband superconductivity of $NbSe_2$ but generally an alternative explanation of the results regarding an anisotropic *s*-wave single band scenario could not be excluded. Due to the current discovery of the various novel superconductors, different novel concepts of the superconductivity have been well established, like *d*-wave pairing in cuprates [**46**] and two gap superconductivity in MgB_2 [**47, 48**]. Since then, interest has been gained considerately in the superconducting order parameter of $NbSe_2$ [**49**]. Recent studies of the superconducting order parameter in $NbSe_2$ largely approve that more than one energy scale is involved [**50-52**]. Zehetmayer *et al.* [**53**] represented the evidence of two-band scenario in $NbSe_2$ through reversible magnetization measurement. The field dependence of the reversible magnetization (M (B)) has been analysed based on Ginzburg Landau (GL) theory, stating that the M (B) cannot be satisfactorily delineated by the anisotropic single-band scenario but by multiband superconductivity associated with one anisotropic band and one almost isotropic band.

Yokoya *et al.* [**54**] investigated on the superconducting energy gap and the spectral function near superconducting transition in $NbSe_2$ resulting Fermi surface sheet dependent superconductivity in the background of low transition temperature multiband system via high-resolution angle-resolved photo emission spectroscopy. They designated both the Se 4*p* and Nb 4*d* derived sheets as the dominating sheets. Boaknin *et al.* [**55**] explored the heat transport study throughout the vortex state down to $T_c/100$ to provide strong evidence for multiband superconductivity in $NbSe_2$. They showed one localized states at fields very near H_{c2} and one delocalized quasiparticle excitations participating in the multiband superconductivity with distinct small and large superconducting gaps on different sheets of the Fermi surface. The gap on the pocket like Γ band is nearly 3 times lesser than the gap on the other two Fermi surfaces. Rodrigo *et al.* [**56**] also gives evidence of the presence of multiband superconductivity in $NbSe_2$ by using scanning tunneling microscopy/spectroscopy experiments indicating the distribution of gap values between 0.7 and 1.4 meV. Fletcher *et al.* [**57**] reported temperature dependence of both in-plane and out-of-plane penetration depths with a radio-frequency tunnel diode oscillation circuit supporting anisotropic superconductivity of this compound. Again, Huang *et al.* [**58**] gave the experimental evidence of the two-gap structure of $NbSe_2$ through specific heat study in external magnetic fields. They suggested two-gap scenario is more favourable than the anisotropic *s*-wave model to describe the gap structure of $NbSe_2$. They represented two-gap scenario with large gap (= 1.26 meV) and small gap (= 0.73 eV) in the two-gap model. The small gap is more isotropic and has a 3D-like feature and is located either on the Se-derived Fermi surface or on the bonding Nb Fermi sheets. However, the low field spin relaxation of ^{8}Li show the wide distribution of the superconducting gaps in $NbSe_2$, which supports the multiband superconductivity [**59**].

The other most fascinating and ongoing study on $NbSe_2$ is the coexistence of CDW and superconductivity and the correlation between them. The CDW transition in layered TMDCs has been studied extensively in the several years. Neutron diffraction studies on 2H-$NbSe_2$ show a

transition from a normal lattice to an incommensurate CDW phase around 30 K. On the other hand, 2H-$NbSe_2$ is a highly anisotropic type-II superconductor below T_c of 7.2 K. Therefore, superconductivity and the CDW ordered state coexist in 2H-$NbSe_2$ below 7.2 K. Sooryakumar *et al.* [**60**] demonstrated the superconducting energy gap in 2H-$NbSe_2$ and its coupling to charge density waves through Raman spectrum analysis. Straub *et al.* [**61**] studied the layered CDW material $NbSe_2$ by angle-resolved photoelectron spectroscopy. They represented the first experimental mapping of the Fermi surface (FS) portions that involved in the CDW transition suggesting that the CDW instability in this material is driven by FS nesting and not by saddle point singularities. Arguello *et al.* [**62**] reported the direct observation of the charge density wave (CDW) phase transition in real space in pristine $NbSe_2$ using atomic resolution scanning tunneling microscopy (STM). Spectroscopic imaging measurements of the real space phase show that an energy gap in $NbSe_2$ occurs at 0.7 eV below the Fermi energy in the CDW phase, indicating that strong electron-lattice interactions and not Fermi surface physics is the dominant source for CDW formation in $NbSe_2$. In contradiction, Borisenko *et al.* [**63**] supported nesting mechanism behind the CDW formation and showed that CDW and superconductivity are two competing phenomena. It anticipates the superconducting gap by eliminating the nested portions of the Fermi surface in contributing to superconductivity. Recently, Gye *et al.* [**64**] discovered that the CDW of 2H-$NbSe_2$ is comprised of two different, energetically competing structures. The lateral Heterostructures of two CDWs are entangled as topological excitations, which generate a CDW phase shift and the incommensuration without a conventional domain wall. However, Lian *et al.* [**65**] reported nicely the interplay of charge density wave and superconductivity in $NbSe_2$ with varying thickness. They showed that as the layer thickness decreases (from bulk to monolayer), the CDW order is gradually enhanced with rising energy gain and strengthened Fermi surface gapping, while superconductivity is weakened due to the increasingly reduced Fermi level density of states in the CDW state. Their results well explained the observed opposite thickness dependencies of CDW and superconducting transition temperatures and uncovered the nature of

competitive interaction between the two collective orders. Xi *et al.* [**66**] described the many-body collective order phase diagram of $NbSe_2$ down to a thickness of one monolayer. They showed superconducting transition temperature decreases on lowering the layer thickness, but charge-density-wave transition temperature increases from 33 K (in the bulk) to 145 K (in the monolayer). Such strange enhancement of charge density waves can be implicated to be a result of considerably enriched electron-phonon interactions in two-dimensional structure and is assumed due to the large blueshift of the collective amplitude vibration. Rossnagel *et al.* [**67**] nicely visualized the Fermi surface of $NbSe_2$ to find its implications on the charge-density-wave mechanism. They reported the detailed experimental and theoretical investigation of the Fermi-surface topology of $NbSe_2$ around the second-order phase transition into incommensurate charge-density-wave phase at 33.5 K. High-resolution angle-resolved photoemission with synchrotron radiation yielded two Nb 4*d*-related Fermi-surface cylinders with a Se $4p_z$-derived pocket around the centre of the Brillouin zone, which opposed the results of Straub *et al.* [**61**] claiming that the driving mechanism for the charge-density-wave transition associated with Fermi-surface nesting. Following to their works, Johannes *et al.* [**68**] investigated actual relation of the Fermi-surface nesting with the charge-density wave in $NbSe_2$ through density functional calculations. They estimated the real part of the noninteracting susceptibility, which represents the magnitude of CDW instability and the imaginary part, which expresses Fermi surface (FS) nesting. They showed that FS nesting isn't responsible for CDW instability in $NbSe_2$ and briefly addressed the contribution of electron-electron interactions in the total susceptibility of $NbSe_2$. Méasson *et al.* [**69**] reported on the experimental evidence for the observation of the superconducting (SC) amplitude mode *i.e.* the pronounced ''Higgs" mode using Raman scattering. They demonstrated that the SC mode in $NbSe_2$ cannot be a simple Cooper pair breaking peak but is associated with the coupling to the CDW amplitude mode.

The last most extensive effort has been done to obtain modification of the above said properties of $NbSe_2$ by applied pressure [**70, 71**], doping, irradiation and layer thickness [**72**]. Hydrostatic pressure increases T_c and

the effective dimensionality of the electronic structure of $NbSe_2$ followed by degradation in T_{cdw} value [**73**]. Again, there are many focussed investigations going on towards the correlation of superconductivity and CDW in the presence of defects. Mutka *et al.* [**74**] showed that less than 1% of irradiation-induced lattice defects in the form of displaced metal atoms have significant contributions on the competition of CDW and superconductivity in $NbSe_2$. He elucidated on the fact that superconducting transition temperature can be enhanced by destroying the long range coherence of the CDW phase. Moreover, the nature of relationship between the interlayer distance and T_c of $NbSe_2$ upon intercalation is also a matter of fundamental interest in understanding the superconductivity of anisotropic, layered compounds. Theoretical investigations on the effect of intercalation on the T_c of $NbSe_2$ predict that the donor-type intercalant suppresses the T_c value, whereas, the accepter-type intercalant raises the T_c until there is no lattice instabilities [**75**]. Yan *et al.* investigated nicely the trend of degradation of T_c with S substitution and Cu intercalation or by both Cu and S substitution in $NbSe_2$ [**76**]. It is also to be noted that Cu intercalation in $NbSe_2$ resulted an unusual S shaped suppression of superconductivity [**77**]. Fan *et al.* [**78**] reported the variation in structural and superconducting properties in Rb intercalated $NbSe_2$ demonstrating a surprising L shaped quick suppression of superconductivity. Their results bring the fact that larger ionic radius, higher valence, and magnetic moment bring a faster suppression of superconductivity in $NbSe_2$. Naik *et al.* [**79**] reported influence of Sn intercalation on superconducting properties of $NbSe_2$ through structural, spectroscopic, magnetic and transport studies. Both T_c and $H_{c2}(0)$ have been suppressed with Sn intercalation. They suggested that there is no correlation between the superconductivity and the CDW transition in the layered structure of $NbSe_2$. Prodan *et al.* [**80**] investigated the surface superstructures in niobium diselenide intercalated by Cu, Co and Fe, which shows that different intercalate fill selectively the available interstitial sites forming composition dependent superstructures with different stacking of the host crystals. Iavarone *et al.* [**81**] used low temperature scanning tunneling microscopy and spectroscopy to study the effect of Co and Mn atomic impurities on the superconducting state of

$NbSe_2$. On the other hand, the effect of Te doping on the superconductivity and charge-density wave in $NbSe_2$ by Wang *et al.* [**82**] revealing that both the *RRR* value and T_c decrease monotonically with increasing Te content and the disorder induced by impurity Te is remarkable. Mohammed Kars *et al.* [**83**] also did the research on the structures of two intercalation compounds $Ge_{0.2}NbSe_2$ and $Ge_{0.3}NbSe_2$ using single crystal X-ray diffraction, high resolution electron microscopy and X-ray microanalysis, shedding light on some different superstructures and diffracted diffuse intensity.

Compiling all the pioneering research works on $NbSe_2$, the unique and remarkable properties are enlisted below that led $NbSe_2$ to consider as an appropriate candidate for the study of fundamental superconducting properties (T_c, H_{c2}, and J_c), dynamics of vortices and the associated pinning mechanism.

1) $NbSe_2$ has transition temperature at 7.2 K and its upper critical field not much larger than 4 T perpendicular (B_{c2}^{c}, *c* direction) and 12 T parallel (B_{c2}^{ab}, *ab* direction) to Nb planes. Accordingly, most part of the superconducting phase diagram is accessible to experiment, in contrast to the high T_c materials. Besides, the large anisotropy associated with the magnetic and electronic properties of $NbSe_2$ are also comparable to the high-T_c superconductors. So, the outcomes of the experimental analysis of $NbSe_2$ can be applicable to the improvement of physical properties of high-T_c superconductors.
2) Large high-quality single crystals of $NbSe_2$ with almost negligible vortex pinning effects can be grown. Introducing a small amount of disorder (e.g. by particle irradiation, doping) may lead to the emergence of the numerous well-known phenomena (peak effect, fishtail effect), which is still discussed a lot by the superconductivity community to improve the field dependence characteristics of J_c.
3) $NbSe_2$ was the first material in which scanning tunneling microscopy was successfully employed for observing vortex cores or distribution, and it is still widely used for such investigations.

This will open the path of controllable manipulation of single vortices in different conditions.

4) The charge-density-wave state, formed about 33 K, allows studying the effect of competing order parameters in layered crystal structure, which is an important issue for high temperature superconductors.
5) Ginzburg number, Gi ($= k_B T_c / H_c^2 \varepsilon \xi^3$), a measure of the importance of fluctuations, is lower (~ 10^{-4}) than the cuprates (~10^{-2}) but much larger than in typical low-T_c materials (~10^{-8}). So, $NbSe_2$ can be considered an ideal system to study the interplay of thermal fluctuations, pinning force density and the elasticity of flux line lattice.

Crystal Structure: $NbSe_2$ is a metallic black material, sometimes with a slightly greenish form [**84**]. $NbSe_2$ has a hexagonal crystal structure of space group 194-$P6_3/mmc$. In 1962, Brixner first reported the unit-cell parameters of $NbSe_2$ and suggested associated structural models [**85**]. Afterward, in rapid progression, several other groups published their investigations on $NbSe_2$ [**86-93**]. Brown and Beerntsen [**86**] investigated polypism among Nb- and Ta-selenides and the formation of single crystals of two-, three- and four layer selenides, providing the information about unit cell parameters and space group data. Revolinsky *et al.* [**89**] identified the different chalcogenides (particularly selenide and telluride) phases in the vicinity of Niobium dichalcogenides ($NbCh_2$) and Tantalum dichalcogenides ($TaCh_2$) using X-ray techniques. Seite *et al.* [**88, 90**] studied the intermediate phases in the selenide and telluride systems of Nb and Ta and Kadijk synopsized all the information about polytypism of $NbSe_2$ in 1971 [**87**]. Huisman *et al.* [**92**] discussed about the non-stoichiometric $Nb_{1+x}Se_2$ and $Ta_{1+x}Se_2$ phases. Revolinsky *et al.* [**93**] investigated the dependence of the superconducting transition temperature on the variation of composition and structure in the two-layered hexagonal $NbSe_2$ and in the four-layered $NbSe_2$. They represented the impact of stoichiometry on the superconductivity highlighting on the difficulty to achieve the equilibrium and reproducibility in the Nb-Se system. TMDCs can be found in different polymorphs called 1T, 2H, 4H and 3R. Here the

numbers indicate the number of layers in the unit cell and the letters denote the symmetry (T-trigonal, H-hexagonal, and R-rhombohedral). Each layer contains three atomic planes with a hexagonally filled plane of metal atoms sandwiched between two planes of chalcogen atoms with a thickness of 6-7 Å. Metal atoms are six-fold coordinated within a layer and their bonding geometry can be either prismatic or octahedral. In the trigonal prismatic phase, the two chalcogenides planes developing a slab are stacked directly above each other, while in the octahedral arrangement they stagger. The different polymorphs of $NbSe_2$ have been recognized [**86, 87, 94**] as the 2H-$NbSe_2$ and 4H(*a*)-$NbSe_2$, which are stable at lower temperatures, and the two other high temperature forms denoted as 1T-$NbSe_2$ and 4H(*d*)-$NbSe_2$ respectively. Besides, there is also another form known as 3R-$NbSe_2$ (also stated to be 3R-$Nb_{1+x}Se_2$). The 2H-$NbSe_2$ and 4H*a*-$NbSe_2$ follow trigonal-prismatic coordination, the 1T-$NbSe_2$ has octahedral coordination, while in the 4H*d*-$NbSe_2$, layers with alternatively octahedral and trigonal prismatic coordination of Nb atom. On the other hand, the 3R-$NbSe_2$ has only prismatic coordination. The preferred phase adopted by $NbSe_2$ depends predominantly on the *d*-electrons, although a certain dependence on the relative size of the atoms plays a prominent role. The most two common crystalline forms of $NbSe_2$ are 2H-$NbSe_2$ and 4H*a*-$NbSe_2$. The 2H-$NbSe_2$ unit cell contains two $NbSe_2$ units with ABAB staking. Each unit is formed from a sandwich of two layers of Se atoms with Nb atom layer between them. The coordination number of Se atoms is 3, while it is equal to 6 for Nb atoms. Each selenium atom is surrounded by three Niobium atoms. Strong covalent bonds exist inside the layers, while there is a weak interaction between adjacent layers as a result of van der Waals coupling. The Se-Nb bonds within a sandwich are covalent bonds, and they form the 2D-hexagonal lattice. The $NbSe_2$ molecular layers are bound by Van der Waals coupling. Thus 2H-$NbSe_2$ is easy to cleave along a plane parallel to the layers. The Se sheet is usually the termination layer after exfoliation.

The spacing between Nb sheets is 6.3 Å. Therefore, the *c*-axis of the unit cell is 12.6 Å, while the *a*-axis lattice constant is 3.6 Å [**35**]. Moreover, the 2H polymorphs can exist in three different modifications, with 2H*a*, 2H*c* and 2H*b*. These three forms have different stacking symmetries. In

2H*a* (AbA CbC) stacking, Nb atoms in one layer are located on top of Nb atoms of the neighbouring layer.

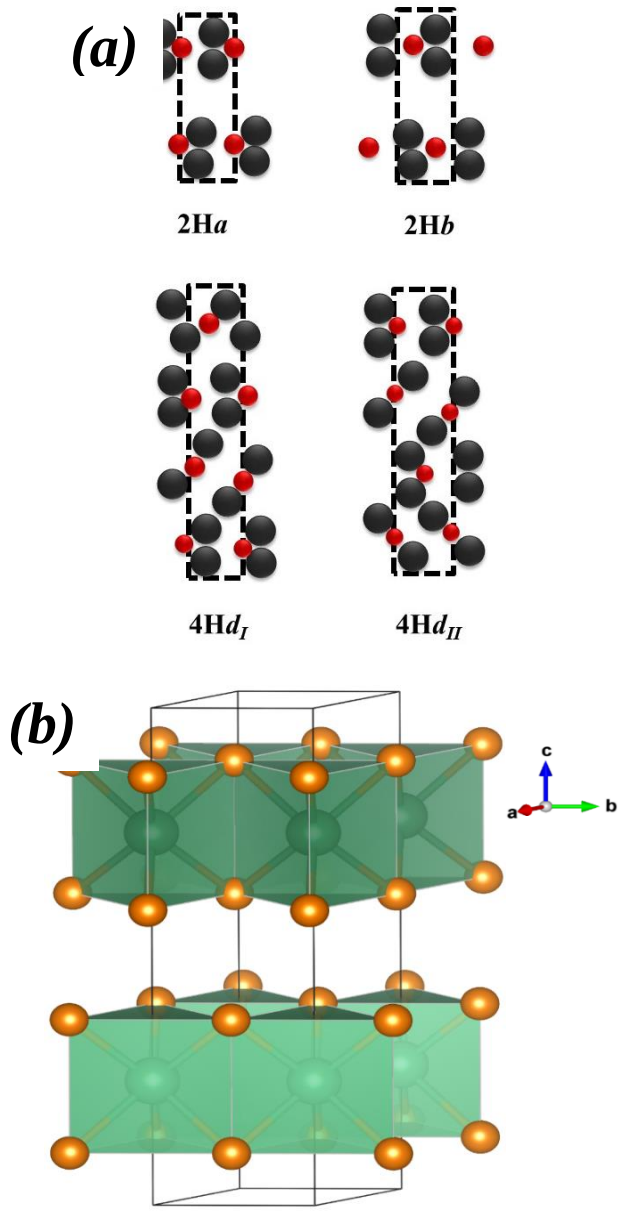

Figure 1.1. *(a) 1120 section diagram of 2Ha-$NbSe_2$ and 2Hb-$NbSe_2$ and two possible models for 4Hd-$NbSe_2$. Transition-metal atom and selenium atom are represented by small red circles and big black circles, respectively; (b) 3D structure of 2H-$NbSe_2$. The unit cell is defined with the c axis perpendicular to the layers, and the a and b axes along the minimal chalcogen - chalcogen distance.*

The 2*Hc* polymorph is characterized by the CaC AcA stacking, *i.e.* any transition metal atom is located on top of two chalcogenides atoms of the subsequent layer. This polytype form does not exist in $NbSe_2$. The 2*Hb* polytypes are obtained for the nonstoichiometric compounds $Nb_{1+x}Se_2$ and $Ta_{1+x}Se_2$, with the excess Nb atoms intercalated in the VdW interlayer gap.

The structures of typical 2Ha-$NbSe_2$, 2Hb-$NbSe_2$ and 4Hd-$NbSe_2$ are shown in Figure 1.1 (*a*) and Figure 1.1 (*b*) represents the 3D-structure of 2H-$NbSe_2$.

Table 1.1. *Physical parameters of* $NbSe_2$ [**12, 77, 87, 95 - 96**]**.**

Property	Value
Molecular formula	$NbSe_2$
Molar mass	250.83 $g.mol^{-1}$
Appearance	Black Metallic luster
Odour	Odourless
Crystal size	$0.04\times 0.04 \times 0.008$ mm^3
Stable phase at 300 K	2H-$NbSe_2$ and 4H(*a*)-$NbSe_2$
boundaries	{100}, {010}, {001}
Space group	$P6_3/mmc$ (#194)
Coordination no.(z)	2
Lattice Constants	$a = b$ =3.4425 (5) Å, c= 12.547 (3) (Å)
Unit cell volume (V)	128.77 (4) $Å^3$
Density	6.467 g/cm^{-3}
Melting point	> 1300°C
Thermal conductivity	70 mW/K cm @ T= 8 K [1]
Electronic specific heat coefficient (γ)	17.4 mJ mol^{-1} K^{-2}
Phonon specific heat coefficient (β)	0.56 mJ $mol^{-1}K^{-4}$
Debye temperature (θ_D)	218 K
Electron-phonon coupling constant (λ_{ep})	0.81
Density of states ($N(E_F)$)	4.08 eV^{-1}
Energy Gap	0.9-1.0 eV @ T= 5.3 K
Seebeck coefficient (S)	-4.08 μV/K @T= 300 K
Resistivity	0.68×10^{-4} Ω-cm @ T= 300 K

2H-$NbSe_2$ is a conventional superconducting material having a highly anisotropic energy gap. 2H-$NbSe_2$ is a normal metal above ≃ 7.2 K, while, it becomes a type-II superconductor below ≃ 7.2 K. Both 2H-$NbSe_2$ and 4H-$NbSe_2$ phases are type-II superconductors having slightly different T_c values. The CDW transition temperature of 4H-$NbSe_2$ (~ 42 K) is much higher than the CDW transition of 2H-$NbSe_2$ (~ 35 K) [**95**]. The negative

value of Seebeck coefficient of 4H-$NbSe_2$ is nearly twice as compared to 2H-$NbSe_2$. The higher room temperature resistivity, RRR ratio, and the absolute value of Seebeck coefficient of 4H-$NbSe_2$ indicate the presence of higher electron density of d-band in 4H-$NbSe_2$ as compared to 2H-$NbSe_2$ [**95**]. However, in this thesis work, we have concentrated on the synthesis and physical properties characterization of 2H-$NbSe_2$ superconductor because of higher T_c value and lesser number of atoms involved in the formation of unit cell. Table 1.1 represents some of the elementary physical parameters of 2H-$NbSe_2$. It should be noted that there is still uncertainty in some of these values. For example, the values for energy gap show some spread in values, which may be the result of the influence of two band superconductivity, like the case for MgB_2.

In $NbSe_2$, electrons can travel easily inside the layers, while simultaneously an overlap of the electronic wave function exist between the layers because of the Van der Waals character of the layer interaction. This fact is strongly linked with the anisotropy of the electronic properties of $NbSe_2$ [**97**]. Hence, $NbSe_2$ signifies a new model system for studying superconductivity in low-dimensional systems [**31, 36**]. Generally, the 2D nature of TMDC materials stimulates the manifestation of electronic instabilities that are determined by Fermi surface nesting. This creates CDW phases in TMDCs. CDW is an ordered quantum fluid of electrons in a linear chain compound or layered materials. The electrons within a CDW form a standing wave pattern and flows through a linear chain compound in a highly correlated fashion. $NbSe_2$ is a well-known TMDC for showing the coexistence of CDW and superconductivity at low temperature as we discussed already in the previous section. Numerous investigations on the Fermi surface and band structure have been accomplished in the normal and superconducting states of $NbSe_2$ to shed light on the coexistence of CDW and superconductivity. The first electronic structure calculations for $NbSe_2$ were reported by Mattheiss in 1973 [**98**]. He derived two bands crossing the Fermi energy and addressed nesting to generate CDW transition in $NbSe_2$. Generally, $NbSe_2$ consists of three Fermi surfaces (small Se-derived pancake surface, the bonding Nb-derived Fermi surface with strong wrapping along z direction and the nearly 2D anti-bonding Nb-derived

Fermi surface), which assists the CDW to persist in the superconducting state [**68, 99**]. Moreover, the interaction of the d-orbitals of Nb atoms with the outer *p*-orbitals of Se atoms in the unit cell assists to understand the band structure and appreciate the shifts of the Fermi energy. Lots of literatures have been reported on the energy bands of two dimensional (2D) $NbSe_2$ and three dimensional (3D) $NbSe_2$ [**98**]. Lebègue *et al.* [**100**] demonstrated nicely the 2D band structure of a single molecular layer of $NbSe_2$. Two prime characteristics have been noticed near the Fermi level of $NbSe_2$. Firstly, the bands across the band gap are comparatively flat due to the "*d*"character of the electronic states at these energies, and secondly, the band state which is pinned at the Fermi level (mainly created from the Nb *d*-orbitals) is separated in energy from all other states.

1.2. Application of Niobium Diselenide

TMDCs have stimulated marvellous research interest because of their numerous fascinating properties for application in superconductor [**12**], photodetector [**12**] and spintronic devices [**30**, **31**, **66, 101-103**]. Current experimental progresses on $NbSe_2$ and its two-dimensional (2D) single crystals have revealed a variety of unusual physical and electronic phenomena, comprising the reduced superconducting transition temperature on reducing the sample thickness to nanoscale [**101, 102**], 2D superconductivity [**30**], the coexistence of charge-density-wave (CDW) order and superconductivity [**101**], the Ising pairing protected by spin-momentum locking in superconductivity [**30**], the tenability of the superconducting and CDW transition temperatures [**66**], and the Bose-metal state under a magnetic field [**103**]. The Ising superconductivity with its auspicious applications in equal spin Andreev reflections [**104**], proximity phenomenon [**105**], engineering Majorana fermions [**104, 106**], and the topological superconductivity [**107**] has accelerate extreme attention in condensed matter physics and material science. The transport, magnetic and superconducting properties of $NbSe_2$ can also be well tuned by introducing both intrinsic and extrinsic defects and implicated in a broad range of applications.

1.3. Scope and Goals of Thesis

The key objective of this thesis is to grow large $NbSe_2$ single crystals with high purity which have versatile fundamental properties in its unique approach contributing to the different fields of condensed matter physics and material science. The initial effort is to synthesize large $NbSe_2$ single crystal first and thoroughly investigate the criteria to improve its different fundamental superconducting properties. The prepared $NbSe_2$ single crystals are employed to magnetic and magnetoresistance measurement to shed light on the dynamics of quantized magnetic vortices and their pinning by materials defects to improve its ability to carry non-dissipative currents. It highlights on the phase transitions, collective creep of vortex lattice and pinning at different kinds of pinning centres of pure as well as doped $NbSe_2$ in response to an external *dc* magnetic field. Novel phase diagrams of doped $NbSe_2$ single crystals have been also constructed at different magnetic fields and temperatures based on the analysis of T_c, H_{c2}, J_c characteristics and pinning mechanism. The comparisons between the phase diagrams of the low and high T_c superconductors will help us to unveil the physics behind the layered high T_c superconductors and may give further the solution to synthesize room temperature superconductors.

1.3.1. Thesis objectives

The specific ideas of the research work plans are classified as follows:

1. Growth of large $NbSe_2$ single crystals using the chemical vapour transport method with Iodine as transporting element.
2. To comprehend the growth mechanism of the formation of large and pure single crystals having higher RRR ratios.
3. Influence of doping on $NbSe_2$ single crystal to study the change of their structural, transport and magnetic properties.
4. To improve the J_c characteristics and the associated pinning mechanism of $NbSe_2$ superconductor in presence of intrinsic and extrinsic defects and construction of phase diagram in all available range of temperatures and magnetic fields for the applications of high electromagnetic fields (*i.e.*, magnetic resonance imaging (MRI) and nuclear magnetic resonance (NMR) machines).

1.3.2. Thesis outline

Regarding the chosen objectives, and evaluating all the information extracted from literature survey, the precise growth of $NbSe_2$ single crystal is implemented successfully. The formation of $NbSe_2$ single crystals is led by simple chemical vapour transport method using Iodine as a transporting agent followed by properties characterizations. In combination with $NbSe_2$ single crystals, the impact of doping on $NbSe_2$ is also investigated through performing systematic characterizations of the defect induced materials to comprehend their physical properties. The different characteristics of pure and doped $NbSe_2$ single crystals then are successfully utilized to form phase diagram based on core interaction and competing vortex phases.

In this thesis, all the above specified works have been demonstrated in the form of eight chapters confined between the introduction chapter (chapter 1) and conclusions chapter (Chapter 8). The chapter subjects are compiled as follows:

Chapter 1, designated as "Introduction to the Superconducting Materials" represents a literature review starting from different kind of (both low T_c and high T_c) superconductors to the highly anisotropic layered transition metal dichalcogenides superconductors where major emphasis is given on the $NbSe_2$ superconductor.

Chapter 2, designated as "Essential Models of Superconductivity" provides the different models of superconductivity those are essential to study the fundamental superconducting properties of $NbSe_2$ in both bulk as well as 2D form.

Chapter 3, designated as "Experimental Techniques" gives the details information of the experimental setup and the preparing procedures employed to the formation of $NbSe_2$ single crystals. A precise description of the several analytical characterization tools is also complied. Further, the preparation of materials involved for the desired measurements is also briefly depicted.

Chapter 4, designated as "Effect of Fe Doping on $NbSe_2$ Single Crystal" represents the effect of iron (Fe) doping in $NbSe_2$ through investigating its structural and superconducting properties. To control the applicability of

superconducting material in high magnetic field and high current density, this doping is accomplished. This work gives a comprehensive analysis regarding critical current density, vortex dynamics and their pinning into the different pinning centres through the magnetization studies.

Chapter 5, designated as "Study of vortex dynamics of $NbSe_2$ single crystals in presence of Cr atoms" provides the alternation of the superconducting properties of $NbSe_2$ due to chromium (Cr) doping through magnetization measurement with different relaxation rate. This chapter focuses on the improvement of J_c characteristics at high magnetic fields. A detailed understanding of the different features associated with pinning force density is also described in this chapter.

Chapter 6, designated as "Study of Structural, Slectronic, Transport and Magnetic Properties in Defect Induced $NbSe_2$" provides in-depth analysis of the impact of intrinsic (via formation of non - stoichiometric $NbSe_2$) as well as extrinsic defect (via incorporation of Fe atoms) to the structural, electronic, transport and magnetic properties of $NbSe_2$. To check the applicability in superconducting spintronic and quantum computing, the coexistence of ferromagnetism and superconductivity is systematically investigated in defect induced $NbSe_2$ through transport and magnetic properties. To observe the effect of both intrinsic and extrinsic defect in the thermally activated flux flow region (TAFF) of $NbSe_2$, magnetoresistance measurements is performed. The band structures and density of sates (DOS) of the above mentioned two cases is also investigated through first-principle density functional theory.

Chapter 7, designated as "Effect of V doping on $NbSe_2$ single crystal and Study of vortex phase diagram" provides the detailed analysis of the effect of vanadium (V) atoms in the disordering of vortex lattice, J_c characteristics and the vortex phases of $NbSe_2$ superconductor. The concentration dependence of the SMP effect and the transitions (*i.e.,* collective to plastic transition, vortex glass critical state to vortex glass transition) between different superconducting states (*i.e.,* vortex solid state, vortex glassy state and vortex liquid state) is studied thoroughly with magnetic and

magnetoresistance measurements. Finally, a vortex phase diagram of V doped $NbSe_2$ is constructed to understand the superconducting properties of anisotropic layered (both low T_c and high T_c) materials.

Chapter 8, designated as "The Conclusions and Scope for Future Work" synopsized the complete studies achieving remarks drawn from the thesis by establishing its title and suggested objectives. This chapter also features the possible opportunity of expanding this work in the near future.

References

[1] Gavaler J. R. (1973), Superconductivity in Nb-Ge films above 22 K, Appl. Phys. Lett., 23, 480-487.

[2] Bednorz J. G., Muller K. A. (1986), Possible high T_c superconductivity in the Ba-La-Cu-O system, Z. Phys. B, 64, 189-193.

[3] Wu M. K. *et al.* (1987), Superconductivity at 93 K in a new mixed-phase Y-Ba-Cu-O compound system at ambient pressure, Phys. Rev. Lett., 58, 908-910.

[4] Maeda H. *et al.* (1988), A new high-T_c oxide superconductor without a rare earth element, Jpn. J. Appl. Phys., 27, L209.

[5] Sheng Z. Z., Hermann A.M. (1988), Superconductivity in the rare-earth-free Tl-Ba-Cu-O system above liquid-nitrogen temperature, Nature, 232, 55-58.

[6] Blatter G., Feigel'man M. V., Geshkenbein V. B., Larkin A. I., Vinokur V. M. (1994), Vortices in high-temperature superconductors, Rev. Mod. Phys., 66, 1125.

[7] Abrikosov A. A. (1957), On the magnetic properties of superconductors of the second group, Sov. Phys. JETP, 5, 1174-1182.

[8] Bertolazzi S., Krasnozhon D., Kis A. (2013), Nonvolatile memory cells based on MoS_2/graphene heterostructures, ACS Nano, 7, 3246-3252.

[9] Cardinal M. F., Castro P. A., Baxi J., Liang H., Williams F. J. (2009), Characterization and frictional behavior of nanostructured Ni-W-MoS_2 composite coatings, Surf. Coat. Technol., 204, 85-90.

[10] Li J., Liu X., Pan L., Qin W., Chen T., Sun Z. (2014), MoS_2-reduced graphene oxide composites synthesized via a microwave-assisted method for visible-light photocatalytic degradation of methylene blue, RSC Adv., 4, 9647-9651.

[11] Radisavljevic B., Radenovic A., Brivio J., Giacometti V., Kis A. (2011), Single-layer MoS_2 transistors, Nat. Nanotechnol, 6, 147-150.

[12] Wang Q. H., Zadeh K. K., Kis A., Coleman J. N., Strano M. S. (2012), Electronics and optoelectronics of two-dimensional transition metal dichalcogenides, Nat. Nanotechnol., 7, 699-712.

[13] Fiori G., Bonaccorso F., Iannaccone G., Palacios T., Neumaier D., Seabaugh A., Banerjee S. K., Colombo L. (2014), Electronics based on two-dimensional materials, Nat. Nanotechnol., 9, 768-779.

[14] Wachter S., Polyushkin D. K., Bethge O., Mueller T. A. (2017), Microprocessor based on a two-dimensional semiconductor, Nat. Commun., 8, 14948.

[15] Perkins F. K., Friedman A. L., Cobas E., Campbell P. M., Jernigan G. G., Jonker B. T. (2013), Chemical vapor sensing with monolayer MoS_2, Nano Lett., 13, 668-673.

[16] Late D. J. *et al.* (2013), Sensing behavior of atomically thin-layered MoS_2 transistors, ACS Nano, 7, 4879-4891.

[17] Cho B. *et al.* (2015), Charge-transfer-based gas sensing using atomic-layer MoS_2, Sci. Rep., 5, No. 8052.

[18] Choi S. Y. *et al.* (2017), Effect of Nb doping on chemical sensing performance of two-dimensional layered $MoSe_2$, ACS Appl. Mater. Interfaces, 9, 3817-3823.

[19] Sanchez O. L., Lembke D., Kayci M., Radenovic A., Kis A. (2013), Ultrasensitive photodetectors based on monolayer MoS_2, Nat. Nanotechnol., 8, 497-501.

[20] Koppens F. H. L., Mueller T., Avouris P., Ferrari A. C., Vitiello M. S., Polini M. (2014), Photodetectors based on graphene, other two-dimensional materials and hybrid systems, Nat. Nanotechnol, 9, 780-793.

[21] Amani M. *et al.* (2015), Near-unity photoluminescence quantum yield in MoS_2, Science, 350, 1065-1068.

[22] Wen Y. *et al.* (2016), Integrated high-performance infrared phototransistor arrays composed of nonlayered PbS-MoS_2 heterostructures with edge contacts, Nano Lett., 16, 6437-6444.

[23] Wen Y. *et al.* (2016), Epitaxial 2D PbS nanoplates arrays with highly efficient infrared response, Adv. Mater., 28, 8051-8057.

[24] Wang Q. *et al.* (2016), High-performance phototransistor of epitaxial PbS nanoplate-graphene heterostructure with edge contact, Adv. Mater., 28, 6497-6503.

[25] Wang Q. *et al.* (2015), BN-enabled epitaxy of $Pb_{1-x}Sn_xSe$ nanoplates on SiO_2/Si for high performance mid-infrared detection, Small, 11, 5388-5394.

[26] Bernardi M., Palummo M., Grossman J. C. (2013), Extraordinary sunlight absorption and one nanometer thick photovoltaics using two-dimensional monolayer materials, Nano Lett., 13, 3664-3670.

[27] Tsai M. L. *et al.* (2014), Monolayer MoS_2 heterojunction solar cells, ACS Nano, 8, 8317-8322.

[28] Furchi M. M., Zechmeister A. A., Hoeller F., Wachter S., Pospischil A., Mueller T., (2017), Photovoltaics in Van der Waals heterostructures, IEEE J. Sel. Top. Quantum Electron, 23, 106-116.

[29] Coleman J. N. *et al.* (2011), Two-dimensional nanosheets produced by liquid exfoliation of layered materials, Science, 331, 568-571.

[30] Xi X., Wang Z., Zhao W., Park J. H., Law K. T., Berger H., Forro L., Shan J., Mak K. F. (2016), Ising pairing in superconducting $NbSe_2$ atomic layers, Nat. Physics, 12, 139-143.

[31] Staley N. E., Wu J., Eklund P., Liu Y., Li L., Xu Z. (2009), Electric field effect on superconductivity in atomically thin flakes of $NbSe_2$, Phys. Rev. B, 80, 184505.

[32] Wilson J. A., Yoffe A. D. (1969), The transition metal dichalcogenides discussion and interpretation of the observed optical, electrical and structural properties, Adv. Phys., 18, 193-335.

[33] Kalikhman V. L., Golubnichaya A. A., Gladchenko E. P., Prokudina V. K., Shchepinova L. P. (1982), Crystal structure and electrical resistivity of MoS_2-NbS_2 alloys produced by self-propagating high-temperature synthesis, Powder Metall. Met. Ceram., 21, 801-803.

[34] Ivanovskaya V. V., Heine T., Gemming S., Seifert G. (2006), Structure, stability and electronic properties of composite $Mo_{1-x}Nb_xS_2$ nanotubes, Phys. Status Solidi B, 243, 1757-1764.

[35] El-Bana M. S., Wolverson D., Russo S., Balakrishnan G., Paul D. M., Bending S. J. (2013), Superconductivity in two-dimensional $NbSe_2$ field effect transistors, Supercond. Sci. Technol., 26, 125020.

[36] Frindt R. F. (1972), Superconductivity in ultrathin $NbSe_2$ layers, Phys. Rev. Lett., 28, 299-301.

[37] Banerjee S. S. *et al.* (2000), Magnetic phase diagram of weakly pinned Type-II superconductors, J. Phys. Soc. Jpn., 69, 262-275.

[38] Ravikumar G. *et al.* (2000), Stable and metastable vortex states and the first-order transition across the peak-effect region in weakly pinned 2H-$NbSe_2$, Phys. Rev. B, 63, 024505.

[39] Tomy C. V. *et al.* (2002), Study of the peak effect phenomenon in single crystals of 2H-$NbSe_2$, Pranama, 58, 925-935.

[40] Bermudez M. M., Louden E. R., Eskildsen M. R., Dewhurst C. D., Bekeris V., Pasquini G. (2017), Metastability and hysteretic vortex pinning near the order-disorder transition in $NbSe_2$: Interplay between plastic and elastic energy barriers, Phys. Rev. B, 95, 104505.

[41] Banerjee S. S. *et al.* (2000), Peak Effect, plateau effect and fishtail anomaly: The reentrant amorphization of vortex matter in 2H-$NbSe_2$, Phys. Rev. B, 62, 11838.

[42] Banerjee S. S. *et al.* (1998), Generic phase diagram for vortex matter via a study of peak effect phenomenon in crystals of 2H-$NbSe_2$, Phys. C, 308, 25-32.

[43] Okamoto J. I., Arguello C. J., Rosenthal E. P., Pasupathy A. N., Millis A. J. (2015), Experimental evidence for a Bragg glass density wave phase in a transition-metal dichalcogenide, Phys. Rev. Lett., 114, 026802.

[44] Eley S. *et al.* (2018), Glassy dynamics in a heavy ion irradiated $NbSe_2$ crystal, Sci. Rep., 8, 13162.

[45] Ganguli S. C., Singh H., Saraswat G., Ganguly R., Bagwe V., Shirage P. M., Thamizhavel A., Raychaudhuri P. (2015), Disordering of the vortex lattice through successive destruction of positional and orientational order in a weakly pinned $Co_{0.0075}NbSe_2$ single crystal, Sci. Rep., 5, 10613.

[46] Yang H. D., Lin J. Y. (2001), Low temperature specific heat studies on the pairing states of high-Tc superconductors: a brief review, J. Phys. Chem. Solids, 62, 1861-1870.

[47] Bonquet F. *et al.* (2001), Phenomenological two-gap model for the specific heat of MgB_2, Europhys. Lett., 56, 856.

[48] H. D. Yang *et al.*, (2001), Order parameter of MgB_2: A fully gapped superconductor, Phys. Rev. Lett., 87, 167003.

[49] T. Han *et al.* (2018), Investigation of the two-gap superconductivity in a few-layer $NbSe_2$-graphene heterojunction, Phys. Rev. B, 97, 060505.

[50] Hess H. F., Robinson R. B., Waszczak J. V. (1990), Vortex-core structure observed with a scanning tunneling microscope, Phys. Rev. Lett., 64, 2711.

[51] Corcoran R. *et al.* (1994), Quantum oscillations in the mixed state of the type II superconductor 2H-$NbSe_2$, J. Phys. Condens. Matter, 6, 4479.

[52] Sanchez D. *et al.* (1995), Specific heat of 2H-$NbSe_2$ in high magnetic fields, Physica B, 204, 167-175.

[53] Zehetmayer M., Weber H. W. (2010), Experimental evidence for a two-band superconducting state of $NbSe_2$ single crystals, Phys. Rev. B: Condens. Matter Mater. Phys., 82, 014524.

[54] Yokoya T., Kiss T., Chainani A., Shin S., Nohara M., Takagi H. (2001), Fermi surface sheet-dependent superconductivity in 2H-$NbSe_2$, Science, 294, 2518-2520.

[55] Boaknin E. *et al.* (2003), Heat Conduction in the Vortex State of $NbSe_2$: Evidence for Multiband Superconductivity, Phys. Rev. Lett., 90, 117003.

[56] Rodrigo J.G., Vieira S. (2004), STM study of multiband superconductivity in $NbSe_2$ using a superconducting tip, Physica C, 404, 306-310.

[57] Fletcher J. D., Carrington A., Diener P., Rodiere P., Giannetta R. W. (2007), Penetration depth study of superconducting gap structure of 2H-$NbSe_2$, Phys. Rev. Lett., 98, 057003.

[58] Huang C. L., Lin J. Y., Chang Y. T., Sun C. P., Shen H. Y., Chou C. C., Berger H., Lee T. K., Yang H. D. (2007), Experimental evidence for a

two-gap structure of superconducting $NbSe_2$: a specific heat study in external fields, Phys. Rev. B, 6, 212504.

[59] Hossain M. D. *et al.* (2009), Low-field cross spin relaxation of ^{8}Li in superconducting $NbSe_2$, Phys. Rev. B, 79, 144518.

[60] Sooryakumar S., Klein M. V. (1981), The superconducting energy gap in 2H-$NbSe_2$ and its coupling to charge density waves, Physica B+C, 105, 422-427.

[61] Straub T., Finteis T., Claessen R., Steiner P., Hufner S., Oglesby C. S., Bucher E., (1999), Charge-Density-Wave Mechanism in 2H-$NbSe_2$: Photoemission Results, Phys. Rev. Lett., 82, 4504.

[62] Arguello C. J. *et al.* (2014), Visualizing the charge density wave transition in 2H-$NbSe_2$ in real space, phys. Rev. B, 89, 235115.

[63] Borisenko S. V. *et al.* (2009), Two energy gaps and fermi-surface "Arcs" in $NbSe_2$, Phys. Rev. Lett., 102, 166402.

[64] Gye G., Oh E., Yeom H. W. (2019), Topological landscape of competing charge density waves in 2H-$NbSe_2$, Phys. Rev. Lett., 122, 016403.

[65] Lian C. S., Si C., Duan W. (2018), Unveiling Charge-Density Wave, Superconductivity, and Their Competitive Nature in Two-Dimensional $NbSe_2$, Nano Lett., 18, 2924-2929.

[66] Xi X., Zhao L., Wang Z., Berger H., Forro L., Shan J., Mak K. F. (2015), Strongly enhanced charge-density-wave order in monolayer $NbSe_2$, Nat. Nanotechnol., 10, 765-769.

[67] Rossnagel K., Seifarth O., Kipp L., Skibowski M., Voß D., Krüger P., Mazur A., Pollmann J. (2001), Fermi surface of 2H-$NbSe_2$ and its implications on the charge-density-wave mechanism, Phys. Rev. B, 64, 235119.

[68] Johannes M. D., Mazin I. I., Howells C. A. (2006), Fermi-surface nesting and the origin of the charge-density wave in $NbSe_2$, Phys. Rev. B, 73, 205102.

[69] Méasson M. A., Gallais Y., Cazayous M., Clair B., Rodière P., Cario L., Sacuto A. (2014), Amplitude Higgs mode in the 2H-$NbSe_2$ superconductor, Phys. Rev. B, 89, 060503I.

[70] Krishnan M., Pervin R., Ganesan K. S., Murugesan K., Lingannan G., Verma A. K., Shirage P. M., Sonachalam A. (2018), Pressure assisted enhancement in superconducting properties of Fe substituted $NbSe_2$ single crystal, 8, 1251.

[71] Arumugam S., Krishnan M., Ishigaki K., Gouchi J., Pervin R., Selvan G. K., Shirage P. M., Uwatoko Y. (2019), Enhancement of superconducting properties and flux pinning mechanism on $Cr_{0.0005}NbSe_2$ single crystal under hydrostatic pressure, Sci. Rep., 9, 347.

[72] Suderow H., Tissen V. G., Brison J. P., Martínez J. L., Vieira S. (2005), Pressure induced effects on the Fermi surface of superconducting 2H-$NbSe_2$, Phys. Rev. Lett., 95.

[73] Chu C. W., Diatschenko V., Huang C. Y., DiSalvo F. J. (1977), Pressure effect on the charge density wave formation in 2H-$NbSe_2$ and correlation between structural instabilities and superconductivity in unstable solid, Phys. Rev. B 15, 1340-1342.

[74] Mutka H. (1983), Superconductivity in irradiated charge-density-wave compounds 2H-$NbSe_2$, 2H-TaS_2, and 2H-$TaSe_2$, Phys. Rev. Lett., 28, 2855.

[75] Motizuki K., Nishio Y., Shirai M., Suzuki N. (1996), Effect of intercalation on structural instability and superconductivity of layered 2*H*-type $NbSe_2$ and NbS_2, 57, 1091-1096.

[76] Yan D. *et al.* (2019), The unusual suppression of superconducting transition temperature in double-doping 2H-$NbSe_2$, Supercond. Sci. Technol., 32, 085008.

[77] Luo H., Nowak J. S., Li J., Tao J., Klimczuk T., Cava R. J. (2017), S shaped suppression of the superconducting transition temperature in Cu-intercalated $NbSe_2$, Chem. Mater., 29, 3704-3712.

[78] Fan X., Chen H., Zhao L., Jin S., Wang G. (2019), Quick suppression of superconductivity of $NbSe_2$ by Rb intercalation, 297, 6-10.

[79] Naik S., Pradhan G. K., Bhat S. G., Behera B. C., Kumar P.S. A., Samal S. L., Samal D. (2019), The effect of Sn intercalation on the superconducting properties of 2H-$NbSe_2$, Phys. C, 561, 18-23.

[80] Prodan A. *et al.* (2001), The surface superstructures in niobium disulfide and diselenide intercalated by Cu, Co and Fe, Surf. Sci., 476, 71 - 77.

[81] Iavarone M., Karapetrov G., Fedor J., Rosenmann D., Nishizaki T., Kobayashi N. (2010), The local effect of magnetic impurities on superconductivity in Co_xNbSe_2 and Mn_xNbSe_2 single crystals, J. Phys.: Condens. Matter, 22, 015501.

[82] Wang H. T., Li L. J., Ye D. S., Cheng X. H., Xu Z. A. (2007), Effect of Te doping on superconductivity and charge-density wave in dichalcogenides 2H-$NbSe_{2-x}Te_x$ (x = 0, 0.1, 0.2), Chin. Phys. Soc., 16, 2471-2475.

[83] Kars M., Herrero A. G., Rebbah A., Diaz L. C. O. (2009), Ge_xNbSe_2 and Ge_xNbS_2 intercalation compounds, Mater, Res. Bull., 44, 1601 -1607.

[84] Kadijk F. (1969), PhD Dissertation, State University, Groningen.

[85] Brixner L. H. (1962), Preparation and properties of the single crystalline AB_2-type selenides and tellurides of niobium, tantalum, molybdenum and tungsten, J. Inorg. Nucl. Chern., 24, 257-263.

[86] Brown B. E., Beerntsen D. J. (1965), Layer structure polytypism among niobium and tantalum selenides, Acta Cryst., 18, 31.

[87] Kadijk F., Jellinek F. (1971), On the polymorphism of niobium diselenide, J. Less Comm. Metals, 23, 437-441.

[88] Selte K., Kjekshus A. (1964), On the structural properties of the $Nb_{(1+x)}Se_2$, Acta Chern. Scand., 18, 697-706.

[89] Revolinsky E., Brown B. E., Beerntsen D. J., Armitage C. H. (1965), The selenide and telluride systems of niobium and tantalum, J. Less Comm. Metals, 8, 63-72.

[90] Selte K., Bjerkelund E., Kjekshus A. (1966), Intermediate phases in the systems niobium-selenium, niobium-tellurium, tantalum-selenium, and tantalum-tellurium, J. Less Comm. Metals, 11, 14-30.

[91] Huisman R., Kadijk F., Jellinek F. (1967), Some new niobium and tantalum sulfides and selenides, J. Less Comm. Metals, 12, 423-424.

[93] Huisman R., Kadijk F., Jellinek F. (1970), The non-stoichiometric phases $Nb_{1+x}Se_2$ and $Ta_{1+x}Se_2$, J. Less Comm. Metals, 21, 187-193.

[93] Revolinsky E., Spiering G. A., Beemtsen D. J. (1965), Superconductivity in the niobium-selenium system, J. Phys. Chem. Solids, 26, 1029-1034.

[94] Kadijk F., Huisman R., Jellinek F. (1964), Niobium and tantalum diselenides, Rec. Trav. Chern., 83, 768.

[95] Naik I., Rastogi A. K. (2011), Charge density wave and superconductivity in 2H- and 4H-$NbSe_2$: A revisit, Pramana, 76, 957-963.

[96] Roeske F., Shanks H. R., Finnemore D. K. (1977), Superconducting - and normal-state thermal conductivity of $NbSe_2$, Phys. Rev. B, 16, 3929-3935.

[97] Bulaevskii L. N. (1975), Superconductivity and electronic properties of layer compounds, Sov. Phys. Usp., 18, 514.

[98] Mattheis L. F. (1973), Band structures of transition-metal-dichalcogenide layer compounds, Phys. Rev. B, 8, 3719-3740.

[99] Takita K. *et al.* (1991), Fermi-surface of 2H-$NbSe_2$ studied by Dehaas-Vanalphen oscillation and positron-annihilation, 185-189, 2717-2718.

[100] Lebegue S., Eriksson O. (2009), Electron structure of two-dimensional crystals from ab initio theory, Phys. Rev. B, 79.

[101] Ugeda M. M. *et al.* (2016), Characterization of collective ground states in single-layer $NbSe_2$, Nat. Phys., 12, 92-97.

[102] Zhang X. *et al.* (2016), Magnetoresistivity plateau of graphene in proximity to superconducting $NbSe_2$, Phys. Rev. B: Condens. Matter, 94, 125404.

[103] Tsen A. W. *et al.* (2016), Nature of the quantum metal in a two-dimensional crystalline superconductor, Nat. Phys., 12, 208-212.

[104] Zhou, B. T. *et al.* (2016), Ising superconductivity and Majorana fermions in transition metal dichalcogenides, Phys. Rev. B, 93, 180501(R).

[105] Wakatsuki R., Law K. T. (2016), Proximity effect and Ising superconductivity in superconductor/transition metal dichalcogenide Heterostructures [arXiv:1604.04898].

[106] Sharma G., Tewari, S. (2016), Yu-Shiba-Rusinov states and topologlical superconductivity in Ising paired superconductors, Phys. Rev. B, 94, 094515.

[107] He W. Y. *et al.* (2018), Nodal topological superconductivity in monolayer $NbSe_2$, Commun. Phys., 1, 40.

CHAPTER 2

Essential Models of Superconductivity

The superconducting behaviour of a material depends on the nature of the material itself. Each superconducting element or alloy has its own characteristic critical temperature, upper critical field and critical current density. These fundamental superconducting parameters show different characteristics in different range of temperatures and magnetic fields and thus control the electromagnetic properties of the superconductor. In this chapter, various models associated with both conventional and unconventional superconductivity are explained elaborately, which are used to characterize the superconducting behaviour of $NbSe_2$ and its doped samples.

2.1. Phenomena of Superconductivity: Its Discovery and Evolution

In 1911, Prof. Kamerlingh Onnes achieved a breakthrough in Physics by discovering the property of superconductivity in mercury at a temperature of a few degrees Kelvin above absolute zero **[1]**. Later he discovered the superconducting behaviour of several different materials having different transition temperatures. Numerous studies have been endeavoured to explain the prime characteristic of a superconductor, namely the property of zero resistance. In 1933, Walther Meissner and Robert Ochsenfeld discovered the complete expulsion of the magnetic field from the interior of the superconductor occurring at $T < T_c\ (H)$, now called as the Meissner-Ochsenfeld effect.

In 1953, the London brothers Fritz and Heinz published a famous article entitled "The electromagnetic equations of the superconductors" **[2]**. Their equations were developed to correctly explain the Meissner effect. Also, they introduced a characteristic parameter for the superconductor, the London penetration depth λ_L, which can be defined as the depth to which a magnetic field is able to penetrate the sample.

In 1957, a new theory, which is considered a milestone in the history of condensed matter physics, was introduced by three physicists, J. Bardeen, L. Cooper and J. R. Schrieffer **[3]**. This so-called BCS theory described a mechanism of superconductivity that is based on Cooper pairing through phonon mediation. A few years later, a new interesting effect was discovered, called the Josephson effect **[4]**. Josephson introduced the possibility of the flow of Cooper pairs between two superconductors connected by a weak link. The DC Josephson effect is obtained when the supercurrent flows in the absence of an applied voltage, whilst the AC Josephson effect is exhibited when the flow of Cooper pairs occurs with an applied voltage between the two superconductors.

The main limitation of using superconductors in many applications has been the low temperatures that are required to keep the material in its superconducting state. This situation changed dramatically in 1986 with the discovery of high temperature superconductors (High-T_c). In 1986, Bednorz and Muller, **[5]** published a paper entitled "Possible High T_c

superconductivity in the Ba-La-CuO system" which discussed the synthesis of a metallic oxygen-deficient compound with the composition $Ba_xLa_{5-x}Cu_5O_{5(3-y)}$ with a transition temperature above 30 K. This discovery of high T_c superconductivity has led to a new era in the field. The discovery was the culmination of the outbreaking research on oxides such as $SrTiO_3$, Li-Ti oxide system **[6]**, $BaPb_{1-x}Bi_xO$ **[7]** and LaBaCuO systems **[8]**.

Chu's group at the University of Texas observed an increase in T_c to 52 K in the LaBaCuO system by application of pressure **[9]** and subsequently made a major contribution in the field of high superconductor. They also reported superconductivity up to 93 K in a ceramic $YBa_2Cu_3O_{7-\delta}$ sample. This discovery of a superconducting critical temperature well above the boiling point of liquid nitrogen opened new era for technologies and condensed matter physicists throughout the world.

Maeda *et al.* **[10]** in Japan first described the existence of superconductivity with a T_c of around 105 K in the BiSrCaCuO system. Other scientists around the world quickly stabilized related Bi-systems with structural formula $Bi_2Sr_2Ca_{n-1}Cu_nO_{2n-4}$ and T_c's of 10 K, 85 K and 110 K for n = 1, 2, 3 respectively. Shortly afterwards, Sheng and Hermann **[11]** discovered superconductivity above 100 K in the thallium-copper oxide system, and the structural formula for the system was established by Hazen *et al.* **[12]** as $Ti_2Ba_2Ca_{n-1}Cu_nO_{2n+4}$ with T_c of 80 K, 110 K and 125 K for n = 1, 2, 3, respectively. TI-2223 apprehended the record for the highest T_c of 125 K for a long period of time until Ott's group in Zurich **[13]** reported superconductivity at about 130 K in the HgBaCaCuO system. This mercury compound saw an increase in T_c up to 160 K with a high-pressure of 150 kbar. Another period started in superconductivity when research was started with the discovery of high T_c superconductivity in Fe-based compound having T_c of 26 K. The discovery of superconductivity in most common ferromagnetic atom Fe opened new path of research towards the understanding of the mechanism behind these high temperature superconductors. Further, many superconductors were discovered in the subsequent years.

More than two decades have passed since the discovery of the first high temperature superconducting (HTS) materials and this period has been enthralling and exciting for physicists as well as material scientists, electrical engineers and chemists working in the area of superconductivity. Enormous progress has been achieved in most of the physical and engineering aspects of superconductivity and there is still a tremendous scope to do more and try to resolve some of the very difficult unsolved problems. Many commercial applications of HTS can now be realised in communication and remote sensing systems with significantly improved performance. Channel filters for mobile communications are now routinely found in many base stations around the world **[14]**.

To summarise, even though the first observation of superconductivity was over a century ago there still seems to be much more to discover in this expanding area of physics.

2.2. Theory of Superconductivity:

The vortex lattice of a Type-II superconductor has been considered as the model system to study the superconducting properties of pure as well as doped $NbSe_2$ single crystal. Different essential models associated with superconducting properties of Type-II superconductor are described elaborately in the next section.

2.2.1. Properties of zero resistance:

The perfect conductivity (zero resistance) is the prime hallmark of a superconducting material (Figure 2.1). The resistance of a superconductor decreases to zero below certain temperature which is known as superconducting critical transition temperature (T_c). In 1911, Prof. Heike Kamerlingh Onnes invented that the electrical resistance of several metals like mercury, lead and tin immediately change into zero below a specific critical value of temperature (T_c) characteristics of the materials. The electrical resistance of a metallic conductor drops gradually as the temperature is lowered. In ordinary conductors, for example copper or silver, this decrease is restricted by impurities and other defects. Even near absolute zero, a real sample of a normal conductor displays some resistance. In a superconductor, the resistance drops abruptly to zero when the material

is cooled below its critical temperature. It is a characteristic of a perfect conductor.

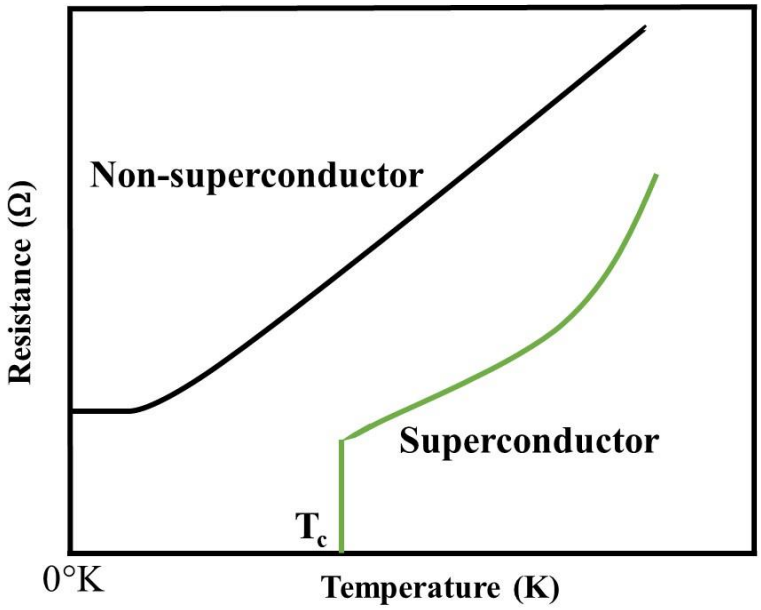

Figure 2.1. *Plot of resistance versus temperature of normal metal and superconductor* ***[1]****.*

2.2.2. The Meissner Effect:

The Meissner effect is the complete expulsion of magnetic flux line from the interior of superconducting materials during its transition to the superconducting state. In 1933, this novel characteristic of superconducting materials has been discovered by Meissner and Ochsenfeld **[15]**. This characteristic is elucidated in Figure 2.2. Superconductors expel external magnetic fields by inducing surface currents that flow across the perimeter of the superconductor. These surface currents generate a magnetic flux density that is equal and opposite of the applied magnetic field and precisely cancels the external applied magnetic field inside the superconductor.

Commonly, the applied magnetic field (H), the magnetic induction (B), the permeability of vacuum (μ_0) and the magnetization (M) of a sample are related with equation (2.1) **[16]**.

$$B = \mu_0 (H+M) \tag{2.1}$$

Where $M = \chi H$, and χ is the magnetic susceptibility. For a perfectly diamagnetic material, we know that $\chi = -1$. Henceforth, $B = \mu_0 H (1-1) = 0$

inside the superconducting sample. This indicates that the material has expelled the magnetic flux from the inside. At a point when a material is cooled below T_c and then a magnetic field is applied, current will be induced to accomplish an unchanged magnetic field inside the material (Figure 2.2) and when temperature is increased above T_c, magnetic field penetrates through the material.

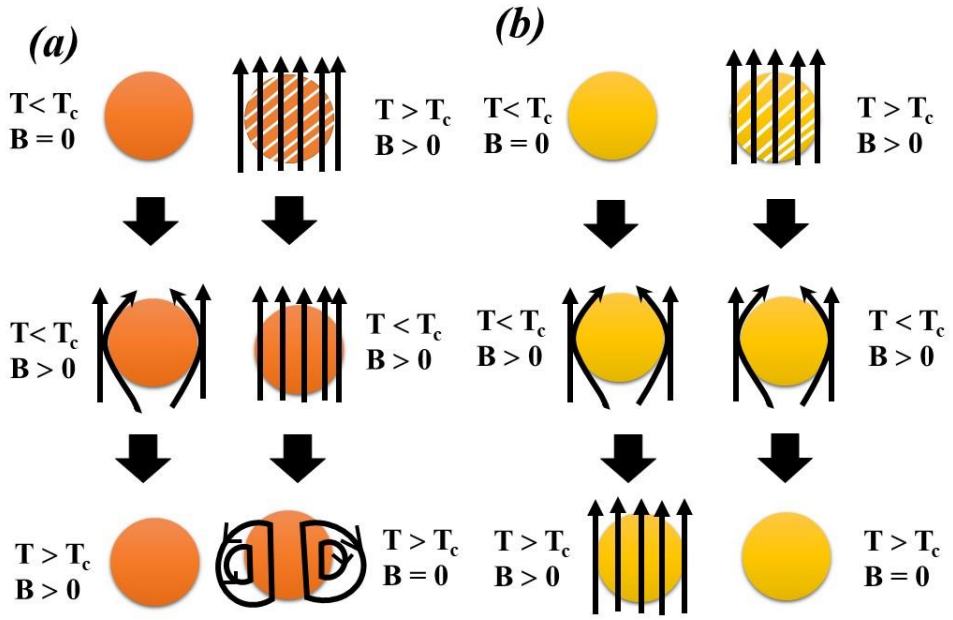

Figure 2.2. *The difference between perfect conductors and superconductors; (a) Perfect conductors when cooled below T_c and then applied magnetic field, flux does not pass through conductor but when first applied field and then temperature is decreased, flux passes through the conductor; (b) Superconductor expels magnetic flux below T_c, whether a field was applied or not* ***[17]****.*

Alternatively, first the magnetic field is applied and then the material is cooled below T_c then the magnetic field is expelled from the interior with some magnetic flux trapped inside the material. Again, with the enhancement of the temperature, magnetic field tries to penetrate through the material. This differentiates a superconducting material from a perfect conductor. Below a definite value of the magnetic field, which is defined as the critical magnetic field (H_c), the material act as a perfect diamagnet and it is in the superconducting state. However, at $H \geq H_c$ superconductivity will be destroyed and the material returns to its normal state **[17]**. The variations in the free energy (per unit volume) of a material

associated with the variations of M are represented by equation (2.2) in presence of an applied field (H_a).

$$\Delta f(H_a) = \mu_0 \int_0^{H_a} M dH \tag{2.2}$$

In the Meissner state M = -H and

$$\Delta f(H_a) = -\mu_0 \int_0^{H_a} (-H) dH = \frac{\mu_0 H_a^2}{2}, \tag{2.3}$$

The onset of superconductivity suppresses the overall energy of the system because of the superconducting condensation energy. When this energy is precisely balanced with the increase in energy associated with the increasing magnetization, the material returns to its normal state and superconductivity will be destroyed. The difference between the free energy of the normal and superconducting states of the material is represented by equation (2.4).

$$f_n(T,0) - f_s(T,0) = \frac{\mu_0 \mu_c^2(T)}{2} \tag{2.4}$$

Henceforth, the critical magnetic field H_c is demonstrated by equation (2.5).

$$H_c(T) = \left(\frac{2}{\mu_0}[f_n(T,0) - f_s(T,0)]\right)^{1/2} \tag{2.5}$$

An empirical formula that designates the temperature dependence of the critical field, H_c, in numerous superconductors is represented with equation (2.6) **[18]**.

$$H_c(T) = H_c(0)\left[1 - \left(\frac{T}{T_c}\right)^2\right] \tag{2.6}$$

2.2.3. London Theory:

The first phenomenological theory of superconductivity was London theory. It was proposed by Fritz and Heinz London in 1935 **[19]**, shortly after the discovery of Meissner effect. A major triumph of the equations of this theory is their ability to explain the two fundamental properties of superconductivity (zero resistance, and perfect diamagnetism). The London theory is based on the two-fluid model and accomplished by altering the electrodynamic equations that defines the (infinite) conductivity of the material.

In classical mechanics, the movement of electrons in a conductor is described by

$$m\frac{d\boldsymbol{v}}{dt} = e\boldsymbol{E} + \frac{m\boldsymbol{v}}{\tau} \tag{2.7}$$

Where τ is the damping time for scattered electrons, e is the electronic charge, m is the electronic mass, $\boldsymbol{v}$ is the electron velocity and $\boldsymbol{E}$ is the applied electric field.

Following from the property of zero resistivity of superconductor, the damping time τ can be neglected and equation (2.7) can be rewritten as:

$$\frac{d\boldsymbol{v}}{dt} = \frac{e\boldsymbol{E}}{m} \tag{2.8}$$

The supercurrent density $\boldsymbol{J_s}$ is given by:

$$\boldsymbol{J_s} = n_s e\boldsymbol{v_s} \tag{2.9}$$

Where $\boldsymbol{v_s}$ is the superconducting velocity and n_s is the superclectron density. By differentiating equation (2.9) with respect to time and substituting into the equation (2.8) we get equation (2.10) in the following form.

$$\frac{d\boldsymbol{J_s}}{dt} = \frac{n_s e^2}{m}\boldsymbol{E} \tag{2.10}$$

Now combining equation (2.10) with the third and fourth Maxwell's equations leads to,

$$\boldsymbol{\nabla} \times \boldsymbol{E} = -\frac{d\boldsymbol{B}}{dt} \Rightarrow \frac{d\boldsymbol{B}}{dt} = \frac{m}{\mu_0 n_s e^2}\nabla^2\left(\frac{d\boldsymbol{B}}{dt}\right) \Rightarrow \nabla^2\dot{\boldsymbol{B}} = \frac{\dot{\boldsymbol{B}}}{\lambda_L^2} \tag{2.11}$$

where $\lambda_L = \sqrt{\frac{m}{\mu_0 n_s e^2}}$, is a characteristics length scale.

Given that the Meissner effect leads to $\boldsymbol{B}$ = 0, the London brothers estimated that equation (2.11) can be applied to $\boldsymbol{B}$ as well as $d\boldsymbol{B}/dT$ and this leads to the London equation

$$\nabla^2\boldsymbol{B} = \frac{\boldsymbol{B}}{\lambda_L^2} \tag{2.12}$$

Where λ_L is known as London penetration depth.

So, the magnetic induction decays within a superconductor having a characteristic decay length λ_L called the London penetration depth.

The solution to equation (2.12) for a semi-infinite **[20]** superconductor (for $x \geq 0$) is

$\boldsymbol{B}(x) = B_0 e^{-\frac{x}{\lambda_L}}\hat{y}$ and $\boldsymbol{J_s}(x) = -\frac{B_0}{\lambda_L}\hat{z}e^{-\frac{x}{\lambda_L}}$ for x ≥ 0 (for the magnetic field $\boldsymbol{B} = B_o\hat{y}$ for x < 0).

Thus, the supercurrents flow in the direction parallel to the surface and perpendicular to B and decrease into the bulk over the same scale λ_L (Figure 2.3).

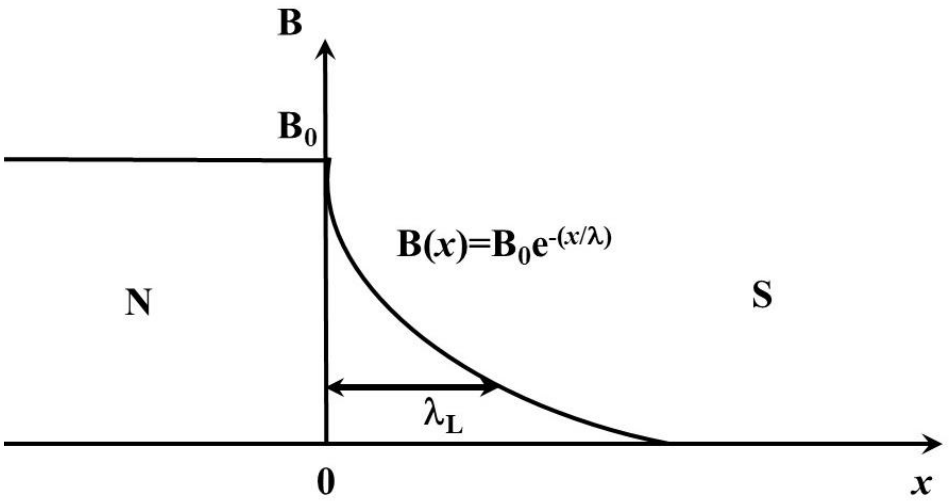

Figure 2.3. *The decay of the magnetic induction B into a superconductor over the scale of the penetration depth, λ_L, at a normal/superconductor (N/S) interface* ***[17]****.*

Hence, the London brothers predicted that a static or low frequency magnetic field is not excluded from a superconductor and penetrates a small distance beyond a normal (*N*)/superconductor (*S*) boundary. The magnetic field induces supercurrent loops at the surface of a finite superconductor producing a magnetic field inside which is equal and opposite of the applied field. Also, the penetration of the magnetic field into the superconductor increase with increasing temperature *T*, and complete penetration occurs at $T \geq T_c$ when the superconducting state is destroyed. London theory did not correctly predict the value of λ_L as $T \rightarrow 0$ **[16, 18]**.

2.2.4. Non-Local Response and Pippard Coherence Length:

Pippard estimated a length scale over which the superfluid density, n_s changes with non-local supercurrent density $\boldsymbol{J_s}$ and magnetic vector potential $\boldsymbol{A}$ **[21]**. He evaluated this length scale using uncertainty principle.

Electrons within the energy range k_bT_c of Fermi energy participate in superconductivity and these electrons have a specific momentum range ($\Delta p \approx \frac{k_bT_c}{v_f}$). This provides $\Delta x \geq \frac{\hbar}{\Delta p} \approx \frac{\hbar v_f}{k_bT_C}$. Consequently, the characteristic length scale is named as coherence length and is represented with equation (2.13).

$$\xi_0 = a\frac{\hbar v_f}{k_bT_C} \tag{2.13}$$

where, *a* is a numerical constant of order unity.

Coherence length in presence of scattering can be characterized by equation (2.14).

$$\frac{1}{\xi} = \frac{1}{\xi_0} + \frac{1}{l} \tag{2.14}$$

where, *l* is the mean free path.

2.2.5. Ginzburg-Landau Theory for Superconductivity:

For inhomogeneous superconductors where the superconducting properties vary spatially, microscopic theory is difficult to establish. This direction is solved with the Ginzburg-Landau (GL) theory of superconductivity [**22**], which concentrates entirely on the superconducting electrons rather than on excitations and was proposed in 1957. Ginzburg and landau developed a theory of superconductivity based on an order parameter or "wave function", *ψ(r)*, which describes the behaviour of the superconducting electrons. The density of objects that are responsible for superconductivity is $n_s^* = |\psi(x)|^2, \left(n_s^* = \frac{n_s}{2}\right)$.

They proposed that in the case of a homogeneous system, when $n_s^*(r) =$ constant, the free energy density can be expanded as a power series of $|\psi|^2$,

$$f_s(T) = f_n(T) + \alpha(T)|\psi|^2 + \frac{\beta(T)}{2}|\psi|^4 + \cdots, \tag{2.15}$$

Where, f_s is the free energy density in the superconducting state, f_n is the free energy density of the normal metal and α, β are Ginzburg-Landau (GL) coefficients. By minimizing equation (2.15) with respect to $|\psi|^2$, the following condition can be obtained,

$$|\psi|^2 = n_s^* = \frac{-\alpha(T)}{\beta(T)} \quad (2.16)$$

where, $\beta(T)$ must be positive. Two situations arise according to the sign of α. For $T > T_c$, $\alpha(T) > 0$ (positive value), the system will be in the normal state as the energy minimum is at $|\psi|^2 = 0$. However, at $T < T_c$, $\alpha(T) < 0$, the system will be in the superconducting state as the minimum energy is at $n_s^* = |\psi_\infty|^2$.

In an inhomogeneous system with applied fields/currents, another two terms are added to the free energy density relation which has the form of equation (2.17).

$$f_s(T) = f_n(T) + \alpha(T)|\psi|^2 + \frac{\beta(T)}{2}|\psi|^4 + \frac{1}{2m^*}|(-i\hbar\nabla - e^*A)\psi|^2 + \mu_0\frac{H^2}{2} \quad (2.17)$$

where m^* is the mass of the object that is responsible for superconductivity ($m^* = 2m_e$) and e^* is the charge of the object that is responsible for superconductivity ($e = 2e^*$).

The pair of well-known GL equations is obtained by minimising the free energy density equation and has the following form:

$$\alpha|\psi| + \beta|\psi|^2\psi + \frac{1}{2m^*}|-i\hbar\boldsymbol{\nabla} - e^*\boldsymbol{A}|^2\psi = 0 \quad (2.18)$$

$$\boldsymbol{J_s} = \frac{-ie^*\hbar}{2m^*}(\Psi^*\boldsymbol{\nabla}\psi - \psi\boldsymbol{\nabla}\psi^*) - \frac{e^{*2}}{m^*}|\Psi|^2\boldsymbol{A} \quad (2.19)$$

where $\boldsymbol{A}$ is the electromagnetic vector potential.

Assuming that the magnetic field in equation (2.18) is equal to zero ($\mathbf{A} = 0$), and dividing the equation by α we find,

$$|\psi| + \beta|\psi|^2\psi - \frac{\hbar^2}{2m^*\alpha}\boldsymbol{\nabla}^2\psi = 0 \quad (2.20)$$

Hence the GL equation introduces a length scale (coherence length (ξ)) over which the superconducting order parameter varies spatially (Figure 2.4),

$$\xi_{GL}(T) = \sqrt{\frac{\hbar^2}{2m^*|\alpha(T)|}} \quad (2.21)$$

GL coherence length is of the order of Pippard coherence length for a clean superconductor well below T_c. This is described as the shortest characteristic lengthscale over which $\Psi(r)$ can vary.

GL theory also allows one to write the London penetration depth in a new form. London penetration depth (λ_L) can be described by equation (2.22).

$$\lambda_L = \sqrt{\frac{m^*}{\mu_0 e^2 n_s}} = \sqrt{\frac{m^*}{\mu_0 e^2\left(-\frac{\alpha}{\beta}\right)}} = \sqrt{\frac{m^*\beta}{2\mu_0 e^2|\alpha|}} \quad . \tag{2.22}$$

(As for $T < T_c$, $n_s^* = \frac{n_s}{2} = |\psi|^2 = -\frac{\alpha}{\beta}$)

One of the successes of the GL theory is in being able to deal with the mixed state that arises in type II superconductors.

Moreover, Ginzburg and Landau introduced an important parameter that distinguishes between type-I and type-II superconducting materials. The GL parameter is the ratio between the penetration depth, λ and the coherence length, ξ is represented by equation (2.23). For type-I materials $\kappa < \frac{1}{\sqrt{2}}$ and for type-II materials $\kappa > \frac{1}{\sqrt{2}}$.

$$\kappa = \frac{\lambda}{\xi} \tag{2.23}$$

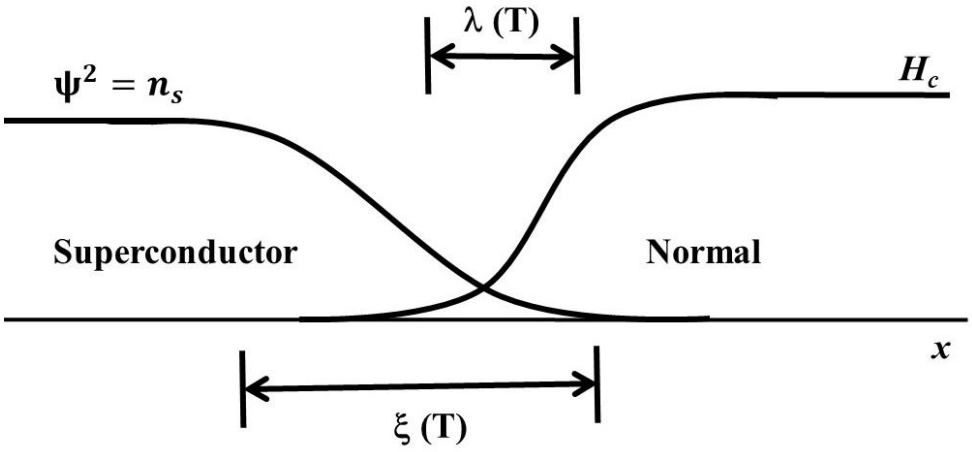

Figure 2.4. *Sketch of the interface between coexisting normal and superconducting domains [**18**].*

2.2.6. BCS Theory:

In 1956, Cooper **[23]** proposed the idea that superconductivity was related with bound pair of electrons, each having equal but opposite spin and momenta. The pairs are bound together by an electron-phonon interaction. In 1957 Bardeen, Cooper and Schireffer **[24]** used a many body microscopic theory to demonstrate that this leads to superconductivity with a finite energy gap for an indefinitely, small attractive interaction, *V*. It

states that a net attractive interaction that is mediated by phonons bounds two electrons near the Fermi level. This bound state is known as Cooper pair. Subsequently, the whole system condensates into a phase coherent ground state which results the phenomena of superconductivity.

The origin of attractive interaction between the two electrons in a Cooper pair can be explained with the theory of Fröhlich (1950) as follows; an electron moving through a medium will attract nearby positive charged nuclei of the surrounding atoms in the lattice via Columbic interactions. This deformation of lattice causes another electron, with opposite spin, to move into the region of higher positive charge density giving rise to effective attractive interaction between the two electrons. The competition between the attractive interaction between Cooper pair and the repulsive screened Coulomb interaction results a net attractive interaction between the two electrons. This mechanism of attraction is illustrated in Figure 2.5.

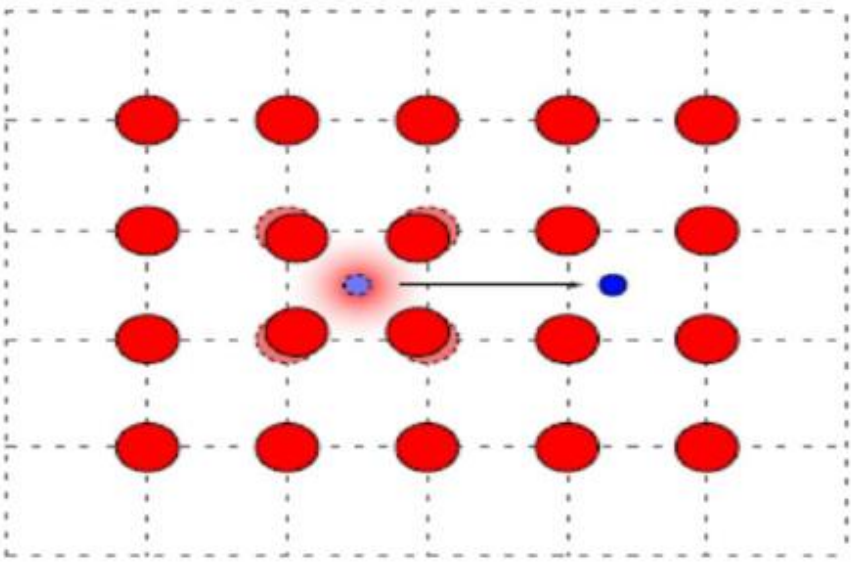

Figure 2.5. *Illustration of the mechanism of the Cooper pair formation as a result of lattice polarization* ***[25]****.*

Cooper proposed that Fermi sea is unstable against the formation of at least one bound pair. This can be expressed with the addition of two electrons to a Fermi sea at T = 0. Considering the equal and opposite momenta k and -k (to have zero angular momenta), the two-electron antisymmetric wavefunction can be constructed. Solving the Schrödinger equation for the antisymmetric wavefunction we can get the energy of the

bound state as $E = 2E_F - 2\hbar\omega_D e^{-\frac{2}{N(0)V}}$ where *N(0)* is the density of states at the Fermi level for one spin orientation.

Electrons in a normal conductor are Fermions and follow Fermi statistics **[26]**. In contrast, Cooper pairs of electron can be considered as the Bosons which are regulated by Bose-Einstein statistics. Cooper pairs can fill the same quantum states. BCS theory elucidated many experimental observations like the existence of an energy gap, 2Δ (0), in the quasiparticle spectrum. It predicted to have a value of 3.52 $K_B T_c$ in the weak coupling limit. Another feature of the BCS theory is that it treats with the metal in terms of quasiparticles rather than electrons. A quasiparticle is a mixture of electron and hole states.

2.2.7. Type I and Type II Superconductors:

Based on the Ginzburg-Landau parameter($\kappa = \frac{\lambda}{\xi}$), superconducting materials are classified into two categories. For $< \frac{1}{\sqrt{2}}$, the superconductor shows complete flux expulsion up to some critical field H_c, above which it becomes normal. These type of superconductors are called type-I superconductors. Type-I superconductors are generally elements or simple alloys.

For $\kappa > \frac{1}{\sqrt{2}}$, up to certain field H_{c1} called lower critical field the response is completely diamagnetic. Above H_{c1} it is energetically favourable for the superconductor to form normal regions within which the external field penetrates. These normal regions are separated by superconducting regions between them where there is no flux penetration. The normal region dominates over superconducting region with increasing magnetic field. Above H_{c2}, called upper critical field, the material becomes completely normal. Type-II superconductors are mostly used for industrial application because these types of superconductors are able to retain superconductivity even at very high external magnetic fields (> 50 T). The state (of a type-II superconducting material) having both normal and superconducting regions for applied fields H (where $H_{c1} < H < H_{c2}$) is called mixed state. Normal regions having magnetic flux (integer multiple of flux quantum) pass through it. These regions are called vortices.

To screen the magnetic field that is penetrating through the sample, a screening current flow at the edge of each vortex. Depending of the direction of applied magnetic field, screening current flowing at the edge of each vortex has same sense. As a result, vortices feel mutual repulsion among themselves. So, to minimise the repulsive interaction energy, the vortices tend to align periodically in the form of triangular (hexagonal) lattice. The nearest neighbour separation between the vortices is $a_0 = 1.075(\frac{\Phi_0}{B})^{\frac{1}{2}}$. This periodic array of vortices is called flux line lattice (FLL) or Abrikosov vortex lattice. Figure 2.6 shows the regular array of Abrikosov vortex lattice. The regular array of superconducting vortex state can be destroyed by applying external magnetic fields, crystalline defects, impurities etc. and the system become disorder. So, the vortex lattice (VL) in a type-II superconductor provides an extremely versatile system to study various phases associated with the order-disorder transition.

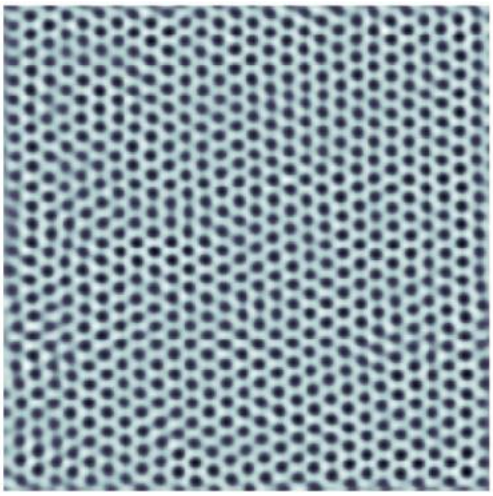

Figure 2.6. *Abrikosov vortex lattice imaged on $NbSe_2$, a typical type II superconductor at an applied magnetic field of 2 T* ***[27]****.*

2.2.8. Vortex Matter:

A. A. Abrikosov **[28]** established the theory of vortices to depict the intermediate state of type-II superconductors when the magnetic field exceeds H_{c1}. Physically, when a magnetic field is applied to a type-II superconductor it enters the material as discrete flux lines, which produce tubular regions parallel to the applied magnetic field. These tubes form

around normal cores and each contain the same amount of flux, equal to one flux quantum $\Phi_0 = \frac{h}{2e} = 2.07 \times 10^{-15}$ Tm^2. These normal regions are enclosed by a matrix of superconductor, which can still transport supercurrent. The magnetic flux in each tube is developed by a vortex of persistent supercurrents circulating around the core. Energetically it is favourable for the flux lines to form a regular periodic array called the vortex lattice in samples with low disorder. For high current and field applications large values of J_c are obtained in type-II superconductors by the controlled introduction of crystal defects which pin the flux lines and prevent them from moving and dissipating energy.

2.2.9. Critical Current in Type-II Superconductor:

The practical applicability of a superconducting material depends upon the ability of carrying a usefully high current in the presence of strong penetrating field without dissipation of energy. Any appreciable dissipation leads to heating, which degrades the performance. Further, it also leads to intolerable catastrophic flux jumps. The origin of the dissipation is the Lorentz force density. When flux lines pass through the superconductors in the mixed state in the form of vortices, supercurrent *(J)* generates Lorentz force upon each vortex. These vortices stay in their state as far as the Lorentz force is not as much as the pinning force. At some value of J (*i.e.*, J_c), the Lorentz force overcomes the pinning force such that the vortices starts to move in a steady motion with a velocity limited by viscous drag. This is known as flux flow. However, for strong currents, the vortices begin to move due to a reduced pinning force associated with thermal initiation of the FLL. This movement is usually more irregular and much slower. This is defined as the flux creep. There will always be thermally activated flux "creep", in which vortices hop from one pinning site to another, and in some cases, this will occur at a measurable rate. Hence, for practical applications, flux flow must be avoided, and the creep rate held to a low level. If the pinning is sufficiently strong, vortex motion can be made small enough so that the superconductor acts much like a perfect conductor.

For a finite current density J, the Lorentz force density can be represented by equation (2.24):

$$\boldsymbol{F} = \boldsymbol{J} \times \frac{\boldsymbol{B}}{c} \tag{2.24}$$

Due to this force the flux lines will tend to move transverse to the current with velocity ***v***. This will induce an electric field of magnitude

$$\boldsymbol{E} = \boldsymbol{B} \times \frac{\boldsymbol{v}}{c} \tag{2.25}$$

This acts parallel to ***J***, so a finite power ***E.J*** is dissipated resulting in non-zero resistance. So, for an ideal type-II superconductor in mixed state, a finite current, no matter how small, will drive it to the normal state. This problem can be avoided with the incorporation of point disorder (impurities, vacancies etc.) in real systems. These point disorders play the role of pinning centres for the vortices. For the formation of a vortex, superconductivity is destroyed locally. By passing through pinning centre, the energy gained is $\sim \pi\xi^2 L_i \left(\frac{1}{2}\mu_0 H_c^2\right)$. Here L_i is the linear extension of the pinning centre. So, the vortices would prefer to pass through pinning centres. To move the vortices out of this potential trap, a finite current density is required. It is called critical current density (J_c).

2.2.9.1. Bean's Critical State Model:

Bean's critical state model, introduced by C.P. Bean in 1962, gives a macroscopic explanation of the irreversible magnetization behaviour (hysteresis) of hard type-II superconductors. This model depends on the experimental observations and considers only two states involving perfect diamagnetism and mixed state, with a sharp change **[29, 30]**. The Bean critical-state model contributes a phenomenological description for the hysteretic magnetization of type-II superconductors in a varying external magnetic field. The magnetic field penetrates into these superconductors in the form of superconductive electron current vortices. Each of the vortices transports a similar amount of magnetic flux, thus the magnetization depends upon the vortex distribution. As per Bean model, in a type-II superconductor the distribution of vortices is determined by the balance between electromagnetic driving forces and pinning forces. At whatever point the external magnetic field is changed, magnetic vortices begin to enter or leave the superconductor through its boundary. When the region

appears where the driving forces overcome the pinning, the arrangement of vortices relocates itself into another meta-stable state to such an extent that all vortices are pinned again and the balance with the external field at the boundary is re-established. Since the unpinned vortices move quickly, the system rapidly alters itself to the changing external conditions, and thus a quasi-stationary model with immediate interactions is justified.

In the Bean's model, the flux-density profiles are simply straight lines of slope $4\pi J_c/c$, which simplifies qualitative discussion. Figure 2.7 (*a*) illustrates the profiles for flux penetrating into a thick slab of thickness *d* as the external field *H* is increased. As it is evident from the Figure 2.7 (*a*), we get equation (2.26), which represents the maximum external field that can be completely screened out at the midplane of the superconductor. It the applied field is now reduced and eventually reversed in direction; the successive field profiles are shown in Figure 2.7 (*b*).

$$H_s = \frac{2\pi J_c d}{c} \tag{2.26}$$

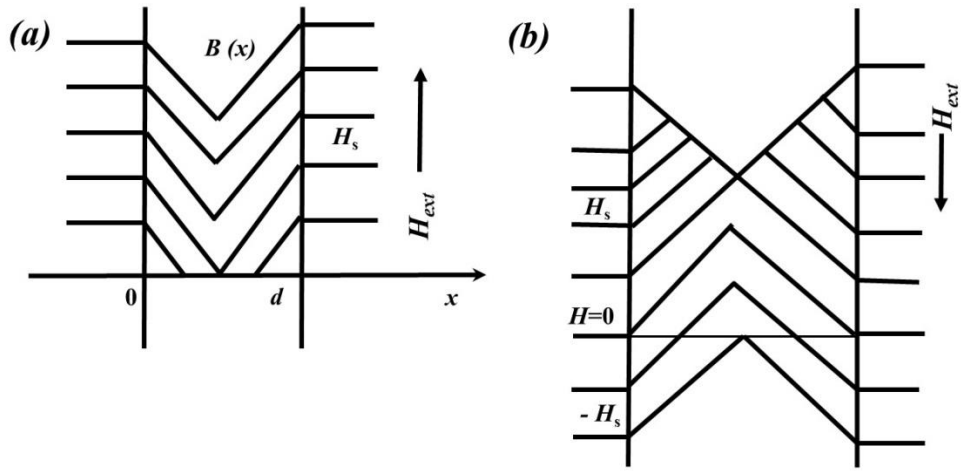

Figure 2.7. *Internal flux-density profiles in a slab subjected to (a) increasing and (b) decreasing external field. H_s is the maximum applied field that can be screened at the midplane. The occurrence of cancelling flux densities in (b) when H_{ext} = - (1/2) H_s* ***[16]***.

Note that a very substantial amount of flux may be left trapped in the slab after the external field is reduced to zero. One may even have flux densities which change sign in the interior of the slab. In that case, one would expect some annihilation of opposing vortices to occur, but if the pinning is strong, this would affect only a thin layer at the crossover of ***B***

from one sense to the other. As is evident from this figure, there is much hysteresis, and associated irreversibility, in the cycling of these "hard" superconductors. For example, if the external field is cycled through a maximum field $H_m < H_s$, one can see that the area inside the hysteresis loop $\oint BdH$ (hence the energy Q dissipated as heat per cycle) will increase as H_m^3. On the other hand, if $H_m >> H_s$, then $Q \alpha H_m$. These hysteresis losses limit the value of type II superconductors for ac applications.

2.2.9.2. Peak Effect Phenomenon:

The peak effect phenomena **[31]** is the occurrence of an anomalous enhancement of the J_c, *i.e.*, the pinning force per flux line, at high magnetic fields near the normal-state phase boundary (the H_{c2} line) in low-T_c systems and nearly coincident with the melting line in the HTSC's **[31]**. The exact causes of the peak effect are uncertain **[32-34]**, but it is widely regarded as the result of a rapid softening of the lattice and the occurrence of plastic deformations **[32]** and proliferation of topological defects **[33, 35]** in the FLL. The lattice is expected to be amorphous at and above the peak position in J_c **[35, 36]**.

2.2.9.3. Second Magnetization Peak Effect phenomenon:

For some superconductors, the J_c values estimated from the magnetization hysteresis loops (MHLs) increase with the external magnetic field after the first peak of penetration field. This is the so-called fishtail effect or second magnetization peak effect. This feature has been perceived in the clean and high-quality single crystals of cuprate superconductors. The anomalous second peak appears at different fields for $REBa_2Cu_3O_{7-\delta}$ (REBCO) bulks (RE = rare earth element) at different temperatures **[37]**. However, the peak position is temperature independent for Bi-based and TI-based cuprate **[38, 39]**. This is due to the different origins of SMP effect in REBCO and in Bi-or TI-based cuprates, and has not got final agreement. The second peak effect has been also found and reported in polycrystalline samples of the FeAs-1111 phase **[40-43]**. However, it has not been reported in the FeAs-122 phase either in polycrystalline or single crystal samples.

The effect thus deserves a detailed investigation on single crystals of different superconducting materials.

2.2.10. The Effect of Pinning:

Properties of the superconducting materials can be improved with the incorporation of internal as well as external defects in a material. These defect centres appear as pinning canters for flux line lattice. The defects can be localized defects, such as departures from stoichiometry at the atomic scale, or more extended defects, such as dislocations, grain boundaries, inclusions of second phases, twin planes, etc. The energy of a flux line will be different if it passes through a defect centre, instead of passing to the side. The resulting force tends to "pin" flux lines in particularly favourable positions relative to the underlying material. When the magnetic flux lines are trapped or pinned in the vortex state inside of a superconducting material, such phenomenon is called Flux pinning. This flux pinning causes a field gradient in the superconductor and offers a nonzero critical current in the material by retarding flux motion. From a practical standpoint the goal is to find a means to introduce sufficient pinning to raise significantly the flux line melting temperature, and therefore the effective resistive transition temperature.

2.2.10.1. Pinning Mechanisms in Type-II Superconductors:

The collective pinning model of Larkin and Ovchinnikov is the prominent treatment to study the influence of pinning by randomly distributed weak point defects. There are also various approaches which are suitable for describing strong or correlated defects like twin boundaries. Consequently, it is worthwhile to discuss several origins of pinning which are essential in type-II superconductors. The following discussion will give a basis for determining the applicability of various theories of the impact of pinning.

2.2.10.1.1. Superconducting nature of the pinning centres:

Flux-lines interact with pinning centres because the superconducting properties of the pinning centres are different from those of the bulk of the superconductor. The strength of the interaction is a function of the

magnitude of this difference. The difference may be small, and manifest itself as a difference in critical temperature, critical field, or Ginzburg-Landau κ. The difference may be large, as is the case when the pinning centre is non-superconducting. The largest difference, and the strongest pinning, arises when the pinning centre is ferromagnetic **[44, 45]**. Of all the various possibilities, only two are believed responsible for flux-pinning in most commercial superconducting materials. These are *(i)* small differences in κ (superconducting pinning centre) and *(ii)* non-superconducting pinning centre. The variation in κ is associated with changes in the normal state resistivity, due to the composition fluctuations **[46]**, non-uniform distributions of dislocations **[47, 48]** or martensite transformation. Non-superconducting pinning centres can be normal metal, insulator or void. Bibby *et al.* **[49]** has shown that the pinning strength of the non-superconducting particles is independent of the nature of the particles. If non-superconducting metallic particles have a diameter $\leq$ the superconducting coherence length ξ of the matrix, the proximity effect will induce them to become superconducting, and their presence can be regarded as producing a change in κ. These two type of pinning centres give rise to 'superconducting pinning (or, $\Delta\kappa$ pinning)' and 'normal pinning'.

2.2.10.1.2. Size dependent pinning mechanisms:

There are three types of pinning mechanism in type-II superconductors depending on the dimension of pinning centres. Pinning centres can be classified by the number of their dimensions which are large compared with the inter flux-line spacing d ($= 1.07(\phi_0/B)^{1/2}$). Point pins are regions whose dimensions in all direction are less than d. A point pin can only interact with only flux line at a time. Point pinning occurs due to the irregularities in the crystal structural. Line pins, such as dislocations or needle shaped precipitates, have one dimension long compared with d. When lying parallel to the local direction of B, they can interact with one flux line over their whole length. Lying at an angle to B they can interact with several flux lines. Grain-, twin- and martensite boundaries, stacking faults, dislocation arrays such as sub-grain, polygonized boundaries, plate-

like precipitates, and the surface of the superconductor may have two dimensions greater than *d* and act as surface pins. They have the strongest influence when their plane normal is parallel to the direction of the Lorentz force. The importance of pinning by twin planes in YBCO was demonstrated experimentally by Kwok *et al.* [**50, 51**].They measured the J_c as a function of the orientation of the FLL relative to crystal axes and found a sharp peak when the field was within ~1°of the twin plane. However, volume pins, with all dimensions larger than *d*, are large precipitates and thick-walled dislocation cell-structures resulting from cold-deformation. Flux-lines interact with the surface of volume pins, and the important parameter is the projected area of surface in the direction of the Lorentz force. In order to understand the vortex pinning mechanism, it is necessary to calculate the pinning force density (F_p) from the critical current density and applied field, using the formula $F_p = HJ_c$ at low temperatures. Dew-Hughes **[52]** proposed a formula in order to explain single vortex pinning mechanism, the pinning force $f_p = F_p/F_{p,\max}$ as a function of reduced field (H/H_{irr}).

2.2.10.1.3. Structural pinning (Interaction between the vortices and the pinning centres):

A vortex can be trapped or pinned due to the presence of spatial variations in the free energy of the FLL. Almost any kind of defect can create local minima in the free energy landscape, e.g. crystalline imperfection, columnar defects, grain boundaries, thickness variations of a film, *etc*. Depending on the interaction between the vortex and the pinning centre, a distinction can be made between two contributions to the pinning mechanism: core pinning and electromagnetic pinning. Core pinning is the origin of flux pinning at most point defects and nano engineered pinning sites, and refers to the local variation of T_c or κ which reduces the free energy if the vortex core is located at the position of the (normal) defect or pinning centre. Electromagnetic pinning is due to the kinetic energy of the confined screening currents around the defect and the perturbation of the magnetic field of a vortex. Theoretically, it can be described by assuming the presence of an anti-vortex image, in analogy with electrostatics.

Thickness variations of a film can lead to the admixture of this type of pinning. The vortices are pinned at the locations of smallest thickness where their energy is lowest. The typical length scale for this kind of pinning is the penetration depth. Both the core and the electromagnetic contributions define the pinning, which eventually controls the J_c of a superconductor. The core pinning is estimated by the short-range disorder in *GL* coefficient and the mean free path (l) of charge carriers **[53]**. The spatial variation of the *GL* coefficient associated with the disorder of T_c is defined as δT_c pinning. On the other hand, the δl pinning shows the variation in l near pinning centres. The disorder parameter, δ which determines the spatial variation due to the point defects, provides characteristic temperatures in case of δT_c pinning and δl pinning.

2.2.10.2. Larkin-Ovchinnikov Theory of Collective Pinning:

A perfectly periodic and rigid FLL cannot be effectively pinned by any random collection of pinning sites. It is because for any position of the FLL relative to the pinning landscape, there will be an equal number of random pinning sites exerting forces adding to the Lorentz force as opposing it, which sums up to zero net force. It is the elastic response of the FLL to these pinning forces which results in a finite volume pinning force. For most real systems, the pins are either too strong, too extended or too correlated for calculation by statistical theory. In the limit of weak pinning and assuming a random collection of pins, the concept of collective pinning was introduced by Larkin and Ovchinnikov [**54**]. The interaction between FLL has a range of λ_L which is large for high κ materials. The concentration of pinning centres n_p is often very large for a real system, resulting ${n_p}^{-1/3} << \lambda_L$. So, the collective treatment of pinning forces is suitable.

In the collective pinning model, it is supposed that there is no long range order present in the FLL. Instead there is finite volume V_c within which short range order exists and the FLL is periodic. When a current below the critical value is passed, each of the volumes V_c is displaced independently by the Lorentz force for a distance less than ~ ξ, so that the

pinning force compensates the Lorentz force. The random pinning forces would add in the manner of random walk resulting in a net force $\sim \sqrt{N} \propto \sqrt{V_c}$. Where $N = nV_c$ is the total number of pinning centres in volume V_c, n is no. density of pinning centres. For applied current density J_c, the Lorentz force is JBV_c. At critical current density, Lorentz force equals to the maximum pinning force. If f is pinning force per unit volume then we have

$$J_c B V_c = f n^{\frac{1}{2}} V_c^{\frac{1}{2}} \Longrightarrow J_c = \frac{1}{B} \frac{f n^{\frac{1}{2}}}{V_c^{\frac{1}{2}}} \tag{2.27}$$

So, we can see that for perfectly ordered vortex lattice $V_c \to \infty$ hence $J_c \to 0$. For disordered vortex lattice, V_c is finite and hence J_c is non-zero.

If L_c and R_c are correlation lengths along and transverse to the field directions, then we have $V_c = R_c^2 L_c$. Since the lattice correlations are lost if the distortion distance ~ ξ. So, for distortions L_c and R_c for tilt and shear respectively the strains are of the order ξ/L_c and ξ/R_c, respectively. So, the resulting increase in the elastic free energy per unit volume can be represented by equation (2.28).

$$\frac{1}{2}\left(C_{66}\left(\frac{\xi}{R_c}\right)^2 + C_{44}\left(\frac{\xi}{L_c}\right)^2\right) \tag{2.28}$$

where C_{66}, C_{44} are the elastic moduli for FLL shear and tilt.

The pinning force acts only through a distance ~ ξ before changing randomly. Therefore, we have the net free-energy change per unit volume in the presence of pinning sites,

$$\delta F = \frac{1}{2} C_{66}\left(\frac{\xi}{R_c}\right)^2 + \frac{1}{2} C_{44}\left(\frac{\xi}{L_c}\right)^2 - f\xi \frac{n^{\frac{1}{2}}}{V_c^{\frac{1}{2}}} \tag{2.29}$$

Minimising the free energy with respect to L_c and R_c we get,

$$L_c = \frac{2C_{44}C_{66}\xi^2}{nf^2},\ R_c = \frac{2^{\frac{1}{2}} C_{44}^{\frac{1}{2}} C_{66}^{\frac{3}{2}} \xi^2}{nf^2},\ V_c = \frac{4C_{44}^2 C_{66}^4 \xi^6}{n^3 f^6}$$

$$\delta F_{min} = \frac{n^2 f^4}{8C_{44}C_{66}^2\xi^2},\ J_c = \frac{1}{B}\frac{n^2 f^4}{2C_{44}C_{66}^2\xi^3} \tag{2.30}$$

Therefore, a larger pinning energy and larger critical current have been acquired for a softer FLL (smaller elastic moduli).

In summary, *various models associated with both conventional and unconventional superconductivity are explained, which are used to characterize the superconducting behaviour of $NbSe_2$ and its doped samples in future chapters.*

References

[1] Onnes H. K. (1911), Further experiments with liquid helium. C. On the change of electric resistance of pure metals at very low temperatures etc. IV. The resistance of pure mercury at helium temperatures, KNAW, Proceedings, 13 II, 1910-1911, 1274-1276.

[2] London F., London H. (1935), The electromagnetic equations of the superconductor. Proceedings of the Royal Society of London, Series A, Math. Phys. Sci., 149 (866), 71-88.

[3] Bardeen J., Cooper L. N., Schrieffer J. R. (1957), Theory of superconductivity, Phys. Rev., 108, 1175.

[4] Josephson B.D. (1957), Possible new effects in superconductive tunnelling, Phys. Lett., 108, 1175.

[5] Bednorz J. G., Muller K.A. (1986), Possible high T_c superconductivity in the Ba-La-Cu-O system, Zeitschrift für Physik B Condensed Matter, 64, 189-193.

[6] Mousa A., Grimes N. (1980), A note on the preparation of the high transition temperature superconductor lithium titanate, J. Mater. Sci., 15, 793-795.

[7] Sleight A. W., Gillson J. L., Bierstedt P. E. (1975), High-temperature superconductivity in $BaPb_{1-x}Bi_xO_3$ system, Solid State Commun., 17, 27-28.

[8] Michel C., Errakho L., Raveau B. (1985), The oxygen defect perovskite $BaLa_4Cu_5O_{13.4}$, A metallic conductor, Mater. Res. Bull., 20, 667-671.

[9] Wu M. K. *et al.* (1987), Superconductivity at 93 K in a new mixed-phase Y-Ba-Cu-O compound system at ambient pressure, Phys. Rev. Lett., 58, 908-910.

[10] Maeda H. *et al.* (1988), A new high-T_c oxide superconductor without a rare-earth element, Japanese Journal of Applied Physics part 2-letters, 27, L209-L210.

[11] Sheng Z. Z., Hermann A.M. (1988), Bulk superconductivity at 120 K in the Tl-Ca/Ba-Cu-O system, Nature, 332, 138-139.

[12] Hazen R. M. (1990), Crystal structures of high-temperature superconductors, Physical Properties of high-temperature superconductors II, DM Ginsberg, (ed.), New Jersey, World Scientific, 121-198.

[13] Schilling A. *et al.* (1993), Superconductivity above 130 K in the Hg-Ba-Ca-Cu-O system, Nature, 363, 56-58.

[14] Fossheim, K., Sudboe, A., (2004), Superconductivity: Physics and applications, First ed. Wiley, Trondheim, Norway, pp. 1-430 (ISBN 0470844523, 9780470844526, 9780470026441).

[15] Meissner W., Ochsenfeld R. (1933), Ein neuer Effekt bei Eintritt der Supraleitfähigkeit, Naturwiss., 21, 787-788.

[16] Sheahen, T. (1994), Introduction to high-temperature superconductivity, First ed. Springer, pp-1-578 (ISBN 9780306447938, 0306447932, 0306470616).

[17] Mourachkine, A. (2004), Room temperature superconductivity, Cambridge International Science Publishing, United Kingdom, pp. 1-310 (ISBN 1-904602-27-4).

[18] Tinkham, M. (1996), Introduction to Superconductivity, Second edition McGraw-Hill, New York, pp. 1- 454 (ISBN 0-07-064878-6).

[19] London F., London H (1935), The electromagnetic equations of the superconductor, Proc. R. Soc. Lond. A, 149, 71-88.

[20] London, F. (1961), Superfliuds, vol. 1: macroscopic theory of superconductivity, Dover Publications, pp. 1-191 (ISBN 0486600440).

[21] Pippard A. B. (1953), An Experimental and theoretical study of the relation between magnetic field and current in a superconductor, Proc. R. Soc. Lond. A, 216, 547-568.

[22] Ginsburg V.L., Landau L. D. (1950), On the theory of superconductivity, Zh. Eksp. Teor. Fiz., 20, 1064.

[23] Cooper L.N. (1956), Bound electron pairs in a degenerate Fermi gas, Phys. Rev., 104, 1189-1190.

[24] Bardeen J., Cooper L. N., Schrieffer J. R. (1957), Microscopic theory of superconductivity, Phys. Rev., 106, 162-164.

[25] Mvller, A., (2012), Designer 3D magnetic mesostructures, PhD thesis, Bath University.

[26] Fermi E. (1928), Eine statistische Methode zur Bestimmung einiger Eigenschaften des Atoms und ihre Anwendung auf die Theorie des periodischen Systems der Elemente., Z. Physik, 48, 73-79.

[27] Ganguly S.C. *et al.* (2015), Disordering of the vortex lattice through successive destruction of positional and orientational order in a weakly pinned $Co_{0.0075}NbSe_2$ single crystal, Sci. Rep., 5, 10613.

[28] Abrikosov A. (2004), Nobel lecture: Type-II superconductors and the vortex lattice, Rev. Mod. Phys., 76, 975-979.

[29] Bean C. P. (1962), Magnetization of hard superconductors, Phys. Rev. Lett., 8, 250-253.

[30] Bean C. P. (1964), Magnetization of high-field superconductors, Rev. Mod. Phys., 36, 31-39.

[31] Kwok W. K., Fendrich J. A., Van der Beck C. J., Crabtree C. W. (1994), Peak Effect as a Precursor to Vortex Lattice Melting in Single Crystal $YBa_2Cu_3O_{7-\delta}$, Phys. Rev. Lett., 73, 2614-2617.

[32] Bhattacharya S., Higgins M. J. (1993), Dynamics of a disordered flux line lattice, Phys. Rev. Lett., 70, 2617.

[33] Tang C., Ling X., Bhattacharya S., Chaikin P. M. (1996), Peak effect in superconductors: melting of Larkin domains, Europhys. Lett., 35, 597.

[34] Larkin A. I., Marchetti M. C., Vinokur V. M. (1995), Peak effect in twinned superconductors, Phys. Rev. Lett., 75, 2992.

[35] Banerjee S. S. *et al.* (1998), Anomalous peak effect in $CeRu_2$ and 2H-$NbSe_2$: fracturing of a flux line lattice, Phys. Rev. B, 58, 995.

[36] Gammel P. L. *et al.* (1998), Structure and correlations of the flux line lattice in crystalline Nb through the peak effect, Phys. Rev. Lett., 80, 833-836.

[37] Welp U., Kwok W. K., Crabtree G. W., Vandervoot K. G., Liu J. Z. (1990), Magnetization hysteresis and flux pinning in twinned and untwinned $YBa_2Cu_3O_{7-\delta}$ single crystals, Appl. Phys. Lett., 57, 84.

[38] Yeshurum Y., Bontemps N., Burlachkov L., Kapitulnik A. (1994), Dynamic characteristics of the anomalous second peak in the magnetization curves of Bi-Sr-Ca-Cu-O, Phys. Rev. B 49, 1548-1551.

[39] Hardy V. *et al.* (1994), The fishtail effect in different Tl based single crystals. A possible interplay with the electronic anisotropy, Physica C, 232, 347-358.

[40] Yang G. *et al.* (1993), Competing pinning mechanisms in $Bi_2Sr_2CaCu_2O_y$ single crystals by magnetic and defect structural studies, Phys. Rev. B, 48, 4054.

[41] Moore J. D. *et al.* (2008), Evidence for supercurrent connectivity in conglomerate particles in $NdFeAsO_{1-\delta}$, Supercond. Sci. Technol., 21, 092004R.

[42] Senatore C., Flükiger R., Cantoni M., Wu G., Liu R. H., Chen X. H. (2008), Upper critical fields well above 100 T for the superconductor $SmFeAsO_{0.85}F_{0.15}$ with $T_c = 46$ K, Phys. Rev. B, 78, 054514.

[43] Yamamoto A. *et al.* (2008), Evidence for two distinct scales of current flow in polycrystalline Sm and Nd iron oxypnictides, Supercond. Sci. Technol., 21, 095008.

[44] Alden T. H., Livingstone J. D. (1966), Ferromargnetic particles in a type-II superconductor, J. Appl. Phys., 37, 3551.

[45] Campbell A. M., Evetts J. E., Dew-Hughes D. (1968), Pinning of flux vortices in type II superconductors, Phil. Mag., 18, 313-343.

[46] Witcomb M. J., Dew-Hughes D. (1973), Superconductivity of heat-treated Nb-65 at. % Ti alloy, J. Mater. Sci., 8, 1383-1400.

[47] Dew-Hughes D. (1966), Hard superconductors, Mater. Sci. Engng, 1, 2-29.

[48] Dew-Hughes D. (1971), The metallurgical enhancement of type II superconductors, Rep. Prog. Phys., 34, 821.

[49] Bilby B. A., Christian J. W. (1961), The crystallography of martensitic transformations, J. Iron Steel Inst., 197, 122-131.

[50] Kwok W. K., Welp U., Crabtree G. W., Vandervoort K. G., Hulscher R., Liu J. Z. (1990), Direct observation of dissipative flux motion and pinning by twin boundaries in $YBa_2Cu_3O_{7-\delta}$ single crystals, Phys. Rev. Lett., 64, 966-969.

[51] Kwok W. K., Welp U., Vinokur V. M., Fleshler S., Downey J., Crabtree G. W. (1991), Direct observation of intrinsic pinning by layered structure in single-crystal $YBa_2Cu_3O_{7-\delta}$, Phys. Rev. Lett. 67, 390-393.

[52] Dew-Hughes D. (1974), Flux pinning mechanisms in type II superconductors, Philos. Mag., 30, 293-305.

[53] Blatter G., Feigel'man M. V., Geshkenbein V. B., Larkin A. I., Vinokur V. M. (1994), Vortices in high-temperature superconductors, Rev. Mod. Phys., 66, 1125-1388.

[54] Larkin A. I., Ovchinnikov Y. N. (1979), Pinning in type II superconductors, Journal of Low Temperature Physics, 34, 409-428.

CHAPTER 3

Experimental Techniques

This chapter represents the detailed description of experimental methods that are employed to synthesize and characterize the $NbSe_2$ single crystals for investigating the physical properties defined in this thesis. Firstly, a brief description of the different crystal growth techniques is presented which includes melt growth, vapour growth, solution growth techniques along with an elaborate description of the iodine vapour transport method. Secondly, a brief review of the various analytical tools including their principle of operations for material characterizations is summarized.

3.1. Sample Growth Technique

3.1.1. Different Kinds of Crystal Growth Techniques:

This section is focussed on the details of the crystal growth techniques which are employed to grow large single crystals of different kinds of materials depending on the requirement of various applications. Single crystals are regular arrangement of basic building blocks (such as atoms, ions, molecules) that is preserved on the macroscopic scale. The crystal lattice of the whole sample is continuous and unbroken to the edges of the samples, with no grain boundaries. The absence of the defects associated with grain boundaries provides single crystals unique properties, especially mechanical, optical and electrical, which can also be anisotropic, depending on the form of crystallographic structure. Single crystals are essential in research specially condensed-matter physics, materials science, surface science, *etc*. Single crystals are broadly used for the study of intrinsic properties and crystalline structures and in innovative applications. Single crystal of silicon is used in the fabrication of semiconductors. Microprocessor fabrications depend on the formation of large single crystals. Most of the superconducting materials are highly anisotropic in nature. Only in single crystals it is possible to study the directional dependence of various properties. So, single crystals are used to estimate the anisotropy associated with fundamental superconducting parameters such as lower and upper critical fields, coherence length, penetration depth and critical current density. Intrinsic characterization of high-quality single crystals boosts the premise for scheming a variety of applications like magnetic imaging and storage, electronic power transmission and high speed signal propagation on strip lines. These are equally used for full determination of the fundamental structures of pure superconducting phases to accelerate the invention of room temperature superconductors and predicting the existence of unfamiliar superconducting compounds.

The growth of single crystals is a challenging task which involves the arrangement of atoms, molecules or ions in a repeating pattern. It depends upon the characteristics of the materials under investigation, such as its melting point, volatile nature, solubility in water or other organic solvents and so on. There are numerous approaches to grow single crystals,

certain procedure of which is appropriate to a certain compound. The methods using for crystal growth can be a small inexpensive technique to a sophisticated growth process with crystallization times ranging from minutes, hours, days and to months. The crystal growth techniques involve in the transport of crystal constituents in the solid, liquid or vapour phase. Hence, the basic growth methods can be classified as solid growth, vapour growth, melt growth and solution growth based on phase transformation. Figure 3.1 represents the classification of different crystal growth methods.

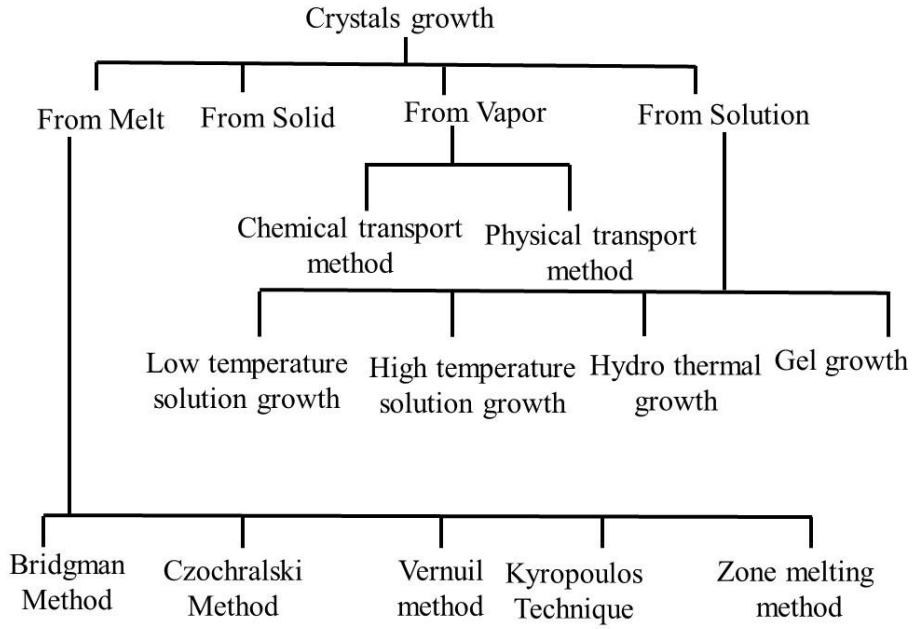

Figure 3.1. *Classification of Single crystal growth techniques.*

3.1.1.1. Melt Growth:

Melt growth is the process of crystallization of fusion and resolidification of the pure material, crystallization from a melt on cooling the liquid below its freezing point. In this technique, there are no impurities introduced in the growth process except the possible contamination from crucible materials and surrounding atmosphere. The rate of growth is normally much higher than possible by other methods. It is commercially the most important method of single crystal growth. The growth from the melt can further be classified into various techniques such as *i*) Bridgmann method, *ii*) Czochralski method, *iii*) Vernuil method, *iv*) Zone melting method, *v*) Kyropoulos technique, *vi*) Skull melting. CaF_2, CeF_3, $Bi_4Ge_3O_{12,}$ *etc*. materials are grown by Bridgmann method. On the other hand, the

materials which are synthesised with Czochralski method are YAG with dopants, YAP with dopants, $LiNbO_3$, $Pb_5Ge_3O_{11,}$ *etc.*

3.1.1.2. Vapour Growth:

The growth of single crystal from vapour phase is likely the most flexible of all crystal development forms. High purity crystals can be synthesised from vapour phase by condensation, sublimation and sputtering of essential materials. Crystallization from vapour is widely used to grow bulk crystal, epitaxial films, and thin coatings of high melting point. Techniques for growing crystals from vapour are divided into two types. They are *i*) Chemical transport method, *ii*) Physical transport method. Chemical transport method involves a chemical transport in which material is transported as chemical compound, which decomposes in the growth area **[1, 2]**. This process is used to synthesis all the samples used in this thesis and discussed elaborately in the next section. Physical transport method involves in the direct transport of materials by evaporation or sublimation from a hot source zone to a cool region. II-VI compounds (ZnS, CdS) are widely grown in this method either in vacuum or with a moving gas stream.

3.1.1.3. Solution growth:

In this method, crystals are grown from aqueous solution. This method is widely used for producing bulk crystals. The four major types of solution growth technique are *i*) Low temperature solution growth, *ii*) High temperature solution growth, *iii*) Hydro thermal growth, *iv*) Gel growth. Hydrothermal growth is suitable for single crystal growth of SiO_2, ZnO, *etc*. The Gel method has been applied to the study of crystal formation in human system such as cholesterol stores, different kinds of hormones etc.

3.1.2. Chemical Vapour Transport (CVT) method:

The most often used method for the growth of single crystal is chemical vapour transport method in which reversible and heterogeneous reactions are involved to transport the source material as a volatile material to the crystallization region **[3-6]**. The systematic research and description of CVT reactions was carried out by Schafer in the 1950s and 1960s **[1]**. The pure and crystalline species of various solids could be made with the help of CVT reaction like metals, metalloid and intermetallic phases as well

as halides, chalcogen halides, pnictides and many others. Selecting a suitable transporting agent is an important subject in this method. In the process of CVT, a condensed phase, typically solid is volatilized in the presence of a gaseous reactant (transport agent) and deposited elsewhere in the form of crystals. The deposition will take place if there are different external conditions (like temperature, pressure) for the chemical equilibrium at the position of crystallization than at the position of volatilization. Usually, different temperatures are applied for volatilization and crystallization as shown in Figure 3.2.

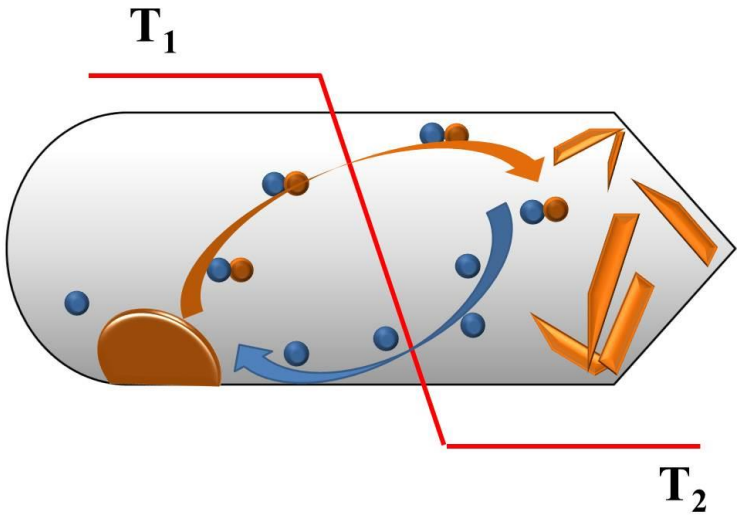

Figure 3.2. *Scheme of CVT experiments for crystallization of solids in a temperature gradient.*

Various transport agents like halogens (iodine, chlorine) and halogen compounds are used for CVT technique. The parameters that can be optimized for an effective CVT reaction are growth temperature, transport direction, rate of mass transport, choice of the transport agent and the free energy of the reaction. Transport is governed through two processes (convection and diffusion). Though larger crystals can be formed by enhancing the transport rates esteeming convection, the crystals become inhomogeneous and are disposed to having more defects. The source and sink temperatures have been altered depending on the free energy of the reaction between the species. Single Crystals of various 2D transition metal dichalcogenides (MoS_2, $MoSe_2$, TaS_2, $TaSe_2$, NbS_2, $NbSe_2$ etc.) showing

different intriguing properties have been successfully achieved by this process.

3.1.3. Synthesis Procedure (Iodine Vapour Transport Method):

High quality single crystals of $NbSe_2$ characterized in this thesis were synthesized by standard iodine vapour transport method with precursors Nb (99.95%), Se (99.999%) and iodine (I_2). The precursors Nb and Se were mixed appropriately in suitable stoichiometric ratio in an agate motor and then pelletized in the form of circular pellets of diameter ~ 1.2 cm by applying pressure using a hydraulic press. Iodine concentration was taken as ~ 5 mg cm^{-3} of quartz tube. Circular pellets (~ 4 gm) were sealed in quartz tube followed by the evacuation of the tube at a pressure of 2.5×10^{-5} mbar in the atmosphere of liquid nitrogen. The quartz tubes with length ~ 20 cm and internal diameter 1.3 cm were utilized for single crystal growth. Vapour transport reactions take place in a temperature gradient. So, the tubes were heated in a two-zone furnace with temperature gradient of about 150 ºC to create the separate environment for the charge zone (zone of volatilization) and growth zone (zone of crystallization). The two zone furnace was kept in a horizontal position to keep convection as part of the gas motion as small as possible. Figure 3.3(*a*) represents the schematic diagram of the two zone furnace which demonstrates the crystals growth process in a temperature gradient, set by a programmed temperature controller. T_1 and T_2 indicate the temperatures of zone 1 and zone 2, respectively with $T_1 > T_2$. The pellets were placed in the high temperature zone (T_1) so that the charges can be volatilised in the form of a chemically intermediate phase. The intermediate phase diffuses to a region of lower temperature T_2. Here the chemical intermediate decomposes and deposits the single crystal of $NbSe_2$. The initial increment of the temperatures of both zones was kept at 4 ºC/hr. The mobility of Nb and Se atoms were enhanced by using iodine which forms the intermediate phase with Nb. The reaction between Nb and Se occurs through an exothermic reaction at an approximate temperature of 550 °C. After that the temperatures of both zones were kept at 900 ºC for one day. For occurrence of the complete reaction, the temperatures of charge zone (zone 1) and growth zone (zone 2)

of two zone furnace were kept at 850°C and 700°C for one week, respectively. Then the furnace was forcefully shutdown to avoid the formation of triselenides.

The equilibrium reaction, which is responsible for the transport of intermediate phase in the growth zone, can be designated by equation (3.1).

$$2NbSe_2 + 2I_2 \rightleftharpoons 2NbI_2 + 2I_2 \quad (3.1)$$

At the growth temperature, the dissociation of the di-iodide to the tetra-iodide occurs which deposits the diselenide following the reaction represented by equation (3.2).

$$2NbI_2 + 2Se_2 \rightleftharpoons NbI_4 + NbSe_2 + Se_2 \quad (3.2)$$

The tetra-iodide cycles to the reaction end of the system, where it reacts with more Diselenide. The process continues until all the charge is transported to the growth region.

The image of Figure 3.3(*b*) shows a sealed quartz tube containing the full-grown single crystal after the removal from two zone furnace. Similar procedures were followed to make single crystals of $NbSe_{1.85}$, Fe_xNbSe_2, Cr_xNbSe_2, and V_xNbSe_2 with the requisite precursors. It is absolutely essential to avoid the condensation of liquid oxygen or moisture within the tubes prior to sealing. For this purpose the tubes are annealed at 1000 °C for 24 hours before putting into the two zone furnace. The single crystals of nearly 4 mm x 4 mm size were obtained using this technique.

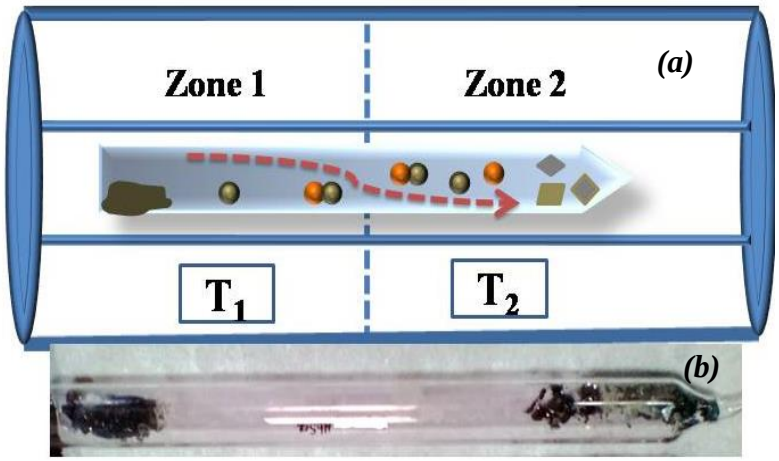

Figure 3.3. *The schematic diagram for synthesis of single crystals through the chemical vapour technique; (a) two zone furnace in which the quartz tube is placed at temperature gradient; (b) shows the quartz tube in which single crystals are formed.*

3.2. Analytical characterization tools

3.2.1. X-ray Diffraction:

The X-ray diffraction (XRD) pattern of a crystalline substance is a rapid analytical technique mostly utilized for phase identification of a crystalline material which can give the information about unit cell dimensions **[7]**. X-ray diffraction technique is utilized to estimate structural characteristics such as lattice parameters, strain, grain size, phase composition, orientation and thermal expansion. In 1916, Debye and Scherrer **[8]** first produced the powder diffraction pattern. It is established on the concept of constructive interference of monochromatic X-rays and a crystalline sample. These X-rays are generated using a cathode ray tube and is filtered to produce monochromatic radiation which is then focused toward the sample.

Theory: The wavelength of X-rays is equivalent to the interatomic distances of crystals. This makes the X-rays to be diffracted from a crystalline specimen by irradiating on it following to the Bragg's law. Bragg's law gives the conditions required for constructive interference for a particular wavelength. According to Bragg's law:

$$n\lambda = 2dsin\theta \tag{3.3}$$

Where *d* represents the spacing between two crystal planes *i. e.* interplanar distance, *n* is an integer, λ is the wavelength of the X-ray beam, θ is acute angle between the incident ray and the scattering. Figure 3.4 explains the Bragg's law where 1 and 2 represent the incident rays and $1'$ and $2'$ represent the diffracted rays. The method, which is employed in XRD measurement, record the intensity of the diffracted X-ray beam with the help of a camera or a diffractometer as a function of Bragg's scattering angle (2θ), the incident wavelength and the specimen's orientation as shown in Figure 3.5. The same family of crystal planes of a specimen produces a diffraction peak at a specified angle. The spacing between the diffracting planes of the atoms determines the peak positions which are the unique properties of a specimen.

The diffraction pattern of a material, as attained experimentally, are compared with standard powder diffraction files published by the

international center for diffraction data (ICDD) and thus the information of all the composition of a specimen can be extracted. ICDD is formally known as joint committee on powder diffraction standards (JCPDS).

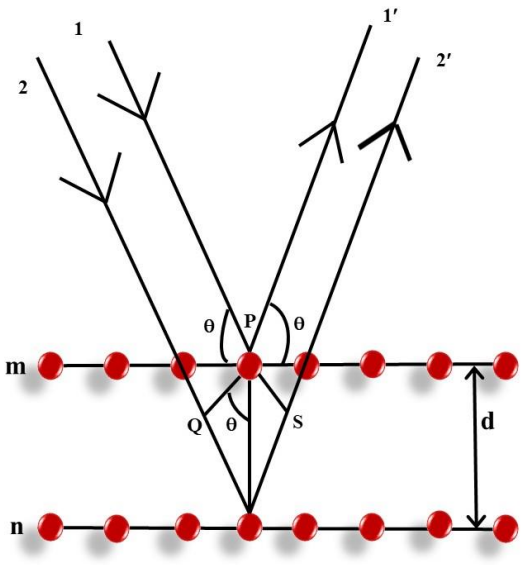

Figure 3.4. *The diffraction process in direct lattice space. Parallel rays are incident on the atomic planes and are scattered as shown.*

A Bruker D8 Advance X-ray diffractometer with CuK_α radiation (λ = 1.54Å) was used to analyse the phase formation and phase purity of the samples presented in this thesis. In this diffractometer incident angle of X-ray beam is changed continuously to record a spectrum of intensity versus angle between incident and diffracted beam. The diffractometer consists of an X-ray tube, incident beam optics, sample holder, receiving side optics and a detector. The X-rays are produced in cathode ray tube by heating filament to high energy electrons, accelerated towards the object by applying electric field and bombarded on the target specimen. These X-rays are diffracted by the sample and are converged at the receiving slits before they enter a detector. A detector records this X-ray signal and converts the signal to a count rate which is then output to a device such as a printer or computer monitor. The XRD pattern of the samples in this thesis are collected in the 2θ range of 10-80° and analysed with the help of FullProf software.

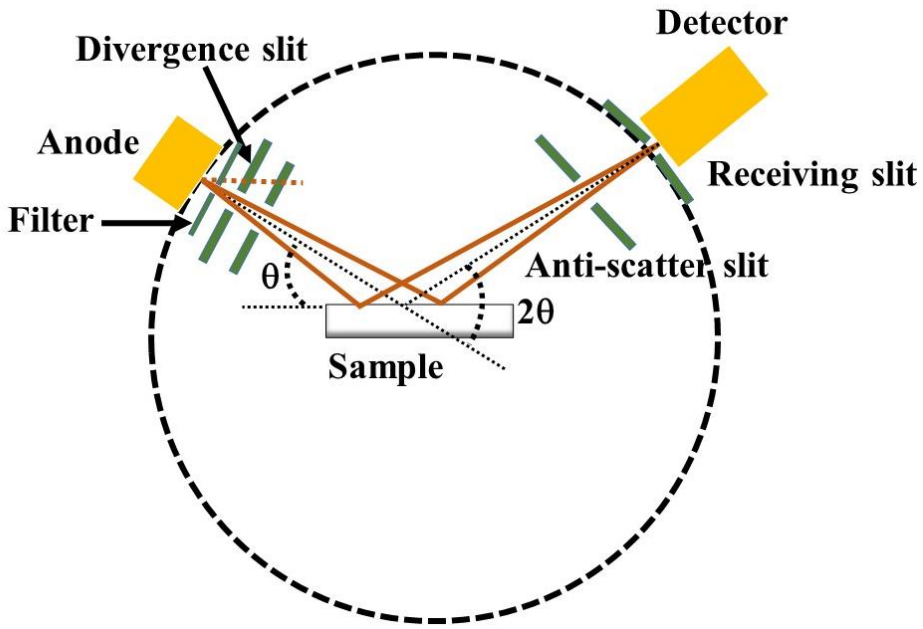

Figure 3.5. *Schematic diagram of X-ray diffractometer showing different components of an XRD. The dotted circles represent the goniometer where the sample is placed in the centre. A divergent source of x-rays is focused on the flat plate sample which then diffracted and collected by the detector. The diffraction pattern is recorded by rotating both the source and the detector at an angle* θ

3.2.2. Scanning Electron Microscopy and Energy Dispersive X-ray Spectroscopy:

The structure and topographies of different kind of surfaces associated with different specimen can be realized nicely by scanning electron microscopy (SEM) with a beam of electrons. The secondary electrons created by the specimen generates image of the sample with high magnification which comprehends the information about the topological characteristics. The elevated magnification, larger depth of focus, greater resolution and the simplification of the procedure of image interpretation make SEM as one of the most intensely employed microscopic analytical tools in research areas today **[9]**.

Theory: SEM utilizes a beam of electrons over a preferred range of electron energies to yield an image with high resolution. An SEM entails the parts: (i) an electron gun, (ii) electromagnetic lens system, (iii) detectors and (iv) a stage or sample holder for imaging the sample (as shown in Figure 3.6).

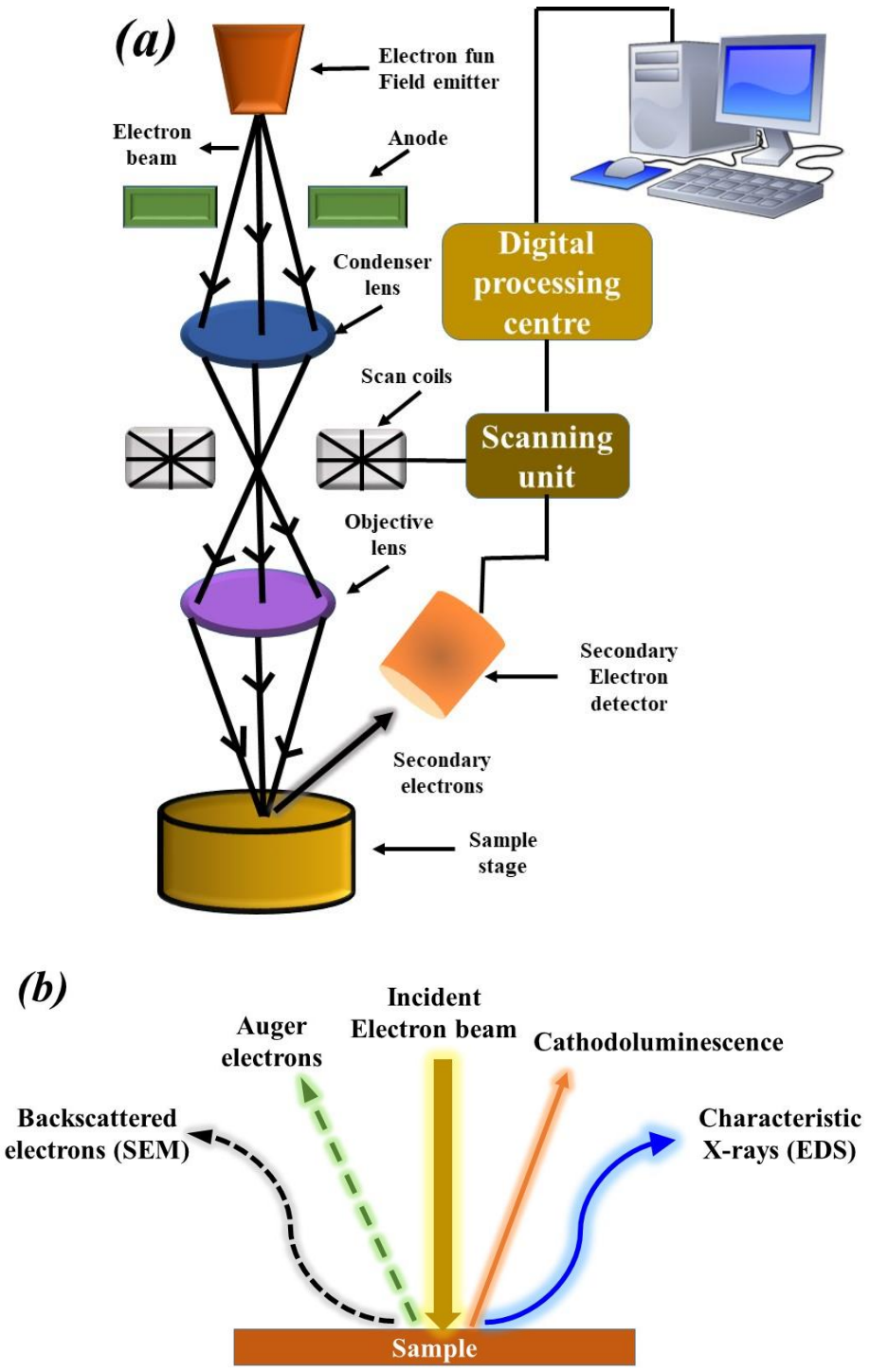

Figure 3.6. *The schematic diagram of (a) SEM, and (b) its working principle.*

To produce a strong penetrating beam of high energy, two sorts of electron guns are used. These are Conventional Thermionic gun and Field emission gun. The conventional thermionic gun consists of a tungsten filament which generates sufficient energy so that the electrons can overcome the work function of the material of filament and emerges as a

highly intense electron beam. The field emission gun consists of a sharply pointed Muller-type emitter at several kilovolts negative potential relative to a nearby electrode to provide sufficient potential gradient at the emitter surface for field electron emission. The emerging highly intense beam is then controlled and focused by electro-magnetic lenses (condenser lens, scan coils, stigmator coils and objective lens) and the apertures in the column towards the sample following a vertical line.

The interaction between the high energy electron beam and the sample causes either inelastic scattering (*i.e.,* involve with atomic electrons) or elastic scattering (*i.e.*, involve with the atomic nucleus). This interaction generates backscattered electrons (BSEs), secondary electrons (SEs), and characteristics X-rays. When an electron energy (excited from the sample) is less than 50 eV, it emerges as SEs, and when the energy of the electron beam is greater than 50 eV, it emerges as BSEs. Different sort of detectors are used to perceive different kinds of beams like Everhart-Thornely detector which is employed to detect the SE electrons. The SE beam is usually used to generate definite image of the surface of a sample. In contrast BSE electrons give the information about atomic number contrast besides the topographic contrast. However, X-ray provides the composition of a substrate (Figure 3.6).

The sample is mounted in a sample holder after it is covered by a conductive layer. It is then implanted to an exchange chamber into the high vacuum part of the microscope and attached on a moveable stage. It can be repositioned in the chamber and can be tilted, rotated and moved in Z direction to generate images at different orientations. The modern electron microscope utilizes field emission technology for ultra-high resolution of electron imaging, which is far superior to conventional scanning electron microscopes.

In order to be observed with SEM, sample is prepared following some procedures. The sample is made conductive for current by coating it with an extremely thin layer (1.5-3.0 nm) of gold or gold-palladium. Furthermore, the sample must be able to hold the high vacuum and should not lose water molecules or gases to interrupt the vacuum. Metals, polymers and crystals are usually less challenging and retain their structure in the

SEM. Here the surface morphology of $NbSe_2$ single crystals have been investigated through field emission scanning electron microscopy (FESEM, Supra 55 Zeiss, and UK).

This system has another associated apparatus called the EDS analyzer (Oxford Instruments, UK), which is utilized for compositional analysis and elemental mapping of the layered structure of the $NbSe_2$ single crystals used in this thesis. Energy Dispersive X-ray spectroscopy (EDS) is an analytical technique which is operated to acquire the elemental analysis or chemical characterization of a material. The principle of this tool is based on the fact that when a beam of electrons falls on the sample, an electron being excited jumps from an internal nuclear shell to an external nuclear shell that results a hole in the former position of an electron. Consequently, another higher energy electron comes to fill the position of the hole and the excess energy emerges as X-ray. The discharged energy contains the characteristic of the energy difference between these two energy levels, thus gives the information about the electronic structure of the components involved in the specimen. An X-ray detector is used to record the number and energy of X-rays generated in the specimen investigated under the irradiation of the electron beam. The energy spectra contain peaks which give the information about the elemental composition of the sample.

3.2.3. Transmission Electron Microscopy:

A transmission electron microscope (TEM) is an extremely effective device that uses a beam of highly energetic electrons to examine objects on the microscopic scale for characterizing crystal structure of different materials and microstructure simultaneously by diffraction and imaging techniques. We get evidence about the morphology (size, shape, arrangement of particles on scale of atomic diameters), crystallographic information and micro-chemical state with an appreciable spatial resolution **[10]**. TEM can be used to study the growth of layers, their composition and defects in semiconductor.

Theory: TEM operates on the same principles as the light microscope but uses electrons instead of light. It consists of a high energy electron beam

which is generated in the electron gun (Thermionic Gun, Field Emission Gun) to analyse the specimen. The electron beam is accelerated under vacuum, focused by condenser lens (electromagnetic bending of the electron beam) into a small, thin, coherent beam. This beam is restricted by the condenser aperture, which excludes high angle electrons. The beam then strikes the specimen and the resulting interaction between the electron beam (Figure 3.7) and specimen provides the subsequent results:

- A part of the high energy electron beam transmitted through the specimen depending upon the thickness and electron transparency of the specimen. This transmitted portion is focused by the objective lens into an image on phosphor screen or charge coupled device (CCD). These transmitted electrons suffer no interaction and no loss of energy in the specimen which carries information about the structure of the sample. The transmitted beam gives a bright field image of the specimen. The darker areas of the image represent those areas of the specimen that fewer electrons are transmitted through while the lighter areas of the image represent those areas of the sample that more electrons were transmitted through.
- Part of the electron beam scattered (both elastic and inelastic way) while passing through the specimen.
- While passing through the specimen, elastically scattered electrons get diffracted from their original path. It results no loss of energy and the transmission of the scattered electron beam occurs through the remaining portion of the specimen. Elastic scattering is usually coherent when the specimen is extremely thin and crystalline. Dark field image is produced by the scattered electron beam where the transmitted electron beam is blocked by the primary aperture.
- All incident electrons which are scattered by same atomic spacing would be scattered by the same angle and will result Bragg's diffraction. This diffracted beam gives us the evidence about the orientation, atomic arrangements, and phases present in the area being examined. Diffraction image is formed when one of the

diffracted beams is selected by using a selected area diffraction aperture.

- There is also inelastic interaction that occurs between the incident electrons and the specimen, which results loss of electron energy. Due to the energy of change, electrons after inelastic scattering become incoherent. The loss of energy associated with the inelastic scattering of electrons can be measured through Electron Energy Loss Spectroscopy (EELS). This information is mainly used for analytical analysis such as elemental composition, chemical bonding and valence and conduction band electronic properties.

Analogous to SEM, a modern TEM consists of filament, an objective lens system, magnification system, a specimen stage and data recording and chemical analysis system. In TEM, sample preparation is a crucial technique as the sample has to pass through several procedures to be thin enough so that electron beam can penetrate it easily.

To characterize the samples in our research work, high-resolution transmission electron microscopy (HRTEM, Tecnai G2 F20 S-Twin) technique and HRTEM-JEOL JEM 2100 was used. The samples were prepared by sonicating the samples in propanol for 30 minutes which results the dispersion of sample in propanol. Then the dispersion was casted on the copper TEM grid with a micropipette, which was permitted to dry for another 60 minutes inside a heating furnace to evaporate the solvent. The $NbSe_2$ samples are observed through TEM in the bright field as well as dark field imaging modes. The modern high-resolution transmission electron microscopy (HRTEM) is an excellent device for imaging at the atomic scale and has outstanding methodical performance. The SEAD pattern containing a series of spots is collected to analyse the crystal structure. HRTEM images are analysed with ImageJ software, which is a public domain Java-based image processing program.

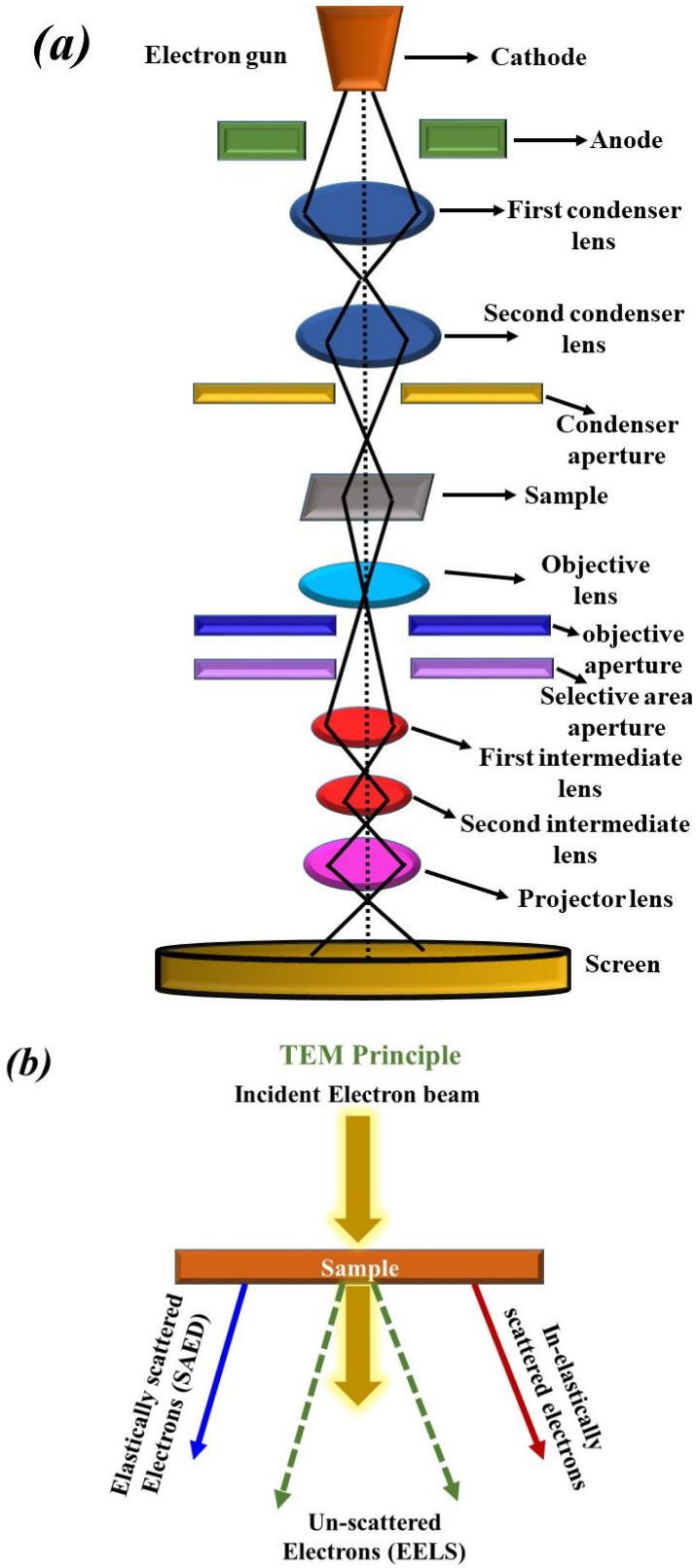

Figure 3.7. *Schematic representation of (a) TEM, and (b) its working principle.*

3.2.4. X-ray Photoelectron Spectroscopy:

X-ray photoelectron spectroscopy (XPS) is a surface-sensitive spectroscopic technique for measurement of the material's surface,

developed by the noble laureate Kai Siegbahn in the 1960s **[11]**. XPS measurements are involved for identifying the elemental composition of a sample surface, the empirical formula of materials, chemical state, presence of any contamination on the material surface, and the electronic state of the elements that exist within a material. So, it not only shows the composition of a material but also gives the information about the other element they are bonded to.

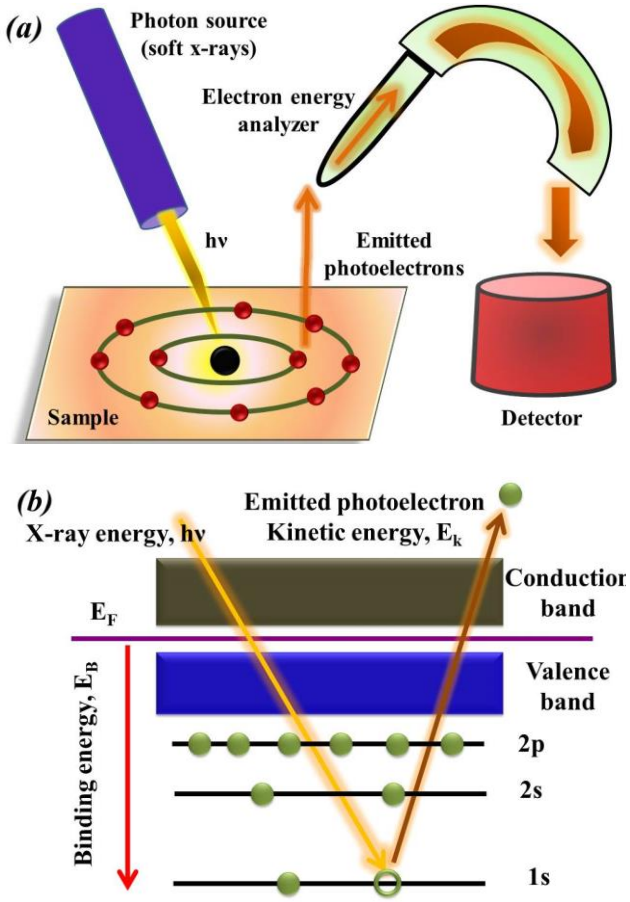

Figure 3.8. *Schematic of the x-ray photoelectron spectroscopy showing its basic components.*

Theory: XPS spectra involve the irradiation of a material with a beam of X-rays while simultaneously measuring the kinetic energy and number of electrons that escape from the top (~ 0 to 10 nm) of material's surface that being analysed. In XPS, soft X-rays of energy 100 – 2500 eV is generally utilized to investigate the core levels of the material surface under ultra-high vacuum. Generally, when the X-rays of sufficient energy fall on the sample, it excites the core-level electrons of the bound states resulting the

ionization and emission of the core electrons (photoelectrons) (Figure 3.8). The emitted photoelectrons are then detected by a hemispherical electron analyzer which measures their kinetic energy. To count the number of electrons during the acquisition of a spectrum with a minimum error, XRS detectors must be operated under high vacuum (UHV) conditions. Based on the theory of the photoelectric effect, the electron analyzer generates an energy spectrum of the detected photoelectrons versus detected binding energy following to the relation given by Ernest Rutherford **[12]** as represented by equation (3.4).

$$E_B = h\nu - (E_k + \Phi) \qquad (3.4)$$

where, E_B represents the binding energy of the photoelectrons, $h\nu$ is the photon energy and E_k represents the kinetic energy of the emitted photoelectrons with "Φ" as a work function of the spectrometer.

The XPS measurement of the synthesized $NbSe_2$ single crystal was implemented using a Kratos Axis spectrometer with Al K_α source ($h\nu$ = 1886.6 eV) in an ultra-high vacuum chamber. Survey scan data were collected at the pass energy of 50 eV and using a high energy hemispherical detector analyser (HDA). The vacuum chamber consists of various probes, anlyzers, and detectors. The pressure inside the ion-pumped analysis reactor is maintained upto 1.0×10^{-9} mbar throughout the data procurement. The shifting in the binding energy values due to the surface charging effects is resolved considering the C1s peak (binding energy value of 285 eV) as the standard reference. The precision of the binding energy values is in the range of ± 0.2 eV.

3.2.5. Physical Properties Measurement System (PPMS) – Vibrating Sample Magnetometer (VSM):

The PPMS (Quantum Design, USA) is considered as a unique tool in determining several physical characteristics such as transport and magnetic properties based on specifically planned measurement options. Sample background consists of magnetic fields up to ± 90 kOe and the temperature range of 1.9 - 400 K. Its innovative flexible structure allows various characteristics in one device that makes the PPMS as one of the most resourceful instrument. The PPMS consists of sealed sample chamber

with 2.6 cm diameter sample access, pulse tube (PT410, Cryomech, UK), cryogen-free cooling technology and versatile sample mounts couple with 12 electrical leads made into the chamber insert. PPMS is controlled by a microprocessor-controlled device (Model 6000) that has current or voltage sources using an integrated visual basic interface within the Windows-based MultiVu software. Figure 3.9 displays PPMS 90kOe associated with the VSM **[13, 14]**.

3.2.5.1. Outline of VSM module:

The VSM P525 (Quantum Design, USA) option, designed for the PPMS is a fast and sensitive DC magnetometer where the measurement is done by vibrating the sample adjacent to a detection (Pickup) coil and simultaneously the induced voltage is recorded. Simon Foner invented VSM in 1955 and reported in 1959 **[15]**. Figure 3.10 represents the Photograph of a VSM and detection coil (M/s Quantum Design, USA) **[14]** and Figure

Figure 3.9. *Photograph of a PPMS-VSM setup available at the CHPR, Bharathidasan University, Tiruchirappalli.*

3.11 describes the working principles of VSM, respectively. VSM is employed to measure the magnetic hysteresis loops and conduct the temperature - dependent magnetization measurements with a static magnetic field. The compact gradiometer pickup coil configuration, which has comparatively large oscillation amplitude (1-3 mm peak) and a

frequency of 40 Hz, is capable of determination of changes in magnetization less than 10-6 emu at a data rate of 1 Hz.

The VSM option for the PPMS mainly contains a VSM linear motor transport (head) for oscillating the sample, a coil set puck for detection, electronics for driving the linear motor transport and detecting the response from the pickup coils, and a copy of the MultiVu software application for automobile and control. The signals are recorded using two pickup coils, large coil and small-bore coil. Small bore is used for magnetization measurement at ambient pressure whereas large bore is used for pressure dependent magnetization measurement.

3.2.5.2. Principle of VSM and measurement procedure:

The fundamental principle of a VSM is based on the Faraday's law of induction **[15, 16]**, which can be represented by the following equation (3.5).

$$\boldsymbol{V_{coil} = \frac{d\emptyset}{dt}} \tag{3.5}$$

Where V_{coil} is the induced voltage and $\frac{d\emptyset}{dt}$ represents the change in magnetic flux.

The sample to be measured is kept in the middle of a paddle shaped sample rod by GE varnish. The sample rod is then inserted through the VSM motor into the PPMS Dewar. The magnetization of a sample upsurges due to the enhancement of the magnitude of the magnetic field and the alteration in flux generates a voltage signal, which is recorded by the pickup coil located near the sample. The signal is generally small, and is amplified by a lock-in amplifier at a specific frequency. The signal measured by the pickup coil is directly proportional to the magnetization of the sample and independent of the external field intensity.

The magnetization measurements of the proposed samples presented in this thesis were carried out in ZFC and FC modes in the Centre of High Pressure Research of Bharathidasan University. In ZFC mode, the sample was cooled initially in zero magnetic field and the data was recorded on warming by applying an external magnetic field, whereas in FC mode the data was recorded upon cooling without removing the applied magnetic field. Isothermal magnetization curves near the superconducting transitions

were accomplished for all the samples in order to investigate both the reversible magnetization and irreversible magnetization associated with versatile vortex dynamics of $NbSe_2$. During the measurement of temperature dependence of ZFC and FC curves, the temperature was measured by continuously keeping the sweep rate at 1 K/min. The ZFC and FC hysteresis loops of $NbSe_2$ were measured with the sweep rate of 100 Oe/sec.

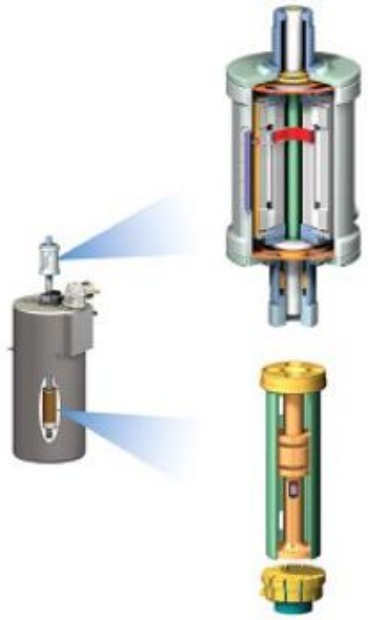

Figure 3.10. *Photograph of a VSM and detection coil (M/s Quantum Design, USA).*

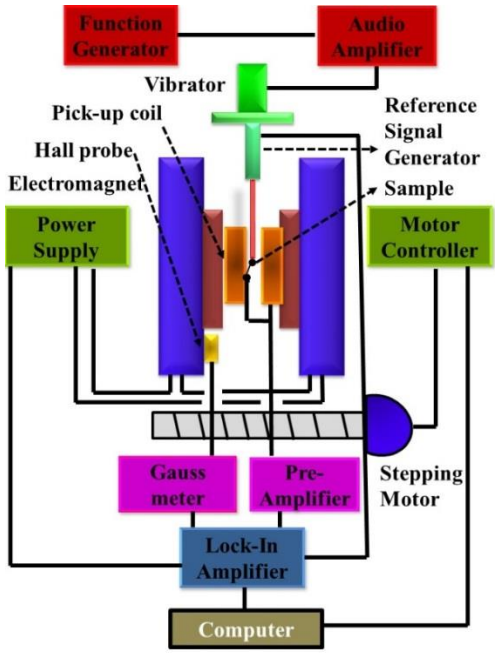

Figure 3.11. *The schematic diagram of Vibrating Sample Magnetometer (VSM).*

3.2.6. Resistivity/Magnetoresistance Set-up:

Many conventional methods are generally used for the resistivity measurement of different materials **[17, 18]**. The method used in this thesis to complete the resistivity measurement of the proposed samples is four probe method. It permits measurements of resistivity in samples having a wide variety of shapes, including the resistivity of small volumes within the bigger pieces. In this method, four sharp probes are placed on the flat surface of the material to be measured, current is passed through the outer electrodes, and the floating potential is measured across in the inner pair. To prevent minority carrier injection and make good contacts, the surface on which the probes rest, is mechanically exfoliated. The insert for resistivity measurements is the most important tool in the resistivity and/or magnetoresistance set-up at extremely low temperatures. It has been designed and developed to provide cryogenic environment inside liquid helium storage Dewar for various measurements such as resistivity, heat capacity etc., in the absence of magnetic field. The sample space temperature of this insert can be varied from 1.5 K to 300 K and it requires very less amount of liquid helium. To generate high magnetic field and low temperature environment, a superconducting magnet system, purchased from Oxford instruments is used. This system consists of a superconducting solenoid, which can produce magnetic field up to 80 kOe at 4.2 K. This system can be operated in the persistent mode using a persistent current switch, which is formed by wrapping a small heater around a short segment of the magnet's superconducting wire.

The insert for the resistivity and magnetoresistance measurements contains a sample holder which is made of square OHFC copper block ($12\times12\times40$ mm^3). At the top of each face of the copper block, a cigarette paper is attached with GE varnish to insole the samples electrically from the sample holder. Four samples can be loaded on each face. At the four corners of the block, copper strips are attached, on which PCB strips have been attached to make electrical terminals. From these terminals four uninsulated copper wires (two each for current and voltage leads) for each sample are taken for electrical contacts. The electrical contacts on samples

are made with the help of silver paste or indium solder. For temperature measurement, a calibrated Cernox temperature sensor (model no. CX-1050-SD) is fixed in the sample holder using GE7031 varnish. The sensor has been calibrated with respect to a calibrated Cernox temperature sensor purchased from Lakeshore Cryogenics. A pairwise twisted manganin wire is wounded around both the ends of the copper block as a heater for homogeneous heating. This copper block is connected to about a meter long SS tube of diameter 10 mm. On the SS tube ten equally spaced copper baffles of thickness 1 mm and diameter 36 mm are brazed. These baffles act as a radiation shield and also utilized the enthalpy of outgoing He gas for efficient cooling. The copper wires of SWG 44 (0.081 mm diameter) are utilized as electrical leads from sample and temperature sensor to the room temperature end of the insert. For the sample holder heater, SWG 34 (0.234 mm diameter) copper wire is used. The voltage leads as well as current leads are pair-wise twisted separately, for each sample holder. Since large numbers of copper wire are coming from room temperature to the sample holder, it may prevent to achieve the lowest temperature. Therefore careful thermal anchoring has been done to overcome this problem.

In this insert, sixteen samples can be loaded at a time. It can be used for resistivity measurements in absence of magnetic field in the temperature range of 1.5-300 K, with the general-purpose variable temperature insert. For in-field measurements same resistivity insert is used with the magnet system, which provides a magnetic field up to 100 kOe and temperature variation 1.5 to 300 K. The samples are fixed on sample holder with the help of GE varnish. Silver paint is used for making electrical contacts. In some cases indium contacts are also used. After making the contact the insert is placed inside the cryostat (VTI or magnet system) for resistivity and magnetoresistance measurements.

The schematic diagram of the electrical connections between the various electronic instruments used in this set up is shown in Figure 3.12. Lakeshore temperature controller (DRC-93CA) is used for measuring and controlling the temperature of the sample holder. For selecting the different samples Keithley Switching System (model 7002) is used. A nanovolt

scanner card (model 7168) is used for switching between the voltage leads of different samples and a general-purpose scanner card (model 7056) for switching between the current leads. Keithley source meter (model 2400) is used for sending the current through the current leads, and the voltage across the voltage leads is measured by Keithley sensitive digital voltmeter (model 182). The automation is written Quick Basic. A PC (HP486) is used for controlling and automated data collection using IEEE-488 interface. The measurement is started by controlling the temperature of interest using Lakeshore temperature controller. After controlling the temperature, the scanner selects a particular sample. Then through the current lead a specified current is passed through the sample and voltage is measured again. It cancels the offset voltage generated due to thermos emf, which is independent of the current direction. The process is repeated few times to improve the accuracy of the measurement. After that the scanner selects the next sample for measurement and repeats the process. Since one nanovolt scanner card can scan voltage of only eight samples, at present it is possible to do the measurement of maximum eight samples at a time. Once the measurement of all the samples are completed the temperature controller sets next temperature. The process of measurement is repeated after achieving the required temperature stability. The collected data is plotted online as resistance versus temperature on the computer monitor.

The resistivity (ρ) is determined from the resistance (R) following equation 3.6.

$$\rho = \left(\frac{A}{l}\right) R \tag{3.6}$$

Where A is the area perpendicular to current direction and l is the distance between the voltage leads.

The magnetoresistance ($\Delta\rho/\rho$), which is defined as

$$\frac{\Delta\rho}{\rho} = \frac{\rho(H,T)-\rho(0,T)}{\rho(0,T)} \tag{3.7}$$

can be measured in two different modes; (*i*) Magnetoresistance as a function of temperature at constant magnetic field, which is obtained from the measured resistance as a function of temperature in zero magnetic field and in presence of constant magnetic field. (*ii*) Magnetoresistance as function of magnetic field at constant temperature can be obtained by

measuring the resistance at various magnetic fields at that temperature. If the magnetic field is parallel to the current direction it is known as the longitudinal magnetoresistance and if it is perpendicular to the current direction it is known as the transverse magnetoresistance. The magnetoresistance data presented in this thesis is the longitudinal magnetoresistance.

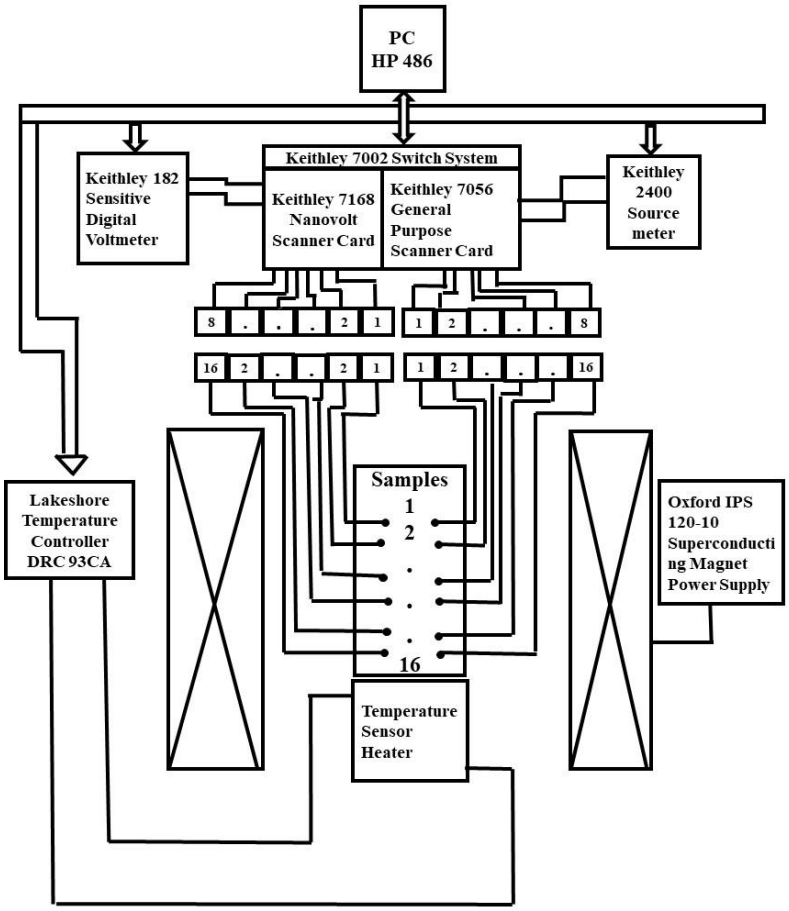

Figure 3.12. *Block diagram of Resistivity/Magnetoresistance set up.*

In our thesis work, we have measured resistance of $NbSe_2$ and doped $NbSe_2$ single crystals as a function of temperature at 2K-300 K temperature to investigate the superconducting transition and the effect of intrinsic and extrinsic defects in UGC-DAE Consortium for Scientific Research, Indore. Magnetoresistance measurement as a function of temperature at constant magnetic field was also accomplished of various samples.

In summary, in this chapter the single crystal growth techniques and various characterization techniques are successfully demonstrated.

References

[1] Schäfer H. (1962), Chemische Transportreaktionen, Verlag Chemie, Weinheim/Bergstr, German, pp 1-142 (DOI: 10.1002/bbpc.19620661032).

[2] Binnewies M., Glaum R., Schmidt M., Schmidt P. (2012), Chemical Vapor Transport Reactions-Methods. Materials, Modeling, Advanced Topics on Crystal Growth, Berlin, pp 1-305 (DOI: 10.5772/55547).

[3] Schäfer H. (1971), Thermodynamische gesichtspunkte bei der auswahl chemischer transportvorgänge, J. Cryst. Growth, 9, 17-30.

[4] Kaldis, E. (1974), Principles of the Vapour Growth of Single Crystals. In: Goodman C. H. L. (Eds.) Crystal Growth, Springer, Boston, MA, pp 49-191 (ISBN 978-1-4757-1274-2).

[5] Mercier J. (1982), Recent developments in chemical vapor transport in closed tubes, J. Cryst. Growth, 56, 235-244.

[6] Lenz M., Gruehn R. (1997), Developments in measuring and calculating chemical vapor transport phenomena demonstrated on Cr, Mo, W, and their compounds, Chem. Rev., 97, 2967-2994.

[7] Dinnebier, R. E., Billinge, S. J. L. (Eds.) (2008), Powder Diffraction: Theory and Practice, RSC Publishing, Cambridge, UK, pp 1-582 (ISBN 978-0-85404-231-9).

[8] Cullity, B. D., Stock, S. R. (2001), Elements of X-Ray Diffraction, 3rd edition, Prentice Hall, Inc., New Jersey, pp 1-531 (ISBN 9789332535169).

[9] Vernon-Parry K. D. (2000), Scanning electron microscopy: An introduction, III-Vs Review, 13, 40-44.

[10] Williams, D. B., Carter, C. B. (1996), The Transmission Microscope, Springer, pp 1-275, (ISBN 978-0-387-76501-3).

[11] Konigsberger, D. C., Prince, R. (1988), X-Ray Absorption: Principles, Applications, Techniques of EXAFS, SEXAFS and XANES, Wiley: New York (ISBN: 978-0-471-87547-5).

[12] Hollander J. M., Jolly W. L. (1970), X-Ray photoelectron spectroscopy, Acc. Chem. Res., 3, 193-200.

[13] Cullity, B. D., Graham, C. D. (2009), Introduction to Magnetic Materials, Second ed., John Wiley & Sons, Inc., New Jersey, pp 1-537 (ISBN 978-0-471-47741-9).

[14] Physical Property Measurement System Vibrating Sample Magnetometer User's Manual, Quantum Design, USA.

[15] Foner S. (1959), Versatile and Sensitive Vibrating-Sample Magnetometer, *Rev. Sci. Instrum*., 30, 548-557.

[16] Jackson, J. D. (2007), Classical Electrodynamics, 3RD ed., John Wiley & Sons, New work, pp 1-832 (ISBN 8126510943, 9788126510948).

[17] Vander Pauw L. J. (1958), A method of measuring specific resistivity and Hall effect of discs of arbitrary shape, Philips Res. Repts., 13, 1-9.

[18] Scofield J. H. (1987), AC method for measuring low-frequency resistance fluctuation spectra, Rev. Sci. Instrum., 58, 985-993.

CHAPTER 4

Effect of Fe Doping on Niobium Diselenide ($NbSe_2$) Single Crystal

D*ifferent dopants such as* Co^{2+}, Fe^{3+}, Fe^{2+}, Sn^{4+}, Cu^{2+} *etc. are adequately efficient* ***[1-3]*** *to control the superconducting properties of* $NbSe_2$*, and there is no doubt that these doping investigations give significant information to understand the physical properties of* $NbSe_2$*. As already discussed,* $NbSe_2$ *is a promising candidate among all transition metal dichalcogenides for studying of different physical properties* ***[4]****. Due to the layered structure* ***[5]****,* $NbSe_2$ *shows large anisotropy in the electrical* ***[6]****, mechanical and magnetic properties. Here iron atoms are added to the layered structure of* $NbSe_2$ *to give some insight into the* J_c *characteristics and pinning mechanism.*

To study the doping effect in the vortex dynamics of layered superconductors, we have first chosen magnetic element iron (Fe), where Fe belongs to group-VIII. Fe is *d*-block transition metal element with ionic radii of 0.63 nm which is ferromagnetic in nature. The prime objective of this chapter is to study the effect of Fe doping on $NbSe_2$ single crystal and investigate their structural and superconducting properties. The superconducting properties include the enhancement of critical current density (J_c), improvement of pinning mechanism and also the interaction between vortices and pinning centres. To improve the superconducting properties, it is very important to control the magnetic field dependence of J_c characteristics due to sharp reduction of the J_c values with increasing magnetic field making it inapplicable in practical purpose. Irradiation **[7]** and foreign atom doping are two most efficient procedures to improve superconducting J_c characteristics **[8]**. The defects created due to the addition of foreign atom changes elasticity of the vortex lattice which compensates with the change in pinning force density (F_p) **[9]**. The destabilization created due to the defects leads variety of pinning regime like weak collective pinning regime and strong pinning regime **[10]**. The transverse (R_c) and longitudinal (L_c) correlation length that are estimated from the three dimensional (3D) nature of the crystal structure **[11]** give some deep insight into the short range order of vortex lattice created due to the random distribution of the weak pins. Banerjee *et al.* **[12, 13]** gives the experimental evidence on the vortex dynamics specially the peak effect phenomena based on the transition from order to disorder of vortex lattice from J_c study and theoretical explanation on pinning strength.

Most of the literature in Fe-doped $NbSe_2$ single crystal focusses on the change of transport properties such as resistance, magnetoresistance, Hall effect due to the presence of Fe impurities. Hillenius *et al.* **[16]** studied the temperature dependence of the susceptibility measurement in the range 1.3-300 K for Fe intercalated $NbSe_2$ single crystals for the Fe concentration range from 0 to 33 %. Curie-Weiss behaviour is reported at higher temperatures and a susceptibility maximum at lower temperatures with a long-range ordered antiferromagnetic state at higher Fe concentration. Similarly, Morris *et al.* **[17]** depicted nicely the Kondo effect and its

anisotropic nature with the direction of magnetic fields in Fe doped $NbSe_2$ in the range 0.25% to 5%. However, $NbSe_2$ with the addition of Fe is also investigated through low temperature scanning tunnelling microscopy and spectroscopy showing the change in its superconducting properties **[1]**. Dai *et al.* **[18]** reported the changes of the electronic, magnetic and structural properties in $NbSe_2$ single crystals using scanning tunneling microscope (STM) and atomic force microscope (AFM) probing induced by Fe doping. They observed that the formation of Fe superlattice in Fe_xNbSe_2 at the higher concentration of Fe atoms (above $x > 0.20$) replacing the CDW superlattice with a reduced but stable energy gaps in the electronic spectrum. Fasano *et al.* **[19]** reported the magnetic decorations of the vortex structures of Fe doped $NbSe_2$ single crystal which shed light on the correlation between the topology of vortex structure and the J_c characteristics in disordered vortex phase. Noto *et al.* **[20]** showed magnetoresistance and temperature dependence of the electrical resistivity in the Fe doped $NbSe_2$ single crystals indicating the presence of interband scattering. However, despite of all these findings, a systematic experimental study on J_c characteristics and pinning mechanism with variation in doping concentration is somewhat limited. Complete understanding regarding the interaction between the vortices and the defects driven in presence of random pinning potential of Fe atoms are necessary to optimize the J_c characteristics at different layered superconductors. So, Fe doped $NbSe_2$ single crystal is a very interesting field to explore as it will help to improve further the practical applicability of anisotropic, layered Fe based superconducting materials.

This chapter demonstrates the temperature and magnetic field dependence of magnetization measurement and the change of the magnetic hysteresis loop (MHL) of $NbSe_2$ and Fe_xNbSe_2 (with $x = 0.0008, 0.0011$) single crystals. The magnetic field dependence of the J_c characteristics of these samples is investigated based on Larkin-Ovchinnikov (LO) collective pinning model **[21]**. Further the effect of core interaction is discussed to show the change in the vortex pinning mechanism due to Fe doping. The

magnetic field dependence of the pinning force density is also shown in this chapter to investigate further improve of J_c on increasing magnetic field.

4.1. Materials and Method

Materials: Niobium (Nb, 99.95%; Alfa Aesar), Selenium (Se, 99.999%; Alfa Aesar), iron (99.99%; Alfa Aesar) and Iodine (I_2, 99.998%; Alfa Aesar).

Method: The large single crystals of $NbSe_2$ and Fe_xNbSe_2 (with x = 0, 0.0008, 0.0011) were grown through the method of chemical vapour transport reactions using iodine as a transporting agent. The precursor, Nb, Se and Fe were grinded in an agate motor to form pellet without any further refinement. Circular pellets (~ 4 gm) were sealed in quartz tube by evacuating the tube at a pressure of 2.5×10^{-5} mbar. The quartz tubes with length ~ 20 cm and internal diameter 1.3 cm were utilized for single crystal growth. The tubes were heated in a two-zone furnace with temperature gradient of about 150 ºC. The pellets were placed in the high temperature zone (T_1) so that the charges can be volatilised in the form of a chemically intermediate phase. The intermediate phase diffuses to a region of lower temperature. Here the chemical intermediate decomposes and deposits the single crystals of $NbSe_2$ and Fe_xNbSe_2. The initial increment of the temperatures of both zones was kept at 4 ºC/hr. The reaction between Nb and Se occurs through an exothermic reaction at an approximate temperature of 550°C. For occurrence of the complete reaction, the temperatures of charge zone (zone 1) and growth zone (zone 2) of two zone furnace were kept at 850 °C and 700 °C for one week, respectively. The furnace was forcefully shutdown to avoid the formation of triselenides. The obtained single crystals were characterized further for structural and physical properties.

4.2. Results and Discussion

4.2.1. Structural properties:

X-Ray diffraction: The XRD patterns of $NbSe_2$, $Fe_{0.0008}NbSe_2$ and $Fe_{0.0011}NbSe_2$ single crystals are represented in Figure 4.1. All XRD peaks of the single crystals are indexed with the hexagonal phase of $NbSe_2$ (space

group P63/mmc), suggesting that all the crystals are phase pure according to the JCPDS card no. 01-070-5612 with $a = b = 3.442$ Å and $c = 12.547$ Å. It has been observed from Figure 4.1 that the strong directional growths along the (00*l*) planes, indicating that all the single crystalline samples are orientated along the *c*-axis. The addition of Fe atoms in $NbSe_2$ does not show any additional impurity peaks confirming the phase purity of the samples without any change in their hexagonal phase.

However, it has been noticed from Figure 4.1 that the suppression of the (008) peak intensity with an increase in the (006) and (004) relative intensities. It gives the hint of growth along the (006) and (004) directions with an increase in Fe concentration and confirms the Fe incorporation into the $NbSe_2$ lattice. The intensities of (0010), (0012) and (0014) are relatively very small (almost in the background level).

Due to the comparable ionic size of Fe^{3+} (0.645 Å in CN = 6) and Nb^{4+} (0.68 Å in CN = 6), Fe^{3+} ions can easily replace Nb^{4+} ions in the $NbSe_2$ lattice without any lattice distortion. It can result the Vegard's law type behaviour in the lattice parameters. Again, due to the presence of van der Waals gap, layered TMDs offer space for the intercalation of smaller cations. As the doping level of Fe atoms is less than 5 % in our case, it is very difficult to detect by XRD. The estimated *c*-axis lattice parameter of $NbSe_2$ is in good agreement with the standard JCPDS data and has been found to be $c = 12.55(5 \pm 4)$ Å. It is observed that an insignificant shift in the *c*-axis lattice parameter in $Fe_{0.0008}NbSe_2$ within the error bar. The peak positions shift towards the lower two theta value with increase in Fe concentration (*i.e.*, $Fe_{0.0011}NbSe_2$). The estimated *c*-axis lattice parameters are provided in Table 4.1. It is observed that the *c*-lattice parameter increases slightly in $Fe_{0.0011}NbSe_2$. Analysing above results, where defects are created by foreign atoms **[2, 3]**, support the successful incorporation of Fe atoms between the Nb-Se-Nb layers as Fe clusters.

Unit cell lattice parameter for a hexagonal structure of $NbSe_2$ and Fe_xNbSe_2 has been calculated using equation (4.1), as shown in Table 4.1.

$$\frac{1}{d^2} = \frac{4}{3a^2}(h^2 + (hk) + k^2) + \frac{l^2}{c^2} \qquad (4.1)$$

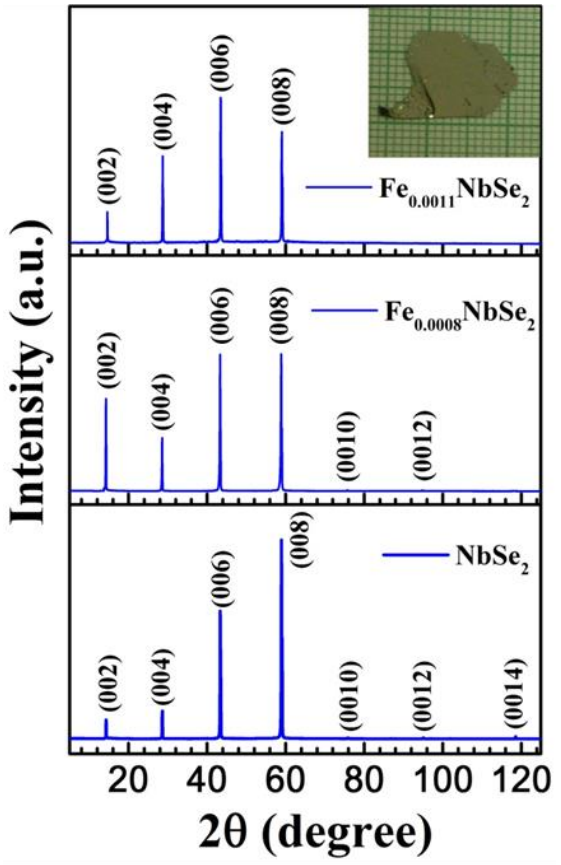

Figure 4.1. *XRD pattern of $NbSe_2$, $Fe_{0.0008}NbSe_2$, $Fe_{0.0011}NbSe_2$ single crystals and the inset shows the typical photograph of the single crystal of $NbSe_2$.*

The variation in the estimated full width at half maxima (*FWHM*) (Table 4.1) with doping concentration shows non-systematic or negligible variation. There might be two probable reasons for the non-systematic change in *FWHM* with doping concentration; first is due to the change in the structure of $NbSe_2$ and second is due to internal compressive micro strain.

Table 4.1. *Estimated structural parameters for $NbSe_2$ and Fe_xNbSe_2 (x = 0.0008, 0.0011) single crystals.*

Sample	*c* (Å)	*FWHM*			
		(002)	*(004)*	*(006)*	*(008)*
$NbSe_2$	12.555±0.004	0.12	0.12	0.16	0.12
$Fe_{0.0008}NbSe_2$	12.559±0.003	0.11	0.12	0.14	0.14
$Fe_{0.0011}NbSe_2$	12.568±0.005	0.07	0.17	0.21	0.27

4.2.2. Superconducting properties:

4.2.2.1. Temperature dependent magnetization studies:

To study the evolution of superconducting properties with Fe incorporation in Fe_xNbSe_2, we first investigated the temperature dependent magnetization behaviour. Figure 4.2 ((*a*-1)-(*c*-4)) displays the temperature dependence of the magnetization measurement of pure and Fe_xNbSe_2 in presence of 0.0005 T, 0.05 T, 0.2 T and 1 T magnetic field in both zero field cooled (ZFC) and field cooled (FC) modes. The deviation of the ZFC curves from zero magnetization value gives the diamagnetic transition temperature (T_c) at each magnetic field and indicated by red arrow in Figure 4.2.

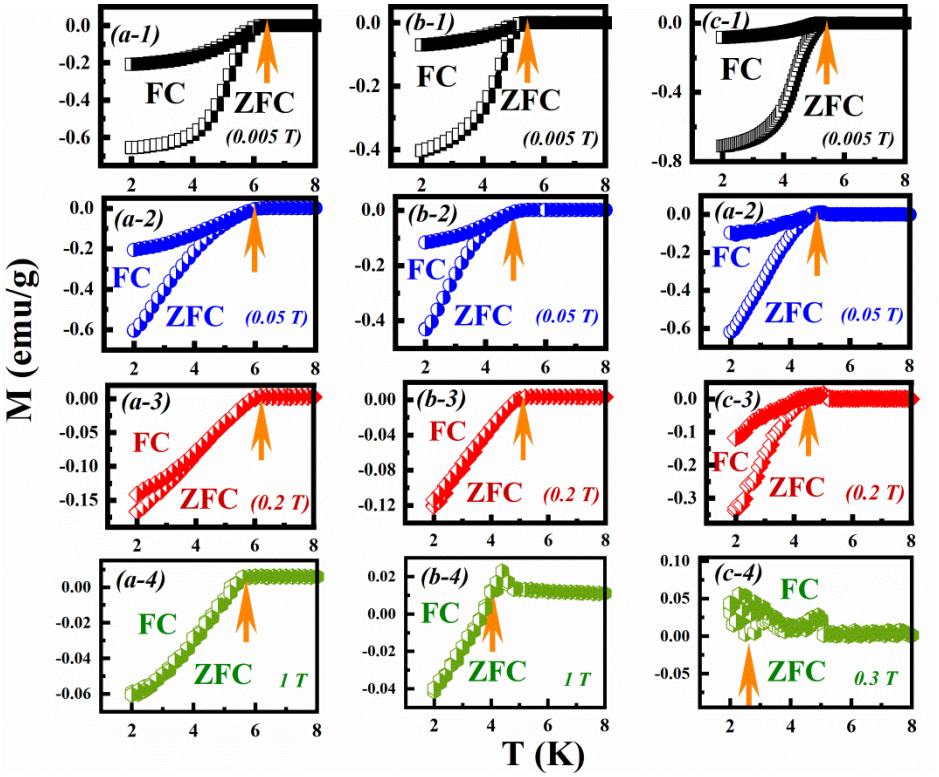

Figure 4.2. *Shows the temperature dependence of magnetization measurements of pure $NbSe_2$ single crystal at (a-1) 0.005 T (a-2) 0.05 T(a-3) 0.2 T (a-4) 1 T magnetic field; $Fe_{0.0008}NbSe_2$ single crystal at (b-1) 0.005 T (b-2) 0.05 T (b-3) 0.2 T (b-4) 1 T magnetic field; and $Fe_{0.0011}NbSe_2$ single crystal at (c-1) 0.005 T (c-2) 0.05 T (c-3) 0.2 T and (c-4) 0.1 T magnetic field.*

The T_c values are decreased systematically with increasing magnetic fields for both $NbSe_2$ and Fe_xNbSe_2. This suggests that the reduction of the shielding effect of supercurrent with increasing magnetic fields. At higher magnetic fields both ZFC and FC curves merge. It is due to the rapid

destruction of superconducting region overcoming the pinning effects associated with defects. However, Figure 4.2. shows the T_c values also shift systematically to lower temperatures with increasing concentration of Fe in Fe_xNbSe_2. This indicates that the Fe-incorporation appears as the disruptive for superconducting Cooper pair electron densities in $NbSe_2$. Similar results have been described by Luo *et al.* **[2]** and Naik *et al.* **[3]**, where such suppression in T_c values with the doping of foreign atoms has been acknowledged in Cu_xNbSe_2 and Sn_xNbSe_2. Here we can conclude that this may be due to either the electron doping of the $NbSe_2$ layer that results on Fe intercalation or to the magnetic disorder accounted for Fe incorporation. The degradation of T_c values with both Fe doping as well as with increase in magnetic field is listed in Table 4.2.

Table 4.2. *The variation of T_c with magnetic fields and Fe concentration for $NbSe_2$ and Fe_xNbSe_2 (x = 0.0008, 0.0011) single crystals.*

Sample	T_c (K) (@ 0.005 T)	T_c (K) (@ 0.05 T)	T_c (K) (@ 0.2 T)	T_c (K) (@ 1 T)
$NbSe_2$	**6.4**	**6.2**	**5.8**	**5.0**
$Fe_{0.0008}NbSe_2$	**5.4**	**5.1**	**4.8**	**3.6**
$Fe_{0.0011}NbSe_2$	**5.2**	**4.6**	**4.3**	**NA**

4.2.2.2. Upper limit of superconductivity:

To obtain the evolution of *H-T* phase diagram with Fe-incorporation, we estimated the upper limit of magnetic fields (*i.e.*, the H_{c2} values) upto which the superconductivity of Fe_xNbSe_2 exists. The upper critical fields of $NbSe_2$, $Fe_{0.0008}NbSe_2$ and $Fe_{0.0011}NbSe_2$ are estimated from the *M-T* curve considering the onset point of the superconducting transition at each magnetic field **[22]**. The $H_{c2}(T)$ values of the samples are plotted as a function of temperature in Figure 4.3, which is fitted with the anisotropic *G-L* single band formula, $H_{c2} = H_{c2}(0)[(1 - T/T_c)^a]^b$, with a = 1.39 and b = 1 associated with the large gaps that open in the Nb bands **[23]**. From the H_{c2} *(T) vs. T* graph, it can be noticed that Fe incorporation in pure $NbSe_2$ diminishes the H_{c2} *(T)* value appreciably.

The H_{c2} *(0)* values calculated using the G-L fitting of $NbSe_2$, $Fe_{0.0008}NbSe_2$ and $Fe_{0.0011}NbSe_2$ are tabulated in the Table 4.3. The appreciable decay of the H_{c2} *(0)* values in Fe_xNbSe_2 samples indicates that the Fe impurity destroys the superconducting properties by enhancing the pair-breaking phenomena in the presence of magnetic field **[24]**. To find the orbital effect in pair breaking, we have considered the Werthamer-Helfend-Hohenberg (WHH) formula **[25]** for type-II superconductors as shown in equation (4.2).

$$H_{c2}^{orb}(0) = -0.693T_c(dH_{c2}/dT)_{T=Tc} \quad (4.2)$$

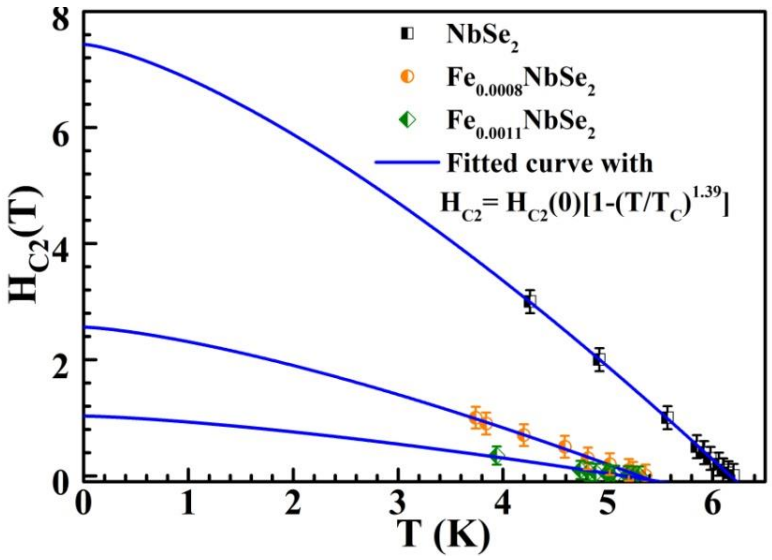

Figure 4.3*. The dependence of the upper critical field (H_{c2}) on temperature and the corresponding fit of the sample $NbSe_2$, $Fe_{0.0008}NbSe_2$ and $Fe_{0.0011}NbSe_2$ using Ginzburg-Landau phenomenological equation.*

The $H_{c2}^{orb}(0)$ represents the orbitally limited upper critical field in presence of magnetic field. The $H_{c2}^{orb}(0)$ values are also summarized in Table 4.3. Table 4.3 indicates that the $H_{c2}^{orb}(0)$ values are comparable to H_{c2} *(0)* values of $NbSe_2$ and Fe_xNbSe_2 suggesting orbital effect has large contribution in pair breaking mechanism in presence of external magnetic fields. The Pauli limiting upper critical field, H_p (0) of $NbSe_2$ and Fe_xNbSe_2 are extracted using equation (4.3) for BCS (Bardeen-Cooper-Schrieffer) type superconductors **[26, 27]**.

$$H_p\,(0) = 1.84T_c \quad (4.3)$$

The H_p (0) values of both $NbSe_2$ and Fe_xNbSe_2 are much larger than the obtained H_{c2} *(0)* values. This implies that Pauli paramagnetic pair breaking effect has negligible contribution in determining the upper limit of critical field in $NbSe_2$ and Fe_xNbSe_2. Thus, orbital pair breaking mechanism is dominating for both cases. The Ginzburg-Landau coherence length (ξ_{GL} (0)) is estimated to the range from 72 Å for $NbSe_2$ to ~177 Å for $Fe_{0.0011}NbSe_2$ using the equation (4.4).

$$\mu_0 H_{c2} = \frac{\phi_0}{2\pi\xi_{GL}^2} \tag{4.4}$$

where ϕ_0 is the quantum of magnetic flux.

Table 4.3. *Upper critical field at zero temperature (H_{c2} (0)), $(dH_{c2}/dT)_{T=Tc}$ value, Orbital limited upper critical field ($(H_{c2}^{orb}(0))$, Pauli limiting upper critical field (H_p (0)) and superconducting coherence length (ξ_{GL}) of $NbSe_2$ and Fe_xNbSe_2 (x = 0.0008, 0.0011) single crystals.*

Sample	$H_{c2}(0)$ (T)	$(dH_{c2}/dT)_{T=Tc}$ (T/K)	$H_{c2}^{orb}(0)$ (T)	$H_p(0)$ (T)	$\xi(0)$ (Å)
$NbSe_2$	**7.4**	**-1.3**	**5.8**	**12**	**72**
$Fe_{0.0008}NbSe_2$	**2.6**	**-0.54**	**2.0**	**9.9**	**110**
$Fe_{0.0011}NbSe_2$	**1.0**	**-0.09**	**0.32**	**9.6**	**177**

4.2.2.3. Hysteresis loop (*M vs. H* curve) analysis:

The hysteresis loops (*M* - *H*) of pure and Fe_xNbSe_2 are shown in Figure 4.4 at 2 K, 2.5 K, 3 K, 3.5 K, 4 K and 5 K temperatures. The hysteresis loop in the *M vs. H* curves of both $NbSe_2$ and Fe_xNbSe_2 reflect the presence of irreversible magnetization at low magnetic fields (~ 0.3 T). This confirms the presence of both intrinsic (*i.e.*, $NbSe_2$) and extrinsic (*i.e.*, Fe_xNbSe_2) defects which causes the pinning of magnetic fluxes.

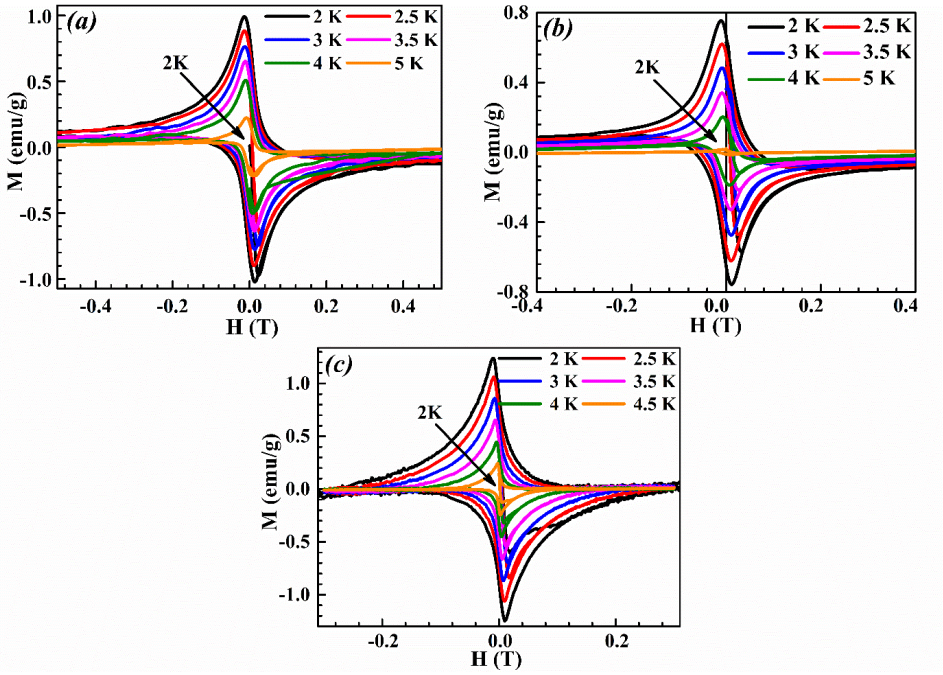

Figure 4.4. *Displays the Isotherm magnetization (M-H) curves of (a) pure $NbSe_2$ at 2 K, 2.5 K, 3 K, 3.5 K, 4 K, 5K (b) $Fe_{0.0008}NbSe_2$ at 2 K, 2.5 K, 3 K, 3.5 K, 4 K, 5K (c) $Fe_{0.0011}NbSe_2$ at 2 K, 2.5 K, 3 K, 3.5 K, 4 K, 4.5K temperatures.*

4.2.2.4. Magnetic field dependence of irreversible field (H_{irr}) study:

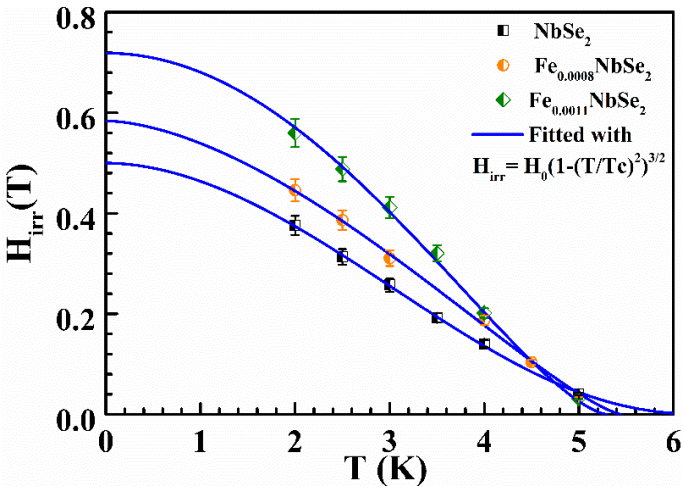

Figure 4.5*. Temperature dependence of the irreversible field $H_{irr}(T)$ for $NbSe_2$, $Fe_{0.0008}NbSe_2$ and $Fe_{0.0011}NbSe_2$ single crystals with the solid lines represent the fitted results using* $H_{irr}(T) = H_{irr}(0)[1-(T/T_C)^2]^{\frac{3}{2}}$.

To observe the crossover of FLL from irreversible magnetization region to reversible region, we have estimated the irreversible field (H_{irr}). At a given temperature, for fields below H_{irr}, the vortices are pinned effectively and above, they move freely (*i.e.*, the melting of vortex lattice). H_{irr} *(T)* values of $NbSe_2$ and Fe_xNbSe_2 are calculated from the

magnetization loop (*M-H* loop) using the criteria of zero critical current density due to depinning **[28, 29]** of the magnetic fluxes. Enhancement of the irreversible field with Fe concentration suggests that the applicability of the superconductors can be improved by doping with foreign atom like Fe. The temperature dependence of the H_{irr} *(T)* is well fitted with $H_{irr}(T) = H_{irr}(0)[1-(T/T_C)^2]^{\frac{3}{2}}$ as shown in Figure 4.5. This gives the clear evidence of the three dimensional (3D) nature of giant flux creep **[30, 31]** in $NbSe_2$, $Fe_{0.0008}NbSe_2$ and $Fe_{0.0011}NbSe_2$.

Table 4.4. *The estimated H_{irr} (0) values from M-H curves for $NbSe_2$ and Fe_xNbSe_2 (x = 0.0008, 0.0011) single crystals.*

Sample	$H_{irr}(0)$ (T)
$NbSe_2$	**0.72**
$Fe_{0.0008}NbSe_2$	**0.58**
$Fe_{0.0011}NbSe_2$	**0.50**

4.2.2.5. Magnetic field dependence of critical current density study:

The critical current density, J_c (A/cm^2) is calculated using the magnetization width, $\Delta M = [M_+(H) - M_-(H)]$ of the *M* - *H* loop from Bean's model **[32, 33]**. Figure 4.6 (*a* - *c*) represent the plot of J_c as a function of magnetic field at different temperatures (2 K - 5 K) for $NbSe_2$, $Fe_{0.0008}NbSe_2$ and $Fe_{0.0011}NbSe_2$. Figure 4.6 (*d*) shows the J_c (*H*) curves of all three samples at 2 K temperature for comparison. From the Figure 4.6 (*d*), the J_c (*H* = 0) values are estimated from the magnetic hysteresis loop (*MHL*) at 2 K temperature and shown in Table 4.5.

The J_c (*H* = 0) values of $NbSe_2$, $Fe_{0.0008}NbSe_2$ and $Fe_{0.0011}NbSe_2$ at 2 K are 138997 A/cm^2, 261738 A/cm^2 and 357280 A/cm^2, respectively and drop significantly towards the lower values with increasing magnetic field. The variation in J_c *(0)* values suggests that magnetic impurity (Fe) can boost the J_c value of $NbSe_2$ at a considerably small amount due to the presence of layered structure. $Fe_{0.0011}NbSe_2$ displays higher J_c *(0)* values in contrast to the $Fe_{0.0008}NbSe_2$ because of the enhanced pinning of magnetic flux lines in defect structures associated with increase of point pinning

centres. This hints the presence of weak pinning phenomena at the surrounding of magnetic impurities which act as point pinning centres.

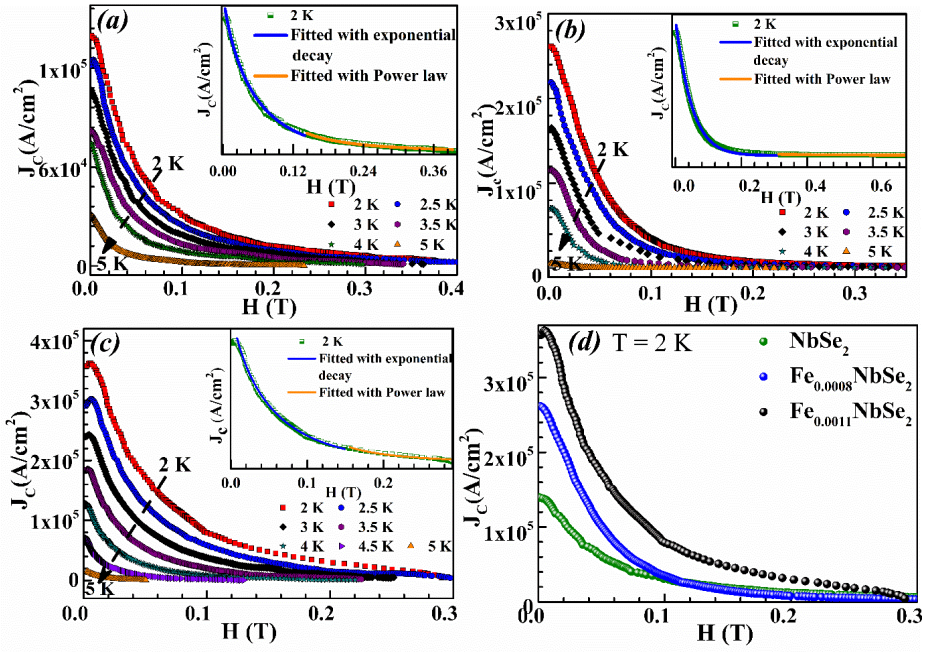

Figure 4.6. *Displays the critical current density at 2 K, 2.5 K, 3 K, 3.5 K, 4 K and 5 K temperatures of the sample (a) pure $NbSe_2$ (b) $Fe_{0.0008}NbSe_2$ and (c) $Fe_{0.0011}NbSe_2$ estimated from the (M-H) curves. Field dependence of J_c curve at 2 K using the collective pinning model is shown in the inset of Figure (a), (b) and (c). The red fitted line represents the exponential decay of the J_c at the small bundle region and the green lines (not clearly visible due to overlapping) indicate the power law dependence of J_c on magnetic field at the large bundle pinning region,* ***(d)*** *critical current density plot at 2 K temperature of $NbSe_2$, $Fe_{0.0008}NbSe_2$ and $Fe_{0.0011}NbSe_2$ single crystal.*

According to the weak collective pinning model **[34]**, the spatial fluctuation of the superconducting properties (including T_c, κ, l, *etc*.) appears due to the presence of intrinsic and extrinsic disorder. It introduces different pinning regions like single vortex (*sv*), small-bundle (*sb*), large-bundle (*lb*) and the charge-density-wave (CDW)-type relaxation of the FLL in vortex phase diagram. Single vortex pinning region which is separated from the small bundle region through H_{sb} (crossover field from single vortex pinning region to small bundle pinning region) is independent of magnetic field due to the negligible interaction between the vortices. To show the field independent behaviour of J_c in the single vortex pinning region, the J_c values are also plotted in log-log scale as shown in Figure 4.7 (*a-c*). In the field range $H_{sb} < H < H_{lb}$ (where H_{lb} stands for the crossover

from the small bundle pinning region to large bundle pinning region), J_c shows exponential decay with increase in magnetic field in the form:

$$J_C(H) = J_C(0)exp\left[-(H/H_0)^{\frac{3}{2}}\right] \quad (4.5)$$

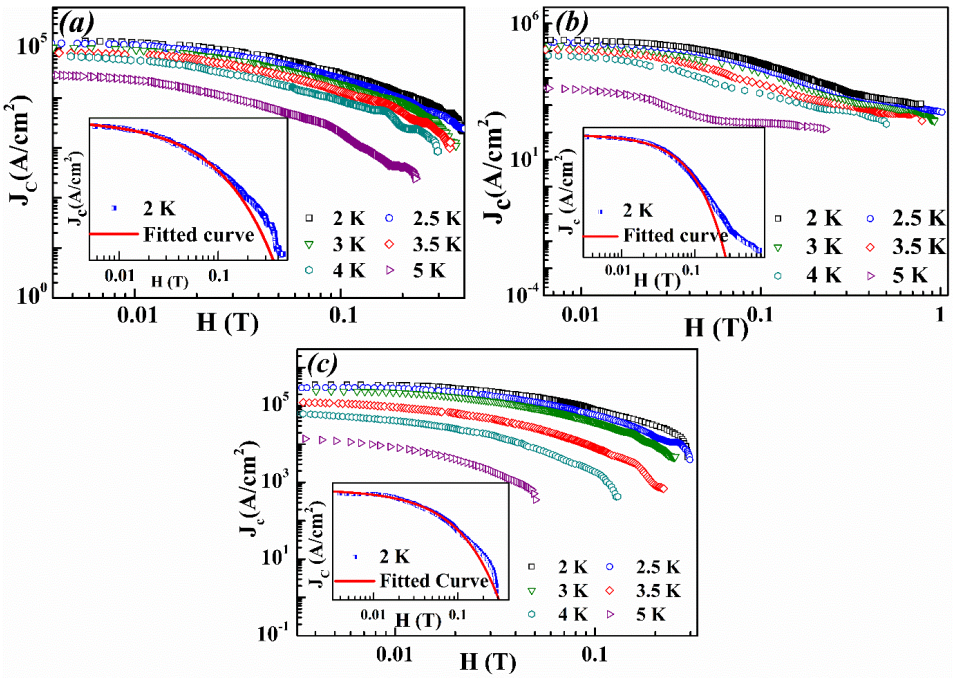

Figure 4.7*. Shows the J_c plot of (a) pure $NbSe_2$ (b) $Fe_{0.0008}NbSe_2$ (c) $Fe_{0.0011}NbSe_2$ in the log-log scale. The inset shows collective pinning model fitting at log-log scale at temperature of 2 K.*

Table 4.5. *The estimated $J_c(0)$ values from M - H curves for $NbSe_2$ and Fe_xNbSe_2 (x = 0.0008, 0.0011) single crystals.*

Sample	J_c (0) (A/cm^2) (@T=2 K)
$NbSe_2$	1.4×10^5
$Fe_{0.0008}NbSe_2$	2.6×10^5
$Fe_{0.0011}NbSe_2$	3.6×10^5

The insets of Figure 4.7 (*a-c*) show good agreement with equation (4.5). There is an exponential dependence of J_c value in all the samples with magnetic field in small bundle pinning region. On the other hand, the J_c values show algebraic dependence on magnetic field (H) in the large bundle pinning region. The fitted curves that are shown in the insets of Figure 4.6 (*a-c*), expose the $H^{3.2}$ dependence of J_c at 2 K temperature. So,

the study of the vortex dynamics of $NbSe_2$ and Fe_xNbSe_2 indicates the presence of single vortex region with zero interaction at low magnetic fields and collective pinning regions (small bundle pinning and large bundle pinning region) near intermediate fields.

4.2.2.6. Study of pinning mechanism:

4.2.2.6.1. Interaction between the vortices and pinning centres:

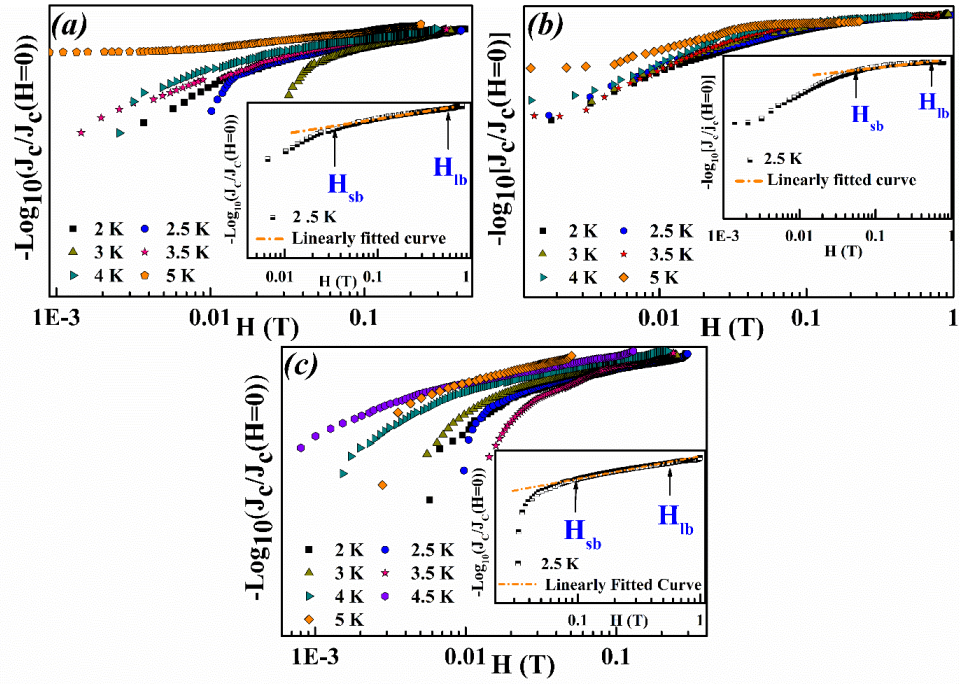

***Figure 4.8**. Double -logarithmic plots of $-log_{10}[J_c(H)/J_C(H=0)]$ vs. the applied field (H) of **(a)** $NbSe_2$ (b) $Fe_{0.0008}NbSe_2$ (c) $Fe_{0.0011}NbSe_2$. The inset represents the H_{sb} and H_{lb} values calculated at temperature of 2 K.*

The interaction between the core region of vortices and the pinning centres is described by core pinning. The core pinning occurs in the background of random pinning potential introduced by pinning centres around the magnetic fluxes. The core interaction in type-II superconductor reveals the coupling of the locally distorted superconducting properties with the periodic variation of the superconducting order parameter. It is estimated by the short-range disorder in Ginzburg-Landau (*GL*) coefficient and the mean free path (l) of charge carriers **[34]**. The spatial variation of the *GL* coefficient associated with the disorder of T_c is defined as δT_c pinning. On the other hand, the δl pinning shows the variation in l near pinning centres. The disorder parameter, δ which determines the spatial variation due to the point defects, provides characteristic temperatures in

case of δT_c pinning and δl pinning. Qin *et al.* **[30]** represented the temperature dependence behaviour of H_{sb} values for δT_c and δl pinning. Equation (4.6) and equation (4.7) demonstrate the different H_{sb} characteristics for δT_c and δl core pinning, respectively.

$$H_{sb} = H_{sb}(0)\left(\frac{1-t^2}{1+t^2}\right)^{\frac{2}{3}} \tag{4.6}$$

$$H_{sb} = H_{sb}(0)\left(\frac{1-t^2}{1+t^2}\right)^{2} \tag{4.7}$$

$NbSe_2$ shows δT_c pinning because of the presence of intrinsic defects. The doped samples show δl pinning as the pinning occurs through the variation in l associated with Fe impurity (*i.e.*, extrinsic defects). In case of superconductors like single crystalline MgB_2 **[35]**, YBCO, the dominant pinning mechanism is δT_c pinning while C substituted MgB_2 shows δl pinning as the main pinning mechanism associated with the shortening of the mean free path due to substituted C atoms [**36]**.

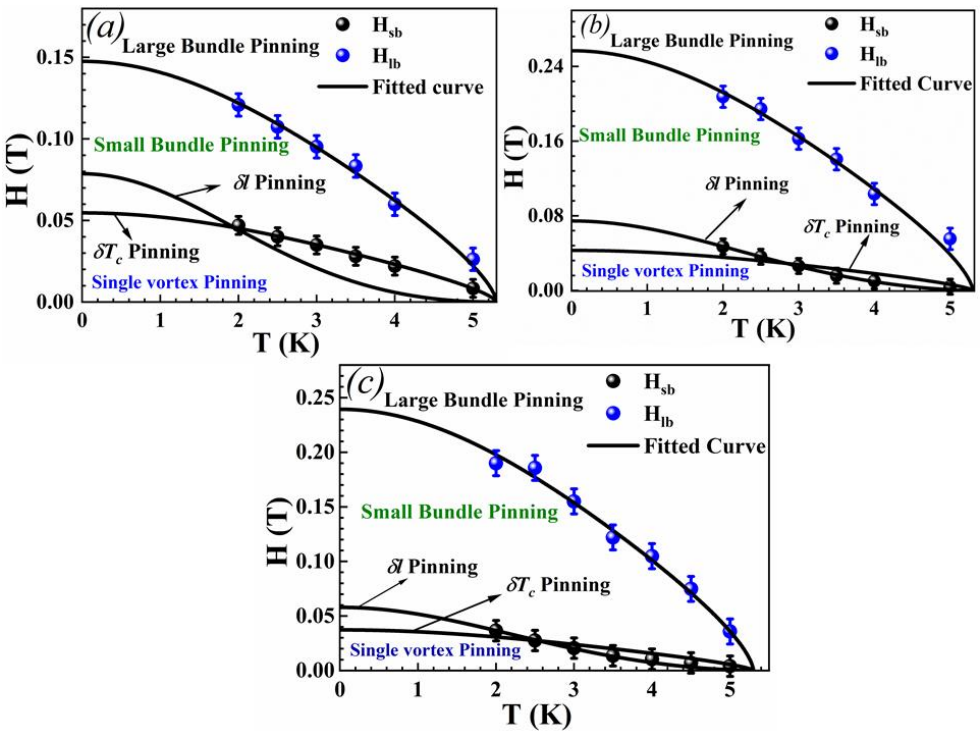

Figure 4.9. *Demonstrates the temperature dependence of the H_{sb} and H_{lb} for (a) $NbSe_2$ (b) $Fe_{0.0008}NbSe_2$ (c) $Fe_{0.0011}NbSe_2$ fitted with the δl and δT_c pinning mechanism, respectively*

Figure 4.9 (*a*) reveals that the single vortex pinning region is comparable to the small bundle pinning region in pure $NbSe_2$. However, the small bundle pinning region and large bundle pinning region take larger

place in the *H-T* phase diagram in Fe_xNbSe_2 as shown in Figure 4.9 (*b*, *c*). It reflects the extreme disorder state of vortex lattice in Fe_xNbSe_2. Due to the incorporation of Fe atoms in $NbSe_2$, the interaction between the vortices increases as the fluxes deviate from their original position to find a region of minimum potential around point defects. So, the core interaction results δT_c pinning in pure $NbSe_2$ and δl pinning in Fe_xNbSe_2. Further, the Fe atoms introduce a competitive nature between the single vortex, small bundle and the large bundle pinning regions.

4.2.2.6.2. Size dependent pinning mechanism:

Further to investigate the pinning mechanism depending on the size (1D, 2D, 3D) of pinning centres, we have evaluated the pinning force density using the relation, $F_P = \mu_0 \mathrm{H} \times J_c$. Fietz *et al.* **[37]** first showed the scaling behaviour of F_p at different temperatures using the H_{c2} dependence of J_c characteristics. Dew-Hughes **[38]** proposed a universal formula to describe the pinning force on the basis of crystal dimensionality. The proposed universal formula is $f_p(h) = F_P/F_{P,max} = Ah^p(1-h)^q$, where *A*, *p*, *q* are the scaling parameters and the value of $p = 1$ and $q = 2$ representing the point pinning mechanism with $h_{peak} \sim 0.33$ and h is reduced magnetic field $(= H/H_{irr})$. On the other hand, Kramer **[39]** provided a similar form of magnetic field dependence of reduced pinning force density $f\left(= F_p/F_{p,max}\right)$ with $p = 0.5$, $q = 2$ and $h_{peak} \sim 0.2$ based on the surface pinning phenomena.

Figure 4.10 (*a* - *c*) shows the *f* values as a function of h $(= H/H_{irr})$ at different temperatures for $NbSe_2$ and Fe_xNbSe_2. The fitted curve of each sample in Figure 4.10 (*a* - *c*) exhibit scaling behaviour similar to the MgB_2 samples **[40]**. The field dependence of f characteristics of $NbSe_2$ and Fe_xNbSe_2 at temperatures 3.5 K and 4 K deviates appreciably from the curves at lower temperatures. It suggests that only single pinning mechanism cannot explain the pinning mechanism in $NbSe_2$ and Fe doped samples.

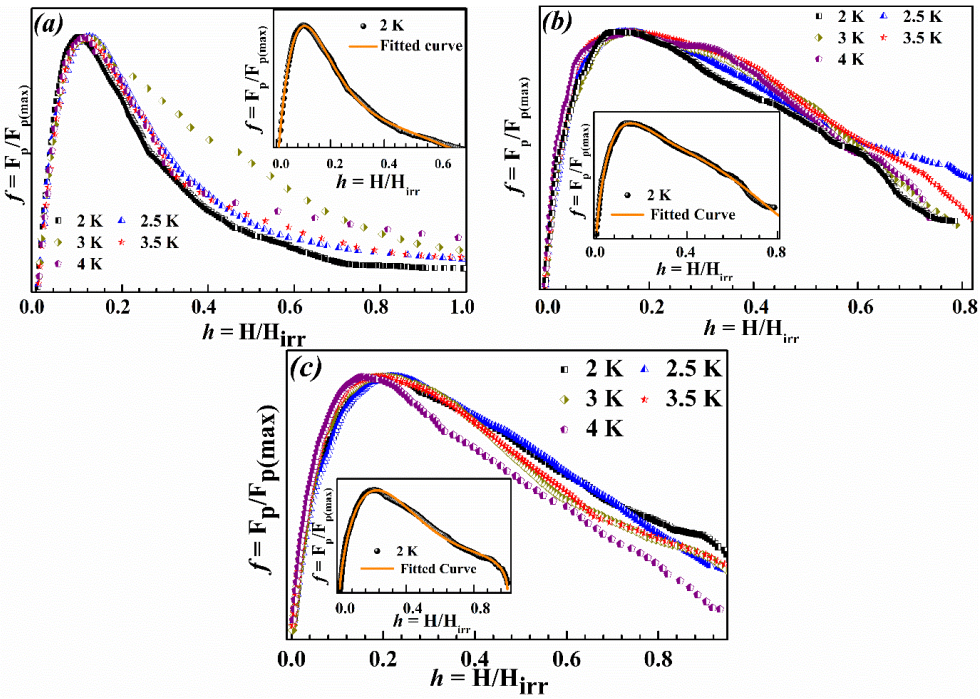

***Figure 4.10**. Shows the field dependence of the reduced pinning force for the sample (a) $NbSe_2$ (b) $Fe_{0.0008}NbSe_2$ (c) $Fe_{0.0011}NbSe_2$ at temperatures 2 K, 2.5 K, 3 K, 3.5 K, 4K respectively. The inset plot shows the fitted results using the scaling law $f = Ah^p(1-h)^q + Bh^r(1-h)^s$ at temperature of 2 K.*

The magnetic field dependence curves of $NbSe_2$ at 2 K temperature are fitted with the Dew-Hughes point pinning model with the $p = 0.95$ and $q = 3.74$ along with surface pinning with $r = 0.52$ and $s = 1.37$ in the form,

$$f = Ah^p(1-h)^q + Bh^r(1-h)^s \qquad (4.8)$$

The fittings are shown in the inset of Figure 4.10 (*a* - *c*). The appearance of the surface pinning in $NbSe_2$ single crystal is due to the layered Se-Nb-Se structure with the higher value of q parameter reflecting the presence of dense point pinning centres. The broadening of the f_p curves with $f_{p,max}$ at higher $h\ (= H/H_{irr})$ value in $Fe_{0.0008}NbSe_2$ and $Fe_{0.0011}NbSe_2$ indicates the enhancement of the pinning centres in the Fe incorporated single crystals compared to $NbSe_2$.

4.3. Summary

In this chapter, we have observed that the single crystals of $NbSe_2$, $Fe_{0.0008}NbSe_2$ and $Fe_{0.0011}NbSe_2$ have been successfully synthesized through chemical vapour transport method to investigate the alternation of

superconducting properties due to the addition of Fe atoms. XRD results confirm the single crystalline nature of pure and Fe_xNbSe_2 samples. It confirms the incorporation of Fe atoms in Fe_xNbSe_2. The X-ray diffraction patterns show no secondary phase related to Fe doping. The temperature dependence of magnetization measurement shows the significant degradation of the T_c values with both increasing magnetic fields and Fe doping. The $H_{c2}(0)$ values of Fe_xNbSe_2 are reduced to very lower values (as compared to pure $NbSe_2$) which reveal the enhancement of pair breaking phenomena due to the presence of Fe defects. The magnetic hysteresis loop analysis shows the irreversible magnetization in both $NbSe_2$ and Fe_xNbSe_2, which is associated with defect induced flux pinning. The magnetic hysteresis curves provide the $H_{irr}(0)$ values which shows largest value at highest Fe concentration (Fe ~ 0.0011) in comparison to $NbSe_2$. As H_{irr} directly proportional to J_c, it indicates that J_c characteristics can be improved by Fe doping. Bean's critical model provides the magnetic field dependence of J_c characteristics from the *M vs H* curves demonstrating the significant enhancement of J_c *(0)* values associated with Fe doping in $NbSe_2$. It confirms the presence of weak collective pinning in both $NbSe_2$ and Fe_xNbSe_2. The flux pinning phenomena is investigated based on interactions between the fluxiods and the inhomogeneities in crystal structure. δT_c pinning is extracted as a dominating core pinning mechanism in $NbSe_2$ whereas the Fe doped samples show δl pinning as main core pinning phenomena. The small bundle pinning and the large bundle pinning region take larger part in the *H-T* phase diagram compared to the single vortex pinning region in Fe_xNbSe_2. The reduced pinning force density shows both surface pinning and the point pinning in $NbSe_2$ while the Fe_xNbSe_2 shows enhancement of the point pinning mechanism. So, the pinning of the vortices in $NbSe_2$ and Fe_xNbSe_2 associated with various types of micro structural inhomogeneities, such as inter- and intra- grain boundaries, precipitation of secondary phases is ruled out through the present investigation due to the presence of point sized defects. The current results are an important in view of basic understanding of the vortex dynamics in layered superconductors and technological applications.

References

[1] Iavarone M., Karapetrov G., Fedor J., Rosenmann D., Nishizaki T., Kobayashi N. (2010), The local effect of magnetic impurities on superconductivity in Co_xNbSe_2 and Mn_xNbSe_2 single crystals, J. Phys. Condens. Matter, 22, 015501.

[2] Luo H., Nowak J. S., Li J., Tao J., Klimczuk T., Cava R. J. (2017), S-shaped suppression of the superconducting transition temperature in Cu-intercalated $NbSe_2$, Chem. Mater., 29, 3704-3712.

[3] Naik S., Pradhan G. K., Bhat S. G., Behera B., Anil Kumar P. S., Samal S. L., Samal D. (2019), The effect of Sn intercalation on the superconducting properties of 2H-$NbSe_2$, Phys. C, 561, 18-23.

[4] Ugeda M. M. *et al.* (2016), Characterization of collective ground states in single-layer $NbSe_2$, Nat. Phys., 12, 92-97.

[5] Huang C. L., Lin J. Y., Chang Y. T., Sun C. P., Shen H. Y., Chou C. C., Berger H., Lee T. K., Yang H. D. (2007), Experimental evidence for a two-gap structure of superconducting NbSe2: A specific-heat study in external magnetic fields, Phys. Rev. B, 76, 212504 (1 - 4).

[6] El-Bana M. S., Wolverson D., Russo S., Bending S. J. (2013), The surface superstructures in niobium disulfide and diselenide intercalated by Cu, Co and Fe, Supercond. Sci. Technol., 26, 125020 (1-10).

[7] Prodan A., Marinkovic V., Rojsek M., Jug N., VanMidden H. J. P., Boswell F.W., Bennett J. C., Bohm H. (2001), The surface superstructures in niobium disulfide and diselenide intercalated by Cu, Co and Fe, Surf. Sci., 476, 71-77.

[8] Iavarone M., Di Capua R., Karapetrov G., Koshelev A. E., Rosenmann D., Claus H., Malliakas C. D., Kanatzidis M. G., Nishizaki T., Kobayashi N. (2008), Effect of magnetic impurities on the vortex lattice properties in $NbSe_2$ single crystals, Phys. Rev. B, 78, 174518.

[9] Karkin A. E., Yangirov M. R., Akshentsev Y. N., Goshchitskii B. N. (2011), Superconductivity in iron silicide $Lu_2Fe_3Si_5$ probed by radiation-induced disordering, Phys. Rev. B, 84, 054541 (1-7).

[10] Haberkorn N., Kim J., Gofryk K., Ronning F., Sefat A. S., Fang L., Welp U., Kwok W. K., Civale L. (2015), Enhancement of the critical current density by increasing the collective pinning energy in heavy ion

irradiated Co-doped $BaFe_2As_2$ single crystals, Supercond. Sci. Technol., 28, 055011 (1-7).

[11] Cheng F., Liu Y., Ma Z., Hossain M. S. A., Somer M. (2016), Improved superconducting properties in the $Mg^{11}B_2$ low activation superconductor prepared by low-temperature sintering, Sci. Rep., 6, 25498 (1-7).

[12] Zhou W., Xing X., Wu W., Zhao H., Shi Z. (2016), Second magnetization peak effect, vortex dynamics, and flux pinning in 112-type superconductor $Ca_{0.8}La_{0.2}Fe_{1-x}Co_xAs_2$, Sci. Rep., 6, 22278 (1-10).

[13] Angurel L. A., Amin F., Polichetti M., Aarts J., Kes P. H. (1997), Dimensionality of collective pinning in 2H-$NbSe_2$ single crystals, Phys. Rev. B, 56, 3425-3432.

[14] Banerjee S. S. *et al.* (1998), Anomalous peak effect in $CeRu_2$ and 2H-$NbSe_2$: Fracturing of a flux line lattice, Phys. Rev. B, 58, 995-999.

[15] Tomy C. V., Pal D., Banerjee S. S., Ramakrishnan S., Grover A. K., Bhattacharya S., Higgins M. J., Balakrishnan G., Paul M. (2002), Study of the peak effect phenomenon in single crystals of 2H-$NbSe_2$, PRAMANA - J PHYS., 58, 925-935.

[16] Hillenius S.J., Coleman R.V. (1979), Magnetic susceptibility of iron-doped 2H-$NbSe_2$, Phys. Rev. B, 20, 4569 - 4576.

[17] Morris R. C., Young B. W., Coleman R. V. (1974), Anisotropic Kondo resistance in Fe doped $NbSe_2$, AIP conference proceedings, 18, 292.

[18] Dai Z., Xue Q., Gong Y., Slough C. G., Coleman R. V. (1993), Scanning-probe-microscopy studies of superlattice structures and density-wave structures in 2H-$NbSe_2$, 2H-$TaSe_2$, and 2H-TaS_2 induced by Fe doping, 48, 14543.

[19] Fasano Y., Menghini M., De La Cruz F., Paltiel Y., Myasoedov Y., Zeldov E., Higgins M. J., Bhattacharya S. (2002), Order-disorder phase transition in $NbSe_2$: absence of amorphous vortex matter, Phys. Rev. B, 66, 020512 (R).

[20] Noto K., Morohashi S., Arikawa K., Muto Y. (1980), Temperature and magnetic field dependence of the electrical resistance in pure and Fe-doped 2H-$NbSe_2$, physics B+C, 99, 204 - 208.

[21] Larkin A. I., Ovchinnikov Y. N. (1979), Pinning in type II superconductors, J. Low Temp. Phys., 34, 409 - 428.

[22] Badica P., Kondo T., Kudo T., Nakamori Y., Orimo S., Togano K. (2004), Magnetization measurements on Li_2Pd_3B superconductor, Appl. Phys. Lett., 85, 4433-4435.

[23] Zehetmayer M., Weber H. W. (2010), Experimental evidence for a two-band superconducting state of $NbSe_2$ single crystals, Phys. Rev. B, 82, 014524 (1-5).

[24] Khim S., Kim J. W., Choi E. S., Bang Y., Nohara M., Takagi H., Kim K. H. (2010), Evidence for dominant Pauli paramagnetic effect in the upper critical field of single-crystalline $FeTe_{0.6}Se_{0.4}$, Phys. Rev. B, 81, 184511 (1-5).

[25] Werthamer N. R., Helfand E., Hohenberg P. C. (1966), Temperature and Purity Dependence of the Superconducting Critical Field, H_{c2}. III. Electron Spin and Spin Orbit Effects, Phys. Rev., 147, 295.

[26] Bardeen J., Cooper L. N., Schrieffer J. R. (1957), Microscopic theory of superconductivity, Phys. Rev., 106, 162 - 164.

[27] Bardeen J., Cooper L. N., Schrieffer J. R. (1957), Theory of superconductivity, Phys. Rev., 108, 1175 - 1204.

[28] Shirage P. M., Tanaka Y., Iyo A. (2010), The critical current density, irreversibility line, and flux pinning properties of $Ba_2CaCu_2O_4(O,F)_2$ high-T_c superconductor, J. Appl. Phys., 107, 093905 (1 - 6).

[29] Shirage P. M., Iyo A., Shivagan D. D., Tanaka Y., Kito H., Kodama Y. (2008), Irreversibility line and flux pinning properties in a multilayered cuprate superconductor of $Ba_2Ca_3Cu_4O_8(O,F)_2$ (T_c = 105 K), Supercond. Sci. Technol., 21, 075014 (1 - 5).

[30] Qin M. J., Wang X. L., Liu H. K., Dou S. X. (2002), Evidence for vortex pinning induced by fluctuations in the transition temperature of MgB_2 superconductors, Phys. Rev. B, 65, 132508 (1 - 4).

[31] Prischepa S. L., Della Rocca M. L., Maritato L., Salvato M., Di Capua R., Maglione M. G., Vaglio R. (2003), Critical currents of MgB_2 thin films deposited in situ by sputtering, Phys. Rev. B, 67, 024512 (1 - 4).

[32] Bean C. P. (1962), Magnetization of hard superconductors, Phys. Rev. Lett., 8, 250-253.

[33] Bean C. P. (1964), Magnetization of High-Field Superconductors, Rev. Mod. Phys., 36, 31 - 39.

[34] Blatter G., Feigel'man M. V., Geshkenbein V. B., Larkin A. I., Vinokur V. M. (1994), Vortices in high-temperature superconductors, Rev. Mod. Phys., 66, 1125-1388.

[35] Shi Z. X., Pradhan A. K., Tokunaga M., Yamazaki K., Tamegai T., Takano Y., Togano K., Kito H., Ihara H. (2003), Flux-pinning properties of single crystalline and dense polycrystalline MgB_2, Phys. Rev. B, 68, 104514 (1 - 6).

[36] Wang J., Zeng R., Kim J. H., Lu L., Dou S. X. (2008), Effects of C substitution on the pinning mechanism of MgB_2, Phys. Rev. B, 77, 174501 (1 - 7).

[37] Fietz W. A., Webb W. W. (1969), Hysteresis in superconducting alloys-temperature and field dependence of dislocation pinning in niobium alloys, Phys. Rev., 178, 657 - 667.

[38] Dew-Hughes D. (1974), Flux pinning mechanisms in type II superconductors, Philos. Mag., 30, 293 - 305.

[39] Kramer E. J. (1973), Scaling laws for flux pinning in hard superconductors, J. Appl. Phys., 44, 1360 - 1370.

[40] Martínez E., Mikheenko P., Martínez-López M., Millán A., Bevan A., Abell J. S. (2007), Flux pinning force in bulk MgB_2 with variable grain size, Phys. Rev. B, 75, 134515 (1 - 8).

CHAPTER 5

Study of Vortex Dynamics of Niobium Diselenide ($NbSe_2$) Single Crystals in Presence of Cr Atoms

T*he reversible magnetization (M_r) in the intermediate state of type-II superconductor has been depicted nicely by Z. Hao and J. R. Clem in connection with the condensation energy (i.e. electromagnetic energy). They linked it with the supercurrent density (J) and magnetic field energy* ***[1]****. However, the intermediate state consists of reversible as well as irreversible magnetization (M_{irr})* ***[2, 3]****. Various vortex states are reported in different superconductors which give contributions to the reversible and irreversible magnetization* ***[4, 5]****. These result various anomalous characteristics such as peak effect, fishtail effect associated with the pinning of fluxes, which includes point pinning* ***[6]****, surface pinning* ***[7]****, and bulk pinning mechanism* ***[8]****. In this chapter, we reported the presence of fishtail effect and other vortex dynamics associated with reversible and irreversible magnetization of $NbSe_2$ in presence of Cr atoms.*

The presence of internal defects (*i.e.,* in nano range) and/or the external defects (produced *via* neutron radiation) generally arise point pinning mechanism in vortex lattice. Moreover, surface pinning of the flux line lattice (FLL) is associated with the variation in potential energy due to the Bean-Livingstone (BL) surface barrier effect and grain boundary pinning **[9]**. The competition between attractive force (*i.e.,* among vortex and its image vortex) and repulsive force (*i.e.,* among the vortex and the surface-shielding effect of *J*) leads BL surface barrier effect, which result sharp low field peak in the pinning force density. F_p is categorised with a universal scaling law by Dew-Hughes **[10]** and Fietz-Webb **[11]**, which is linked with different sources of pinning. Moreover, bulk pinning follows short-range interaction between vortices, which typically emerges at higher magnetic field through large size particles. Amongst the various types of superconducting elements, polycrystalline granular superconductor like MgB_2 accelerates the technical applicability in the industrial research areas. It has been established that the surface pinning in MgB_2 emerges because of grain boundary pinning effect. It enhances the J_c value appreciably at low magnetic field region. However, the J_c (H) diminishes rapidly at higher magnetic field regions towards H_{c2} **[12]**. Later, Pallecchi *et al.* **[13]** have reported the enhancement of the J_c value upto 1 Tesla (T) by creating defects with neutron irradiation. The defects act as the point pinning centres which make a slow decay of J_c (H) value with increasing magnetic field. Furthermore, the foreign particles such as C **[14]**, SiC **[15]** produced point defects in MgB_2 superconductor that boosted the pinning mechanism. It creates both the surface pinning mechanism and point pinning mechanism. The high-T_c cuprate based superconductor shows bulk pinning as a dominating pinning mechanism at low temperatures through analysing the F_p characteristics. Surface barrier effect has been also reported in these superconductors. Additionally, several pure and doped superconductors reveal an anomaly in the J_c characteristics related to the different flux pinning mechanism known as ‘peak effect’ and ‘fishtail effect’.

The “fishtail” effect appears in the magnetization hysteresis loop of different kind of superconductors because of the formation of secondary

peak (*e.g.* $YBa_2Cu_3O_{1-\delta}$ (YBCO) **[16]**, $Bi_2Sr_2CaCu_2O_y$ (BSCCO) **[17]**, Nb_3Sn **[18]**). Daeumling *et al.* **[19]** detected the fishtail effect in the YBCO superconductor. He showed that the fishtail effect is induced due to the defects, which are formed from the oxygen deficit clusters. However, Genoud *et al.* **[20]** synthesized extremely clean YBCO single crystal through proper oxidation process which shows the absence of fishtail effect. So, we can conclude that the fishtail effect depends on the type of superconductors according to these debatable observations. For example, the second magnetization peak (SMP) effect is observed in high T_c cuprate (e.g. BSCCO) superconductor due to the transition of ordered 3D flux line to disordered 2D pancake vortices **[17, 21]**. On the other hand, SMP effect occurs in another extremely anisotropic 2212 type curate superconductor $Bi_2Ba_2CaCu_2O_x$ because of the Bean Livingstone's surface barrier effect. According to the BL's surface barrier effect, the flux penetration is hindered at the edge of crystal surface caused by the repulsive force. This force is exerted by the fluxes that are formed inside the crystal **[22]**. Like cuprates, various theories were reported for the occurrence of SMP effect in Fe based superconductors. For example, the origin of SMP effect in $SmFeAsO_{0.85}F_{0.15}$ superconductor is the transition of 3D disordered vortex lattice to 2D nature **[23]**. Moreover, both the vortex lattice (VL) phase transition and the crossover from collective creep to plastic creep cause the SMP effect in the magnetization loop of $Ba(Fe, Co)_2As_2$ **[24]**. SMP appears in the classical low-T_c superconductor (e.g. $Sc_5Ir_4Si_{10}$) due to the softening of vortex line when the external magnetic field is close to the upper critical field **[25]**. Similarly, MgB_2 shows the transition of the low field Bragg glass phase to high field amorphous vortex glass phase associated with the SMP effect **[26]**. Various research groups investigated the origin of SMP effect in different kind superconducting materials which are summarized in Table 5.1. Recently, Song *et al.* **[27]** described the prominent SMP effect of pristine $Ba_{1-x}K_xFe_2As_2$ single crystal with ($0.25 \leq x \leq 0.52$) in association with the orthorhombic phase domain boundary and the inhomogeneity in the dopant distribution. Additionally, Babu *et al.* **[28]** investigated the difference on the characteristics and origin between the SMP and peak

effect phenomena in $Ca_3Rh_4Sn_{13}$ single crystal through the analysis of spectral fluctuation in noise distribution of magnetization data across the SMP and peak effect regions. This indicates that dynamic research is going on in this field to comprehend the physical scenario of fishtail effect which is still in discussion and yet to be evaluated. Subsequently, it is crucial to realize the actual mechanism behind the presence of fishtail effect to disentangle the improvement of J_c at low as well as higher magnetic field.

Large single crystals of Cr_xNbSe_2 were synthesized through chemical vapour transport method to find out the origin of fishtail effect through flux dynamics and magnetization relaxation studies **[29, 30]**. $NbSe_2$ has H_{c2} value as high as 14 T, with an anisotropic behaviour in J_c characteristics just as F_p **[31, 32]**. In addition, Koorevaar *et al.* directed the 2D nature of F_p characteristics in the layered structure of $NbSe_2$, which follows the collective pinning theory. Here the peak effect anomaly has been characterised by the crossover from 2D FLL to 3D FLL while the magnetic field is applied perpendicular to the layers **[33]**. Similarly, Sugawara *et al.* reported a prominent peak in the highly anisotropic F_p characteristics of S-doped $NbSe_2$ superconductor when the applied magnetic field is perpendicular to the crystal surface. However, the magnetic field dependence of F_p didn't show any peak when the applied magnetic field is parallel to the layers **[3]**. Our previous studies on Fe_xNbSe_2 single crystal expose J_c value as high as 3 x 10^5 A/cm^2 without any F_p peak. It shows both the point pinning and the surface pinning mechanism linked with the anisotropy of layered structure **[34 - 37]**. This study inspires us to explore more insight into the vortex dynamics adding with other dilute point defect pinning centres.

In this chapter, we represent the evolution of the J_c characteristics and the corresponding pinning mechanism in $NbSe_2$ single crystal by incorporating dilute amount of Cr impurities. Initially, we perceived the enhancement of J_c in $Cr_{0.0005}NbSe_2$ from magnetization measurement but it is restricted only at low magnetic field regions. The J_c value decreases rapidly with increasing magnetic field. By examining the magnetization data using several fundamental models **[38]**, we shown that the point defects initiated by Cr atoms alter the vortex creep movement at higher

magnetic field resulting SMP effect at highest Cr concentration. This presence of SMP effect in magnetic hysteresis loop is confirmed by the magnetic field dependence of dynamical relaxation rate indicating the elastic (*E*) – plastic (*P*) crossover of FLL. Moreover, the interactions between the core regions of FLL and defect structure are explored through core δl and δT_c pinning. We have also estimated the size dependent pinning mechanism in Cr_xNbSe_2 by studying the reduced magnetic field dependence of reduced pinning force density. It shows BL surface barrier effect at nearly zero magnetic field and point pinning and surface pinning at low magnetic field in $Cr_{0.0005}NbSe_2$. $Cr_{0.0009}NbSe_2$ and $Cr_{0.0012}NbSe_2$ also include higher field peak associated with lattice softening. The obtainable results give broad idea for improvement of the J_c characteristics. It also provides the basic understanding about the pinning mechanism in low T_c superconductor.

Table 5.1. *Different types of superconductors and possible reasons behind SMP effect.*

Sample	Type of superconductors	Possible reasons behind SMP effect
BSCCO	Unconventional strong layered cuprate SC	Transition of the ordered 3D flux line to disordered 2D pancake vortices.
$Bi_2Ba_2CaCu_2O_x$	2212 type strong layered and highly anisotropic cuprate superconductor	BL's surface barrier effect.
YBCO	Layered cuprate superconductor	Crossover of flux dynamics from elastic to plastic creep region.
LiFeAs [1]	111 type layered Fe based superconductor	Phase transition of vortex lattice i.e. the VL model.

$SmFeAsO_{0.85}F_{0.15}$	1111 type highly anisotropic strong layered Fe based superconductor	Three-dimensional (3D) to 2D disordered vortex phase transition.
$Ba(Fe, Co)_2As_2$	122 type layered Fe based superconductor	Both collective to plastic crossover of flux line lattice and vortex lattice phase transition (VL) are proposed.
$YNi_2B_2C/LuNi_2B_2C$ [2]	Conventional tetragonal superconductor with stacks of alternating rock salt Lu(Y)C and Ni_2B_2 layers	Phase transition of vortex lattice from quasi Bragg glass state to a multi-domain vortex glass phase.
MgB_2	Layered superconductor	Transition of the flux line lattice from low field Bragg glass phase to a high field amorphous vortex glass phase.
$NbSe_2$	Conventional layered superconductor	Soften of the vortex line when external field is close to the upper critical field and crossover of the elastic stiff flux line lattice to the plastic soft flux line lattice.
Cr_xNbSe_2 [Present work]	Conventional layered superconductor	Elastic to plastic creep transition of flux line lattice.

5.1. Materials and Method

Materials: Niobium (Nb, 99.95%; Alfa Aesar), Selenium (Se, 99.999%; Alfa Aesar) and Chromium (99.99%; Alfa Aesar), Iodine (I_2, 99.998%; Alfa Aesar).

Method: Cr_xNbSe_2 single crystals with x = 0.0005, 0.0009 and 0.0012 were grown following chemical vapour transport method by using Iodine as a strong transporting agent. The necessary precursors like Niobium (Nb), 99.95%, Selenium (Se) 99.99%, and Chromium (Cr) 99.99% purity were bought and used as received without any further purification. The precursors were pressed at a pressure of 5 ton to form pellets after mixing with proper stoichiometric ratio. The Cr_xNbSe_2 pellets with appropriate amount of iodine were sealed in a quartz tubes retaining a pressure of $9x10^{-6}$ mbar in presence of liquid nitrogen atmosphere. The well-sealed quartz tubes were heated inside a two-zone furnace fixing the charge zone and growth zone temperatures at 800°C and 720°C, respectively for one week. We follow the same procedure for formation of single crystals of Cr_xNbSe_2 as that of the Fe_xNbSe_2 single crystals.

5.2. Results and Discussion

5.2.1. Structural properties:

5.2.1.1. X-Ray diffraction:

Initially, the material properties of Cr_xNbSe_2 single crystal are investigated for structural information. The X-ray diffraction (XRD) patterns of Cr_xNbSe_2 single crystals are shown in Figure 5.1. The peak position of the single crystals reveals that all peaks are associated with the hexagonal phase with $P6_3/mmc$ space group (JCPDS Card No. 01-070-5612). All the samples show the presence of only (00*l*) planes which confirm the single crystalline nature of all samples. No sign of impurity peak is found in the Cr_xNbSe_2, suggesting the growth of high purity single crystals. Table 5.2 summarizes the parameters estimated from the XRD peak position. Increase in doping concentration indicates slight peak shift towards lower theta, which is due to the incorporation of Cr atoms in the lattice. The ionic size of Cr^{3+} (0.615 Å in CN = 6) is analogous to the Nb^{4+} (0.68 Å in CN = 6). So, Cr^{3+} ions can easily substitute Nb^{4+} ions in the $NbSe_2$ lattice without any lattice distortion. However, there will be decrease of lattice parameters ('*a*' and '*c*') if Cr^{3+} replaces Nb^{4+} ions following Vegard's Law. As the doping level of Cr atoms is less than 5% in our case, it is very difficult to comment on substitution or intercalation of Cr atoms

into the lattice. However, our results confirm the incorporation of Cr atoms in $NbSe_2$ layer structure.

The unit cell lattice parameter for Cr_xNbSe_2 samples has been calculated using equation (5.1), as shown in Table 5.2.

$$\frac{1}{d^2} = \frac{4}{3a^2}(h^2 + (hk) + k^2) + \frac{l^2}{c^2} \quad (5.1)$$

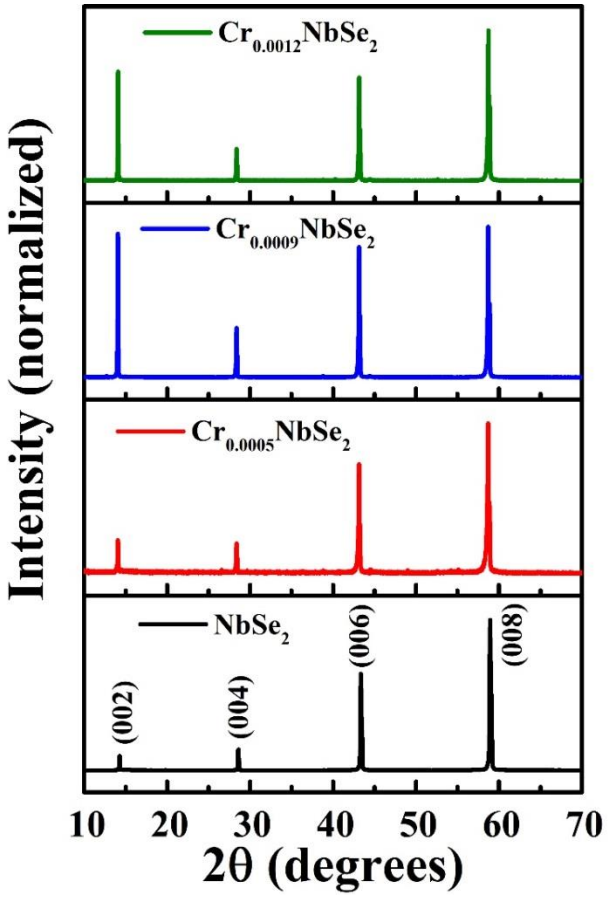

Figure 5.1. *XRD pattern of $NbSe_2$ and Cr_xNbSe_2 (with x = 0.0005, 0.0009 and 0.0012) single crystals.*

Table 5.2. *Estimated structural parameters for Cr_xNbSe_2 (x = 0.0005, 0.0009, 0.0012) single crystals.*

Sample	*c* (Å)	*FWHM*			
		(002)	(004)	(006)	(008)
$NbSe_2$	12.555±0.004	0.12	0.12	0.16	0.12
$Cr_{0.0005}NbSe_2$	12.562±0.005	0.10	0.13	0.10	0.16
$Cr_{0.0009}NbSe_2$	12.563±0.002	0.09	0.11	0.11	0.13
$Cr_{0.0012}NbSe_2$	12.578±0.003	0.08	0.10	0.1	0.12

5.2.1.2. X-Ray photoelectron spectroscopy (XPS), HRTEM and SAED analysis:

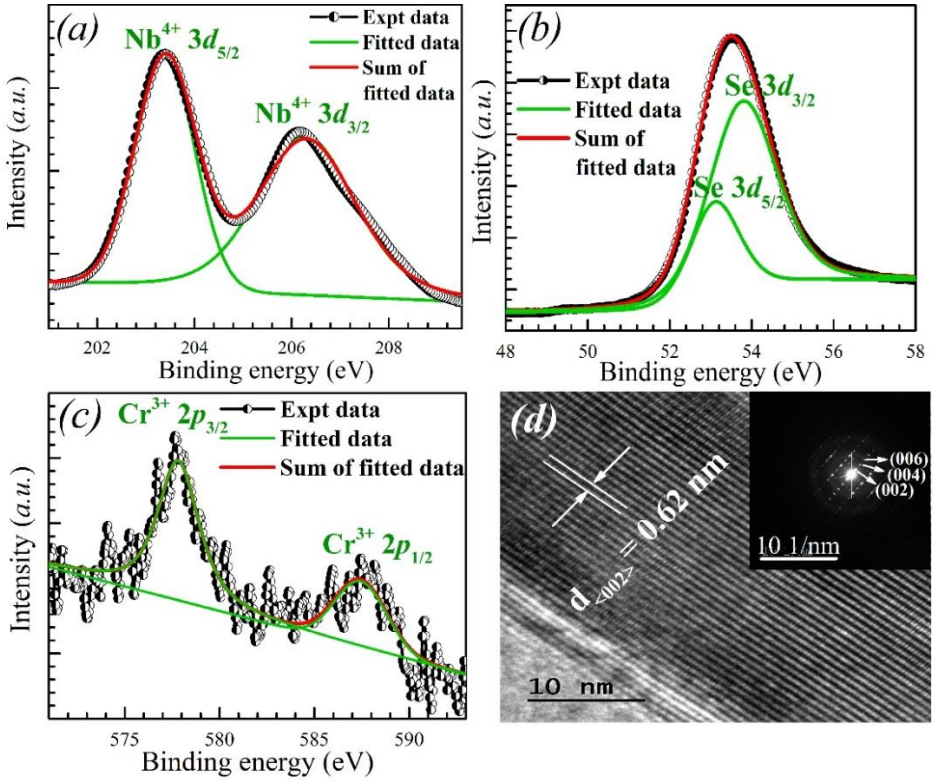

Figure 5.2. *Displays the X-ray photoemission spectroscopy (XPS) spectra of the (a) Nb 3d (b) Se 3d and (c) Cr 2p peaks from $Cr_{0.0012}NbSe_2$ single crystal. Figure (d) Represents HRTEM image of $Cr_{0.0012}NbSe_2$. Inset: SAED pattern of the single crystalline $Cr_{0.0012}NbSe_2$.*

Figure 5.2. shows the high-resolution X-ray photoelectron spectroscopy (XPS) spectra of $Cr_{0.0012}NbSe_2$ single crystal. It reveals characteristic doublet peak at 203.4 and 206.1 eV correspond to Nb $3d_{5/2}$ and $3d_{3/2}$ states, respectively (Figure 5.2 (*a*)). The obtained binding energy (BE) difference between the doublet 3*d* (2.7 eV) peaks is in good agreement with the reported value of Nb^{4+} oxidation state **[39]**. The shoulder of the Nb^{4+} peak is due to the presence of Nb^{5+} (Nb^{5+} $3d_{5/2}$) ion in $NbSe_2$ which is associated with the Nb_2O_5 in $Cr_{0.0012}NbSe_2$. Figure 5.2 (*b*) shows the spectra of Se 3d core level presenting two distinct peaks of Se $3d_{5/2}$ and $3d_{3/2}$ at 53.2 and 54.1 eV, respectively that agrees with the spectra of $NbSe_2$ **[40, 41]**. The oxidation state of Cr is determined by analysing the Cr 2*p* spectra, shown in Figure 5.2 (*c*). The two peaks at 577.8 and 587.3 eV can be assigned to Cr $2p_{3/2}$ and $2p_{1/2}$ respectively, having a BE difference of 9.5 eV **[42, 43]**. The Cr environment for the $2p_{3/2}$ peak indicates the presence of the

Cr^{+3} state in $Cr_{0.0012}NbSe_2$ **[44]**. Conclusively, the XPS spectra of the Cr 2*p* region indicate the successful incorporation of Cr atoms in $NbSe_2$ matrix. Moreover, the high resolution TEM (HRTEM) and Selected Area Electron Diffraction (SAED) pattern successfully illustrate the lattice structure of $Cr_{0.0012}NbSe_2$ as shown in Figure 5.2 (*d*). HRTEM result indicates the interplanar spacing of 0.62 nm that is consistent with that of the $NbSe_2$ (002) plane. The SAED pattern (in the inset of Figure 5.2 (*d*)) confirms the single crystalline nature of $Cr_{0.0012}NbSe_2$. The pattern consists of (002), (004) and (006) planes, matches well with those of XRD results.

5.2.2. Superconducting properties:

5.2.2.1. Temperature dependent magnetization studies:

The superconducting properties of the Cr_xNbSe_2 samples have been studied after confirming the successful incorporation of Cr atoms in $NbSe_2$ matrix from the structural characterization. Here a detailed analysis is accompanied to observe the effect of Cr atoms on the superconducting transition of $NbSe_2$ single crystal. The T_c value, which is estimated from the point of deviation of ZFC curve from zero magnetization value (shown by vertical black arrows (↑) in Figure 5.3), started nearly at ~ 5.9, 5.4, and 4.5 K (at 0.005 T) in Cr_xNbSe_2 (x = 0.0005, 0.0009, and 0.0012), respectively. So, the T_c value of $NbSe_2$ is reduced with incorporation of Cr atoms in Cr_xNbSe_2 **[35]**. These reductions in T_c values indicate the enhancement of electron scattering phenomena with Cr doping in Cr_xNbSe_2 **[45]**. Similar trend of degradation in T_c values were reported by Iavarone *et al.* **[46]** in case of Co_xNbSe_2 and Mn_xNbSe_2 single crystals.

Table 5.3. *The variation of T_c with magnetic fields and Cr concentration in $NbSe_2$ and Cr_xNbSe_2 (x = 0.0005, 0.0009, 0.0012) single crystals.*

Sample	T_c(K) (@0.005 T)	T_c(K) (@0.05 T)	T_c(K) (@0.2/0.3 T)	T_c(K) (@1 T)
$NbSe_2$	6.4	6.2	5.8	5.1
$Cr_{0.0005}NbSe_2$	5.9	5.8	5.7	4.5
$Cr_{0.0009}NbSe_2$	5.4	5.1	5.0	4.5

$Cr_{0.0012}NbSe_2$	4.5	4.1	3.9	3.1

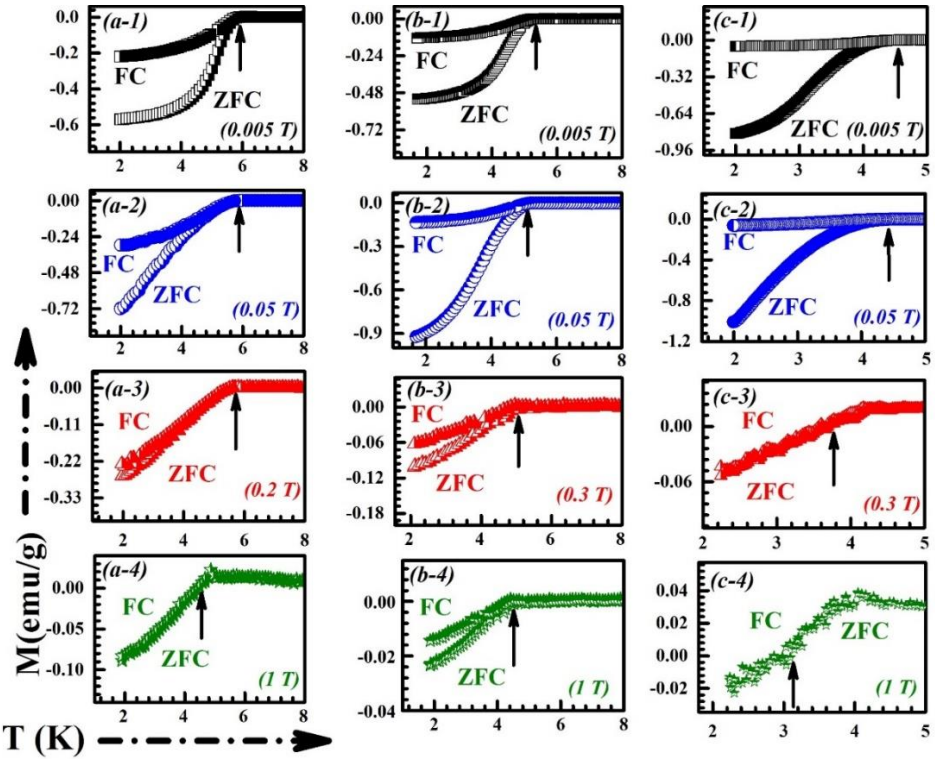

Figure 5.3. *Display the temperature dependence magnetization measurement of Cr_xNbSe_2 (x = 0.0005, 0.0009, and 0.0012) single crystal at different magnetic fields (vertical black arrows (↑) indicate the superconducting transition temperature (T_c)).*

Moreover, a rapid reduction of T_c is also detected with increasing magnetic field. This is because of the increasing of orbital pair breaking mechanism, which diminishes the cooper pair electron densities. However, in case of Cr_xNbSe_2, Pauli pair breaking may also contribute in the process of pair breaking, which we will discuss in the proceeding section. The degradation of T_c with both Cr doping as well as with increase in magnetic field is systematically shown in Table 5.3. The degradation of T_c with increasing doping concentration is almost identical in both Fe_xNbSe_2 and Cr_xNbSe_2 case **[35]**. Comparably, the reduction of T_c is more rapid with increasing magnetic field in Fe_xNbSe_2 than Cr_xNbSe_2. Also, we observed a significant deviation between the ZFC and FC magnetization curves in Cr_xNbSe_2 at low magnetic fields. This is due to the pinning of remnant magnetic fluxes after removal of magnetic field and confirms the presence of large density of pinning centres.

5.2.2.2. Upper limit of superconductivity:

The H_{c2} (0) values of Cr_xNbSe_2 are estimated following the Ginzburg-Landau (*G-L*) model of anisotropic single band superconductivity. It has the form, $H_{c2}(T) = H_{c2}(0)\left[\left(1-\frac{T}{T_c}\right)^{a}\right]^{b}$ with the *G-L* parameters, a = 1.39 and b = 1. These parameters reveal the anisotropic single band nature of Cr_xNbSe_2 superconductors, which is associated with Nb 4*d* bands crossing the quasi-2D Fermi surface of Cr_xNbSe_2. It is worth to referencing that because of the uncertain contribution of the Se bands in the superconducting properties of $NbSe_2$ **[47]**, the multiband nature isn't considered in the present study. The estimated H_{c2} (0) values are tabulated in Table. 5.4, which indicates the rapid destruction of the superconducting order parameter at the presence of magnetic field as represented in Figure 5.4. However, here we show that the H_{c2} values are much higher than Fe_xNbSe_2 [35] which may be associated with the faster reduction of T_c values with increasing magnetic fields.

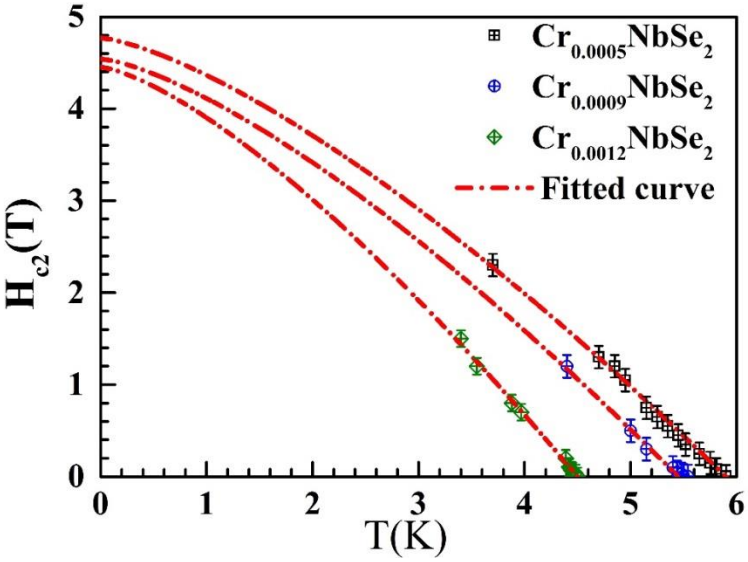

Figure 5.4. *Represents the temperature dependence of H_{c2} (T) values of Cr_xNbSe_2 (x = 0.0005, 0.0009, and 0.0012) single crystal and fitted with the Ginzburg-Landau anisotropic single band equation, H_{c2} (T) = H_{c2} (0) [1-(T/T_c)$^{1.39}$].*

Further we have calculated the $H_{c2}^{orb}(0)$ and H_p (0) values of Cr_xNSe_2 as shown in Table 5.4. The $H_p(0)$ values are higher than the estimated $H_{c2}(0)$ values that indicates Pauli pair breaking mechanism less

participates in the pair breaking mechanism in presence of Cr atoms in Cr_xNbSe_2. Surprisingly, like Fe_xNbSe_2, $H_{c2}^{orb}(0)$ values are comparable to the experimental H_{c2} (0) values of Cr_xNbSe_2. This is because of the strong contribution of orbital effect in pair breaking mechanism. The orbital pair breaking mechanism reduces the H_{c2} (0) values from the H_p (0) values. The ξ_{GL} *(0)* values are evaluated to the range from 83 Å for $Cr_{0.0005}NbSe_2$ to ~ 86 Å for $Cr_{0.0012}NbSe_2$ as presented in Table 5.4.

Table 5.4. *The H_{c2} (0), $H_{c2}^{orb}(0)$, $H_p(0)$ and ξ_{GL} (0) values of $NbSe_2$, $Cr_{0.0005}NbSe_2$, $Cr_{0.0009}NbSe_2$ and $Cr_{0.0012}NbSe_2$ single crystals are summarized.*

Sample	$H_{c2}(0)$ (T)	$(dH_{c2}/dT)_{T=Tc}$ (T/K)	$H_{c2}^{orb}(0)(T)$	$H_p(0)$ (T)	ξ (0) (Å)
$NbSe_2$	7.4	-1.3	5.8	12	72
$Cr_{0.0005}NbSe_2$	4.8	-0.80	3.3	11	83
$Cr_{0.0009}NbSe_2$	4.5	-0.85	3.2	9.9	85
$Cr_{0.0012}NbSe_2$	4.4	-1.0	3.0	8.3	86

5.2.2.3. Hysteresis loop (*M vs. H* curve) analysis:

The magnetic field depended magnetization curves of Cr_xNbSe_2 are represented at 2 K, 2.5 K, 3 K, 3.5 K, 4 K and 5 K with the applied magnetic field parallel to the *a-b* plane as shown in Figure 5.5. The magnetization curves show asymmetric nature similar to the *BL* shape indicating the prominent surface-barrier effect. Surface-barrier effect makes hindrance to the entrance of magnetic fluxes in the superconducting region and excludes the possibility of volume pinning. However, the magnetic hysteresis loops (MHLs) of the isothermal magnetization curves describe nicely the irreversible region of the vortex lattice in Cr_xNbSe_2. Also, at highest Cr concentration (*i.e.* $Cr_{0.0012}NbSe_2$), the hysteresis curves show prominent SMP like behaviour at all temperatures near H_{c2} (Figure 5.5 (*c*)). In order to realize the physical origin of SMP phenomenon, we have estimated the dynamical relaxation rate (Q) and intrinsic activation energy

(U_c). The related physical scenario as well as the affecting factors to the SMP effect in $Cr_{0.0012}NbSe_2$ is discussed later in detail.

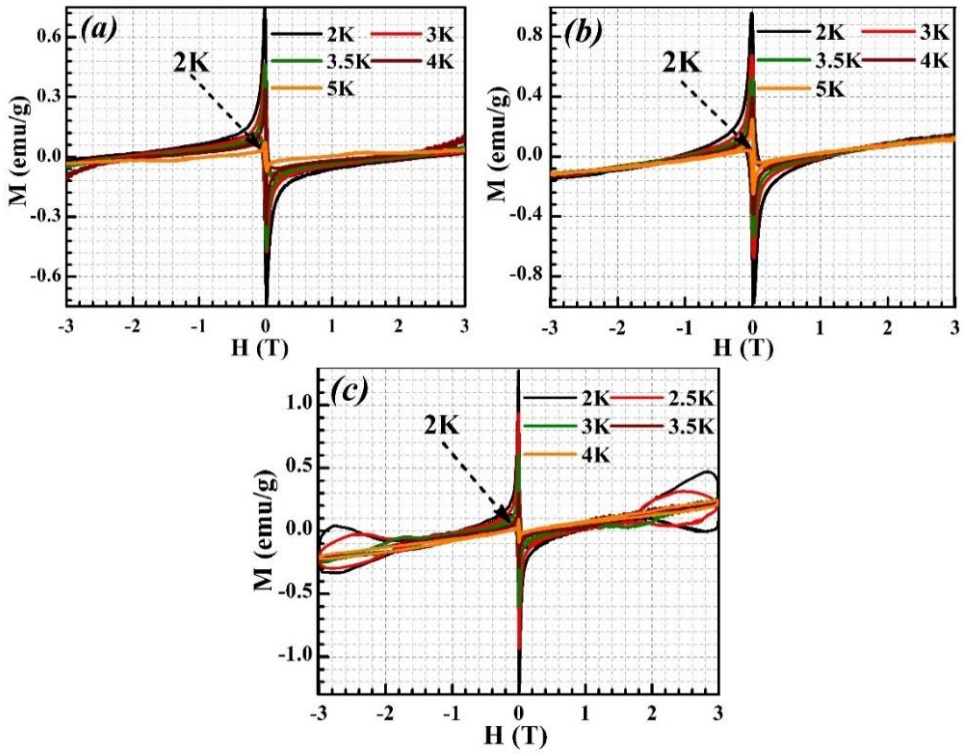

Figure 5.5. *Displays the magnetic field depended magnetization plot of (a) $Cr_{0.0005}NbSe_2$ (b) $Cr_{0.0009}NbSe_2$ (c) $Cr_{0.0012}NbSe_2$ at different temperatures with magnetic field applied parallel to the a-b plane.*

5.2.2.4. Magnetic field dependence of critical current density study:

The key parameter J_c (H) values have been evaluated from MHLs for investigating the vortex dynamics in Cr_xNbSe_2 using the Bean's critical state model as shown in equation (5.2).

$$J_c = 20\Delta M/\big(b(1 - b/3l)\big) \tag{5.2}$$

Here ΔM is defined as the $\big(\Delta M = M_{\downarrow}(H) - M_{\uparrow}(H)\big)$ width of the hysteresis loop, b and l are the width and length of the samples ($b < l$) **[48, 49]**.

As shown in Figure 5.6 (*a*, *c*, *e*), the estimated J_c (H = 0 T, T = 2 K) values are represented in Table 5.5 for Cr_xNbSe_2 (x = 0.0005, 0.0009 and 0.0012), respectively, which are larger than pure $NbSe_2$ and Fe_xNbSe_2 **[35]**. However, the J_c values decrease rapidly after zero magnetic field regions.

To comprehend the J_c characteristics with applied magnetic field we have redrawn the Figure 5.6 (*a*, *c*, *e*) in log-log scale as appeared in Figure 5.6 (*b*, *d*, *f*). At near zero magnetic fields (Figure 5.6 (*a*, *c*, *e*) and Figure

(5.6 (*b*, *d*, *f*)), the field independent behaviour of J_c is observed confirming the presence of single vortex pinning region (S_V).

Table 5.5. *The estimated J_c (0) values from M-H curves for $NbSe_2$ and Cr_xNbSe_2 (x = 0.0005, 0.0009, 0.0012) single crystals.*

Sample	J_c (0) (A/cm^2) (@T = 2 K)
$NbSe_2$	1.4×10^5
$Cr_{0.0005}NbSe_2$	2.3×10^5
$Cr_{0.0009}NbSe_2$	3.5×10^5
$Cr_{0.0012}NbSe_2$	4.0×10^5

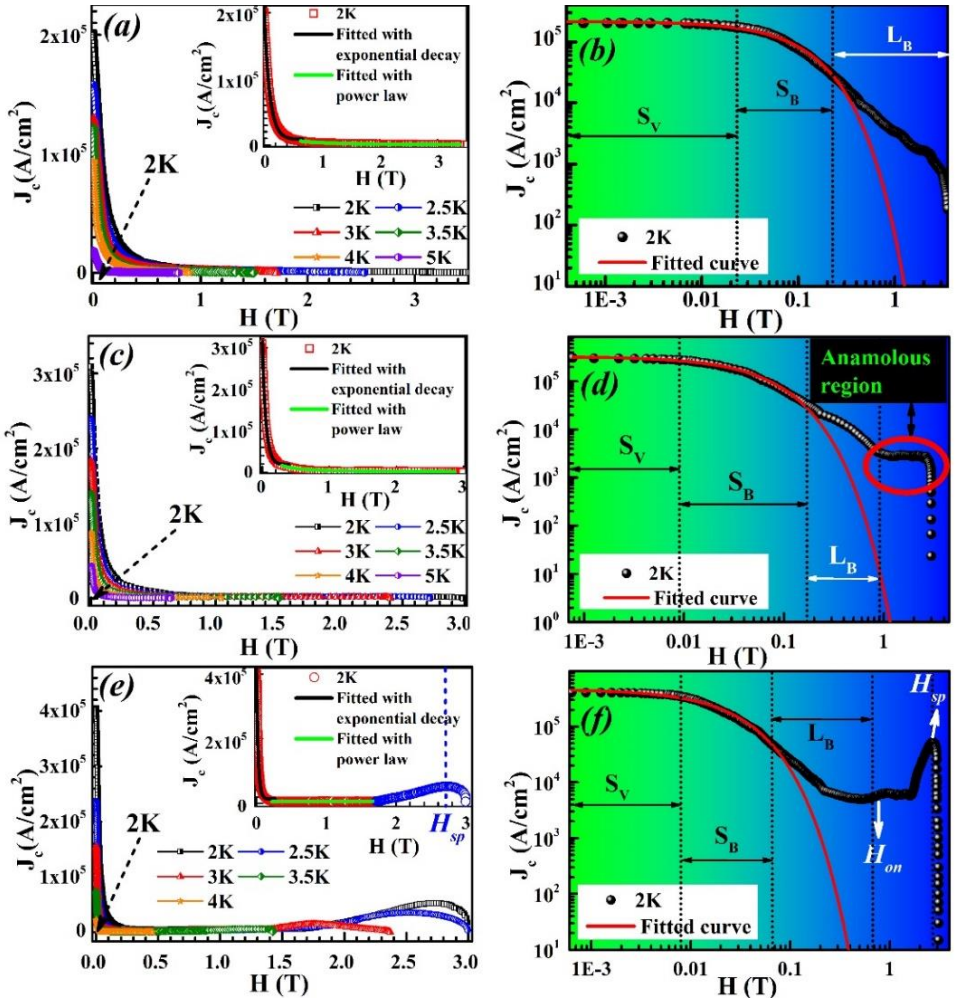

Figure 5.6. *Represents the J_c value as a function of magnetic field at different temperatures for (a) $Cr_{0.0005}NbSe_2$, (c) $Cr_{0.0009}NbSe_2$, and (e) $Cr_{0.0012}NbSe_2$. The inset includes the fitted curves using exponential decay model (black line) in the S_B region and*

power law model (green line) in the L_B region at 2 K. Inset of (e) indicates the H_{sp} value at which the SMP occurs. Figure (b), (d), and (f) represented the different anomalous region of vortex dynamics in log-log scale at 2 K.

This is due to the negligible correlation between the vortices. Here the vortices being separated from each other by lattice constant considered as individual system. Figure 5.6 (*a*, *c*, *e*) shows an exponential decay of J_c in the intermediate region of magnetic field, which is fitted with equation (5.3) as shown by black solid line in the inset of Figure 5.6 (*a*, *c*, *e*). This region is designated by small bundle pinning (S_B) region as shown in figure 5.6 (*b*, *d*, *f*) in the log-log plot. Here more vortices enter into the FLL and respond in the form of small vortex bundle to the external magnetic fields. Finally, the J_c values at higher magnetic field region follow power law fitting by equation (5.4). It is shown by green solid line in the inset of Figure 5.6 (*a*, *c*, *e*)) and designated as large bundle pinning region *(L_B)* in Figure 5.6 (*b*, *d*, *f*). Here vortices move in the form of large bundle.

$$J_c(H) = J_0(0)exp\left[-\left(\frac{H}{H_0}\right)^{\frac{3}{2}}\right] \tag{5.3}$$

$$J_c \propto H^{-\propto} \tag{5.4}$$

Now we will concentrate on the evolution of magnetic field dependence of J_c characteristics with Cr concentrations. Figure 5.6 (*b*) shows the collective creep motion (small bundle, large bundle) of vortices of $Cr_{0.0005}NbSe_2$ causing the final degradation of J_c by decreasing the effective activation energy. The distance between the vortices in S_B and L_B regions of $Cr_{0.0005}NbSe_2$ is still greater than the coherence length resulting negligible inter-vortex interaction. On the other hand, Figure 5.6 (*f*) shows an anomalous enhancement of J_c at high magnetic field in $Cr_{0.0012}NbSe_2$ following a sudden decrease after reaching a maximum value at H_{sp}. However, this peak is suppressed and moved to lower magnetic field region with enhancement of temperature as shown in Figure 5.6 (*c*).

5.2.2.5. Estimation of dynamical relaxation rate (Q) and intrinsic activation energy (U_c):

In order to realize the effect of Cr impurity on the SMP effect, we have computed the precise crossover point of the FLL in $Cr_{0.0012}NbSe_2$. For

this the *M-H* measurement has been accomplished with different sweeping rate (*dH/dt*). The magnetic field dependence of dynamical relaxation rate (*Q*) and intrinsic activation energy (U_c) are estimated from magnetization curves. The dynamical relaxation rate is stated as follows:

$$Q \equiv \frac{d \ln J_c}{d \ln(dB/dt)} = \frac{d \ln(\Delta M)}{dln(dB/dt)} \tag{5.5}$$

The magnetic hysteresis loops of $Cr_{0.0012}NbSe_2$ are illustrated in Figure 5.7 (*a*) with *dH/dt* of 50 Oe/sec and 150 Oe/sec at 2 K. The slight increase of ΔM value with enhancing *dH/dt* designates that SMP effect is associated with higher *dH/dt*. The *Q* (*H*) values (Figure 5.7 (*b*)), estimated using *dH/dt* and ΔM values, display a minimum value at 0.82 T (H_{min}) that is close to the H_{on}.

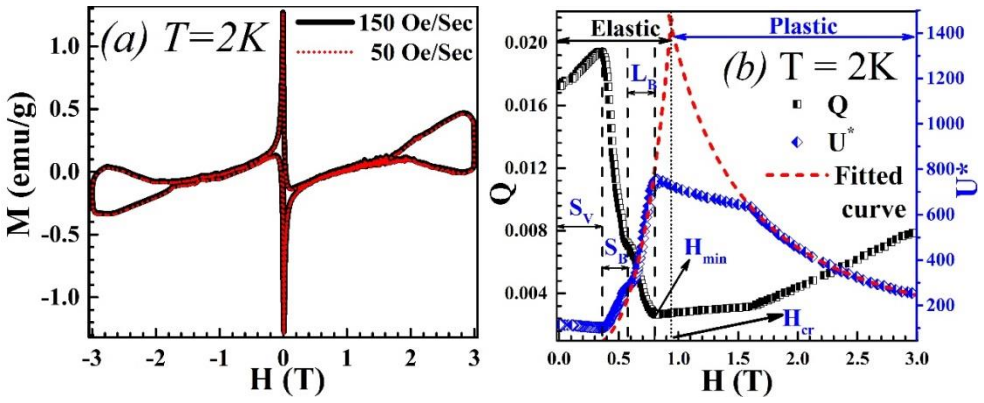

Figure 5.7. *(a) Shows the magnetic hysteresis loop curve of $Cr_{0.0012}NbSe_2$ at different sweeping rate, (b) Represents the magnetic field dependence behaviour of the dynamical relaxation rate (Q) and apparent activation energy ($U^*=U_C/K_B$). H_{min} represents the minimum value of dynamical relaxation rate Q and H_{cr} denotes the crossover field of elastic to plastic creep dominated region. Vertical dash lines separate the Sv, S_B, and L_B regions.*

The relationship between the *Q* and U_c is defined by equation (5.6).

$$\frac{T}{Q\ (T, B_e)} = \frac{U_C(T, B_e)}{K_B} + \mu\big(T, B_e\big)CT \tag{5.6}$$

where B_e, μ and *C* are the local magnetic induction, glassy exponent and a weakly temperature dependent parameter. At such low temperature (2 K), μCT has insignificant value compared to the U_c/K_B, so here, $T/Q \approx U_c/K_B$ is considered and accordingly we can assume that U^* is comparable to U_c/K_B. Figure 5.7 (*b*) represents the apparent activation energy ($U^* = T/Q$) vs. *H*

plots at 2 K. The positive curvature region of $U^*(=U_c/K_B)$ *vs* H curve at low and intermediate magnetic field regions is indicated as elastic region according to the elastic manifold theory. Furthermore, the negative curvature after H_{cr} (~ 0.9 T) at higher magnetic field is designated as the plastic region. The elastic creep dominated region and the plastic creep dominated regime are separated by the characteristic field (H_{cr}). It is worth mentioning that H_{on} almost agrees with the H_{cr} value and H_{sp} arises at the dominating plastic creep regime.

It can be concluded that the dominating pinning mechanism, which emerges from various sort of intrinsic and extrinsic defects results only elastic deformation of magnetic flux line (*i.e.* elastic creep region) in $Cr_{0.0005}NbSe_2$. However, the larger set of weak pinning centres increase the pinning force density noticeably in $Cr_{0.0012}NbSe_2$. This overcomes the dissipation energy arising from Lorentz force and thermal fluctuation and results the SMP effect in $Cr_{0.0012}NbSe_2$ **[37]**. Another reason might be the enhancement of the effective disorder of vortex lattice owing to the weak pinning potential of Cr impurities that reduces the stiffness of FLL. This may introduce the plastic deformation of soft FLL **[50]** of $Cr_{0.0012}NbSe_2$ which is considered as the possible cause of SMP effect after H_{on} (point after which SMP started). Similar kind of SMP effect is detected by Zhou *et al.* **[6]** which is associated with the plastic distortion of FLL in Co-co-doping in 112-type superconductor $Ca_{0.8}La_{0.2}Fe_{1-x}Co_xAs_2$. In $Cr_{0.0009}NbSe_2$, pinning energy becomes equal to dissipation energy of the FLL at higher magnetic field. As a consequence, an anomalous field independent J_c region is observed near H_{c2} (Figure 5.6 (*d*)). This reveals that Cr impurities tune the elastic to plastic (*E* - *P*) deformation of vortex lattice in Cr_xNbSe_2.

5.2.2.6. Study of pinning mechanism:

5.2.2.6.1. Type of interaction between the vortices and pinning centres:

Moreover, to check the impact of the local disorder of FLL on superconductivity, the correlation between core region of vortices and the pinning centres are estimated through different characteristic temperatures of δT_c and δl mechanism **[51]**. δT_c pinning designates the interaction via the spatial variation of T_c throughout the sample due to the pinning centres. On

the other hand, δl pinning defines the interaction owing to the fluctuation of l. The temperature dependence of δT_c and δl mechanism for H_{sb} (crossover field from S_V to S_B region) are described by equation (5.7) and equation (5.8) [51]:

$$H_{sb} = H_{sb}(0)\left(\frac{1-t^2}{1+t^2}\right)^{2/3} \tag{5.7}$$

$$H_{sb} = H_{sb}(0)\left(\frac{1-t^2}{1+t^2}\right)^{2} \tag{5.8}$$

In $Cr_{0.0005}NbSe_2$, Cr impurities trigger the fluctuations in l by acting as scattering pinning centres, which result δl core pinning (Figure 5.8 (*a*)). By increasing the concentration, the inhomogeneous distribution of Cr impurities throughout the sample broadens the T_c value and hence generates the δT_c pinning in $Cr_{0.0009}NbSe_2$ (Figure 5.8 (*b*)) **[52]**.

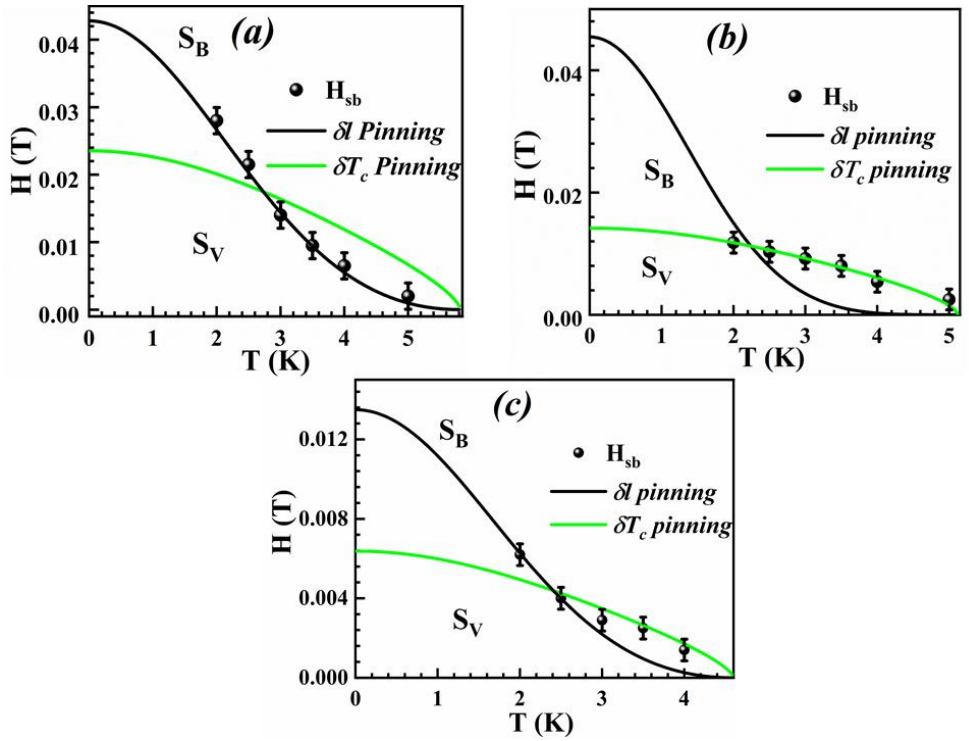

Figure 5.8. *Represents the temperature dependence behaviour of H_{sb} values for (a) $Cr_{0.0005}NbSe_2$, (b) $Cr_{0.0009}NbSe_2$, and (c) $Cr_{0.0012}NbSe_2$. The black solid line and green solid line are the fitted curves, which follow δl and δT_c pinning mechanism, respectively.*

Figure 5.8 (*b*) also shows the appreciable reduction of single vortex region compare to small bundle pinning region indicating the strong coupling between the vortices and pinning centres. However, Figure 5.8 (*c*) shows almost equal contribution of δT_c pinning and δl pinning in

$Cr_{0.0012}NbSe_2$ single crystal. This is because of strong temperature dependence of both δT_c and δl pinning that influences the core interaction **[53]**. δl pinning conducts the core interaction at low temperatures and its contribution is diminished with enhancement of the temperature. On the other hand, for the temperatures close to T_c, the fluctuation in T_c enhances the δT_c interaction. This makes the temperature dependence behaviour of δT_c pinning reverse to δl pinning. Therefore, we can conclude that the interaction of the vortex lattice turns from δl to δT_c pinning with increase of Cr atoms and finally shows both l and T_c fluctuation in the highest Cr_xNbSe_2. Thus the pinning mechanism is advanced due to presence of core interaction in Cr_xNbSe_2 superconductors.

5.2.2.6.2. Size dependent pinning mechanism:

In order to further develop the crucial landscapes of pinning potential in Cr_xNbSe_2, magnetic field dependence of F_p was estimated. In superconducting material, F_p displays three types of peak depending on the size of pinning centres. It includes the low field *BL* peak, intermediate peak associated with bulk pinning and high field peak near H_{c2}. The highly intense lower and higher field peaks in F_p are noticeable mainly in single crystalline samples. However, intermediate peaks are mostly observed in polycrystalline samples due to the strong bulk pinning mechanism. Figure 5.9 (*a* - *c*) demonstrations the normalized flux pinning force density ($f_p = F_p/F_{p\,(max)}$) as a function of reduced magnetic field ($h = H/H_{c2}$).

Figure 5.9 (*a*) displays the prominent zero field peak indicating the *BL* surface barrier effect in $Cr_{0.0005}NbSe_2$. Here magnetic fluxes must overcome the barrier that is formed because of the edge potential **[25]**. Similar strong surface pinning mechanism is also observed in untwined $YBa_2Cu_3O_{7-\delta}$ single crystal **[54]**. However, there is no intermediate and higher field peaks in Figure 5.9 (*a*) indicating the absence of volume pinning and lattice softening. All the f_p curves for 2 K ≤ T ≤ 5 K of Figure 5.9 (*a* - *c*) didn't collapse into one unified curve. Hence one pinning mechanism can't explain the magnetic field dependence nature of f_p in Cr_xNbSe_2. The experimental data of $Cr_{0.0005}NbSe_2$ are fitted with equation

(5.9) considering p = 0.8 and q = 2.6 in Dew Hughes model and r = 0.51 and s = 3.5 in Kramer's model at the low magnetic field region.

$$f_p = Ah^p(1-h)^q \tag{5.9}$$

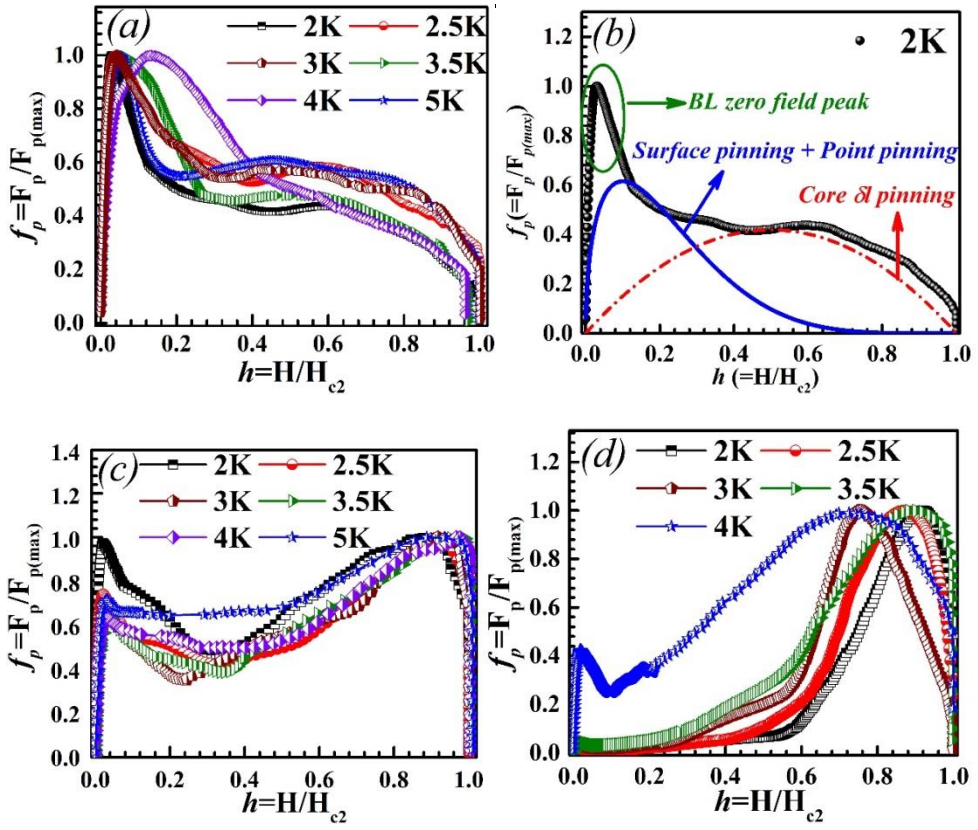

Figure 5.9. *(a) Represents* the f_p *(=*$F_p/F_{p(max)}$*) as a function of reduced magnetic field (h) of* $Cr_{0.0005}NbSe_2$*. at 2 K, 2.5 K, 3 K, 3.5 K, 4 K and 5 K temperatures. (b) the scaling behaviour of* f_p *(=*$F_p/F_{p\,(max)}$*) at 2 K temperature of* $Cr_{0.0005}NbSe_2$ *single crystal. The sharp zero field peak is encircled as the Bean-Livingstone surface barrier peak. The blue solid line is the fitted curve at low magnetic field region considering the contribution from both the surface pinning and point pinning. The red dotted line represents the contribution from core δl pinning at intermediate and higher magnetic field regions. (c) the* f_p *vs. h curve of* $Cr_{0.0009}NbSe_2$ *at 2 K, 2.5 K, 3 K, 3.5 K, 4 K and 5 K temperatures, and (d)) the* f_p *vs. h curve of* $Cr_{0.0012}NbSe_2$ *at 2 K, 2.5 K, 3 K, 3.5 K and 4 K temperatures.*

Figure 5.9 (*b*) represents the Dew-Hughes and Kramer's fit by the blue solid line. In case of intermediate and high fields regions, the f_p curves follow core δl pinning as presented by red dotted line. The surface pinning (associated with Kramer's model) at low magnetic fields indicates the parallel alignment of the external magnetic fluxes to resolve themselves into the region of minimum potential **[35]**. However, point pinning gives the hints of the presence of dense point pinning centres in $Cr_{0.0005}NbSe_2$

single crystal. Sang *et al.* **[55]** stated both the point pinning and the δl pinning in $FeSe_{0.5}Te_{0.5}$ single crystal that results giant enhancement in flux pinning associated with Co-impurities.

Further, Figure 5.9 (*c*) represents the BL zero field peak at near zero magnetic field and prominent higher field peak near H_{c2} in $Cr_{0.0009}NbSe_2$. However, it is difficult to distinguish the impact of different pinning mechanism in $Cr_{0.0009}NbSe_2$ because of the overlapping of zero field and higher field peak. Pippard *et al.* **[56]** described the higher field's peak due to the softening of shear modulus of FLL associated with random pinning potential. Later, Bhattacharya *et al.* **[57]** elaborately clarified the presence of this peak as a consequence of the change from interaction-dominated coherent motion of the elastic FLL to the disorder-dominated plastic motion of soft FLL. The onset of peak region is caused by the plastic flow instabilities of vortex medium. Finally, Figure 5.9 (*d*) shows the highly intense peak of $Cr_{0.0012}NbSe_2$ single crystal near H_{c2}. It seems that FLL is more relaxed in $Cr_{0.0012}NbSe_2$ compare to other Cr concentration. Both the zero-field peak and the core interaction (i.e. the δl and δT_c pinning) are significantly suppressed by high field peak in $Cr_{0.0012}NbSe_2$. This is because of the creeping of FLL following to the path of less variation of point pin densities. The fluctuation of pin densities determines the path of flux creeping throughout the crystal. Therefore, the different pinning mechanisms are successfully explored in Cr_xNbSe_2, which involved BL surface barrier effect at zero magnetic fields, point pinning and surface pinning at low magnetic fields and the lattice softening at the higher field regions. Thus, Cr impurities improve the J_c characteristics of $NbSe_2$ at low as well as higher magnetic field regions. On the other hand, Fe_xNbSe_2 illustrates the involvement of only point pinning and surface pinning mechanism in the pinning landscape and thus, results rapid destruction of the J_c values at higher magnetic field regions **[35]**.

5.3. Summary

In conclusion, Cr_xNbSe_2 single crystals with x = 0.0005, 0.0009 and 0.0012 were successfully investigated to study the influence of Cr doping on the vortex dynamics of $NbSe_2$ superconductor via magnetization measurement.

Cr atoms noticeably enhance the J_c value up to $4x10^5$ A/cm^2 in Cr_xNbSe_2 single crystals. With increasing the Cr concentrations, diverse anomalous characteristics of J_c are observed at higher magnetic field. The prominent fishtail effect of MHL curves in $Cr_{0.0012}NbSe_2$ exposes that single crystalline nature and optimal doping are two essential circumstances for enhancing the practical applicability of superconducting material at higher magnetic fields. To investigate the physical origin of SMP in J_c, we studied the magnetic field dependence of dynamical relaxation rate. The positive curvature of the U^* vs H curve changes to negative curvature at the characteristic field H_{cr} indicating the crossover from elastic to plastic region. H_{on} approximately agrees with H_{cr} and H_{sp} locates at the plastic creep dominated region. So, $Cr_{0.0012}NbSe_2$ single crystal demonstrates the SMP effect which supports the *E-P* crossover. $Cr_{0.0005}NbSe_2$ shows δl pinning due to the interaction between the core region of vortices and the pinning centres. However, the interaction is improved by increasing Cr concentration. $Cr_{0.0012}NbSe_2$ allows both δl and δT_c core interaction. These δl and δT_c core pinning strongly turn the 3D magnetic fluxes into 2D nature by enhancing the coupling between the vortices in the pinning potential of Cr atoms. $Cr_{0.0005}NbSe_2$ shows point pinning and surface pinning at low magnetic field region. Moreover, it supports the δl pinning at intermediate and high magnetic field regions along with the BL surface barrier effect near zero field region. The softening of the vortex lattice is enhanced gradually with increasing Cr concentration resulting out the intense peak in F_p at higher field in $Cr_{0.0009}NbSe_2$ and $Cr_{0.0012}NbSe_2$. The softening of the FLL designates the effective disorder of the FLL with degradation of the long-range order of the vortex lattice. There is no intermediate peak in the magnetic field dependence of f_p characteristics in Cr_xNbSe_2 superconductor, indicating the insignificant contribution of the bulk pinning in pinning mechanism.

Reference

[1] Hao Z., Clem J. R. (1991), Limitations of the London model for the reversible magnetization of type-II superconductors, Phys. Rev. Lett., 67, 2371 - 2374.

[2] Husaníková P., Fedor J., Dérer J., Šoltýs J., Cambel V., Iavarone M., May S. J., Karapetrov G. (2013), Magnetization properties and vortex phase diagram of Cu_xTiSe_2 single crystals, Phys. Rev. B, 88, 174501.

[3] Sugawara K., Yokota K., Tanokura Y., Sekine T. (1993), Anisotropic flux finning in layered superconductor 2H-$NbSe_{2-x}S_x$. In: Bando Y, Yamauchi H (Eds) Advances in Superconductivity V. Springer, Tokyo.

[4] Nishizaki T., Naito T., Kobayashi N. (1998), Anomalous magnetization and field-driven disordering transition of a vortex lattice in untwinned $YBa_2Cu_3O_y$, Phys. Rev. B, 58, 11169.

[5] Ganguli S. C., Singh H., Saraswat G., Ganguly R., Bagwe V., Shirage P., Thamizhavel A., Raychaudhuri P. (2015), Disordering of the vortex lattice through successive destruction of positional and orientational order in a weakly pinned $Co_{0.0075}NbSe_2$ single crystal, Sci. Rep., 5, 10613.

[6] Zhou W., Xing X., Wu W., Zhao H., Shi Z. (2016), Second magnetization peak effect, vortex dynamics, and flux pinning in 112-type superconductor $Ca_{0.8}La_{0.2}Fe_{1-x}Co_xAs_2$, Sci. Rep., 6, 22278.

[7] Kitaguchi H., Matsumoto A., Kumakura H., Doi T., Yamamoto H., Saitoh K., Sosiati H., Hata S. (2004), MgB_2 films with very high critical current densities due to strong grain boundary pinning, Appl. Phys. Lett., 85, 2842 - 2844.

[8] Kim M. S., Jung C. U., Park M. S., Lee S. Y., Kim K. H. P., Kang W. N., Lee S. I. (2001), Prominent bulk pinning effect in the MgB_2 superconductor, Phys. Rev. B, 64, 012511.

[9] Kugel K. I., Rakhmanov J. D. (1992), Phys. C, 196, 17 - 26.

[10] Dew-Hughes D. (1974), Flux pinning mechanisms in type II superconductors, Philos. Mag., 30, 293 - 305.

[11] Fietz W. A., Webb W. W. (1969), Hysteresis in superconducting alloys-temperature and field dependence of dislocation pinning in niobium alloys, Phys. Rev., 178, 657.

[12] Eisterer M., Zehetmayer M., Weber H. W. (2003), Phys. Rev. Lett., 90, 247002.

[13] Pallecchi I., Tarantini C., Aebersold H. U., Braccini V., Fanciulli C., Ferdeghini C., Gatti F., Lehmann E., Manfrinetti P., Marré D., Palenzona A., Siri A. S., Vignolo M., Putti M. (2005), Enhanced flux pinning in neutron irradiated MgB_2, Phys. Rev. B, 71, 212507.

[14] Wang J. L., Zeng R., Kim J. H., Lu L., Dou S. X. (2008), Effects of C substitution on the pinning mechanism of MgB_2, Phys. Rev. B, 77, 174501.

[15] Martínez E., Mikheenko P., López M. M., Millán A., Bevan A., Abell J. S. (2007), Flux pinning force in bulk MgB_2 with variable grain size, Phys. Rev. B, 75, 134515.

[16] Abulafia Y., Shaulov A., Wolfus Y., Prozorov R., Burlachkov L., Yeshurun Y., Majer D., Zeldov E., Wühl H., Geshkenbein V. B., Vinokur V. M. (1996), Plastic Vortex Creep in $YBa_2Cu_3O_{7-x}$ Crystals, Phys. Rev. Lett., 77, 1596 - 1599.

[17] Olson C. J., Zimányi G. T., Kolton A. B., Grønbech-Jensen N. (2000), Static and dynamic coupling transitions of vortex lattices in disordered anisotropic superconductors, Phys. Rev. Lett., 85, 5416 - 5419.

[18] Lortz R., Musolino N., Wang Y., Junod A., Toyota N. (2007), Origin of the magnetization peak effect in the Nb_3Sn superconductor, Phys. Rev. B, 75, 094503.

[19] Daeumling M., Seuntjens J. M., Larbalestier D. C. (1990), Oxygen-defect flux pinning, anomalous magnetization and intra-grain granularity in $YBa_2Cu_3O_{7-\delta}$, Nature, 346, 332-335.

[20] Erb A., Genoud J. Y., Marti F., Däumling M., Walker E., Flükiger R. (1996), Reversible suppression of the so-called fishtail effect in ultra pure single crystals of $YBa_2Cu_3O_{7-\delta}$ achieved by proper oxygenation, J. Low Temp. Phys., 105, 1023 - 1028.

[21] Zhao H. J., Wu W., Zhou W., Shi Z. X., Misko V. R., Peeters F. M. (2016), Reentrant dynamics of driven pancake vortices in layered superconductors, Phys. Rev. B, 94, 024514.

[22] Kopylov V. N., Koshelev A. E., Schegolev I. F. (1990), The role of surface effects in magnetization of high-T_c superconductors, Physica C, 170, 291 - 297.

[23] Senatore C., Flükiger R., Cantoni M., Wu G., Liu R. H., Chen X H (2008), Upper critical fields well above 100 T for the superconductor $SmFeAsO_{0.85}F_{0.15}$ with T_c = 46K, Phys. Rev. B, 78, 054514.

[24] Prozorov R. *et al.* (2008), Vortex phase diagram of $Ba(Fe_{0.93}Co_{0.07})_2As_2$ single crystals, Phys. Rev. B, 78, 224506.

[25] Sun Y., Shi Z. X., Gu D. M., Miura M., Tamegai T. (2010), Peak effect of flux pinning in $Sc_5Ir_4Si_{10}$ superconductors, J. Appl. Phys., 108, 073920.

[26] Pissas M., Lee S., Yamamoto A., Tajima S. (2002), Peak effect in single crystal MgB_2 superconductor for H ‖ c-axis, Phys. Rev. Lett., 89, 097002.

[27] Song D., Ishida S., Iyo A., Nakajima M., Shimoyama J. I., Eisterer M., Eisaki H. (2016), Distinct doping dependence of critical temperature and critical current density in $Ba_{1-x}K_xFe_2As_2$ superconductor, Sci. Rep., 6, 26671.

[28] Babu M. S., Pal D. (2014), Study of the noise in the magnetization data across the second magnetization peak and peak effect region in $Ca_3Rh_4Sn_{13}$, Phys. C, 505, 85 - 88.

[29] Ugeda M. M. *et al.* (2016), Characterization of collective ground states in single-layer $NbSe_2$, Nat. Phys., 12, 92 - 97.

[30] Xi X. X., Wang Z. F., Zhao W. W., Park J. H., Law K. T., Berger H., Forro L., Shan J., Mak K. F. (2016), Ising pairing in superconducting $NbSe_2$ atomic layers, Nat. Phys., 12, 139-143.

[31] El-Bana M. S., Wolverson D., Russo S., Balakrishnan G., Paul D. M., Bending S. J. (2013), Superconductivity in two-dimensional $NbSe_2$ field effect transistors, Supercond. Sci. Technol., 26, 125020.

[32] Spiering G. A., Revolinsky E., Beerntsen D. J. (1966), Critical currents in superconducting single crystal niobium diselenide, J. Phys. Chem. Solids, 27, 535 - 541.

[33] Koorevaar P., Aarts J., Berghuis P., Kes P. H. (1990), Tilt-modulus enhancement of the vortex lattice in the layered superconductor 2H-$NbSe_2$, Phys. Rev. B, 42, 1004.

[34] Krishnan M., Pervin R., Ganesan K. S., Murugesan K., Lingannan G., Verma A. K., Shirage P. M., Sonachalam A. (2018), Pressure assisted

enhancement in superconducting properties of Fe substituted $NbSe_2$ single crystal, Sci. Rep., 8, 1251.

[35] Pervin R., Krishnan M., Rana A. K., Kannan M., Arumugam S., Shirage P. M. (2017), Enhancement of superconducting critical current density by Fe impurity substitution in $NbSe_2$ single crystals and the vortex pinning mechanism, Phys. Chem. Chem. Phys., 19, 11230.

[36] Tachiki M., Takahashi S. (1989), Strong vortex pinning intrinsic in high-T_c oxide superconductors, Solid State Commun., 70, 291.

[37] Blatter G., Feigel'man M. V., Geshkenbein V. B., Larkin A. I., Vinokur V. M. (1994), Vortices in high-temperature superconductors, Rev. Mod. Phys., 66, 1125 - 1388.

[38] Larkin A. I., Ovchinnikov Y. N. (1979), Pinning in type II superconductors, J. Low Temp. Phys., 34, 409 - 428.

[39] Wang H. *et al.* (2017), High-quality monolayer superconductor $NbSe_2$ grown by chemical vapour deposition, Nat. Commun., 8, 394.

[40] Boscher N. D., Carmalt C. J., Parkin I. P. 2006, Atmospheric pressure chemical vapour deposition of $NbSe_2$ thin films on glass, Eur. J. Inorg. Chem., (2006), 1255 - 1259.

[41] Wertheim G., DiSalvo F., Buchanan D. (1983), Phys. Rev. B, 28, 3335.

[42] Biesinger M. C., Payne B. P., Grosvenor A. P., Lau L. W. M., Gerson A. R., Smart R. St. C. (2011), Resolving surface chemical states in XPS analysis of first row transition metals, oxides and hydroxides: Cr, Mn, Fe, Co and Ni, Appl. Surf. Sci., 257, 2717 - 2730.

[43] Boscher N. D., Carmalt C. J., Hyett G., Prieto A. G., Pankhurst Q. A., Parkin I. P. (2008), Chromium oxyselenide solid solutions from the atmospheric pressure chemical vapour deposition of chromyl chloride and diethylselenide, J. Mater. Chem., 18, 1667-1673.

[44] Agostinelli E., Battistoni C., Fiorani D., Mattono G., Nogues M. (1989), An XPS study of the electronic structure of the $Zn_xCd_{1-x}Cr_2$(X = S, Se) spinel system, J. Phys. Chem. Solids, 50, 269 - 272.

[45] Axnas J., Holm W., Eltsev Y., Rapp O. (1996), Increased phase-breaking scattering rate in Zn-doped $YBa_2Cu_3O_{7-\delta}$, Phys. Rev. B, 53, R3003 - R3006.

[46] Iavarone M., Di Capua R., Karapetrov G., Koshelev A. E., Rosenmann D., Claus H., Malliakas C. D., Kanatzidis M. G., Nishizaki T., Kobayashi N. (2008), Effect of magnetic impurities on the vortex lattice properties in $NbSe_2$ single crystals, Phys. Rev. B, 78, 174518.

[47] Yokoya T., Kiss T., Chainani A., Shin S., Nohara M., Takagi H. (2001), Fermi surface sheet-dependent superconductivity in 2H-$NbSe_2$, Science, 294, 2518.

[48] Bean C. P. (1962), Magnetization of Hard Superconductors, Phys. Rev. Lett., 8, 250 - 253.

[49] Bean C. P. (1964), Magnetization of high-field superconductors, Rev. Mod. Phys., 36, 31 - 39.

[50] Higgins M. J., Bhattacharya S. (1996), Varieties of dynamics in a disordered flux-line lattice, Physica C, 257, 232 - 254.

[51] Qin M. J., Wang X. L., Liu H. K., Dou S. X. (2002), Evidence for vortex pinning induced by fluctuations in the transition temperature of MgB_2 superconductors, Phys. Rev. B: Condens. Matter Mater. Phys., 65, 132508.

[52] Hauser J. J., Robbins M., DiSalvo F. J. (1973), Effect of 3d impurities on the superconducting transition temperature of the layered compound $NbSe_2$, Phys. Rev. B, 8, 1038 - 1042.

[53] Ghorbani S. R., Wang X. L., Hossain M. S. A., Dou S. X., Lee S. I. (2010), Coexistence of the δl and δT_c flux pinning mechanisms in nano-Si-doped MgB_2, Supercond. Sci. Technol., 23, 025019.

[54] Flippen R. B., Askew T. R., Fendrich J. A., Vanderbeek C. J. (1995), Surface flux pinning in $YBa_2Cu_3O_{7-\delta}$, Phys. Rev. B, 52, R9882(R).

[55] Sang L., Maheswari P., Yu Z., Yun F. F., Zhang Y., Dou S., Cai C., Awana V. P. S., Wang X. (2017), Point defect induced giant enhancement of flux pinning in Co-doped $FeSe_{0.5}Te_{0.5}$ superconducting single crystals, AIP Adv., 7, 115016.

[56] Pippard A. B. (1969), A possible mechanism for the peak effect in type II superconductors, Philos. Mag., 19, 217.

[57] Bhattacharya S., Higgins M. J. (1993), Dynamics of a disordered flux line lattice, Phys. Rev. Lett., 70, 2617 - 2620.

CHAPTER 6

Study of Structural, Electrical, Electronic, Transport and Magnetic Properties in Defect Induced $NbSe_2$

In this chapter we try to focus on the significant characteristics of $NbSe_2$ in presence of the different kinds of defects (Intrinsic and extrinsic). These characteristics depend on the intriguing electronic properties of layered TMD materials that are extremely influenced by their anisotropic crystal structure. As we discussed earlier, different TMDs show different electronic properties based on their band structure formation, density of states at the Fermi level and the structure of the Fermi surface ***[1-4]****. This chapter focuses on studies on defects and to investigate the related changes in the physical properties of $NbSe_2$.*

Diverse transport properties, for example, resistance, magnetoresistance, Hall effect and superconductivity exhibit the strange and intense changes with the external defects **[5, 6]**. Morris *et al.* delineated the Kondo effect elaborately with anisotropic nature in association with the direction of magnetic fields in Fe doped $NbSe_2$ in the range from 0.25% to 5% **[7]**. However, there is an absence of methodical examinations on the disruptive movement of FLL in the thermally activated flux flow region (TAFF) of $NbSe_2$ in the presence of intrinsic and extrinsic defects. The dissipative TAFF region of low and high T_c superconductors still is a massive essential field for investigation specifically for the application of long length cables. The superconducting state of a material is generally well known as dissipation less state. In case of type-II superconductors, the supercurrent is constrained because of the interaction between two opposite forces that act on the magnetic flux lines. One of the forces is pinning force which arises because of the spatial distribution of inhomogeneities. The other force is the Lorentz force that appears due to the supercurrent **[8]**. The movement of the flux lines results dissipation of energy in this region. The dissipation happens when there is 'flux creep' in FLL associated with the dominating pinning force **[9]** and 'flux flow' which is associated with the dominating Lorentz force **[10, 11]**. Conversely, another kind dissipation is also observed which arises due to the thermal fluctuation and independent of supercurrent. It follows the Arrhenius relation in the TAFF region **[12]**. The lowest thermal energy which is essential for flux lines to creep from one pinning centre to different pinning centre is defined as thermal activation energy (TAE). The TAE is being influenced by magnetic field and different orientation of the material. Its characteristics solely depend on system which has different strength of pinning centres, coherence length, and thermal fluctuations of superconducting materials. The calculated TAE value of high T_c superconductor (*i.e.,* BSCCO) is in the range of 300-3000 K **[13]**. However, strong grain boundary pinning of MgB_2 shows the TAE value as high as 10^4 K **[14]**. The comprehension of TAE properties plays a crucial role for the functional appropriateness of superconductors as it damages the effectiveness of the material in presence of high magnetic field. Thermal fluctuation mainly dominates in the thermally activated flux

flow region (TAFF) and vortex flux flow (FF) region of mixed state of a superconductor. It leads the thermal motion of FLL. The Ginzburg number (*Gi*), which measures the thermal fluctuation, demonstrates an estimation of 10^{-2} - 10^{-1} in Cu-O superconductors. Low T_c superconductor such as $NbSe_2$ shows the *Gi* value in the range of 10^{-8}-10^{-7}. $NbSe_2$ shows fewer results previously associated with the TAE properties in TAFF state. This chapter will provide a comprehensive depiction of the resistive movement of FLL through TAFF study of $NbSe_2$ caused by intrinsic and extrinsic defects. Though $NbSe_2$ has very low Gi value, it is chosen for the TAFF study due to its electronic anisotropy like the high T_c superconductors. Another fascinating topic for the discussion of present chapter is the effect of defects on the interaction between two prominent phenomena superconductivity (SC) and ferromagnetism (FM). It is an enthralling scientific topic for a long time in the superconducting spintronic and quantum computing field **[15-18]**. Besides the property of exactly zero *dc* electrical resistance, superconductors also expel magnetic flux lines because of the presence of singlet Cooper pair electrons **[8]**. On the other hand, FM destructs this singlet *s*-wave pairing and therefore, opposes the existence of FM and SC simultaneously **[19, 20]**. However, the appearance of these two novel phenomena was demonstrated in 1970s through the measurement of magnetic and temperature dependence of superconducting properties in $ErRh_4B_4$ and $Ho_{1.2}Mo_6S_8$ superconductors **[21, 22]**. In the late 1990s, the high T_c superconductors showed the presence of SC and weak FM. Here the electrons, accountable for SC and FM arise from different origin **[23, 24]**. However, UGe_2 and URhGe superconductors have electrons which are responsible for both SC and FM properties **[25, 26]**. TMDCs (*e.g.* MoS_2, $NbSe_2$, $SnSe_2$, *etc*.) act as a distinct electronic system for perceiving the connection between SC and FM Among different kinds of elements **[27-29]**. TMDs are known as quasi two-dimensional electronic systems showing usually nonmagnetic properties **[30]**. Changing the magnetic properties of these low-dimensional systems appears as a continuous objective of the widespread study in the spin-electronic devices. Localized magnetic moment is incorporated via defects **[31-32]** along with strain **[33-35]** in two-dimensional nonmagnetic TMDCs to explore the magnetic

properties. Additional important method is the structural alteration via doping of transition metal (TM) atoms **[36-38]**. The intrinsic properties of $NbSe_2$ are easily amenable for such kind of effective alteration to investigate the simultaneous existence of superconductivity and ferromagnetism. Similarly, it can also effortlessly be doped with impurities between the Se-Nb-Se layers **[39]**. Pristine $NbSe_2$ are nonmagnetic in nature due to the presence of Nb atoms. Nb atoms are trigonal prismatically bounded by six Se atoms that pacify the magnetic properties of Nb^{4+} ions **[40-42]**. Several experimental and theoretical studies have been performed to persuade and control the spin structures of $NbSe_2$ superconductor. Manchanda *et al.* reported that the extremely localized magnetic moments can be induced in $NbSe_2$ via creation of Nb vacancies **[43]**. These moments are limited to the Se atoms that are nearby to the vacancies. However, $NbSe_2$ monolayer, having single and double selenium vacancies shows nonmagnetic metallic characteristics. Zhu *et al.* stated that the ferromagnetic ordering of Nb atoms has been incorporated in ultrathin $NbSe_2$ by the polar reductive hydrazine molecule **[28]**. Additionally, the ferromagnetic and antiferromagnetic properties were also found in $NbSe_2$ via incorporation of Co, Fe, and Cr atoms in high concentration. For example, $Cr_{0.25}NbSe_2$ and $Mn_{0.33}NbSe_2$ show weak ferromagnetism having ordering temperatures of 79 K and 22 K while $Fe_{0.26}NbSe_2$ represents antiferromagnetic (AFM) properties with a transition temperature of 122 K **[44]**. The superconducting properties are destructed completely due to these high ordering temperatures. Consequently, it eliminates the probability of coexistence of FM and SC.

In this chapter, we first thoroughly studied the transport characteristics through resistance measurement as a function of temperature and magnetic field for $B||ab$ plane in the TAFF region of mixed state of $NbSe_2$ single crystal by creating Se vacancy (*i.e.,* $NbSe_{1.85}$) and incorporating Fe impurities (*i.e.,* $Fe_{0.0015}NbSe_2$). Additionally, the coexistence of FM and SC has been also studied in $NbSe_{1.85}$ (to observe the effect of the non-stoichiometric ratio of Nb and Se atoms) and $Fe_{0.0015}NbSe_2$ (to observe the effect of very dilute concentration of Fe atoms). The magnetoresistance study shows the broadening of the transition regions in

both $NbSe_{1.85}$ and $Fe_{0.0015}NbSe_2$. This is associated with the inhomogeneities of Se concentration in $NbSe_{1.85}$ and the nanoscale inhomogeneities of Fe concentration in $Fe_{0.0015}NbSe_2$. The TAE values of $NbSe_{1.85}$ and $Fe_{0.0015}NbSe_2$ are lesser than pure $NbSe_2$. In $NbSe_2$ and $Fe_{0.0015}NbSe_2$, TAE follows temperature linearly and consequently, resistance is nicely depicted by Arrhenius relation. In contrast, the resistance of $NbSe_{1.85}$ is well described by modified TAFF method because of the nonlinear reliance of TAE on temperature. The magnetic field dependency of TAE differentiates the Fe intercalated $NbSe_2$ from Se deficient $NbSe_2$. $NbSe_{1.85}$ shows plastic deformation of FLL rather than the elastic deformation of FLL in $Fe_{0.0015}NbSe_2$. The Flux lines exhibit 2D features in the TAFF state of $NbSe_{1.85}$. The temperature dependence of resistance measurement of both $NbSe_{1.85}$ and $Fe_{0.0015}NbSe_2$ show no resistance minima associated with Kondo-like behaviour. Further, first principle calculation of $NbSe_2$, $NbSe_{1.85}$ and $Fe_{0.0015}NbSe_2$ have been accomplished to explore the distinction in band structure and density of state (DOS) in $NbSe_2$ because of Se vacancies and Fe intercalation. It displays that Fe atoms or Se vacancies intensely modulate the superconducting properties of $NbSe_2$. The spin polarization estimation demonstrates the insignificant impact of magnetism of Fe atoms in $Fe_{0.0015}NbSe_2$. Further, the disorder related to Se vacancy and Fe intercalation has been affirmed by the room temperature resistivity measurement. The resistivity curves demonstrate that the Se vacancy and Fe defect reduce the T_c value in $NbSe_{1.85}$ and $Fe_{0.0015}NbSe_2$ because of the presence of disorder and enhancement of scattering phenomena of charge carriers. The signature of both SC and FM transition has been observed from the temperature dependence of magnetization measurement in $NbSe_{1.85}$. The superconducting and ferromagnetic transition temperatures are estimated from DC susceptibility measurements which reveal the presence of itinerant ferromagnetism of 4*d* electrons of Nb atoms in $NbSe_{1.85}$. Moreover, the coexistence of FM and SC is nicely represented in the magnetic hysteresis curve of $NbSe_{1.85}$ though $Fe_{0.0015}NbSe_2$ shows no such kind of evidence. This investigation not just gives the impact of

defects in SC and FM characteristics, yet additionally urges to ponder the impact of deformities on different kinds of superconducting materials.

6.1. Materials and Method

Materials: Niobium (Nb, 99.95%; Alfa Aesar), Selenium (Se, 99.999%; Alfa Aesar), Iron (Fe, 99.99%; Alfa Aesar), and Iodine (I_2, 99.998%; Alfa Aesar).

Method: The single crystals of $NbSe_2$, $NbSe_{1.85}$ and $Fe_{0.0015}NbSe_2$ were grown following to the standard Iodine vapour transport method using precursors Nb (99.95%), Se (99.999%) and Fe (99.99%) purchased. First, the circular pellets of required stoichiometric concentrations were sealed in a quartz tube of length approximately 20 cm after evacuation at a pressure of 2.5 x 10^{-5} mbar. Then the tubes were heated in a two-zone furnace following the procedure as described in our previous studies **[45, 46]**. The mobility of Nb and Se atoms were accelerated by iodine as a transporting agent.

6.2. Result and discussions

6.2.1. Structural properties:

6.2.1.1. X-Ray diffraction:

The XRD patterns of $NbSe_2$, $NbSe_{1.85}$ and $Fe_{0.0015}NbSe_2$ single crystals are represented in Figure 6.1. The diffraction peaks of both $NbSe_2$ and defect induced $NbSe_2$ consist of (002), (004), (006) and (008) crystallographic planes of hexagonal $NbSe_2$ phase with space group $P6_3/mmc$ (JCPDS card no. 01-070-5612). All the diffraction peaks confirm the single crystalline nature of $NbSe_2$, $NbSe_{1.85}$ and $Fe_{0.0015}NbSe_2$. The full-width-at-half-maximum (FWHM) is about 0.06° confirming the high quality and perfect *c*-axis orientation of these single crystals. The lattice constant "*c*" of $NbSe_2$, $NbSe_{1.85}$ and $Fe_{0.0015}NbSe_2$ has been computed using equation (6.1), as shown in Table 6.1.

$$\frac{1}{d^2} = \frac{4}{3a^2}(h^2 + (hk) + k^2) + \frac{l^2}{c^2} \qquad (6.1)$$

The calculated lattice parameter "*c*" of $NbSe_2$ is in good agreement with the previously reported literature for $NbSe_2$ **[45]**. There is no additional impurity peak associated with Fe doping in $NbSe_2$. However, a

slight escalation in lattice parameter is noticed because of 0.15% Fe doping in $NbSe_2$. As we discussed in our previous observations (chapter 5), the ionic size of Fe^{3+} (0.645 Å in CN = 6) is comparable to the Nb^{4+} (0.68 Å in CN = 6). So, externally generated defects of the $Fe_{0.0015}NbSe_2$ manifest the successful intercalation of the Fe atoms in between the Se layers **[3]**.

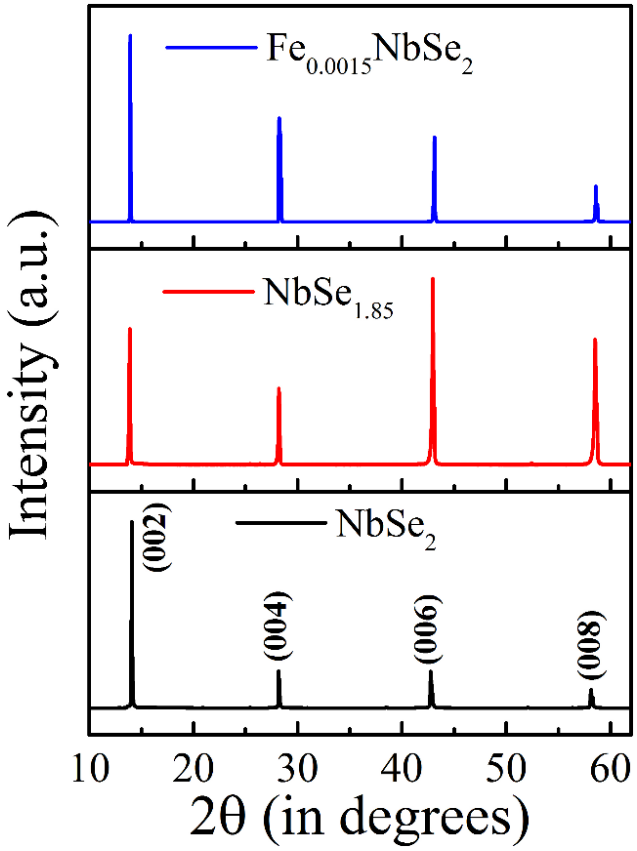

Figure 6.1. *Represents the XRD pattern of $NbSe_2$, $NbSe_{1.85}$ and $Fe_{0.0015}NbSe_2$ single crystals.*

In comparing with the pure $NbSe_2$, no phase change is observed in $NbSe_{1.85}$ associated with the intrinsic defects. However, the formation of the Se defect might be related to the enhancement of the lattice constant "*c*" of $NbSe_{1.85}$ as shown in Table 6.1. The presence of both intrinsic and extrinsic defects and the associated lattice alteration of $NbSe_{1.85}$ and $Fe_{0.0015}NbSe_2$ will discuss elaborately in the transport properties measurement of the next section.

Table 6.1. *The estimated structural parameters for $NbSe_2$, $NbSe_{1.85}$ and $Fe_{0.0015}NbSe_2$ single crystals.*

Sample	*c* (Å)	*FWHM*			
		(002)	(004)	(006)	(008)
$NbSe_2$	12.552±0.004	0.12	0.14	0.14	0.15
$NbSe_{1.85}$	12.623±0.005	0.09	0.17	0.22	0.27
$Fe_{0.0015}NbSe_2$	12.588±0.002	0.09	0.14	0.17	0.18

6.2.1.2. FESEM and EDS analysis:

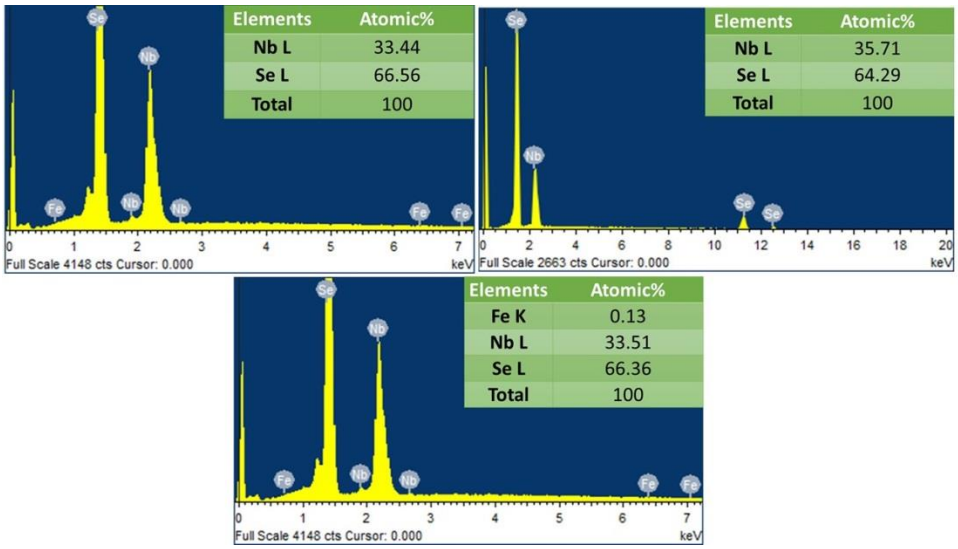

Figure 6.2. EDS analysis of (a) $NbSe_2$, (b) $NbSe_{1.85}$ and (c) $Fe_{0.0015}NbSe_2$ single crystals.

To study the surface morphology, composition and stoichiometry, the FESEM and EDX spectroscopy are carried out for all the single crystal compounds. The EDX spectra (Figure 6.2 (*a*-*c*)) of $NbSe_2$, $NbSe_{1.85}$ and $Fe_{0.0015}NbSe_2$ show the proper elemental composition without having any other phase which further confirms the purity of the materials. The EDX elemental mapping of $NbSe_2$, $NbSe_{1.85}$ and $Fe_{0.0015}NbSe_2$ are shown in Figure 6.3, 6.4 and 6.5. Figure 6.4 shows that there is uniform distribution of Se concentration, in $NbSe_{1.85}$. In $Fe_{0.0015}NbSe_2$ (Figure 6.5), it is not possible to measure the Fe distribution accurately as the best achievable elemental sensitivity of EDS is 0.1% (achieved using standards). However, there might be some inhomogeneity in Fe distribution at nanoscale.

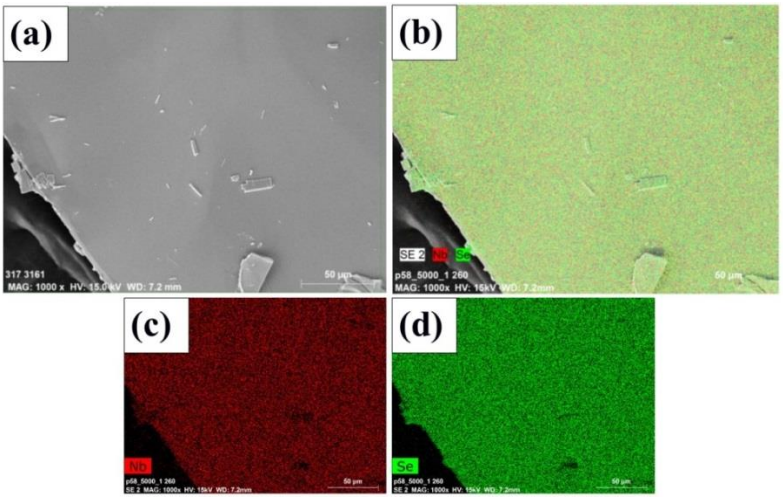

Figure 6.3. *(a) FESEM morphology of pristine $NbSe_2$ and the corresponding EDS colour mapping images of (b) all elements, (c) Nb and (d) Se.*

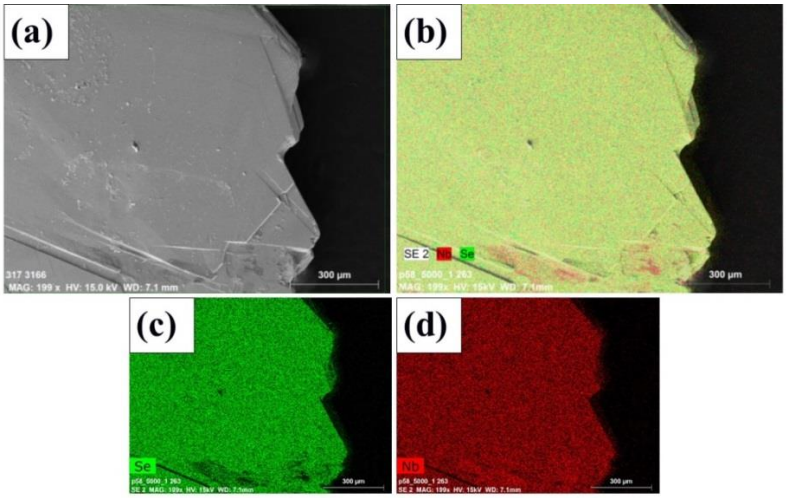

Figure 6.4. *(a) FESEM morphology of $NbSe_{1.85}$ and the corresponding EDS colour mapping images of (b) all elements, (c) Nb and (d) Se.*

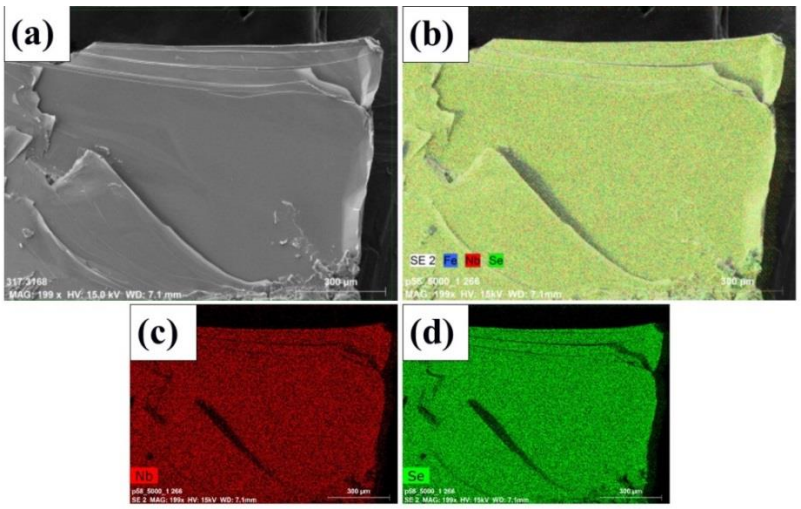

Figure 6.5. *(a) FESEM morphology of $Fe_{0.0015}NbSe_2$ and the corresponding EDS colour mapping images of (b) all elements, (c) Nb and (d) Se.*

6.2.2. Electronic properties by theoretical calculation:

Computational Method:

The electronic structures of $NbSe_2$, $NbSe_{1.85}$ and $Fe_{0.0015}NbSe_2$ have been investigated using first principle density functional theory to make better understanding of the superconducting phenomena. The Cambridge Sequential Total Energy Package Code (CASTEP) **[47]** is used to accomplish the first-principles *ab-initio* simulations. It utilizes the plane-wave pseudo-potential method depending on DFT. In the simulations, we use ultrasoft pseudopotential in the Vanderbilt form that describes the electron-ion interactions. The electronic exchange correlation has been studied with Perdew-Burke-Enzerhof (PBE) functional considering the generalized gradient approximation (GGA) **[48]**. We use the Broyden-Fletcher-Goldfrab-Shanno (BFGS) scheme for geometry optimization of the three compounds. All the simulations are performed constructing the 2×2×1, 2x2x2 and 3x3x1 supercells of three samples. Spin polarized single point energy calculations have been achieved considering the hexagonal phase of space group symmetry $P6_3/mmc$ with ultrasoft pseudopotentials. We take plane wave basis set with energy cut off 600 eV. Monkhorst-Pack scheme is used for sampling the Brillouin zone in the k space **[49, 50]**. The grid size has been taken as 17×17×8 for SCF calculation. For yielding the optimized structures, all atoms have been fully relaxed to converge the magnitude of force on each atom less than 0.01 eV/Å. However, the energy changed per atom is converged to less than 5×10^{-7} eV.

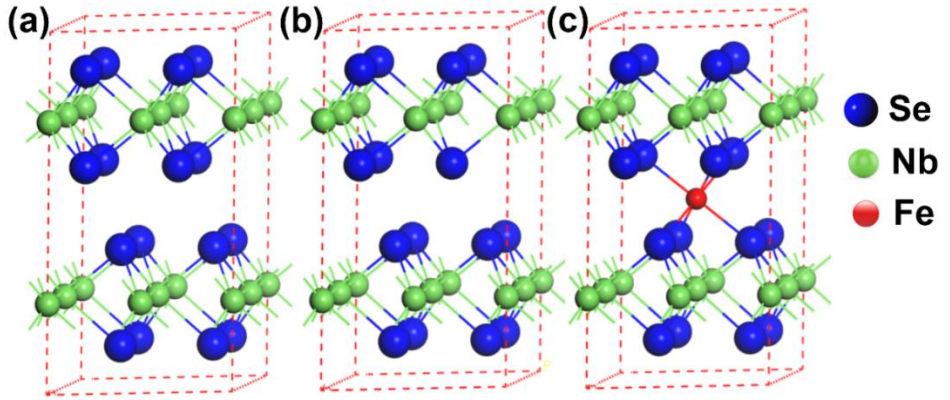

Figure 6.6. *Crystal Structure of 2×2×1 supercells of $NbSe_2$: (a) without doping, (b) with Se vacancy, (c) with intercalation doping of Fe.*

6.2.2.1. Band structure calculation:

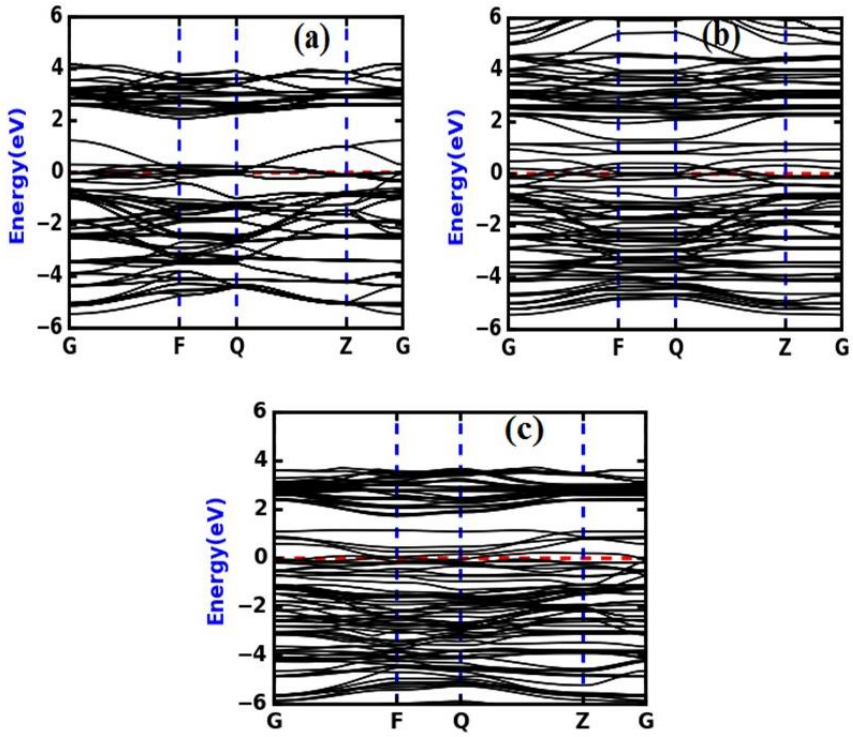

Figure 6.7. *Electronic Band structures of (a) $NbSe_2$, (b) $NbSe_2$ with Se vacancy, and (c) $NbSe_2$ with Fe I-doping along the major high symmetric directions.*

We have considered three models of $NbSe_2$ to investigate the electronic structure theoretically. The models are (*i*) $NbSe_2$ without doping (Figure 6.6 (*a*)) (denoted as undoped), (*ii*) $NbSe_2$ with Se vacancy (Figure 6.6 (*b*)) (mentioned as Se vacancy), (*iii*) Intercalation doping model in which one Fe atom is intercalated between two $NbSe_2$ interlayers (Figure 6.6 (*c*)) (denoted as Fe I-doping). Initially, the lattice constants of $NbSe_2$ are taken as $a = b = 6.8892$ Å and $c = 12.5444$ Å to calculate the electronic structure. After that these parameters are optimized geometrically **[51]**. The band structures and the density of states (DOS) of the above stated three cases have been calculated to realize the influence of Se vacancy and Fe I-doping on the electronic properties of $NbSe_2$. Figure 6.7 (*a*) shows that more than one band cross the Fermi level (E_F) in undoped $NbSe_2$. This shows the metallic characteristics of undoped $NbSe_2$ and supports the previously reported experimental observations **[52]**. The large DOS of $NbSe_2$ at E_F as shown in Figure 6.8 (*a*) gives also the evidence of the metallic characteristics of $NbSe_2$. Figure 6.7 (*b*) and Figure 6.7 (*c*) show the reduction of number of bands crossing the Fermi level for Se deficient as

well as Fe I-doping cases. This indicates the accessibility of the lesser number of electronic states for pairing in both defects induced cases causing the degradation of superconductivity. As compare to the undoped case, there is no gap (defined as the absence of electronic states near 2 eV in the electronic band structures of Figure 6.7 (*a*)) in the conduction band of Fe I-doping and Se deficient $NbSe_2$ as shown in Figure 6.7 (*b*) and Figure 6.7 (*c*).

6.2.2.2. DOS analysis:

Figure 6.8 (*b*) shows the DOS analysis indicating the reduction of DOS in Se deficient $NbSe_2$ at the Fermi level. The DOS also decreases in Fe I-doping case as compare to $NbSe_2$ as shown in Figure 6.8 (*c*).

The partial DOS (pDOS) data of Figure 6.8 (*a* - *g*) expose the Nb 4d bands which are mainly responsible for the availability of DOS at E_F. Thus, for both pristine and defect induced $NbSe_2$, Nb bands take participate in the phenomena of superconductivity. Though both the intrinsic and extrinsic defects diminishes the *p*DOS of Nb at E_F, a peak shift is observed only in extrinsic defect induced $NbSe_2$ (i.e. Fe I-doping case) at the Fermi level as demonstrated in Figure 6.8 (*c*) and Figure 6.8 (*e*). Thus, we can say that both the Se vacancy and Fe I-doping reduce the superconductivity in $NbSe_2$. There is no straight comparison between the theoretical 2x2x1 supercell (with Fe-doping) and the experimentally taken 0.0015 Fe doping $NbSe_2$. Further, we also performed simulations in 2x2x2 or 3x3x1 supercells considering (without Fe doping) 48 (450 electrons) and 54 (458 electrons) atoms, respectively. It gives the information about the effect of smaller concentration of Fe intercalation or Se vacancy in $NbSe_2$.

The simulation estimated with 2x2x2 and 3x3x1 supercells is analogous to the outcomes as we get from 2x2x1 supercell. In addition, larger supercell is considered for randomizing and creating a minimum interaction among the defects. In 2x2x2 supercell four NbSe layers are taken considering three different probable places for Fe intercalation. Simulations of the 2x2x2 supercell have been accomplished with Fe intercalation at all the three probable places and for Se vacancy at different positions. All the considerable cases show nearly comparable outcomes.

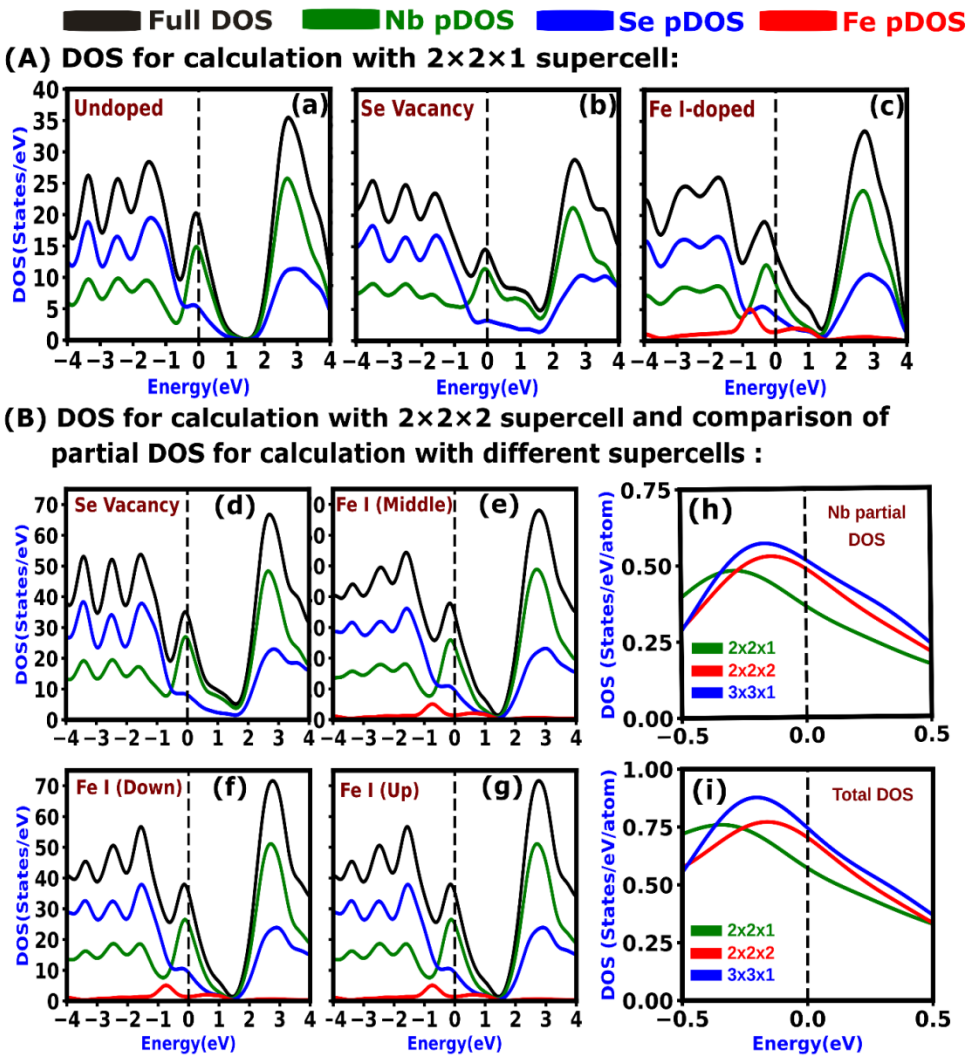

Figure 6.8. *(a) Full density of states (DOS), partial density of states (pDOS) of Nb, pDOS of Se in case of undoped $NbSe_2$ with 2×2×1 supercell.(b) Full DOS, pDOS of Nb, pDOS of Se in case of Se vacancy with 2×2×1 supercell. (c) Full DOS, pDOS of Nb, pDOS of Se, pDOS of Fe in case of Fe intercalation doping with 2×2×1 supercell. (d) Full DOS, pDOS of Nb, pDOS of Se in case of Se vacancy with 2×2×2 supercell. Full DOS, pDOS of Nb, pDOS of Se, pDOS of Fe in case of Fe intercalation doping with 2×2×2 supercell for Fe intercalation position – (e) middle (f) down (g) up. The Fermi level is indicated by the dashed vertical line at zero energy. The change in partial DOS of Nb and the total DOS per atom with Fe intercalation in different supercells is shown in Fig- (h), (i) respectively.*

There is no peak shift with the variation in supercell size in the partial DOS of Nb and the total DOS of Fe I doping case as shown in Figure 6.8 (*h*)-(*i*). No considerable Fe moment is observed in the first principles calculations with spin polarized optimization taking initial high magnetic moment of Fe in both pristine and defect induced $NbSe_2$ with different supercells. This indicates enormous Fe-Se overlaps and in

contradiction of Kondo mechanism behind the suppression of superconductivity in Fe I doping case.

6.2.2.3. Spin polarization calculation:

The spin polarization in percentage is estimated using equation (6.2). Table 6.2 shows the obtainable *P* values in Fe I doping case having different supercells. The estimated *P* value for 2x2x1 supercell (smallest supercell) is 0.6102 % which is very small as represented in Table 6.2.

$$P = [(N_{\uparrow}(E_F) - N_{\downarrow}(E_F))/(N_{\uparrow}(E_F)+N_{\downarrow}(E_F))] \times 100 \quad (6.2)$$

P decreases further for bigger supercell sizes which contains smaller Fe concentration. These outcomes designate clearly the insignificant contribution from Fe magnetism in the actual experimental $NbSe_2$ sample having the smaller (*i.e.*, 0.15%) concentration of Fe atoms than the theoretical one.

Table 6.2. *Calculated values of Polarization (P) are presented for different sizes of the supercells for single Fe atom doping.*

Size of Supercell	Polarization (*P* %)
2x2x1	0.6102
2x2x2	0.2882
3x3x1	0.1730

6.2.2.4. The contour plots of charge density:

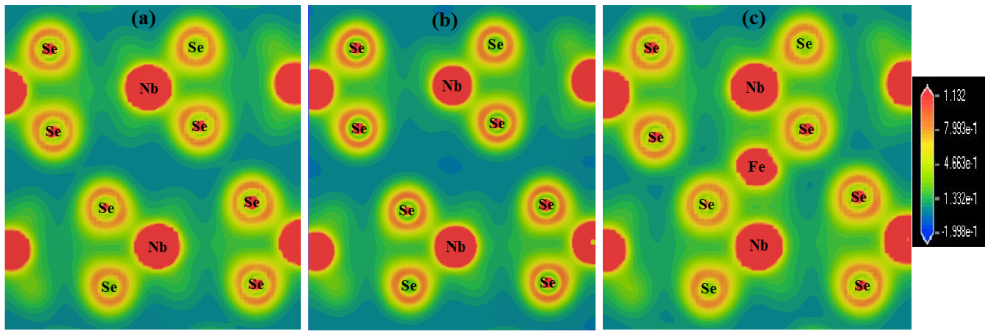

Figure 6.9. *Contour plots of charge densities of (a) undoped $NbSe_2$, (b) $NbSe_2$ with Se vacancy, and (c) $NbSe_2$ with Fe I-doping.*

Figure 6.9 shows the contour plots of charge density for both pristine and defect induced $NbSe_2$. The Se vacancy causes charge depletion between the $NbSe_2$ layers (Figure 6.9 (*b*)) in contrast to the undoped case (Figure 6.9 (*a*)). This indicates the weakening of the Van Der Waals interaction among

the $NbSe_2$ layers and degradation of T_c in $NbSe_{1.85}$ as compare to pristine $NbSe_2$. Electron Localization Function has been estimated for this purpose. We can't remark on the bonding type or charge density depending on Electron Localization Function (ELF) analysis because it gives weak clarification for extremely localized or delocalized system. Furthermore, the given charge density of ELF is with reference to that of the free electron charge density. Therefore, the charge contour plots have been deduced here using the eminent Mulliken population analysis. Additionally, we have considered four layers of NbSe in 2x2x2 supercell that gives three positions for Fe intercalation for simulation. The 2D to 3D like crossover is determined only between the layers of Fe intercalation (Figure 6.9 (*c*)). The 2D character of all the remaining layers retains almost identical characteristics as that of the undoped $NbSe_2$ (hence not exposed for brevity).

6.2.3. Transport properties:

6.2.3.1. Temperature dependent resistivity analysis:

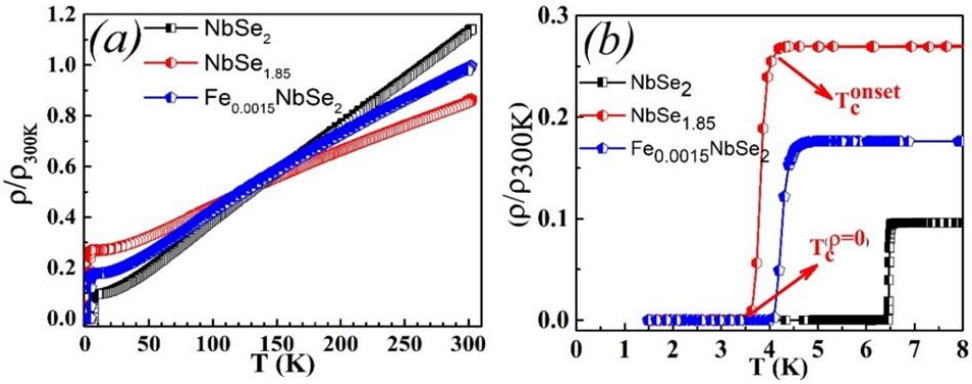

Figure 6.10. *(a) The temperature dependence of normalized resistivity of $NbSe_2$, $NbSe_{1.85}$ and $Fe_{0.0015}NbSe_2$. (b) Enlarged view near the transition region showing T_c^{onset} and $T_c^{(\rho=0)}$.*

The variations in the electronic structure associated with Se vacancy and Fe I doping in $NbSe_2$ have been examined through the room temperature resistivity measurements in $NbSe_2$, $NbSe_{1.85}$ and $Fe_{0.0015}NbSe_2$. It gives us the necessary information about the scattering mechanisms of conduction electrons due to both intrinsic and extrinsic defects. Figure 6.10 (*a*) represents the change of normalized resistivity (ρ/ρ_{300K}) as a function of temperature in $NbSe_2$, $NbSe_{1.85}$ and $Fe_{0.0015}NbSe_2$ single crystals. The

onset transition temperature (T_C^{onset}) and $T_c^{(\rho=0)}$ of $NbSe_2$ have been detected at 6.5 K and 6.4 K, respectively. It gives the clear evidence of superconducting transition. In contrast to pure $NbSe_2$, the (T_c^{onset}) & $T_c^{(\rho=0)}$ decrease to 4.3 K & 3.5 K in $NbSe_{1.85}$ and 4.6 K & 4.1 K in $Fe_{0.0015}NbSe_2$, respectively. The reduction of T_c values in the above two defect induced cases depend on the formation of different charge transfer $NbSe_2$ complexes. Matthesis *et al.* reported that the Fermi level of $NbSe_2$ is adjacent to an esteem intense peak in the plot of density of states through the band structure calculation **[53]**. Chen *et al.* shows the alternation of the intensity and the peak position because of the disorder introduced at different lattice position of $NbSe_2$ complexes **[54]**. The local disorder incorporated in $NbSe_{1.85}$ and $Fe_{0.0015}NbSe_2$ with Se vacancy and Fe I-doping causes the degradation of density of states as shown in DOS calculation of the previous section. It results the rapid reduction of T_c in both defects induced $NbSe_2$. Additionally, the temperature dependent resistivity behaviour shows metallic character in the temperature range of 10-300 K of all samples $i.e.\left(\frac{d\rho}{dT} > 0\right)$. The residual resistivity ratio (*RRR*) of the superconductors have been estimated using the relation, RRR=R (300K)/R (T_c). The *RRR* values of $NbSe_2$, $NbSe_{1.85}$, and $Fe_{0.0015}NbSe_2$ are 11, 3 and 6 calculated from Figure 6.6. Table 6.3 represents the *RRR*, T_c^{onset}, $T_c^{(\rho=0)}$ and ΔT_c values for all the samples.

These outcomes show two distinct phenomena *viz*. intrinsic (owing to the Se vacancies) and extrinsic (owing to Fe I doping) defects in $NbSe_2$. The change in parameters like T_c, ΔT_c, *RRR* values can enlighten on the lattice defects and disorder of a superconductor. A comparatively lesser value of *RRR* in $NbSe_{1.85}$ indicates the presence of defects in the conduction plane as compared to $NbSe_2$. This defect is formed caused by the short-range discontinuation of $NbSe_2$ hexagonal lattice structure due to the destruction of a little fraction of Nb-Se covalent bonds during the formation of $NbSe_{1.85}$ single crystals. It indicates alternation of trigonal prismatic coordination of Nb atoms locally and therefore, there is accumulation of unpaired electrons near the Nb^{4+} ions. This is practically equivalent to the

charge accumulation phenomena around Nb atoms associated with the structural modification in the hydrazine treated 2H-$NbSe_2$ system **[28]**.

Table 6.3. *The RRR values along with* T_c^{onset}, $T_c^{(\rho=0)}$ *and* ΔT_c *are shown below (* T_c^{onset} *and* $T_c^{(\rho=0)}$ *define the transition temperatures that are evaluated using the criteria of 90% of the normal state resistance and* $(\rho = 0)$ *of the transition region of* $NbSe_2$, $NbSe_{1.85}$ *and* $Fe_{0.0015}NbSe_2$. ΔT_c *represents the transition width, which is estimated from the differences between* T_c^{onset} *and* $T_c^{(\rho=0)}$*).*

Sample	T_c^{onset} (K)	$T_c^{(\rho=0)}$ (K)	ΔT_c (K)	$RRR = R(300\ K)/R(T_c)$
$NbSe_2$	6.5	6.4	0.10	11
$NbSe_{1.85}$	4.3	3.6	0.70	3
$Fe_{0.0015}NbSe_2$	4.6	4.1	0.50	6

Again, the lower *RRR* value of $Fe_{0.0015}NbSe_2$ designates the increase of the interband *s-d* scattering and the electron-electron scattering phenomena as compared to pure $NbSe_2$ due to Fe intercalation. Similar kind of results has been observed in Cu_xNbSe_2 as reported by Luo *et al.* **[3]**. The higher ΔT_c value is also a clear indicator of disorder in vortex lattice because the presence of disorder increases dissipative motion of flux line and thus increases the ΔT_c value. Here in this study the ΔT_c value increases significantly in both $NbSe_{1.85}$ (~ 0.7) and $Fe_{0.0015}NbSe_2$ (~ 0.5) compare to $NbSe_2$ (~ 0.1). This confirms the lattice disorder of $NbSe_{1.85}$ and $Fe_{0.0015}NbSe_2$. So, by analysing the room temperature *R-T* measurement we get information about the defect and the corresponding lattice distortion in both intrinsic and extrinsic defect induced $NbSe_2$.

6.2.3.2. Magnetoresistance Study:

The temperature dependence of electrical resistance is also studied under different external magnetic fields along the *ab*-plane for both $NbSe_2$ and defect induced $NbSe_2$ up to 8 T (Figure 6.11). In the zero applied magnetic field, the estimated T_c^{onset} of $NbSe_2$, $NbSe_{1.85}$ and $Fe_{0.0015}NbSe_2$ are 6.55 K, 4.3 K and 4.6 K, respectively, which are in agreement with the

previous room temperature resistivity studies **[55]**. As we have discussed in our previous section, the ΔT_c value of $NbSe_2$ is about 0.1 K which is practically identical to the $FeTe_{0.65}Se_{0.4}$ single crystal **[56]**. This confirms the high quality of the single crystal of $NbSe_2$.

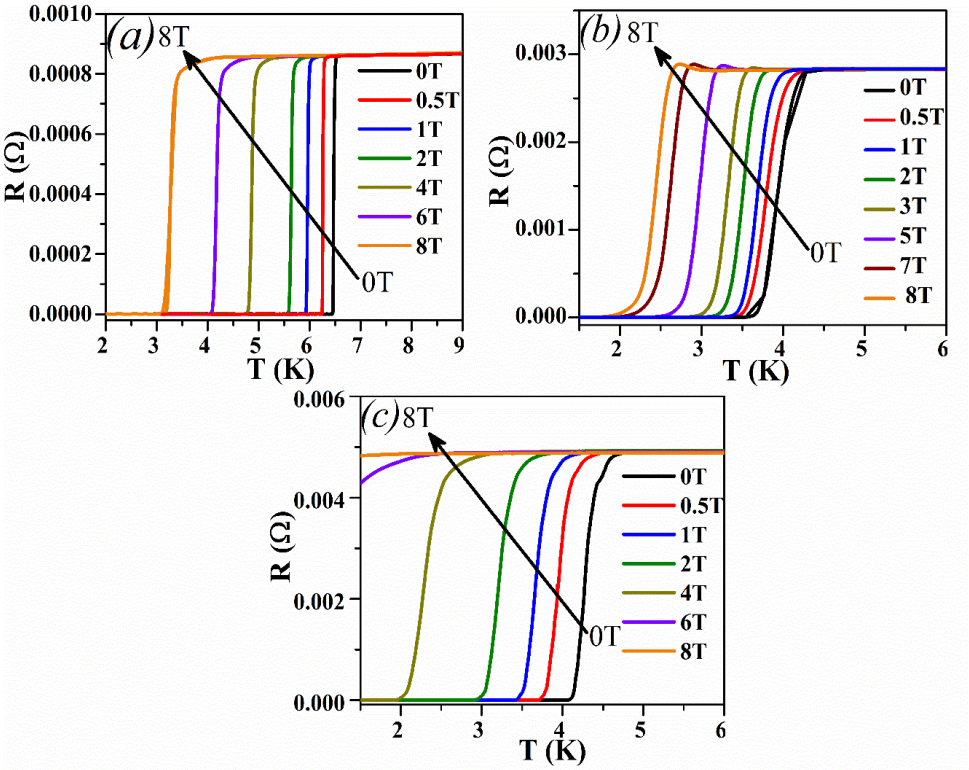

Figure 6.11. *Shows the temperature dependent resistance of (a) $NbSe_2$ (b) $NbSe_{1.85}$ and (c) $Fe_{0.0015}NbSe_2$ single crystal at different applied magnetic fields along ab - plane of crystal surface.*

However, from the magnetoresistance data we observe that both T_c^{onset} and $T_c^{(\rho=0)}$ diminish significantly due to the increasing magnetic field for both pristine and defect induced $NbSe_2$. The reduction of (T_c^{onset}) value with increasing magnetic field indicates the enhancement of the magnetic flux flow in the superconducting region of FLL. This causes the dissipation of supercurrent density in the vortex liquid phase near the transition region. However, the reduction of $T_c^{(\rho=0)}$ values with increasing magnetic field designates the degradation of TAE with the applied magnetic field which is associated with the collective creep motion of FLL and is investigated later in detail **[9, 57]**. Özçelik *et al.* has been described the absence of flux traps with the applied magnetic field in polycrystalline Bi-2212 system that results a magnetic field independent behavior of T_c^{onset}.

However, the strong intergrain transition **[58]** in this system affects the magnetic field dependence nature of $T_c^{(\rho=0)}$. Moreover, from the magnetoresistance measurement, we observe that the transition width ($\triangle T_c = \left(T_c^{onset} - T_c^{\rho=0}\right)$) increases with increasing magnetic field in both cases. The $\triangle T_c$ value appears to be broadened appreciably in $NbSe_{1.85}$ compare to $NbSe_2$ due to the inhomogeneous distribution of Se concentration which is not matched with Nb concentration. On the other hand, the widened transition region in $Fe_{0.0015}NbSe_2$ confirms the inhomogeneous distribution of Fe concentration at the nanoscale which increases the dissipative motion of flux line. In high T_c superconductor, for example, YBCO, the widening of the superconducting transition mostly happens because of the inhomogeneous distribution of labile oxygen **[59]**. Figure 6.11 (*a* - *c*) shows absence of any resistance minima or negative magnetoresistance in the temperature dependence of resistance for $Fe_{0.0015}NbSe_2$. In contrast, Kondo-like resistance minima has been represented by Whitney *et al.* **[60]** followed by negative magnetoresistance in Fe_xNbSe_2 at x = 0.005, 0.05, 0.0166 in parallel as well as perpendicular direction. The simulated electronic properties of $Fe_{0.0015}NbSe_2$ in our previous section with density functional theory support our experimental observation. It shows the negligible effect of Fe moment in Fe I doping case in all size of supercell and excludes the possibility of Kondo mechanism.

6.2.3.3. Temperature dependence of resistance in TAFF region:

Further, the temperature and magnetic field dependence of TAE have been demonstrated with Arrhenius relation and modified TAFF method to shed light on the vortex motion in transition region (*i.e.,* the TAFF region). The temperature dependence of resistance follows equation (6.3) in TAFF region due to the smaller value of J_c and $\frac{JBVL}{T} (\ll 1)$, (where L and V defines the hopping distance and the bundle volume) **[61]**.

$$R = \frac{2R_cU}{T} \exp\left(-\frac{U}{T}\right) = R_{0f} exp\left(-\frac{U}{T}\right) \quad (6.3)$$

$U(= J_{co}BVL)$ is defined here as TAE of FLL **[62, 63]** in TAFF region and $R_c(= \nu_0\, LB/J_{c0})$ represents a constant which is independent of

temperature. Considering $R_{0f}(=\frac{2R_cU}{T}) = cont.$ and linear dependency of TAE on temperature $(U(T,H) = U_0(H)\left(1-\frac{T}{T_c}\right))$, the lnR *vs.* $1/T$ graph provides the Arrhenius relation having the form of $lnR(T,H) = lnR_0(H) - U_0(H)/T$ with $lnR_0(H) = lnR_{0f} + U_0(H)/T_c$. The slope of lnR *vs.* $1/T$ curve gives the U_0 (H) value which is acknowledged as the apparent activation energy with the y intercept as $lnR_0(H)$.

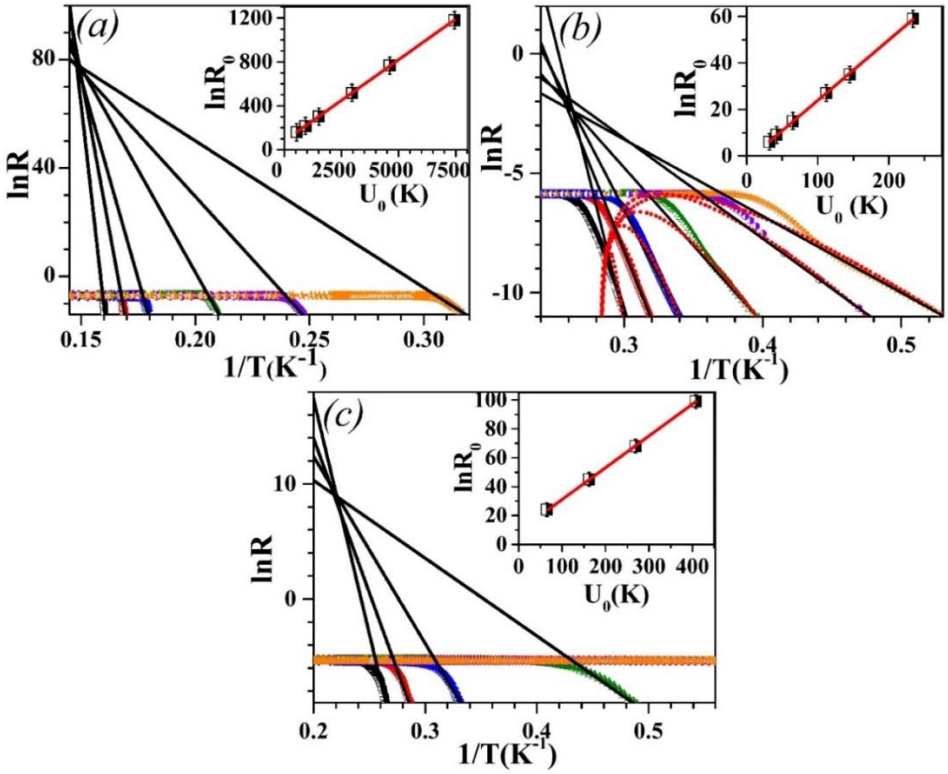

Figure 6.12. *(a) Arrhenius plot of resistance measurement for $NbSe_2$ at $H = 0.5, 1, 2, 4, 6$ and 8 T where the solid lines are linearly fitted to the TAFF region (b) The solid lines are the linear fitting to TAFF region of $NbSe_{1.85}$ and the dotted lines are the fitted curves using modified TAFF relation at $H = 0.5, 1, 2, 5, 7$ and $8\,T$ (c) Similar Arrhenius plot for $Fe_{0.0015}NbSe_2$ at $H = 0.5, 1, 2, 4T$ is shown. Insets in (a), (b) and (c) represent the linear fitting to $lnR_0(U_0)$ vs. U_0 curve derived from Arrhenius plots.*

In contrast, the nonlinear relation of TAE $(U(T,H) = U_0(H)(1-t)^q)$ with temperature is considered in modified TAFF method. It gives the resistance in the TAFF region in the form of equation (6.4). Here U_0 and R_c are acknowledged as the temperature independent parameters **[64]**.

$$lnR = ln(2R_cU_0) + qln(1-T/T_c) - lnT - U_0\,(1-T/T_c)^q/T \qquad (6.4)$$

The applicability of the Arrhenius relation and the modified TAFF method in the TAFF region of above three cases has been estimated following two methods. The first method is the extraction of T_{cross} value at the crossing point of linearly fitted lines in the TAFF regions of ln$R$ vs. 1/T graph at different magnetic fields and compare with T_c^{onset}. Another method is the estimation of inversion of the slope of linearly fitted curve to lnR_0 vs. U_0 and match with T_c^{onset}. The Arrhenius plots of pure $NbSe_2$ single crystal has been characterized in Figure 6.12 (*a*) at magnetic fields of H = 0.5, 1, 2, 4, 6 and 8 T. The U_0 values are calculated from the slopes of fitted lines to the linear regions of Arrhenius plot (as shown by the solid lines in Figure 6.12 (*a*)). The T_{cross} value is evaluated at 6.6 K which is in almost consistent with the experimental T_c^{onset} value of $NbSe_2$. The linear relationship between lnR_0 and U_0 is shown in the inset of Figure 6.12 (*a*). The inverse of the slope of the lineally fitted line to lnR_0 and U_0 curve gives the T_c value as 6.58 K which also supports the T_c^{onset} value. So, the Arrhenius plot provides the precise values of U_0 of pure $NbSe_2$ in the given temperature range. Conversely, Figure 6.12 (*b*) shows both the Arrhenius fitting and the modified TAFF fitting simultaneously of $NbSe_{1.85}$ single crystal in the TAFF regions at H = 0.5, 1, 2, 3, 5, 7 and 8 T. It demonstrates that the solid lines which are fitted linearly to the TAFF region following the Arrhenius relation don't cross accurately at the point of T_{cross}. In the other words, it is not possible get linear fitting to the TAFF region considering the point of intersection at 1/T_c. The Arrhenius plot is restricted only in a limited region of $NbSe_{1.85}$. Additionally, the T_c value estimated from the slope of the linearly fitted line to lnR_0 vs. U_0 curve don't follow T_c^{onset} value of $NbSe_{1.85}$ (as shown in the inset of Figure 6.12 (*b*)). Thus, we can say that the constant prefactor (R_{0f}) and the linear dependence of U_0 on temperature don't provide accurate values of TAE in TAFF region. Song *et al.* reported analogous restriction of Arrhenius fitting and therefore considered modified TAFF method for estimation of U_0 values in the LiFeAs single crystal **[65]**.

So, the modified TAFF method is used to estimate the TAE values of $NbSe_{1.85}$ with equation (6.4) considering three fitting parameters q, R_c and U_0 as represented by dotted red curves in Figure 6.12 (*b*). The curves,

which are fitted taking into consideration the experimental value of T_c is in good agreement with the experimental results. The U_0 values are higher than the values estimated using Arrhenius relation. The estimated q value of $NbSe_{1.85}$ is 2, enlightening the 2D like behaviour of FLL in the TAFF region. Analogous kind of 2D feature of FLL is described in Fe ($Te_{1-x}S_x$) single crystal **[66]**. Again, Figure 6.12 (*c*) represents the Arrhenius plots of $Fe_{0.0015}NbSe_2$ single crystal at the magnetic fields of H = 0.5, 1, 2, and 4 T. The T_{cross} value (4.61 K) of $Fe_{0.0015}NbSe_2$ is nearly coincide with T_c^{onset} (4.6 K). In addition, we extracted the T_c value from the inverse of slope of lnR_0 vs U_0 curve. This is comparable to T_c^{onset}. This signifies that the TAE depends linearly on temperature in $Fe_{0.0015}NbSe_2$. So, it can be concluded here that U_0 depends linearly on temperature for $NbSe_2$ and $Fe_{0.0015}NbSe_2$. The resistive dissipation occurs following to the Arrhenius relation in the TAFF region of $NbSe_2$ and $Fe_{0.0015}NbSe_2$. However, the U_0 values don't depend linearly on the temperature in $NbSe_{1.85}$ and hence, it follows the modified TAFF theory. The $NbSe_{1.85}$ behaves as the 2D system in the thermally assisted TAFF region.

6.2.3.4. Magnetic field dependence of TAE:

Figure 6.13 (*a*-*c*) shows the magnetic field dependence of U_0 of both pure and defect induced $NbSe_2$. U_0 values of $NbSe_2$, $NbSe_{1.85}$ and $Fe_{0.0015}NbSe_2$ are 4607, 1591 and 269 K at 1 T, respectively. U_0 reduces from 7512 K value (at H = 0.5 T) to 528 K value (at H = 8 T) with increasing applied magnetic field for $H \,//ab$ plane in $NbSe_2$. Similarly, U_0 drops from 1596 K value (at H = 0.5 T) to 48 K value (at H = 8 T) in case of $NbSe_{1.85}$ for $H \,//ab$ plane. Analysing the above data, we observe that the U_0 value of $NbSe_{1.85}$ is appreciably small as compare to $NbSe_2$. This is because of the presence of phase incoherent superconducting state which is associated with the thermal fluctuation of order parameter of $NbSe_{1.85}$ around Se vacancies **[8]**. In contrast, the U_0 value reduces from 411 K (at H = 0.5 T) to 66 K (at H = 4 T) in $Fe_{0.0015}NbSe_2$ single crystal. So, the U_0 values of $Fe_{0.0015}NbSe_2$ are reduced to even lower values compare to $NbSe_{1.85}$. This significant reduction of U_0 of $Fe_{0.0015}NbSe_2$ indicates the virtual polarization of Fe impurities in the singlet bound state **[67]**.

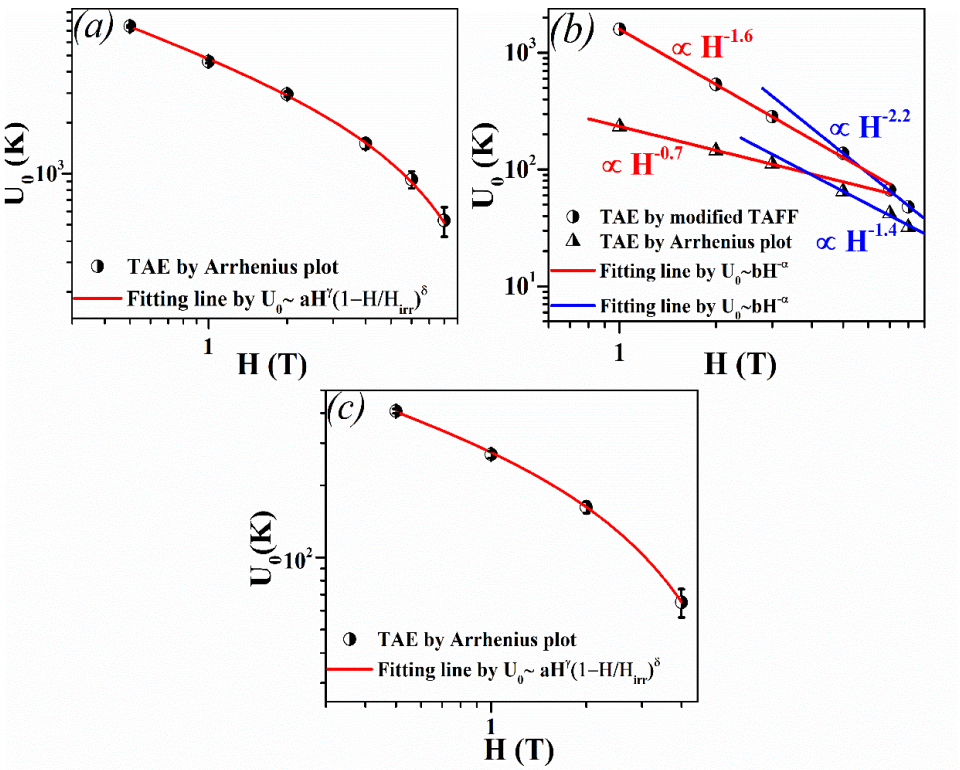

Figure 6.13. *Apparent activation energy is plotted against magnetic field H for (a) $NbSe_2$ (b) $NbSe_{1.85}$ (c) $Fe_{0.0015}NbSe_2$ single crystal on log – log scale. The field dependence of U_0 of $NbSe_2$ and $Fe_{0.0015}NbSe_2$ in (a) and (c) are fitted with $U_0(H) \sim H^{\gamma}(1 - H/H_{irr})^{\delta}$ relation whereas the solid lines in (b) represents power-law fitting with $U_0(H) \sim H^{-\alpha}$.*

Furthermore, Figure 6.13 (*a-c*) represents the magnetic field dependence of U_0 in $NbSe_2$, $NbSe_{1.85}$ and $Fe_{0.0015}NbSe_2$. Figure 6.13 (*a*) shows the parabolic dependence U_0 on applied magnetic field which has the form of equation (6.5).

$$U(H) = aH^{\gamma}\left(1 - (H/H^{*})\right)^{\delta} \tag{6.5}$$

Here H^{*} is defined as the Kramer's scaling magnetic field **[68]** which have same order of magnitude as H_{irr} and a, γ, δ designate the scaling parameters of equation (6.5). Here, $\left(1 - (H/H^{*})\right)^{\delta}$ considers the destruction of the superconducting region in presence of magnetic field and the term, aH^{γ} is associated with the degradation of J_c characteristics caused by the collective creep motion of magnetic flux lines. The fitting parameters, extracted from Figure 6.13 (*a*), have the values a =1057 K, γ = - 0.78, δ = 1.7 with a goodness of fit R^2 = 0.989. These outcomes are similar to the results reported by Kaushik *et al.* **[14]**. Patnaik *et al.* also reported the similar kind of parabolic dependence of U_0 on applied magnetic field which is caused by the grain boundary pinning **[69]**. In our case, the magnetic fluxes entering

the $NbSe_2$ crystal try to align themselves parallel to the Nb-Se-Nb layer resulting the strong surface pinning along *ab* direction **[45]**.

We compare the U_0 values of $NbSe_{1.85}$ in Figure 6.13 (*b*) estimated from both modified TAFF relation and Arrhenius relation. The U_0 values vary significantly at each magnetic field. It can be realized that both curves follow power law dependence with applied magnetic field in the form of equation (6.6).

$$U_0(H) \sim H^{-\alpha} \tag{6.6}$$

Here α is defined as the fitting parameter in the above equation. U_0 values, which are estimated from modified TAFF analysis follows $H^{-1.6}$ relation at low magnetic fields (till 3 T) whereas it follows $H^{-2.2}$ relation at elevated magnetic fields (higher than 3 T). Conversely, U_0 values determined from Arrhenius relation, follows $H^{-0.7}$ relation at the low field region (till 3 T) and $H^{-1.4}$ relation at elevated magnetic field region (higher than 3 T). According to the plastic-flux-creep-theory, the weak pinning causes distortion of the vortex lattice which results entanglement of the vortices and the reduction of U_0 value with the external magnetic field following to the relation $U_0 \propto H^{-0.5}$ **[70, 71]**. As the magnetic field increases, the vortices move rapidly resulting the cutting of the entangled vortices. This causes degradation of the transverse correlation length of FLL. In this region, the U_0 value follows the relation $U_0 \propto H^{-0.7}$ **[72]**. Even quicker degradation of U_0 with external magnetic field hints the presence of strong pinning with the entangled vortex liquid behaviour. The exponents of the power law dependence of $NbSe_{1.85}$ have higher values than the probable values of plastic weak creep model at low as well as high magnetic fields. This designates the appearance of strong pinning associated with plastic creep motion in $NbSe_{1.85}$. Figure 6.13 (*b*) shows a crossover field (~ 3 T) that divides the plastically deformed vortex lattice from more entangled state. The BSCCO single crystals show similar type of crossover field at elevated magnetic fields as reported by Wang *et al.* **[73]**. Additionally, Choi *et al.* reported the crossover magnetic field associated with two different α value due to the evolution of FLL from collective pinning region to plastic

pinning region in $NaFe_{1-x}Co_xAs$ (where x = 0.01, 0.03, and 0.05) single crystals **[74]**.

In contrast, Figure 6.13 (*c*) shows the parabolic dependence of U_0 of $Fe_{0.0015}NbSe_2$ in response of external magnetic field following the equation (6.6). The corresponding parameters that are needed to fit the U_0 *vs. H* curve are a =370 K, γ = - 0.48, δ = 1.8 resulting a goodness of fit R^2 = 0.991. Depending on the previous literature survey, the parabolic degradation of U_0 with applied magnetic field suggests that the FLL is elastically deformed in $Fe_{0.0015}NbSe_2$ **[8]**. This indicates the variation of dependence of U_0 values on applied magnetic field appears due to the presence of different defect concentrations and scattering centres in $NbSe_2$ **[75]**. So, the faster degradation of U_0 with magnetic field following the power law is concluded as the strong plastically deformed vortex lattice in $NbSe_{1.85}$. In contrast, the comparably slow reduction of U_0 in response of external magnetic field is concluded as the elastically deformed FLL in $NbSe_2$ and $Fe_{0.0015}NbSe_2$.

6.2.4. Magnetic properties:

6.2.4.1. Temperature dependent magnetization analysis:

The variation in the superconducting transitions with increasing magnetic fields for both extrinsic and intrinsic defect induced $NbSe_2$ is further examined through temperature dependence of magnetization measurements. Figure 6.14 (*a*) shows the *dc* magnetization curves of $NbSe_{1.85}$ following the protocol of both ZFC and FC in presence of 0.005 T, 0.01 T, 0.05 T and 0.1 T magnetic fields at 2 K to 8 K temperatures. The prominent diamagnetic transition that is induced by supercurrent is confirmed from the sharp drop of the ZFC curves from zero magnetization value. Figure 6.14 (*a1*) shows the dc susceptibility curve of $NbSe_{1.85}$ indicating both ferromagnetic (T_{FM}) and superconducting (T_c) transition at ~ 3.9 & 3.5 K, ~ 3.2 K & 3 K, and ~ 3 & 2.4 K (as shown in Table 6.4) in response of external magnetic field of 0.005 T, 0.01 T and 0.1 T, respectively. The upward turn of the dc susceptibility curve of $NbSe_{1.85}$ designates the FM transition. Li *et al.* **[76]** reported similar kind of transitions associated with the SC and FM phenomena in $Sr_{0.5}Ce_{0.5}FBiS_2$

superconductor. These outcomes confirm the appearance of both SC and FM ordering in $NbSe_{1.85}$.

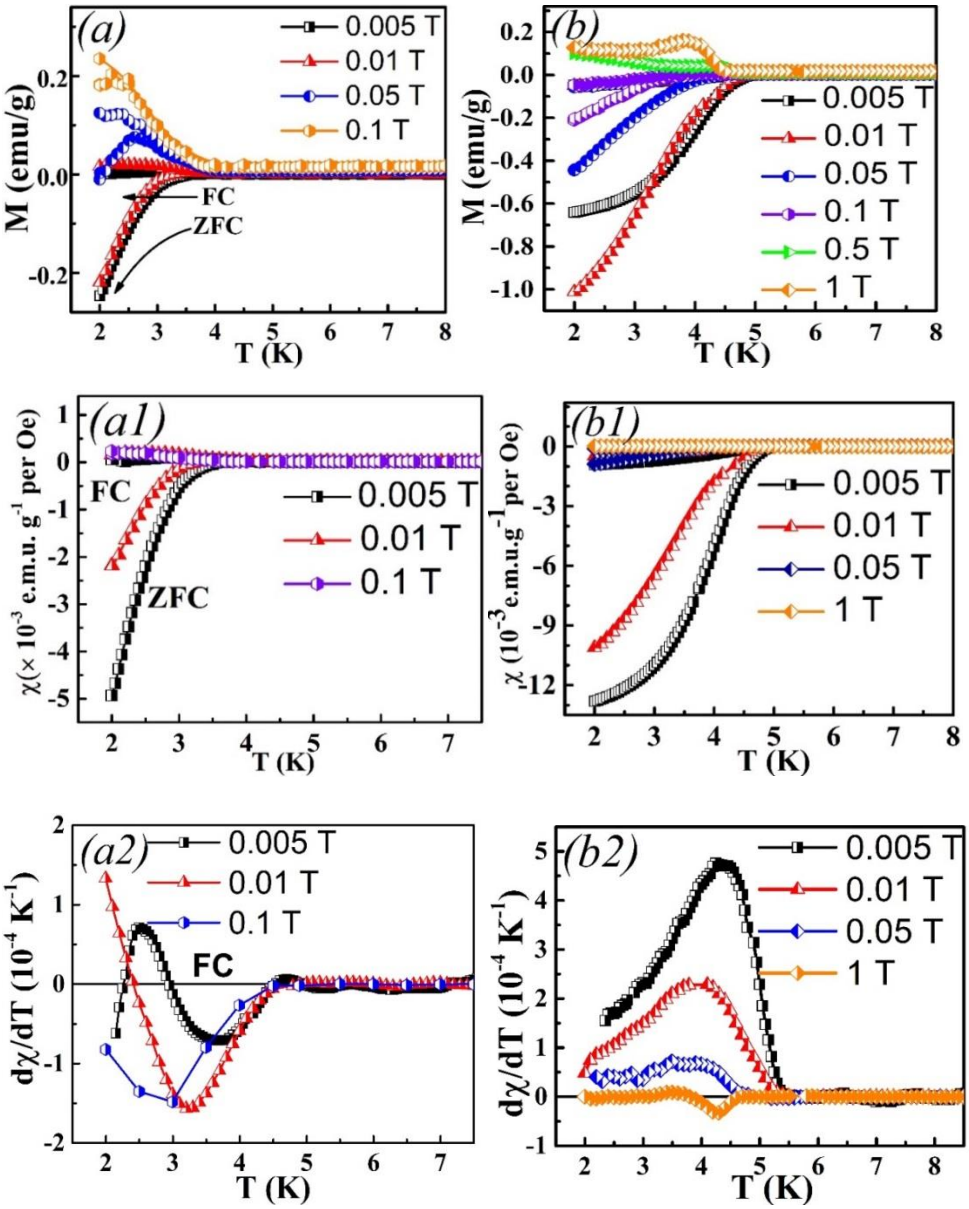

Figure 6.14. *Represents the temperature dependence of magnetization curves of* ***(a)*** *$NbSe_{1.85}$ and* ***(b)*** *$Fe_{0.0015}NbSe_2$ at different applied magnetic fields.* ***(a1)*** *$NbSe_{1.85}$ and* ***(b1)*** *$Fe_{0.0015}NbSe_2$ are DC susceptibility measurement data at H= 0.005T, 0.01T, 0.1T, 0.05T and 1 T magnetic fields;* ***(a2) & (b2)*** *show temperature dependence of derivative plots of $NbSe_{1.85}$ and $Fe_{0.0015}NbSe_2$ at selective applied magnetic fields.*

Additionally, the isothermal magnetization measurement data is represented in the next section which discusses elaborately the concurrence of FM and SC in $NbSe_{1.85}$ system. Figure 6.14 (*a1*) shows the weak drop (~ 2.4 K) of the ZFC curve in susceptibility measurement data connected to

the diamagnetic signal indicates the presence of the weak superconductivity in $NbSe_{1.85}$ at 0.05 T magnetic field. The derivative plots of susceptibility measurement as shown in Figure 6.14 (*a2*) establish the values of T_c and T_{FM} at different magnetic fields which point towards the degradation of T_c in $NbSe_{1.85}$ with increasing magnetic fields. Additionally, the coextistence of SC and FM has been reported by Pachmayr *et al.***[18]** in the $[(Li_{1-x}Fe_x)OH](Fe_{1-y}Li_y)Se$ superconduting system, which demonstrates T_c (~43 K) >> T_{FM} (10 K). However, comparable to the $Sr_{0.5}Ce_{0.5}FBiS_2$ system, our sample show T_c (3.5K at 50 Oe) < T_{FM} (3.9K at 50 Oe) which is associated with the itinerant ferromagnetic state **[77]**. This implies that the 4*d* electrons of Nb atoms might be play the role of itinerant electrons that are intensely interacting with each other and accountable for both superconductivity and ferromagnetism in $NbSe_{1.85}$.

However, this ferromagnetic states appears as the magnetic domains that are short range in nature. This is reasonable to assume that the random defect configuration associated with Se vacancy causes the short range magnetic domains in $NbSe_{1.85}$ and it is usually lesser than the long range spin-ordered coherent state as described by Menard *et al* **[78]**.

Figure 6.14 (*b*) represents the distinctive curves of the *dc* magnetization as a function of temperature in $Fe_{0.0015}NbSe_2$ single crystal following ZFC and FC methods in presence of 0.005 T, 0.01 T, 0.05 T, 0.1 T, 0.5 T and 1 T magnetic fields. The sharp superconducting transition designates the high-quality of the $Fe_{0.0015}NbSe_2$ crystals. There is no upward turn in the χ-T curve of $Fe_{0.0015}NbSe_2$ as shown in Figure 6.14 (*b1*), therefore simply representing the superconducting transitions in both ZFC and FC processes. This eliminates the occurrence of both superconducting and ferromagnetic transition in $Fe_{0.0015}NbSe_2$. Table 6.4 represents the variation in the T_c values of $NbSe_{1.85}$ and $Fe_{0.0015}NbSe_2$ with increasing magnetic fields. Similar trends of degradation in T_c are noticed in $Fe_{0.0008}NbSe_2$ and $Fe_{0.0011}NbSe_2$ superconductors in our previous studies **[45]**. However, Figure 6.14 (*b2*) shows the T_{FM} transition at 4.3 K in the derivative plot of susceptibility measurement at the magnetic field of 1 T. This reveals the ferromagnetic ordering in $Fe_{0.0015}NbSe_2$ at 1 T induced by

Fe impurities. So, we can conclude that the incorporation of small amount of external impurities may result the ferromagnetic transition after T_c. Furthermore, our previous studies on the magnetization plots of $NbSe_2$ indicate that there is no anomaly associated with the ferromagnetic transition at low as well as higher magnetic fields **[45, 79]**.

Table 6.4. *The variation of T_c values with external magnetic fields in $NbSe_{1.85}$ and $Fe_{0.0015}NbSe_2$ single crystals from magnetization studies.*

Sample	$T_c(K)$ (@0.005 T)	$T_c(K)$ (@0.01 T)	$T_c(K)$ (@0.1)	$T_c(K)$ (@1 T)
$NbSe_{1.85}$	3.5	3.0	2.4	NA
$Fe_{0.0015}NbSe_2$	4.9	4.8	3.8	NA

6.2.4.2. Upper limit of superconductivity:

The upper limit of critical magnetic field at 0 K *i.e.* H_{c2} (0) values of $NbSe_{1.85}$ and $Fe_{0.0015}NbSe_2$ have been estimated from the temperature dependence of magnetization measurement. Figure 6.15 represents the H_{c2} (T) *vs.* T curve that is fitted with Ginzburg-Landau (*G-L*) formula reflecting the anisotropic characteristics of Nb bands around the Fermi surface **[80]**. Table 6.5 summarizes the estimated H_{c2} (0) values of $NbSe_{1.85}$ and $Fe_{0.0015}NbSe_2$ which are lesser than $NbSe_2$ **[45]** as reported in the previous chapter. The $H_{c2}^{orb}(0)$ values of both samples are found as 0.098 T (for $NbSe_{1.85}$) and 0.49 T (for $Fe_{0.0015}NbSe_2$) with the initial slopes (dH_{c2}/dT) as shown in Table 6.5 (from the H_{c2} (T) *vs.* T curve). We use the previously described WHH empirical model to estimate the $H_{c2}^{orb}(0)$ values. The $H_{c2}^{orb}(0)$ values indicate the robust influence of spin-orbital coupling in the pair breaking phenomena of both intrinsic and extrinsic defect induced $NbSe_2$ in presence of external magnetic fields. However, the H_p (0) values of $NbSe_{1.85}$ and $Fe_{0.0015}NbSe_2$ extracted following the relation, H_p (0) = $1.84T_c$ of BCS (Bardeen-Cooper-Schrieffer) **[81, 82]** superconductor are also listed in Table 6.5. The H_p (0) values of both superconductors show higher value than the estimated H_{c2} (0). This suggests that Pauli

paramagnetic pair breaking mechanism has insignificant influence in estimating the upper limit of critical field in $NbSe_{1.85}$ and $Fe_{0.0015}NbSe_2$.

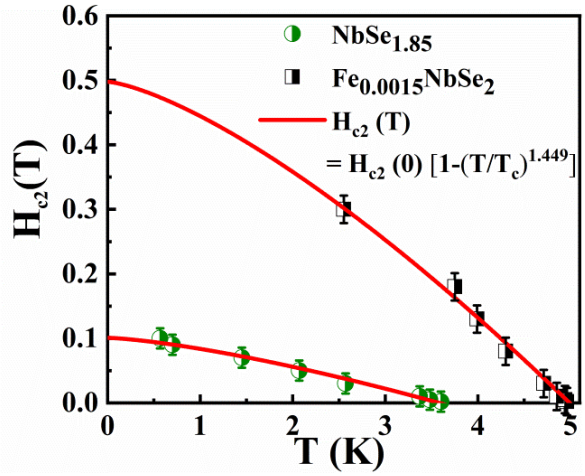

Figure 6.15. *Display the temperature dependence of upper critical field (H_{c2}) and the corresponding fitting using Ginzburg-Landau formula* $\left(H_{c2}(T) = H_{c2}(0)\left(1-\left(\frac{T}{T_c}\right)^{1.449}\right)\right)$.

Therefore, orbital pair breaking mechanism is leading the pair breaking phenomena with increasing magnetic fields for both defects induced $NbSe_2$. The estimated ξ_{GL} (0) values of $NbSe_{1.85}$ and $Fe_{0.0015}NbSe_2$ are represented in Table 6.5.

Table 6.5. *The H_{c2} (0), $H_{c2}^{orb}(0)$, $H_p(0)$ and ξ_{GL} (0) values of $NbSe_{1.85}$ and $Fe_{0.0015}NbSe_2$ are summarized.*

Sample	$H_p(0)$ (T)	$H_{c2}^{orb}(0)$ (T)	H_{c2} (0) (T)	$\xi_{GL}(0)$ (nm)
$NbSe_{1.85}$	6.5	0.09	0.1	57
$Fe_{0.0015}NbSe_2$	9.2	0.49	0.5	25

These outcomes indicate the influence of weak coupling superconductivity similar to the conventional low T_c superconductors. The considerable reduction in H_{c2} (T) values reveals that the disorder, introduced with the Se vacancy and Fe impurities, appear destructive to the superconducting characteristics of $NbSe_2$. This gives the hints of variation in spin-orbit interaction in $NbSe_{1.85}$ through the modifications of its 2D characteristics. Conversely, the comparably small H_{c2} (0) value of

$Fe_{0.0015}NbSe_2$ designates the variations in intrinsic Ising spin-orbit coupling **[83]**.

6.2.4.3. Hysteresis loop (*M vs. H*) analysis:

Figure 6.16 represents the *M vs. H* plots of $NbSe_{1.85}$ and $Fe_{0.0015}NbSe_2$ at 2 K, 2.5 K, 3 K, 3.5 K, 5 K and 5.5 K temperatures. Figure 6.16 (*a*, *b*) reveals the hysteresis loop curves containing both reversible and irreversible magnetization associated with superconductivity of $NbSe_{1.85}$ and $Fe_{0.0015}NbSe_2$ single crystals. A ferromagnetic hysteresis loop is seemed to be overlapped with the superconducting hysteresis loop at 2 K temperature in $NbSe_{1.85}$ as seen in Figure 6.16 (*a*). This unveils the outstanding concurrence of FM and SC phenomena in $NbSe_{1.85}$. The existence of the dual loop indicates the two ordered states (*i.e.* FM and SC) which are solely linked to the Se defects. This comprehends the novel characteristics of this material.

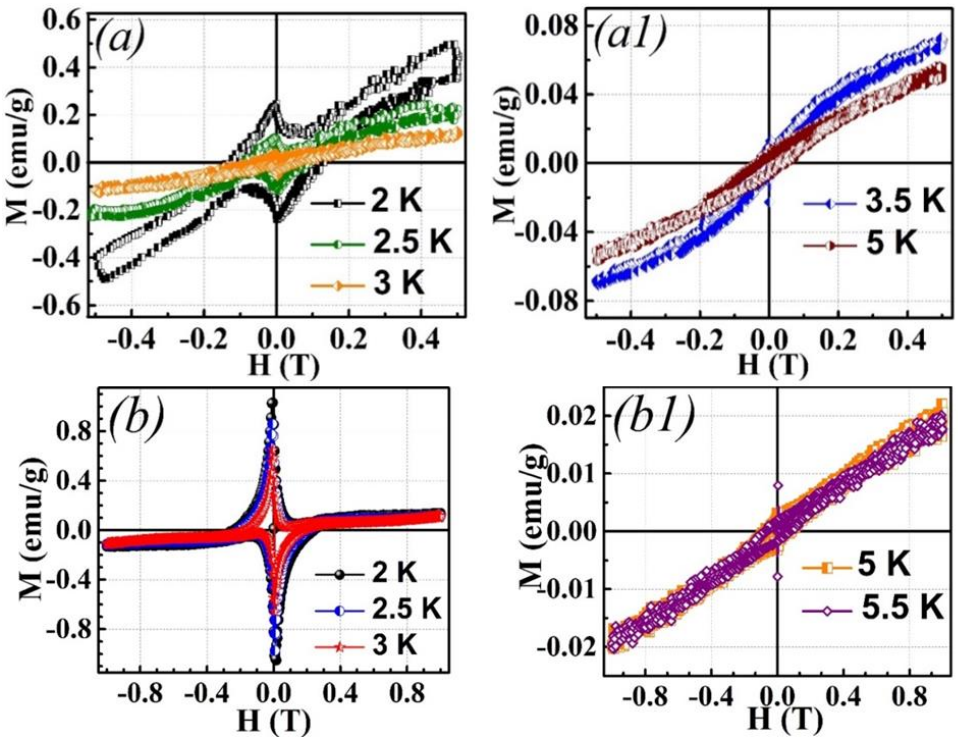

Figure 6.16. *Shows the M-H loops,* ***(****a, a1****)*** *for* $NbSe_{1.85}$ *and* ***(****b, b1****)*** *for* $Fe_{0.0015}NbSe_2$ *at different temperatures.*

In contrast, the ferromagntic superconductor such as UCoGe shows the coexistence of SC and FM. However, there is no superposition between the ferromagnetic and superconducting hysteresis loops in the hysteresis

curve of UCoGe **[84]**. The bulk superconductivity leads at the low magnetic field region in $NbSe_{1.85}$ till 0.07 T and after that the diamagnetic signal is being weakened by the ferromagnetic ordering at 2 K temperature. The *M vs. H* curve of $NbSe_2$ doesn't show any ferromagnetic hysteresis loop **[45]**. Thus, Se-defect results fundamental modifications in the superconducting and magnetic characteristics of the parent material $NbSe_2$. Further, Figure 6.16 (*a1*) shows the superconductivity survives till 0.005 T at 3.5 K. After 0.005 T, there is a complete destruction of superconductivity in $NbSe_{1.85}$. Consequently, the hysteresis curve only represents the ferromagnetic hysteresis loop. This outcome agrees with the *M-T* data as discussed in our previous section. Again, the presence of minor hysteresis loop at 5 K temperature in *M-H* plot impling the weak ferromagnetism in $NbSe_{1.85}$. Surprisingly Figure 6.16 (*b*, *b1*) shows no such kind of overlapping between SC and FM phenomena in the *M-H* hysteresis loop of $Fe_{0.0015}NbSe_2$. At the temperatures of 2 K and 3 K, the superconductivity of $Fe_{0.0015}NbSe_2$ exists only upto low magnetic fields but the densities of Cooper pair electrons are destroyed rapidly with incresing magntic fields. Thus, $Fe_{0.0015}NbSe_2$ only shows paramagnetic nature after T_c. At 5 K and 5.5 K temperatures, the *M vs. H* curve of $Fe_{0.0015}NbSe_2$ displays almost linear behaviour with external magnetic fields with insignificant hysteresis loop as shown in Figure 6.16 (*b1*). The *M* vs. *H* curve of ferromagnetic materials display a linear characteristics at low magnetic fields and a saturation nature at higher magnetic fields described via a saturation field. The saturation field controls the range of the magnetic field which shows the linear behaviour of the magnetization curve. The minor hysteresis loops at low magnetic fields might be appear due to ferromagnetism at higher temperatures, though, it is identical in both $NbSe_{1.85}$ and $Fe_{0.0015}NbSe_2$ and may be consequences of the experimental issues. These results hereafter confirm that the *M vs H* curves of $NbSe_{1.85}$ comprise of both SC and FM characteristics. The Se defects incorporate magnetic moments in $NbSe_{1.85}$ that is short range in order. In contrast, the hysteresis curves of $Fe_{0.0015}NbSe_2$ contain only superconducting characteritics. Consequently it didn't show any localized magnetic moments in $Fe_{0.0015}NbSe_2$ and disdain the coexistence of SC with FM characteristics in extrinsically defect induced $NbSe_2$.

6.2.4.4. Pure Superconducting (Meissner) state:

Figure 6.17 shows the $H_{c1}(T)$ values of $NbSe_{1.85}$ and $Fe_{0.0015}NbSe_2$, which are calculated from the *M-H* curves representing the lower limit of mixed state at different tempeartures. Below H_{c1} value, a superconductor remains in the Meissner state which represents the pure superconducting state having the maximum value of superconducting order parameter in the entire bulk. Figure 6.17 (*a*, *b*) shows the temperature dependence of $H_{c1}(T)$ values which are well fitted with the equation, $H_{c1}(T) = H_{c1}(0)\left(1 - \left(\frac{T}{T_c}\right)^2\right)$. This denotes the BCS type superconductivity of both $NbSe_{1.85}$ and $Fe_{0.0015}NbSe_2$ dissimilar to the MgB_2 superconductor having linear dependence of $H_{c1}(T)$ on temperature **[85]**.

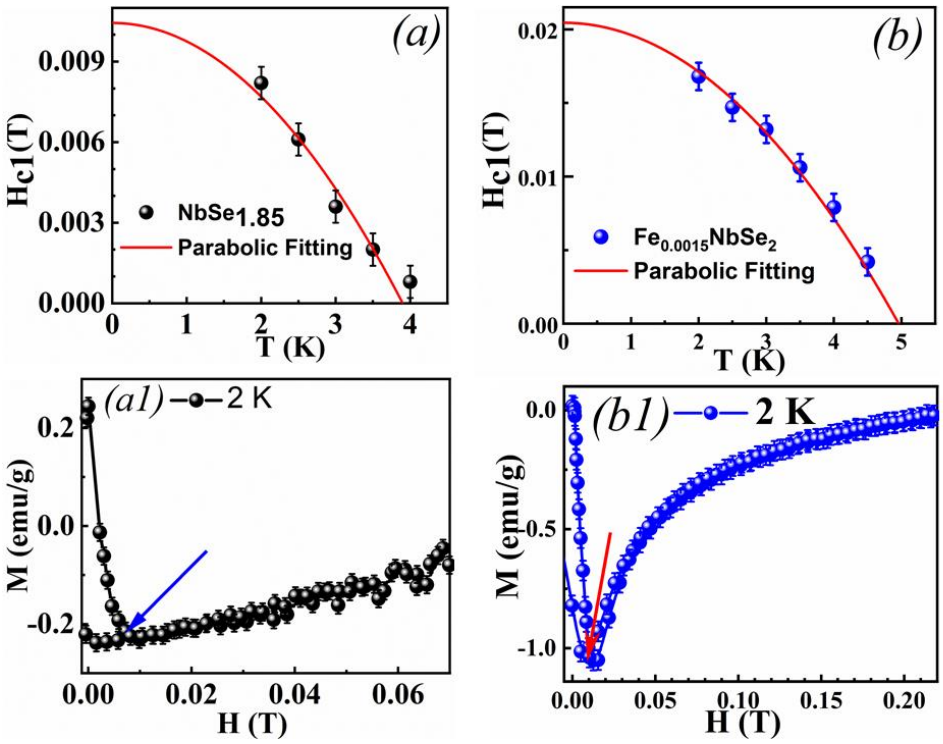

Figure 6.17. *Shows the temperature dependence behaviour of $H_{c1}(T)$ of (a) $NbSe_{1.85}$ and (b) $Fe_{0.0015}NbSe_2$ and the red solid line indicates parabolic fitting using the relation, $H_{c1}(T) = H_{c1}(0)\left(1 - \left(\frac{T}{T_c}\right)^2\right)$. Fig. (a1) & (b1) represent the estimated values of $H_{c1}(T)$ at 2 K temperature and is indicated by red arrows.*

Figure 6.17 (*a1*, *b1*) demonstrate the linear region of magnetization curves as the Meissner state (as represented by the red solid line) and the arrows indicate the H_{c1} values at the deviation of the *M-H* curve from

linearity in the immensely small field region at 2 K temperature. The $H_{c1}(0)$ value might be influenced with the demgnetization factor. The complete evaluation of the demagnetization factor are reported in Cu_xNbSe_2 and $Cr_{0.0005}NbSe_2$ **[3, 86]**. So, both samples, $NbSe_{1.85}$ and $Fe_{0.0015}NbSe_2$ preserve convensional (BCS type) superconductivity similar to $NbSe_2$ despite of having structural defect. So, the *M* - *T* curves successfully represent the FM and SC transition temperatures of $NbSe_{1.85}$. Further, the *M-H* curve addresses the coexistence of FM and SC in $NbSe_{1.85}$. The structural modifications of the crystal structure associated with Se defect induce moments in $NbSe_{1.85}$ in an otherwise nonmagnetic superconductor. $Fe_{0.0015}NbSe_2$ severely diminishes the Cooper pair electron densities by increasing the scattering phenomena and thus, expresses the paramagnetic nature above T_c. This indicates that the structural alteration introduced by external defects with foreign Fe impurities don't induce any localized magnetic moment in $NbSe_2$.

6.3. Summary

The influence of defects that are created in $NbSe_2$ via intrinsic (*i.e.* Se vacancy) and extrinsic method (*i.e.* Fe incorporation) have been studied effectively through structural, electronic, magnetoresistance and magnetization measurements. The structural analysis accomplished by XRD data shows all the samples are highly crystalline in nature with hexagonal structure, corresponding to the space group P63/mmc. The increase of "*c*" lattice parameter with Fe doping gives the hints of intercalation of Fe atoms between the Nb-Se-Nb layers. Room temperature resistivity measurements provide strong evidence about the existence of intrinsic and extrinsic defects in $NbSe_{1.85}$ and $Fe_{0.0015}NbSe_2$ single crystals. Lower RRR and higher ΔT_c values indicate the presence of disorder or impurities in the conduction bands. The variation in the numbers of bands across the Fermi level of $NbSe_2$ superconductor has been nicely exposed by Kohn-Sham density functional theory with inducing the Se vacancy as well as Fe intercalation at the different lattice positions of the hexagonal crystal structure. DOS analysis shows that the metallic properties and the T_c values of $NbSe_{1.85}$ and $Fe_{0.0015}NbSe_2$ are extremely reduced in contrast to pure

$NbSe_2$. It is because of the decrease of partial density of state associated with Nb 4d orbital electrons. These electrons are mostly accountable for the superconductivity of $NbSe_2$. The spin polarized optimization does not result any considerable Fe moment in $Fe_{0.0015}NbSe_2$ in the first principles calculations. This recommends the extreme overlapping of Fe and Se orbitals and contradicts the occurrence of the Kondo mechanism behind the suppression of superconductivity in $Fe_{0.0015}NbSe_2$. Contour plots of charge densities of $NbSe_{1.85}$ show the charge depletion between the $NbSe_2$ layers due to presence of Se related defect. It confirms that the Se vacancy weakens the Van Der Walls interaction between the interlayers of $NbSe_2$. However, the Fe intercalation results 2D to 3D crossover between the layers of Fe incorporation. Further, the magnetoresistance measurements of all samples represent the change in the superconducting properties, especially in the transition region (*i.e.* the TAFF region) with defect incorporation. Arrhenius relation and modified TAFF model were used to investigate the temperature dependence behaviour of resistance in the TAFF region of $NbSe_2$, $NbSe_{1.85}$ and $Fe_{0.0015}NbSe_2$ single crystals. The modified TAFF method gives reasonable values of TAE in $NbSe_{1.85}$ that signifying the nonlinear characteristics of TAE on temperature. $NbSe_{1.85}$ behaves as 2D FLL in TAFF region. Furthermore, TAE shows different magnetic field dependence characteristics in intrinsic and extrinsic defect induced $NbSe_2$. TAE displays parabolic nature in response of magnetic field in $NbSe_2$ and $Fe_{0.0015}NbSe_2$. However, in contrast to $NbSe_2$, $NbSe_{1.85}$ has lower TAE values which show power law dependence on the magnetic field. The lower TAE value is ascribed to the enhancement of thermal fluctuation around the Se defects. The Se defect behaves as strong pinning centres in $NbSe_{1.85}$ causing 2D plastic creep in the TAFF region. Additionally, the modifications of the lattice structure caused by Se deficiency and Fe impurities also influence the magnetic properties in $NbSe_2$. $NbSe_2$ appears as a self-supporting system which shows the coexistence of SC and FM in presence of intrinsic defect. The intrinsic defects cause distortion of FLL around the Se vacancies which decrease the covalent interactions among the Nb and Se atoms. This strengthens the unpaired electron densities near the Nb ions and therefore, ensuing FM order which is short range in nature.

Besides, the extrinsic defect that is introduced with Fe intercalation diminishes superconductivity significantly because of the enhancement of interband scattering. The *M-H* curves of $Fe_{0.0015}NbSe_2$ at different temperatures show no sign of coexistence of FM and SC characteristics. $Fe_{0.0015}NbSe_2$ represents the paramagnetic characteristics after T_c and at the elevated temperatures. This can be concluded that the method of modifications of electronic, resistive and magnetic properties *via* incorporation of intrinsic and extrinsic defects will recommend several ingenious ways for the examination of various coexisting electronic, resistive and magnetic properties in correlated systems.

References

[1] Li H., Chen L., Zhang K., Liang J., Tang H., Li C., Liu X., Meng J., Wang Z. (2014), Atomic structures and electronic properties of 2H-$NbSe_2$: The impact of Ti doping, J. Appl. Phys., 116, 103709.

[2] Morris R. C., Young B. W., Coleman R. V. (1974), Anisotropic Kondo resistance in Fe doped $NbSe_2$, AIP Conf. Proc., 18, 292.

[3] Luo H., Nowak J. S., Li .J, Tao J., Klimczuk T., Cava R. J. (2017), S-shaped suppression of the superconducting transition temperature in Cu-intercalated $NbSe_2$, Chem. Mater., 29, 3704-3712.

[4] Iavarone M., Di Capua R., Karpetrov G., Koshelev A. E., Rosenmann D., Claus H., Malliakas C. D., Kanatzidis M. G., Nishizaki T., Kobayashi N. (2008), Effect of magnetic impurities on the vortex lattice properties in $NbSe_2$ single crystals, Phys. Rev. B, 78, 174518.

[5] Coleman R. V., Fleming R. M., Whitney D. A., Domb E. R., Sellymer D. J. (1976), Localized moments and magnetic interactions in Fe-doped layer compounds $NbSe_2$ and $TaSe_2$, AIP Conf. Proc., 29, 400-401.

[6] Hillenius S. J., Coleman R. V., Domb E. R., Sellmyer D. J. (1979), Magnetic properties of iron-doped layer-structure dichalcogenides, Phys. Rev. B, 19, 4711-4722.

[7] Lian C. S., Si C., Duan W. (2018), Unveiling charge-density wave, superconductivity, and their competitive nature in two-dimensional $NbSe_2$, Nano Lett., 18, 2924-2929.

[8] Blatter G., Feigel'man M. V., Geshkenbein V. B., Larkin A. I., Vinokur V. M. (1994), Vortices in high-temperature superconductors, Rev. Mod. Phys., 66, 1125-1388.

[9] Anderson P. W. (1962), Theory of flux creep in hard superconductors, Phys. Rev. Lett., 9, 309-311.

[10] Kim Y. B., Hempstead C. F., Strnad A. R. (1965), Flux-flow resistance in type-II superconductors, Phys. Rev. Lett., 139, A1163-A1172.

[11] Tinkham M. (1964), Viscous flow of flux in type ii superconductors, Phys. Rev. Lett., 13, 804-807.

[12] Kim J. J., Lee H. K., Chung J., Shin H. J., Lee H. J., Ku J. K. (1991), Flux-creep dissipation in epitaxial $YBa_2Cu_3O_{7-\delta}$ film: Magnetic-field and electrical-current dependence, Phys. Rev. B 43, 2962-2967.

[13] Palstra T. T. M., Batlogg B., Schneemeyer L. F., Waszczak J. V. (1988), Thermally activated dissipation in $Bi_{2.2}Sr_2Ca_{0.8}Cu_2O_{8+\delta}$, Phys. Rev. Lett., 61, 1662-1665.

[14] Kaushik S. D., Braccini V., Patnaik S. (2008), Magnetic field dependence of vortex activation energy: A comparison between MgB_2, $NbSe_2$ and $Bi_2Sr_2Ca_2Cu_3O_{10}$ superconductors, Pramana, 71, 1335-1343.

[15] Coronado E., Gastaldo C. M., Moratalla E. N., Ribera A., Blundell S. J., Baker P. J. (2010), Coexistence of superconductivity and magnetism by chemical design, Nat. Chem., 2, 1031-1036.

[16] Linder J., Robinson J. W. A. (2015), Superconducting spintronics, Nat. Phys., 11, 307-315.

[17] Li L., Richter C., Mannhart J., Ashoori R. C. (2011), Coexistence of magnetic order and two-dimensional superconductivity at $LaAlO_3/SrTiO_3$ interfaces, Nat. Phys., 7, 762-766.

[18] Pachmayr U., Nitsche F., Luetkens H., Kamusella S., Bruckner F., Sarkar R., Klauss H. H., Johrendt D. (2014), Coexistence of 3d-Ferromagnetism and Superconductivity in $[(Li_{1-x}Fe_x)\ OH]\ (Fe_{1-y}Li_y)Se$, Angew Chem. Int. Ed., 54, 293-335.

[19] Bulaevskii L. N., Buzdin A. I., Kulić M. L., Panjukov S. V. (1985), Coexistence of superconductivity and magnetism theoretical predictions and experimental results, Adv. Phys., 34, 175-261.

[20] Matthais B. T., Suhl H., Corenzwit E. (1985), Spin exchange in superconductors, Phys. Rev. Lett., 1, 92.

[21] Fertig W. A., Johnston D. C., DeLong L. E., McCallum R. W., Maple M. B., Matthias B. T. (1977), Destruction of superconductivity at the onset of long-range magnetic order in the compound $ErRh_4B_4$, Phys. Rev. Lett., 38, 987-990.

[22] Ishikawa M., Fischer Ø. (1977), Destruction of superconductivity by magnetic ordering in $Ho_{1.2}Mo_6S_8$, Solid State Commun., 23, 37-39.

[23] Felner I., Asaf U., Levi Y., Millo O. (1997), Coexistence of magnetism and superconductivity in $R_{1.4}Ce_{0.6}\,RuSr_2Cu_2O_{10-\delta}$s(R=Eu and Gd), Phys. Rev. B, 55, R3374.

[24] Bernhard C., Tallon J. L., Niedermayer C., Blasius T., Golnik A., Brücher E., Kremer R. K., Noakes D. R., Stronach C. E., Ansaldo E. J. (1999), Coexistence of ferromagnetism and superconductivity in the hybrid ruthenate-cuprate compound $RuSr_2GdCu_2O_8$ studied by muon spin rotation and dc magnetization, Phys. Rev. B, 59, 14099.

[25] Saxena S. S., Agarwal P., Ahilan K. *et al.* (2000), Superconductivity on the border of itinerant-electron ferromagnetism in UGe_2, Nature, 406, 587-592.

[26] Aoki D., Huxley A., Ressouche E., Braithwaite D., Flouquet J., Brison J. P., Lhotel E., Paulsen C. (2001), Coexistence of superconductivity and ferromagnetism in URhGe, Nature, 413, 613-616.

[27] Lu J. M., Zheliuk O., Leermakers I., Yuan N. F. Q., Zeitler U., Law K. T., Ye J. T. (2015), Evidence for two-dimensional Ising superconductivity in gated MoS_2, Science, 350, 1353-1357.

[28] Zhu X., Guo Y., Cheng H., Dai J., An X., Zhao J., Tian K., Wei S., Zheg X. C., Wu C., Xie Y. (2016), Signature of coexistence of superconductivity and ferromagnetism in two-dimensional $NbSe_2$ triggered by surface molecular adsorption, Nat. Commun., 7, 11210.

[29] Li Z., Zhao Y., Mu K., Shan H., Guo Y., Wu J., Su Y., Wu Q., Sun Z., Zhao A., Cui X., Wu C., Xie Y. (2017), Molecule-confined engineering toward superconductivity and ferromagnetism in two-dimensional superlattice, J. Am. Chem. Soc., 139, 16398-16404.

[30] Kumar P., Skomski R., Pushpa R. (2017), Magnetically ordered transition-metal-intercalated WSe_2, ACS Omega, 2, 7985-7990.

[31] Horzum S., Çakır D., Suh J., Tongay S., Huang Y.-S., Ho C. –H., Wu J., Sahin H., Peeters F. M. (2014), Formation and stability of point defects in monolayer rhenium disulphide, Phys. Rev. B, 89, 155433.

[32] Cai L., He J., Liu Q., Yao T., Chen L., Yan W., Hu F., Jiang Y., Zhao Y., Hu T., Sun Z., Wei S. (2015), Vacancy-induced ferromagnetism of MoS_2 nanosheets, J. Am. Chem. Soc., 137, 2622-2627.

[33] Zhou Y., Wang Z., Yang P., Zu X., Yang L., Sun X., Gao F. (2012), Tensile strain switched ferromagnetism in layered NbS_2 and $NbSe_2$, ACS Nano, 6, 9727-9736.

[34] Zheng H., Yang B., Wang D., Han R., Du X., Yan Y. (2014), Tuning magnetism of monolayer MoS_2 by doping vacancy and applying strain, Appl. Phys. Lett., 104, 132403.

[35] Manchanda P., Sharma V., Yu H., Sellmyer D. J., Skomski R. (2015), Magnetism of Ta dichalcogenide monolayers tuned by strain and hydrogenation, Appl. Phys. Lett., 107, 032402.

[36] Xiang Z., Zhang Z., Xu X., Zhang Q., Wang Q., Yuan C. (2015), Room-temperature ferromagnetism in Co doped MoS_2 sheets, Phys. Chem. Chem. Phys., 17, 15822-15828.

[37] Tedstone A. A., Lewis D. J., O'Brian P. (2016), Synthesis, properties, and applications of transition metal doped layered transition metal dichalcogenides, Chem. Mater., 28, 1965-1974.

[38] Shu H., Luo P., Liang P., Cao D., Chen X. (2015), Layer-dependent dopant stability and magnetic exchange coupling of iron-doped MoS_2 nanosheets, ACS Appl. Mater. Interfaces, 7, 7534-7541.

[39] Prodan A., Marinkovic V., Rojsek M., Jug N., Van Midden H. J. P., Boswell F. W., Bennett J. C., Bohm H. (2001), The surface superstructures in niobium disulfide and diselenide intercalated by Cu, Co and Fe, Surf. Sci., 476, 71-77.

[40] Ugeda M. M., Bradley A. J., Zhang Y. *et al* (2016), Characterization of collective ground states in single-layer $NbSe_2$, Nat. Phys., 12, 92-96.

[41] Huang C. L., Lin J. –Y., Chang Y. T., Sun C. P., Shen H. Y., Chou C. C., Berger H., Lee T. K., Yang H. D. (2007), Experimental evidence for a two-gap structure of superconducting $NbSe_2$: A specific-heat study in external magnetic fields, Phys. Rev. B, 76, 212504.

[42] Malliakas C. D., Kanatzidis M. G. (2013), Nb-Nb interactions define the charge density wave structure of 2H-$NbSe_2$, J. Am. Chem. Soc., 135, 1719-1722.

[43] Manchanda P., Skomski R. (2017), Defect-induced magnetism in two-dimensional $NbSe_2$, Superlattices Microstruct, 101, 349-353.

[44] Voorhoeve-Van Den Berg J. M., Sherwood R. C. (1971), Low-temperature magnetic susceptibilities of $NbSe_2$ containing the first-row transition metals, J. Phys. Chem. Solids, 32, 167-173.

[45] Pervin R., Krishnan M., Rana A. K., Kannan M., Arumugam S., Shirage P. M. (2017), Enhancement of superconducting critical current density by Fe impurity substitution in $NbSe_2$ single crystals and the vortex pinning mechanism, Phys. Chem. Chem. Phys., 19, 11230.

[46] Krishnan M., Pervin R., Ganesan K. S., Murugesan K., Lingannan G., Verma A. K., Shirage P. M. and Sonachalam A. (2018), Pressure assisted enhancement in superconducting properties of Fe substituted $NbSe_2$ single crystal, Sci. Rep., 8, 1251.

[47] Segall M. D., Lindan P. J. D., Probert M. J., Pickard C. J., Hasnip P. J., Clark S. J., Payne M. C. (2002), First-principles simulation: ideas, illustrations and the CASTEP code, J. Phys.: Condens. Matter, 14, 2717-2744.

[48] Perdew J. P., Burke K., Ernzerhof M. (1996), Generalized gradient approximation made simple, Phys. Rev. Lett., 77, 3865-3868. [49] Monkhorst H. J., Pack J. D. (1976), Special points for Brillouin-zone integrations, Phys. Rev. B, 13, 5188-5192.

[50] Pack J. D., Monkhorst H. J. (1977), "Special points for Brillouin-zone integrations"-a reply, Phys. Rev. B, 16, 1748-1749.

[51] Marezio M., Dernier P. D., Menth A., Hull Jr. G. W. (1972), The crystal structure of $NbSe_2$ at 15°K, J. Solid State Chem., 4, 425-429.

[52] Boaknin E. *et al.* (2003), Heat conduction in the vortex state of $NbSe_2$: evidence for multiband superconductivity, Phys. Rev. Lett., 90, 117003.

[53] Mattheiss L. F. (1973), Energy Bands for 2H-$NbSe_2$ and 2H-MoS_2, Phys. Rev. Lett., 30, 784.

[54] Chen L., Li C., Tang H., Li H., Liu X., Meng J. (2014), First-principles calculations on structural, electronic properties of V-doped 2H-$NbSe_2$, RSC Adv., 4, 9573-9578.

[55] Pervin R., Krishnan M., Arumugam S., Shirage P. M. (2019), Coexistence of superconductivity and ferromagnetism in defect-induced $NbSe_2$ single crystals, J. Mater. Sci., 54, 11903-11912.

[56] Khim S., Kim J. W., Choi E. S., Bang Y., Nohara M., Takagi H., Kim K. H. (2010), Evidence for dominant Pauli paramagnetic effect in the upper critical field of single-crystalline $FeTe_{0.6}Se_{0.4}$, Phys. Rev. B, 81, 184511.

[57] Anderson P. W., Kim Y. B. (1964), Hard Superconductivity: Theory of the Motion of Abrikosov Flux Lines, Rev. Mod. Phys., 36, 39-43.

[58] Özçelik B., Gürsul M., Karaçora Nane F., Madre M. A., Sotelo A. (2018), Effect of Na-substitution on magnetoresistance and flux pinning energy of Bi-2212 ceramics prepared via hot-forging process, J. Mater. Sci.: Mater. Electron., 29, 19147-19154.

[59] Khadzhai G. Y., Vovk C. R., Vovk R. V. (2017), Broadening of the superconducting transition in single crystal Y-Ba-Cu-O, J. Low Temp. Phys., 43, 1119-1121.

[60] Whitney D. A., Fleming R. M., Coleman R. V. (1977), Magnetotransport and superconductivity in dilute Fe alloys of $NbSe_2$, $TaSe_2$, and TaS_2, Phys. Rev. B, 15, 3405-3423.

[61] Kang S., Goyal A., Li J., Gapud A. A., Martin P. M., Heatherly L., Thompson J. R., Christen D. K., List F. A., Paranthaman M., Lee D. F. (2006), High-performance high-T_c superconducting wires, Science, 311, 1911-1914.

[62] Shirage P. M., Iyo A., Shivagan D. D., Tanaka Y., Kito H., Kodama Y. (2008), Irreversibility line and flux pinning properties in a multilayered cuprate superconductor of $Ba_2Ca_3Cu_4O_8(O,F)_2$ (T_c = 105 K), Supercond. Sci. Technol., 21, 075014.

[63] Shirage P. M., Tanaka Y., Iyo A. (2010), The critical current density, irreversibility line, and flux pinning properties of $Ba_2CaCu_2O_4(O, F)_2$ high-T_c superconductor, J. Appl. Phys., 107, 093905.

[64] Zhang Y. Z., Ren Z. A., Zhao Z. X. (2009), Thermally activated energy and critical magnetic fields of $SmFeAsO_{0.9}F_{0.1}$, Supercond. Sci. Technol., 22, 065012.

[65] Song Y. J., Kang B., Rhee J. S., Kwon Y. S., (2012), Thermally activated flux flow and fluctuation conductivity in LiFeAs single crystal, EPL, 97, 47003.

[66] Lei H., Hu R., Choi E. S., Petrovic C. (2010), Thermally activated energy and flux-flow Hall effect of $Fe_{1+y}(Te_{1+x}S_x)_z$, Phys. Rev. B, 82, 13425.

[67] Berk N. F., Schrieffer J. R. (1966), Effect of ferromagnetic spin correlations on superconductivity, Phys. Rev. Lett., 17, 433-435.

[68] Kramer E. J. (1973), Scaling laws for flux pinning in hard superconductors, J. Appl. Phys., 44, 1360-1370.

[69] Patnaik S., Gurevich A., Bu S. D., Kaushik S. D., Choi J., Eom C. B., Larbalestier D. C. (2004), Thermally activated current transport in MgB_2 films, Phys. Rev. B, 70, 064503.

[70] Kierfeld J., Nordborg H., Vinokur V. M. (2000), Theory of plastic vortex creep, Phys. Rev. Lett., 85, 4948.

[71] Leo A., Grimaldi G., Guarino A., Avitabile F., Nigro A., Galluzzi A., Mancusi D., Polichetti M., Pace S., Buchkov K., Nazarova E., Kawale S., Bellingeri E., Ferdeghini C. (2015), Vortex pinning properties in Fe-chalcogenides, Supercond, Sci. Technol., 28, 125001.

[72] Vinokur V. M., Feigel'man M. V., Geshkenbein V. B., Larkin A. I. (1990), Resistivity of High-T_c Superconductors in a Vortex-Liquid State, Phys. Rev. Lett., 65, 259-262.

[73] Wang X. L., Li A. H., Yu S., Ooi S., Hirata K., Lin C. T., Collings E. W., Sumption M. D., Bhatia M., Ding S. Y., Dou S. X. (2005), Thermally assisted flux flow and individual vortex pinning in $Bi_2Sr_2Ca_2Cu_3O_{10}$ single crystals grown by the traveling solvent floating zone technique, J. Appl. Phys., 97, 10B114.

[74] Choi W. J., Seo Y. I., Ahmad D., Kwon Y. S. (2017), Thermal activation energy of 3D vortex matter in $NaFe_{1-x}Co_xAs$ ($x = 0.01$, 0.03 and 0.07) single crystals, Sci. Rep., 7, 10900.

[75] Thompson J. R., Sorge K. D., Cantoni C., Kerchner H. R., Christen D. K., Paranthaman M. (2005), Vortex pinning and slow creep in high-J_c MgB_2 thin films: a magnetic and transport study, Supercond. Sci. Technol., 18, 970-976.

[76] Li L., Li Y., Jin Y. *et al.* (2015), Coexistence of superconductivity and ferromagnetism in $Sr_{0.5}Ce_{0.5}FBiS_2$, Phys. Rev. B 91, 14508.

[77] Thakur G. S., Fuchs G., Nenkov K., Haque Z., Gupta L. C., Ganguly A. K. (2016), Coexistence of superconductivity and ferromagnetism in $Sr_{0.5}Ce_{0.5}FBiS_{2-x}Se_x$ ($x = 0.5$ and 1.0), a non-U material with $T_c < T_{FM}$, Sci. Rep., 6, 37526.

[78] Menard G. C. *et al.* (2015), Coherent long-range magnetic bound states in a superconductor, Nat. Phys., 11, 1013-1016.

[79] Pervin R., Krishnan M., Rana A. K., Arumugam S., Shirage P. M. (2018), Effect of Cr atoms in vortex dynamics of $NbSe_2$ superconductor and study of second magnetization peak effect, Mater. Res. Express, 5, 076001.

[80] Zehetmayer M., Weber H. W. (2010), Experimental evidence for a two-band superconducting state of $NbSe_2$ single crystals, Phys. Rev. B, 82, 014524.

[81] Bardeen J., Cooper L. N., Schrieffer J. R. (1957), Microscopic theory of superconductivity, Phys. Rev., 106, 162-164.

[82] Bardeen J., Cooper L. N., Schrieffer J. R. (1957), Theory of superconductivity, Phys. Rev., 108, 1175-1204.

[83] Ilić S., Meyer J. S., Houzet M. (2017), Enhancement of the upper critical field in disordered transition metal dichalcogenide monolayers, Phys. Rev. Lett., 119, 117001.

[84] Aoki D., Flouquet J. (2012), Ferromagnetism and superconductivity in uranium compounds, J. Phys. Soc. Japan, 81, 11003.

[85] Li S. L., Wen H. H., Zhao Z. W., Ni Y. M., Ren Z. A., Che G. C., Yang H. P., Liu Z. Y., Zhao Z. X. (2001), Linear temperature dependence of lower critical field in MgB_2, Phys. Rev. B, 64, 094522.

[86] Arumugam S., Krishnan M., Ishigaki K., Gouchi J., Pervin R., Selvan G. K., Shirage P. M., Uwatoko Y. (2019), Enhancement of superconducting properties and flux pinning mechanism on $Cr_{0.0005}NbSe_2$ single crystal under Hydrostatic pressure, Sci. Rep., 9, 347.

CHAPTER 7

Effect of V Doping on $NbSe_2$ Single Crystal and Study of Vortex Phase Diagram

T*he several characteristics which are associated with disordering and pinning can be ideally studied in the vortex lattice of type-II superconductor* ***[1, 2]****. In a clean superconductor, the VL structure is considered for several factors. The foremost characteristic is the interaction between vortices which orders them into a hexagonal Abrikosov vortex lattice. The other significant characteristic is thermal fluctuation which favours disordering and melts the lattice into vortex liquid phase at a characteristic's temperature* ***[3, 4]****. Structural imperfection (i.e., quenched disorder, twinned boundaries) also plays important role to destroy the long range Abrikosov lattice by creating a disordered background potential in type-II superconductors* ***[5]****. The external pinning centres add more novel pinned vortex phases to the phase diagram of clean superconductor* ***[6, 7]****. This chapter focuses on the nature of these phases and the transition amongst themselves in $NbSe_2$ single crystal in presence of V atoms.*

Two remarkable consequences of the transition between various vortex states are the fishtail effect and the peak effect phenomena. It is well known that the critical current density obtained from the magnetization hysteresis loops decreases with increase of magnetic field due to the dissipative motion of FLL. Some superconductors show enhancement of J_c after the first peak of penetration field with increasing magnetic field. This is known as the fishtail effect or prominent SMP effect. SMP has been detected in high quality and clean crystals of cuprate superconductors **[8, 9]**. This has been also studied in single crystals as well as polycrystalline samples of FeAs-1111 and also in FeAs-122 superconductors **[10-12]**. While in the low T_c superconductors, *e.g.*, Nb_3Sn, MgB_2, *etc.*, peak effect has been generally perceived **[13, 14]**. The peak effect phenomenon, *i.e*. the anomalous enhancement of the J_c and the pinning force per flux line occurs at the H_{c2} line near the normal-state phase boundary in low-T_c systems and almost overlap with the melting line in the HTSC's **[15]**. It is considered as the outcome of rapid softening of the lattice and the phenomenon of plastic deformations **[16]**. This creates topological defects in FLL. As a consequence, the lattice shows amorphous nature at and above the peak position in J_c. In cuprates, the peak effect can only be seen in ultra-clean crystals with a low level of pinning centres which is discussed by Nishizaki *et al.* in YBCO systems **[17]**. Surprisingly, with increasing weak point disorders by electron irradiation **[17]**, the J_c *(H)* peak broadens in clean YBCO and the peak position shifts towards the intermediate fields. This is the clear signature of SMP that differentiates the peak effect. However, the anomalous SMP appears due to different mechanism in different superconducting systems. It appears at different fields for $REBa_2Cu_3O_{7-\delta}$ (*RE*BCO) bulks (*RE* = rare earth element) at different temperatures **[18]**. Contrarily, the peak position is temperature independent for Bi-based and Tl-based cuprate **[19, 20]**. To explore such anomalous behaviour of critical parameter (like J_c) and the associated different vortex states of superconducting material, doping or additions of foreign atoms appear as a potential method. It is also a major concern for technological applications because it is an effective method for improving the structural, superconducting, transport and flux pinning properties that allow

superconductors to be suitable for applications at higher temperatures and magnetic fields. These additives lead to structural stability and aid to understand the structure and diversity of different FLL. In this chapter, we investigated the SMP effect and different vortex phases associated with the phase diagram of V_xNbSe_2 single crystal at different concentration (*i.e.*, x = 0.0007, 0.001, 0.0015) through magnetic and magneto transport measurement. We have done structural characterization to observe the effect of V atoms in lattice constant and phase purity. We have analysed the magnetic field dependence of J_c characteristics at different (H, T) space in $V_{0.0007}NbSe_2$, $V_{0.001}NbSe_2$ and $V_{0.0015}NbSe_2$. The onset of the SMP effect appears as the regime where a three dimensional collectively pinned ordered vortex phase terminate and precisely exposes to vortex glassy phase. The F_p peak near H_{irr} demonstrates the lattice softening and the two dimensional to three dimensional FLL distortions in $V_{0.0007}NbSe_2$ and $V_{0.0015}NbSe_2$. $V_{0.001}NbSe_2$ shows no BL zero field peak and the higher field peak near H_{c2}. The thermally activated vortex motion is studied through Arrhenius relation in the TAFF region of $V_{0.0015}NbSe_2$. The estimated apparent thermal activation energy shows power law dependence on magnetic fields and a crossover field (H_{cr}) that differentiates the plastically deformed vortex liquid state from more entangled state. Finally, we constructed the vortex phase diagram of $V_{0.0015}NbSe_2$ demonstrating the collective creep region, plastic creep region, vortex glassy state and vortex liquid phase in the H-T phase diagram.

7.1. Materials and Method

Materials: Niobium (Nb, 99.95%; Alfa Aesar), Selenium (Se, 99.999%; Alfa Aesar) and Vanadium (V, 99.99%; Alfa Aesar), Iodine (I_2, 99.998%; Alfa Aesar).

Method: The single crystals of $V_{0.0007}NbSe_2$, $V_{0.001}NbSe_2$ and $V_{0.0015}NbSe_2$ were grown through the method of chemical vapour transport reactions using Iodine as a transporting agent. The precursors Niobium (Nb), 99.95%, Selenium (Se) 99.99% and Vanadium (V) 99.99% purity were obtained and grinded in an agate motor to form circular pellet without any further refinement. The pellet (~ 4 gm) was sealed with 2-3 mg of iodine in a

quartz tube at a pressure of 9 x 10^{-6} mbar at the liquid nitrogen atmosphere. Then the sealed quartz tube was heated inside a two zone furnace keeping charge zone and growth zone temperatures fixed at 820˚C and 720˚C, respectively for one week. Similar procedure is used to form large single crystals in our previous studies **[21, 22]**.

7.2. Result and discussions

7.2.1. Structural properties:

7.2.1.1. X-Ray diffraction: First, the crystal structures of V_xNbSe_2 (with x = 0.0007, 0.001, 0.0015) single crystals were characterized by Rigaku Smartlab powder X-ray diffractometer with Cu K_α radiation at room temperature (λ = 1.54 Å) for structural information regarding the phase purity. The X-ray diffraction (XRD) pattern of V_xNbSe_2 single crystal is represented in Figure 7.1 which demonstrates the hexagonal phase with $P6_3/mmc$ space group (JCDPS card no. 01-070-5612). The pattern shows the presence of only (*00l*) plane without any impurity phase confirming the single crystalline nature of V_xNbSe_2. The estimated *c*-axis lattice parameter of $V_{0.0007}NbSe_2$ is equivalent to pure $NbSe_2$ (12.55 (5 ± 4 Å)) **[23]**. However, a slight degradation in "*c*" lattice constant can be observed in higher V doping. Table 7.1 shows evidence of an abrupt reduction in lattice parameter because of V doping followed by a gradual increase up to 0.15% doping.

In contrast, Luo *et al.* **[24]** reported the linear increase of *c*- axis parameter with increasing Cu contents as a signature of the 3*d* metal intercalation in $NbSe_2$. V is the same group elements of Nb. The ionic radius of V^{4+} atom (58 pm) is less than that of Nb^{4+} atom (68 pm) instead of having same coordination number of V^{4+} to that of Nb^{4+}. So, following the Vegard's law, the reduction of *c*-axis parameter can be predicted as the substitution of Nb by V atom in $V_{0.0015}NbSe_2$. Chen *et al.* **[25]** reported that substitution of Nb atom (by V atom) is more energetically favourable than that intercalation of V atom into the interlayer of the 2H-$NbSe_2$ supercell. The detail analysis of the crystallographic cell regarding the position of V atoms in $V_{0.0015}NbSe_2$ is not the subject of this study and is not presented here.

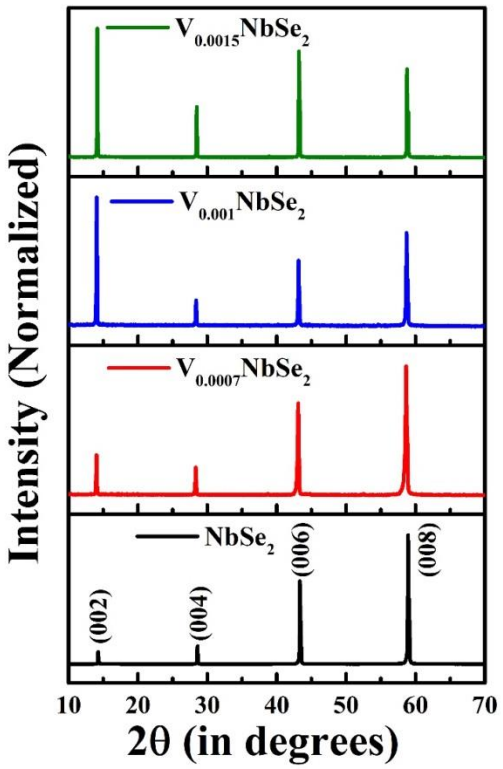

Figure 7.1. *Represents the XRD pattern of $NbSe_2$, $V_{0.0007}NbSe_2$, $V_{0.001}NbSe_2$ and $V_{0.0015}NbSe_2$ single crystals.*

Table 7.1. *Estimated structural parameters for $NbSe_2$, $V_{0.0007}NbSe_2$, $V_{0.001}NbSe_2$ and $V_{0.0015}NbSe_2$ single crystals.*

Sample	*c* (Å)	*FWHM*			
		(002)	(004)	(006)	(008)
$NbSe_2$	12.555±0.004	0.12	0.12	0.16	0.12
$V_{0.0007}NbSe_2$	12.540±0.007	0.13	0.16	0.20	0.24
$V_{0.001}NbSe_{1.85}$	12.513±0.005	0.14	0.16	0.19	0.16
$V_{0.0015}NbSe_2$	12.492±0.004	0.11	0.12	0.10	0.11

7.2.1.2. FESEM and EDS analysis:

The surface morphology, composition and stoichiometry of V_xNbSe_2 (with x = 0.0007, 0.001, 0.0015) have been examined via the FESEM and EDX analysis. Figure 7.2(*a*) and 7.3(*a*) characterize the morphologies of $V_{0.0007}NbSe_2$ and $V_{0.0015}NbSe_2$ which affirms the layer-by-layer formation of the single crystalline compound.

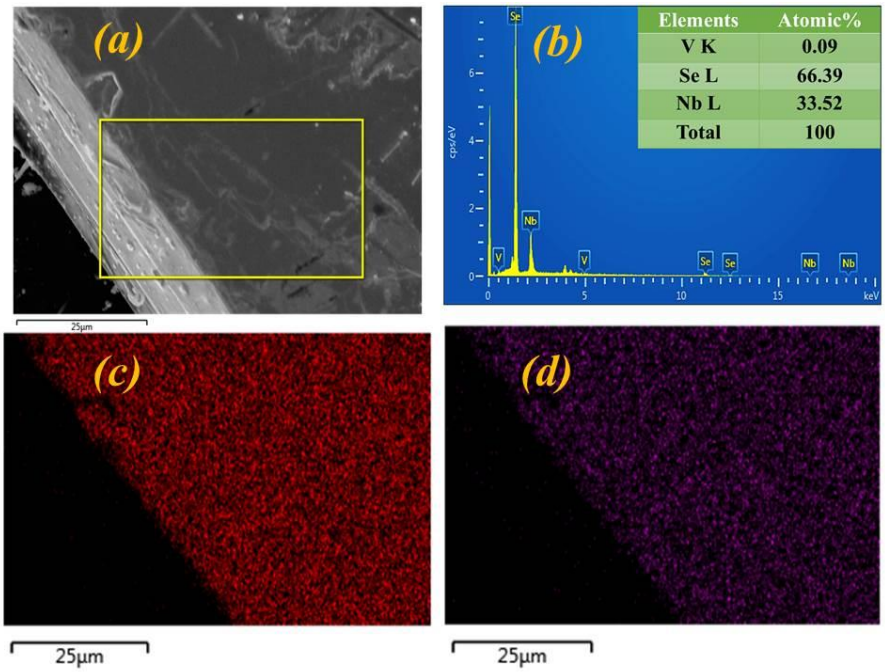

Figure 7.2. *(a) The FESEM morphology of the layered structure of* $V_{0.0007}NbSe_2$ *single crystals and (b) the corresponding EDS analysis. The EDS colour mapping images of (c) Se and (d) Nb.*

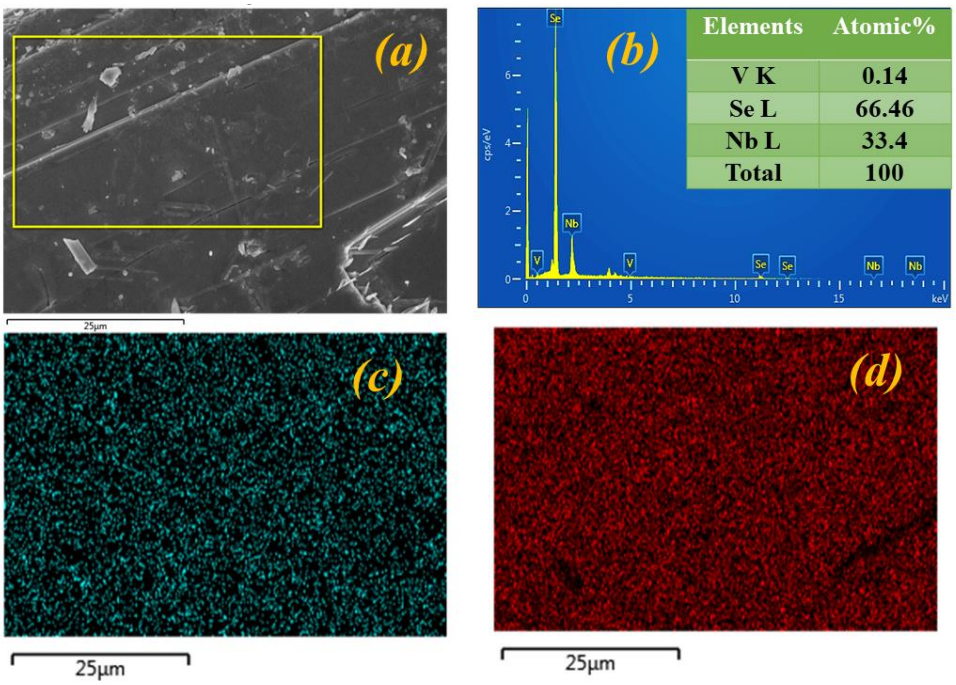

Figure 7.3. *(a) The FESEM morphology of the layered structure of* $V_{0.0015}NbSe_2$ *single crystal and (b) the corresponding EDS analysis. The EDS colour mapping images of (c) Nb and (d) Se.*

Quantitative depiction using the EDX spectrum (Figure 7.2(*b*)) reveals the atomic percentages of V, Se, and Nb as 0.09%, 66.39% and 33.52% in $V_{0.0007}NbSe_2$, respectively. Moreover, the EDX spectrum of $V_{0.0015}NbSe_2$

(Figure 7.3(*b*)) exhibits the atomic percentages of V, Se, and Nb as 0.14%, 66.46% and 33.4%, respectively. The elemental compositions are in the stoichiometric ratios of the as-grown crystal without having any impurity phase. The EDX elemental mapping of $V_{0.0007}NbSe_2$ is shown in Figure 7.2(*c-d*) representing the distinction in the Se and Nb concentration on the selected portion of surface (shown by yellow rectangle of Figure 7.2(*a*)). Figure 7.3(*c-d*) shows the uniform distribution of the Nb and Se concentration. However, it is challenging to record the V distribution of V_xNbSe_2 (with x = 0.0007, 0.001, 0.0015) accurately as the best achievable elemental sensitivity of EDS is 0.1% (comprehended via standards). However, the EDS analysis of V_xNbSe_2 validates the homogeneous insertion of V within the spatial resolution of this measurement, typically of the order of a micrometer.

7.2.2. Superconducting properties:

7.2.2.1. Temperature dependent magnetization studies:

To study the evolution of superconducting properties with V doping in V_xNbSe_2, we investigated the temperature dependence of magnetization measurement in both ZFC and FC processes. Figure 7.4 represents the diamagnetic transitions of $V_{0.0007}NbSe_2$, $V_{0.001}NbSe_2$ and $V_{0.0015}NbSe_2$ single crystals which are estimated by drawing tangents to the deviation of ZFC curves from zero magnetization value at the *dc* magnetic fields of 0.005 T, 0.05 T, 0.5 T and 0.7 T. The ZFC curve shows perfect diamagnetism in the low temperature region with sharp transition at 5.6 K, 4.4 K and 3.65 K, respectively. Table 7.4 represents the T_c values at different magnetic fields in V_xNbSe_2. This suggests that the T_c values shift systematically to lower temperatures with increasing *V* concentration as well as magnetic fields in V_xNbSe_2. The decrease in T_c may be due to the modification of density of states either due to electronic charge transfer to the parent $NbSe_2$ conduction bands and the associated changes in the band structure or the disorder accounted for the V substitution as we observed in Fe_xNbSe_2 and Cr_xNbSe_2. The onset of the T_c values is designated by black arrows in Figure 7.4. This confirms the presence of bulk superconductivity of V_xNbSe_2.

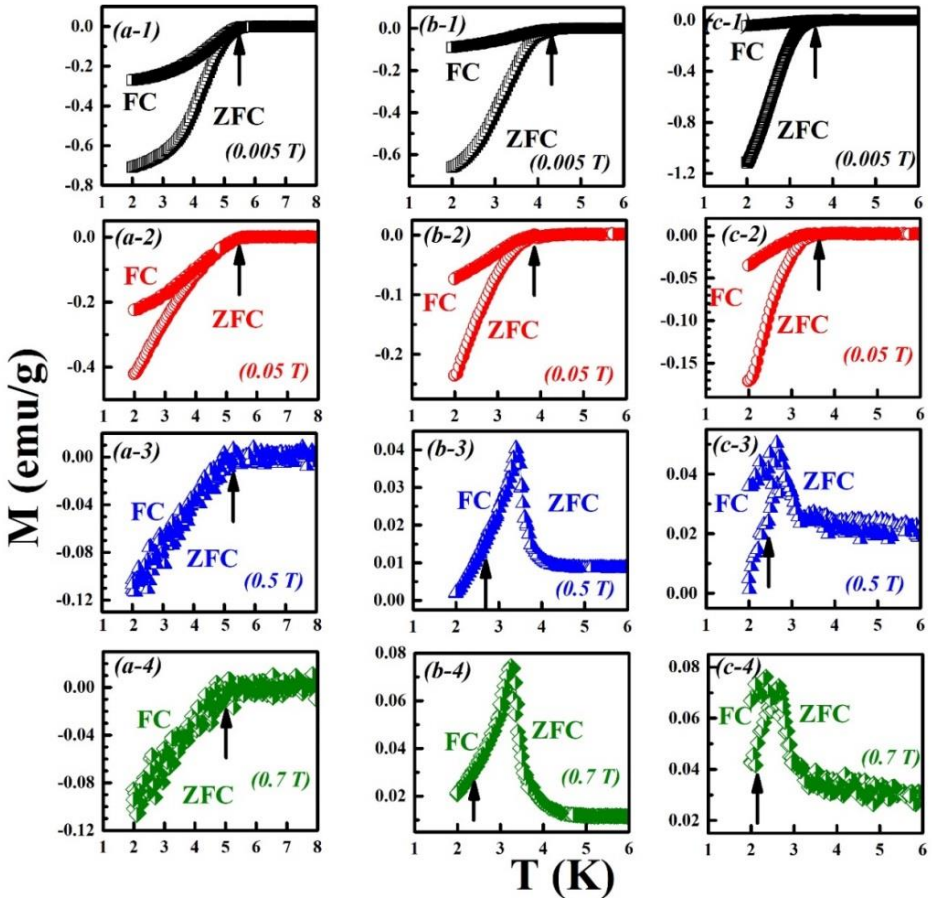

Figure 7.4. *Shows the temperature dependence of magnetization measurements of pure $V_{0.0007}NbSe_2$ single crystal at (a-1) 0.005 T (a-2) 0.05 T(a-3) 0.5 T (a-4) 0.7 T magnetic fields; $V_{0.001}NbSe_2$ single crystal at (b-1) 0.005 T (b-2) 0.05 T (b-3) 0.5 T (b-4) 0.7 T magnetic fields; and $V_{0.0015}NbSe_2$ single crystal at (c-1) 0.005 T (c-2) 0.05 T (c-3) 0.5 T and (c-4) 0.7 T magnetic fields.*

Table 7.2. *The variation of T_c with magnetic fields and V concentration for $NbSe_2$ and V_xNbSe_2 (x = 0.0007, 0.001, 0.0015) single crystals.*

Sample	$T_c(K)$ (@0.005 T)	$T_c(K)$ (@ 0.05 T)	$T_c(K)$ (@ 0.5 T)	$T_c(K)$ (@ 0.7 T)
$NbSe_2$	6.4	6.2	5.8	5.0
$V_{0.0007}NbSe_2$	5.6	5.2	4.9	4.5
$V_{0.001}NbSe_2$	4.4	3.8	2.6	2.5
$Ve_{0.0015}NbSe_2$	3.6	3.2	2.4	1.9

This study indicates that V substitution appears as disruptive for the superconductivity in $NbSe_2$.

7.2.2.2. Upper limit of superconductivity:

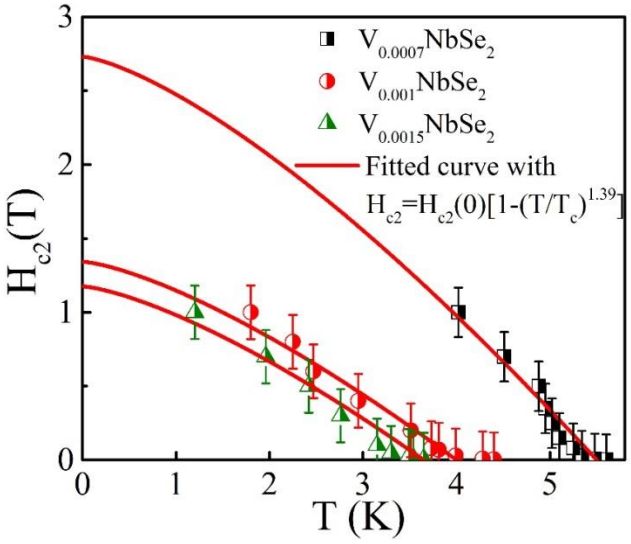

***Figure 7.5**. The dependence of the $H_{c2}(T)$ on temperature and the corresponding fit of $V_{0.0007}NbSe_2$, $V_{0.0009}NbSe_2$ and $V_{0.0015}NbSe_2$ using Ginzburg-Landau phenomenological equation.*

The magnetization measurement permits a further detail analysis in the upper critical field. H_{c2} (T) values which are estimated from the *M-T* curve considering the onset point of the superconducting transition at each magnetic field. It gives slope of $\frac{dH_{c2}}{dT}|_{T_c}$ = -0.4 T/K, -0.2 T/K and -0.14 T/K for $V_{0.0007}NbSe_2$, $V_{0.001}NbSe_2$ and $V_{0.0015}NbSe_2$, respectively (Table 7.3). The H_{c2} (T) *vs. T* plots of V_xNbSe_2 superconductors are shown in Figure 7.5 (*a-c*), which are fitted with the anisotropic G-L single band formula, $H_{c2} = H_{c2}(0)[1-(T/T_c)^a]^b$ with a = 1.39 and b = 1. The H_{c2} *(0)* values of V_xNbSe_2 are estimated from the *G-L* fitting which show lower value than $NbSe_2$ (Table 7.3). This indicates V doping enhances the pair-breaking phenomena in presence of magnetic field compared to $NbSe_2$. The $H_{c2}^{orb}(0)$ values of V_xNbSe_2 are obtained as 1.54 T, 0.6 T and 0.4 T using the Werthamer- Helfand-Hohenberg (*WHH*) formula **[26]**, which suggests the participation of orbital effect in pair breaking mechanism in presence of magnetic fields. However, similar to Cr_xNbSe_2 samples, the H_p *(0)* values are much higher than the H_{c2} *(0)* values in V_xNbSe_2. This indicates that the orbital pair breaking effect lowers the experimental values of H_{c2} *(0)* of

V_xNbSe_2 by supressing the spin paramagnetic effect. The Ginzburg-Landau coherence length (ξ_{GL} *(0)*) is estimated to the range from 109 Å for $V_{0.0007}NbSe_2$, to ~173 Å for $V_{0.0015}NbSe_2$.

Table 7.3. *The H_{c2} (0), $H_{c2}^{orb}(0)$, $H_p(0)$ and ξ_{GL} (0) values of $NbSe_2$, $V_{0.0007}NbSe_2$, $V_{0.001}NbSe_2$ and $V_{0.0015}NbSe_2$ single crystals are summarized.*

Sample	$H_{c2}(0)$ (T)	$(dH_{c2}/dT)_{T=Tc}$ (T/K)	$H_{c2}^{orb}(0)$ (T)	$H_p(0)$ (T)	ξ (0) (Å)
$NbSe_2$	**7.4**	**-1.3**	**5.8**	**12**	**72**
$V_{0.0007}NbSe_2$	**2.7**	**-0.40**	**1.5**	**10**	**109**
$V_{0.001}NbSe_2$	**1.3**	**-0.21**	**0.60**	**8.1**	**158**
$V_{0.0015}NbSe_2$	**1.2**	**-0.14**	**0.40**	**6.7**	**173**

7.2.2.3. Hysteresis loop (*M vs. H* curve) analysis:

The MHLs of V_xNbSe_2, which are measured at different temperatures from 2 K to 5 K, are demonstrated in Figure 7.6 (*a*-*c*). The asymmetric nature of MHL curves indicate that the surface barrier pinning instead of the volume pinning dominates in the low magnetic field region of all V doped $NbSe_2$. Paltiel *et al.* **[27]** has demonstrated the significance of the surface barrier pinning at low magnetic fields in $NbSe_2$ crystal. At the high magnetic field regions, there is an increment of the width of irreversible magnetization (ΔM) with increasing magnetic field indicating the fishtail effect in $V_{0.0007}NbSe_2$, $V_{0.001}NbSe_2$ and $V_{0.0015}NbSe_2$ samples. $V_{0.0007}NbSe_2$ and $V_{0.001}NbSe_2$ show very weak fishtail effect as compared to $V_{0.0015}NbSe_2$. The SMP effect which is associated with the FE can be easily detected in Figure 7.6 (*a*-*c*) at all temperatures especially for $T \geq 2$ K. With increasing the temperature, the peak moves to the lower magnetic field and finally disappears near transition temperature region as shown in Figure 7.6 (*a*-*c*). The detail analysis of this monotonous reduction of the peak position with increasing temperature is discussed in the phase diagram plot later. The analogous mechanism is detected in $REBa_2Cu_3O_{7-\delta}$ (REBCO) superconductors (RE = rare earth element) **[28]**.

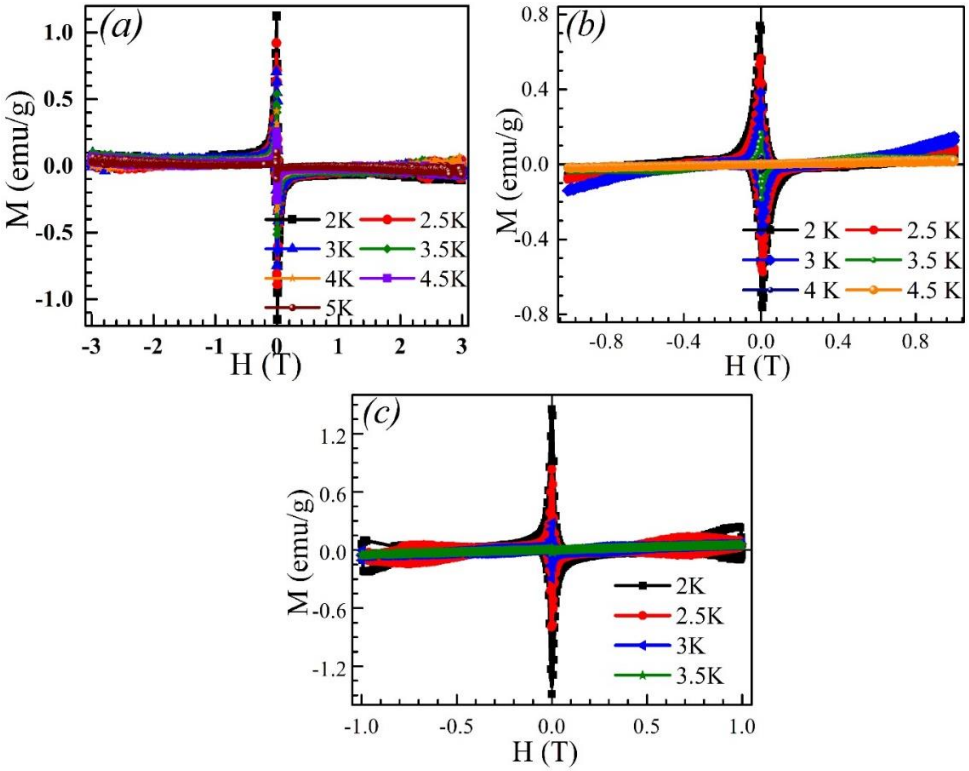

Figure 7.6. *Isotherm magnetization hysteresis loops as a function of magnetic field are shown for (a) $V_{0.0007}NbSe_2$; (b) $V_{0.0015}NbSe_2$; (c) $V_{0.001}NbSe_2$ at temperatures 2 K, 2.5 K, 3 K, 3.5 K, 4 K, 4.5 K and 5 K.*

7.2.2.4. Magnetic field dependence of critical current density study:

To investigate further, the magnetic field dependence of J_c is extracted from the MHL curves using Bean critical state model, $J_c = 20\Delta M / \left[w\left(1 - \frac{w}{3l}\right)\right]$, where ΔM is measured in emu/cm^3, and the width w and the length l of the sample ($w < l$) are measured in cm. **[29]**. The estimated $J_c(0)$ values at 2 K reach to 2×10^5, 4×10^5 and 9×10^5 A/cm^2 for $V_{0.0007}NbSe_2$, $V_{0.001}NbSe_2$ and $V_{0.0015}NbSe_2$, respectively. However, it drops down to 7×10^3 A/cm^2 at 3.5 K for highest V concentration (*i.e.*, $V_{0.0015}NbSe_2$). This indicates all V doped $NbSe_2$ have good current carrying capability.

Figure 7.7 (*a-c*) shows the resulting J_c *(H)* plot of V_xNbSe_2 single crystal in log-log scale at different temperatures. At extremely low magnetic fields (region I of Figure 7.7), a field independent J_c characteristics is observed for all temperatures which is the signature of nearly zero interacting region (*i.e.* the single vortex pinning region or small bundle pinning region) **[23]**. However, J_c decreases with enhancement of

temperature and magnetic fields which indicates the dissipation of energy due to the collective motion of vortices. The J_c *(H)* curves follow a power-law relationship $J_c \alpha H^{-n}$ with n = 2.46 (below H = 0.14 T) for $V_{0.0007}NbSe_2$, n = 1.35 (below H = 0.12 T) for $V_{0.001}NbSe_2$ and n = 1.38 (below H = 0.28 T) for $V_{0.0015}NbSe_2$ at 2 K temperature (region II of Figure 7.5). For a 3D elastic FLL, it is demonstrated by Blatter *et al.* **[2]** that J_c is leaded by a power law J_c *(H)* α H^{-3} in the large bundle-pinning regime. This is a qausi-long range Bragg glass phase where vortices creep in the form of large bundle **[30]**. However, the 2D elastic FLL shows single pancake pinning at low magnetic fields with field independent J_c, then a 2D collective-pinning region at higher fields with $J_c \alpha 1/H$. In case of thermal fluctuations, the n value is found to be as large as 20 which results from the giant flux creep **[2]**.

The relatively lower value of n (*i.e.* $1 < n < 3$) indicates the weak disorders in the 3D elastic FLL of V_xNbSe_2, which results the dissipation of FLL associated with the large bundle flux creep. So, the power-law response of J_c supports the presence of collective creep at low magnetic fields which destructs the long-range order of Abrikosov vortex lattice. Again, the J_c curves deviate from the power law scaling at 0.4 T, 0.3 T and 0.23 T (at 2 K temperature) for $V_{0.0007}NbSe_2$, $V_{0.001}NbSe_2$ and $V_{0.0015}NbSe_2$, respectively and the SMP starts at the onset magnetic field (region-III of Figure 7.7). At 2.5 K, the departure from the power-law response occurs at comparatively lower magnetic fields. The exponent n tends to decrease with increasing temperature within the temperature span of 2 K to 5 K, which is associated with the rate of change of flux creep.

The power-law behaviour of J_c *(H)* also implies the existence of a fairly dense distribution of weak pins in V_xNbSe_2 **[31]**. A fast drop in J_c in Figure 7.7 (*a-c*) is observed after SMP because of the fast creeping of vortices associated with large magnetic field. Besides diminishing the density of cooper pair electrons and reducing T_c, the presence of the V atoms may also be responsible for this novel anomalous vortex state in V_xNbSe_2. However, the analysis of J_c (H) characteristics indicates that the enhancement of the V concentration boosts the SMP effect, like in the case

of $V_{0.0015}NbSe_2$. Ahmed *et al.* **[32]** reported that the Co doping results the similar kind of prominent secondary peak at the optimally doped and overdoped $NaFe_{1-x}Co_xAs$ system. However, another intense peak of J_c *(H)* is observed at the edge of the irreversibility line (where $J_c \rightarrow 0$) in $V_{0.0007}NbSe_2$ and $V_{0.0015}NbSe_2$ (region IV of Figure 7.5) which indicates the peak effect phenomena. The H_{SMP} and H_p mark (as indicated by the red arrows in Figure 7.7(*c*)) the maxima accompanying the SMP and the PE phenomena of $V_{0.0015}NbSe_2$.

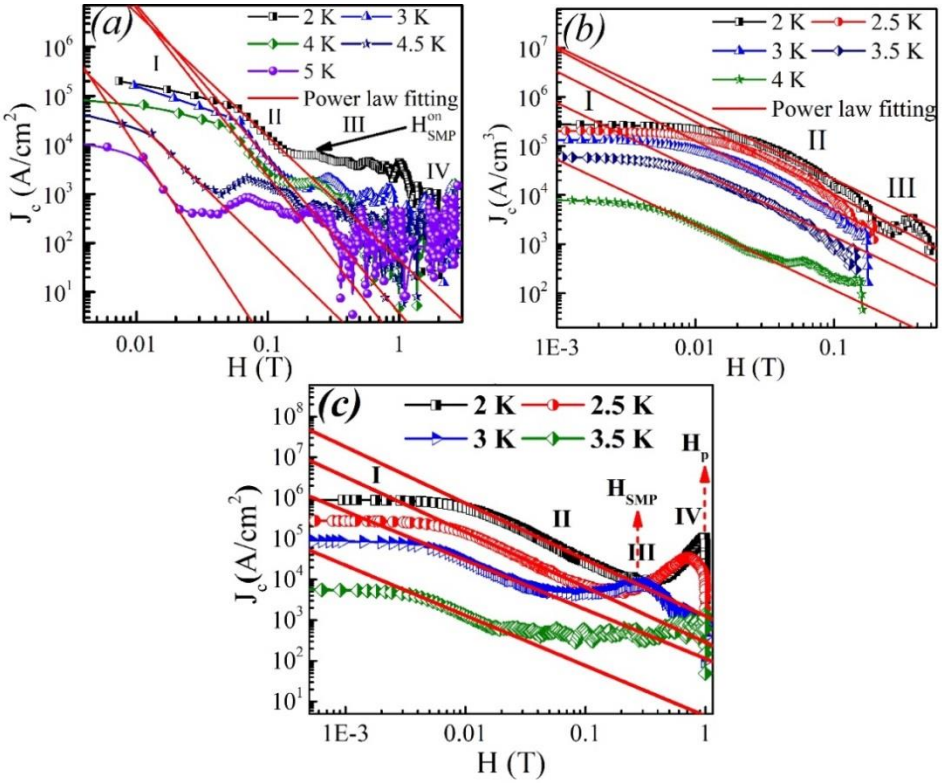

Figure 7.7. *The J_c-H diagram of (a) $V_{0.0007}NbSe_2$ at 2 K, 3 K, 4 K, 4.5 K and 5 K temperatures; (b) $V_{0.001}NbSe_2$ at 2 K, 2.5 K, 3 K, 3.5 K and 4 K temperatures; (c) $V_{0.0015}NbSe_2$ at 2 K, 2.5 K, 3 K and 3.5 K temperatures. The red solid lines correspond to the power-law decay according to the $J_c \propto H^{-n}$ for H||ab plane. Region I, II, III, IV indicate the non-interacting pinning region, large bundle pinning region, SMP region and the PE region, respectively. The black arrow of (a) represents the onset of SMP effect of $V_{0.0007}NbSe_2$ at 2 K temperature. The red arrows of (c) indicate the peaks associated with SMP and PE effect of $V_{0.0015}NbSe_2$.*

The evolution of J_c *(H)* curves in V_xNbSe_2 is comparable to the quenched disorder dominated $NbSe_2$ as reported by Banerjee *et al.* **[33]**. They demonstrated the collective pinning of ordered vortex lattice at intermediate fields and peak effect phenomena in the vicinity of highly

disorder (*i.e.*, at the amorphous limit) vortex lattice in J_c characteristics of $NbSe_2$ at t (= T/T_c (0)) = 0.973, 0.983, 0.990. The peak effect evolves to FE with increasing temperature towards the transition region. The evolution of J_c *(H)* curves from the PE to the FE phenomena has been also reported in $YBa_2Cu_3O_{7-\delta}$ **[34, 35]**. In contrarily, the J_c characteristic of $V_{0.0007}NbSe_2$ and $V_{0.0015}NbSe_2$ show SMP anomaly along with the indication of PE effect near the irreversibility line.

Table 7.4. *The estimated J_c (0) values from M-H curves for $NbSe_2$ and V_xNbSe_2 (x = 0.0007, 0.001, 0.0015) single crystals.*

Sample	**J_c (0) (A/cm^2) (@T = 2 K)**
$NbSe_2$	**1.4×10^5**
$V_{0.0007}NbSe_2$	**2.0×10^5**
$V_{0.001}NbSe_2$	**3.2×10^5**
$V_{0.0015}NbSe_2$	**9.3×10^5**

7.2.2.5. Study of pinning mechanism:

7.2.2.5.1. Size dependent pinning mechanism:

In order to find out the type of pinning mechanism operating in the FE or SMP region, the F_p value is evaluated using $F_p = J_c \times H$. As we discussed earlier, Dew-Hughes proposed a model in terms of elementary pinning forces to explain pinning mechanism ignoring the flux line elasticity and flux creep effect **[36]**. In this model the F_p follows a scaling relation $f_p = Ah^p(1-h)^q$ with p = 1, q = 1 for volume pinning, p = 1, q = 2 for normal core point pinning with $h_{max} \sim 0.33$, and p = 0.5, q = 2 for normal surface pinning mechanism with $h_{max} \sim 0.2$. Here h is defined as $h = H/H_{irr}$ where H_{irr} is obtained from the zero value of J_c in the J_c - H curves.

Figure 7.8 (*a-c*) represent the normalized pinning force density ($f_p = F_p/F_{p,\,max}$) as a function of reduced field ($h = H/H_{irr}$) of V_xNbSe_2 at different temperatures. Figure 7.8 (*a*) represents the noticeable zero-field peak suggesting the BL surface barrier effect in $V_{0.0007}NbSe_2$. This indicates the presence of edge potential which hindrances the magnetic fluxes to enter or leave the surfaces of single crystals. Similar features have been observed in

Cr_xNbSe_2 single crystals. In the intermediate fields, the overlapping of different peaks of $V_{0.0007}NbSe_2$ make difficult to differentiate the influence of different pinning mechanisms. All the f_p curves didn't fall into one curve which indicates more than one pinning mechanism involved in the pinning force density at the intermediate magnetic field. The presence of high field peak is also observed in $V_{0.0007}NbSe_2$ near H_{c2}. Here, the peak seems with the external magnetic field parallel to the *ab* plane, demonstrates the enhancement of the anisotropy with entering the screw dislocations at the onset of the high field peak and hence, results softening of the vortex lattice.

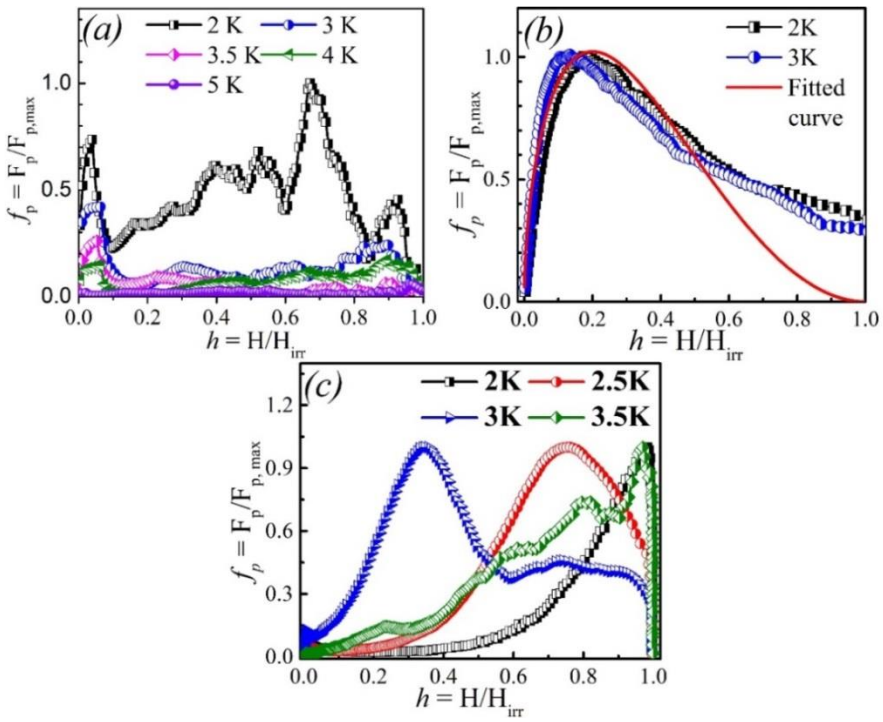

Figure 7.8. *The normalised pinning force density ($f_p = F_p/F_{p,max}$) vs. the reduce field ($h = H/H_{irr}$) diagram of (a) $V_{0.0007}NbSe_2$ at 2 K, 3 K, 3.5 K, 4 K and 5 K temperatures, (b) $V_{0.001}NbSe_2$ at 2 K and 3 K temperatures, (c) $V_{0.0015}NbSe_2$ at T = 2 K, 2.5 K, 3 K and 3.5 K temperatures.*

Figure 7.8 (*c*) also shows the BL zero field peak and highly intense peak near H_{irr} in $V_{0.0015}NbSe_2$ like $V_{0.0007}NbSe_2$. However, in contrast to $V_{0.0007}NbSe_2$, the zero- field peak at each temperature is suppressed highly by higher field peak in $V_{0.0015}NbSe_2$. The peak of f_p doesn't follow the normal point pinning and surface pinning mechanism in $V_{0.0015}NbSe_2$. So, it can be predicted that another mechanism is responsible for this kind of high field peak. There are lots of literature surveys about the peak effect in F_p of

$NbSe_2$ system **[37]**. According to these analyses, peak effect in $NbSe_2$ appears only when a dimensional crossover occurs. Koorevaar *et al.* **[38]** reported high field's peak in F_p in thin single crystals of $NbSe_2$ which sets at about $b_{co} \approx 0.8H_{c2}$ in fields directed perpendicular to the layers. The onset of the peak is demonstrated as the transition to three-dimensional FLL disorder following to the considerable reduction of tilt modulus. This means that $V_{0.0015}NbSe_2$ acts as a three-dimensional anisotropic vortex lattice with flexible FLL structures allowing a rapid relaxation of diamagnetic magnetization.

The variation of F_p with H and most significantly the peak in F_p near H_{c2} *i.e.*, the "peak effect", has also been studied extensively by Pippard *et al.* **[39].** He ascribed it to the softening of the elastic modulus of the FLL and the easy compliance of the same to the pinning configuration. However, it is observed (from Figure 7.8 (*c*)) that the peak of f_p shifts to h = 0.33 for T = 3 K which indicates the point pinning mechanism as a dominating one in $V_{0.0015}NbSe_2$. Even at higher temperature (T = 3.5 K) there is an overlap of peaks associated with different pinning mechanism due to thermal fluctuation. So, it can be concluded that due to the rapid softening of the tilt modulus and hence of the FLL, the high field peak appears in $V_{0.0015}NbSe_2$. The onset of the peak supports crossover from 2D to 3D disorder of FLL with the presence of 3D collective pinning (3DCP) before H^{on}. As the temperature increases, the F_p peak shifts to lower magnetic field indicating point pinning as a dominating pinning mechanism in $V_{0.0015}NbSe_2$.

Moreover, in order to shed light on the geometry of pinning centres in $V_{0.001}NbSe_2$, the normalized pinning force is fitted with the equation (7.1):

$$f(h) = ah^{0.5}(1-h)^2 + bh(1-h)^2 \qquad (7.1)$$

The f_p curves are well fitted with equation (7.1) as shown in Figure 7.8 (*b*). The fitting parameters (*a*, *b*) indicate that the surface pinning dominates over the point pinning mechanism. The V impurities act here as point pinning centres. As we stated above, Dew-Hughes also indicated that h_{max} = 0.33 and 0.2 corresponding to the point core pinning and surface pinning, respectively. Thus, H_{max} = 0.2 in the $V_{0.001}NbSe_2$ indicates towards the surface core pinning as the dominating pinning mechanism. There is also a

clear deviation of f_p *vs.* h curves from the fitted plot following equation (7.1) at higher magnetic fields, which refers to the onset of flux creep phenomena. The presence of BL zero-field peak and the high field peak are not observed in the f_p - h plot of $V_{0.001}NbSe_2$, which excludes the possibility of BL surface barrier effect and the lattice softening in $V_{0.001}NbSe_2$ single crystal.

7.2.3. Magnetoresistance Study:

Figure 7.9 (*a*) shows the temperature dependence of the normalized resistance ($R/R_{300\,K}$) of $V_{0.0015}NbSe_2$ demonstrating a metallic characteristic ($dR/dT > 0$) between T ≈ 50 K temperature and 300 K temperature similar to $Fe_{0.0015}NbSe_2$ single crystals [48]. The residual resistivity (ρ_0), room temperature resistivity (ρ_{300}) and the residual resistivity ratio ($RRR = (\rho(300\ K)/\ \rho(T_c))$ of $V_{0.0015}NbSe_2$, which are calculated from Figure 7.9 (*a*), have values 6.5×10^{-5} Ω-cm, 7.58×10^{-4} Ω-cm, 6.95, respectively. In $V_{0.0015}NbSe_2$, ρ_0 was estimated by assuming a power law dependence for the ideal resistance ($R_i = R\text{-}R_0$).

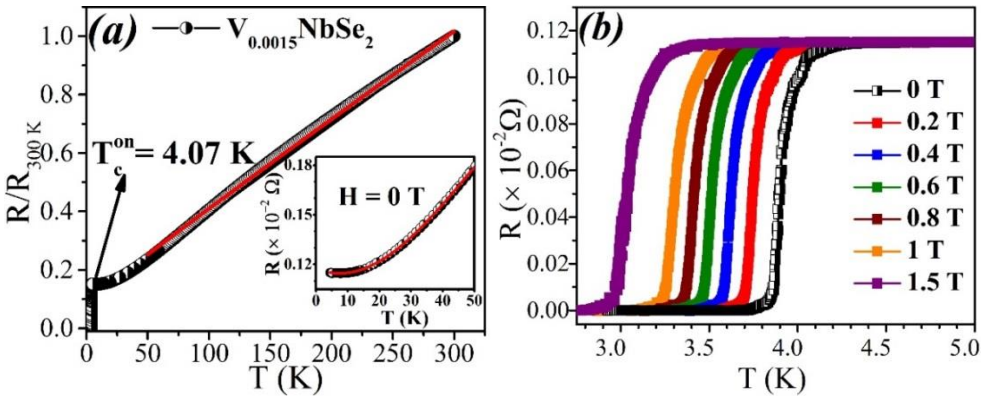

Figure 7.9. *(a) Normalised temperature dependent resistance plot of $V_{0.0015}NbSe_2$ indicating metallic characteristics (indicated by red solid line) in the temperature interval 50 K < T < 300 K. The inset shows excellent fitting of the data from 4 K to 50 K considering electron-electron scattering (~ T^2) and interband scattering (~ T^3). (b) Resistance measurement of $V_{0.0015}NbSe_2$ at 0.2 T, 0.4 T, 0.6 T, 0.8 T, 1 T and 1.5 T magnetic fields along the ab-plane of the crystal surface.*

Low temperature region (5 K ≤ T ≤ 50 K) of $R\ (T)$ of $V_{0.0015}NbSe_2$ (inset of Fig. 7.9 (*a*)) shows good fitting considering the contribution from

electron-electron scattering (~ T^2) and phonon mediated inter-band *s-d* scattering (~ T^3) which can be attributed to the disorder induced by V impurities. Furthermore, by taking the criteria of 90% R_n (where R_n indicates the resistance at T= 5 K), the onset transition temperature at zero field ($T_c^{on}(H=0)$) is estimated at 4.07 K, while the zero resistance temperature ($T_c^{(R=0)}$) is as 3.7 K. The $T_c^{on}(H=0)$ value of $V_{0.0015}NbSe_2$ shifts to lower temperature as compare to $NbSe_2$ (~ 6.5 K) as we observed in our previous magnetization study **[23]**. The possible reason of the degradation of T_c of $V_{0.0015}NbSe_2$ has been discussed elaborately in the previous section. Figure 7.9 (*b*) represents the temperature dependence of resistance at 0.2 T, 0.4 T, 0.6 T, 0.8 T, 1 T and 1.5 T magnetic fields in the highest V concentration (*i.e.*, $V_{0.0015}NbSe_2$).

7.2.3.1. Glassy transition:

Further to investigate the presence of the glassy state of FLL in $V_{0.0015}NbSe_2$, we have studied the magnetoresistance data at different magnetic fields. The electrical resistance is studied below the TAFF region following to the vortex glass theory. The temperature dependence of resistance in the vortex - glass critical region (*i.e.* the region between vortex glass transition temperature (T_g) and vortex glass critical temperature (T^*)) follows the linear relation $R\,(T) \propto (T - T_g)^s$, where s is the critical exponent **[40]**.

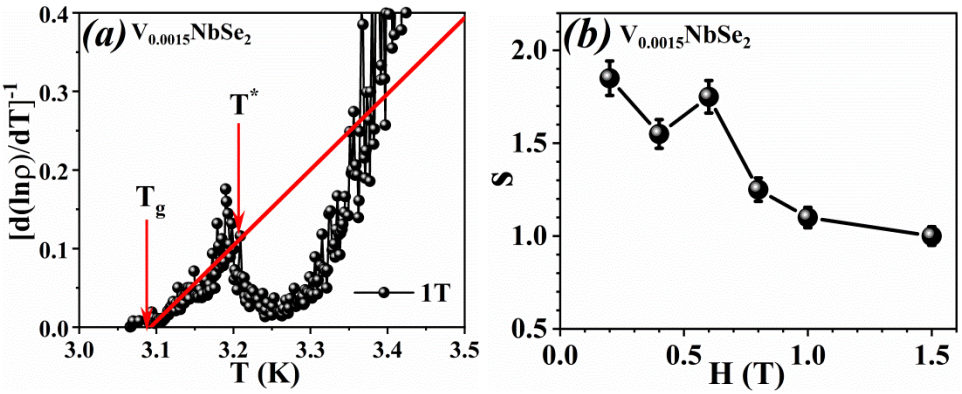

Figure 7.10. *(a) Inverse logarithmic derivative of resistance of $V_{0.0015}NbSe_2$ at H = 1 T. The red solid line represents the fitting to vortex glass critical region using the relation $[d(lnR)/dT]^{-1} = (1/s)(T - T_g)$. The red arrows indicate the vortex glass transition temperature (T_g) and vortex glass critical temperatures (T^*); (b) The magnetic field dependence of critical exponent s (H).*

As shown in Figure 7.10 (*a*), the linear resistance below vortex glass critical temperature T^* (as indicated by red arrow) is well described by this equation and a straight line is shown in the critical region of the glass transition of $\left[\frac{\partial lnR}{\partial T}\right]^{-1}$ *vs.* T plot. The T_g value at each magnetic field is determined from the extrapolation as shown by red arrow of Figure 7.10 (*a*). Here T^* is described as the temperature which departs from the linear electrical resistance of the vortex glass state and is approximately equal to the temperature at the lower side deviating from the TAFF fitting. In Figure 7.10 (*b*), the estimated critical exponent *s* is plotted as a function of magnetic field which is smaller than 2.7 for all magnetic fields. This is the lower limit of *s* predicted by 3D vortex glass theory **[2]**. So, it can be concluded here that the vortices are frozen to 2D vortex glassy state below TAFF region and coincide with the region of SMP effect at lower magnetic fields.

7.2.3.2. Temperature dependence of resistance in TAFF region:

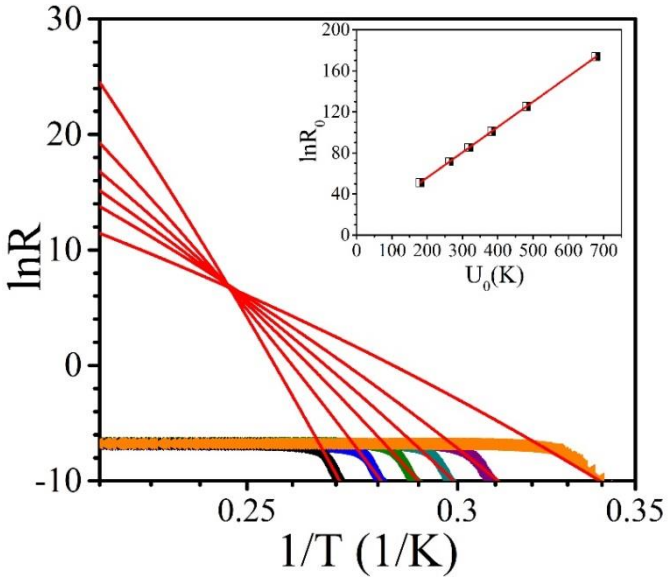

Figure 7.11. *Arrhenius plot of resistance of $V_{0.0015}NbSe_2$ at H = 0.2 T, 0.4 T, 0.6 T, 0.8 T, 1 T and 1.5 T magnetic fields where the solid lines are linearly fitted to the TAFF regions.*

Now to investigate the effect of V substitution on the motion of thermally activated vortices in TAFF region of $NbSe_2$, we evaluated the temperature and magnetic field dependence of thermal activation energy from the magnetoresistance measurement of $V_{0.0015}NbSe_2$. The broadening

of the superconducting transition width in external magnetic field is strongly related to the thermally activated flux flow mechanism.

Considering the lower value of J_c and *JBVL* (<< 1), (where *V* and *L* are the bundle volume and hopping distance) the temperature dependence of resistance in TAFF region can be described as

$$R = \frac{2R_cU}{T} exp\left(-\frac{U}{T}\right) = R_{0f} \exp(-\frac{U}{T}) \quad (7.2)$$

Where U $(= J_{C0}bVL)$ symbolises TAE of FLL in TAFF region and $R_c = v_0LB/J_{c0}$ is a temperature independent constant. Assuming $R_{0f}\left(= \frac{2R_cU}{T}\right)$ = constant and linear dependence of TAE on temperature (*i.e.*, U (T, H) = $U_0(H)\left(1-\frac{T}{T_c}\right)$) , the relation between ln$R$ vs. 1/T provides the Arrhenius plot letting $lnR\ (T,H) = lnR_0(H) - U_0(H)/T$ where $lnR_0(H) = lnR_{of} + U_0(H)/T_c$. The slope of *lnR* vs. *1/T* curve gives $U_0(H)$ value which is known as apparent activation energy with the y intercept as $lnR_0(H)$.

Figure 7.11 demonstrates the Arrhenius plots of $V_{0.0015}NbSe_2$ single crystal at magnetic fields of H = 0.2 T, 0.4 T, 0.6 T, 0.8 T, 1 T and 1.5 T in TAFF region. The U_0 value is extracted from the slope of the fitted line to the linear region of Arrhenius plot (as presented by the solid lines in Figure 7.11). All the fitted lines intersect at T_{cross} at 4.06 K which is in good agreement with T_c^{onset} of $V_{0.0015}NbSe_2$. The inset of Figure 7.11 shows the linear relationship between lnR_0 and U_0 with the T_c value (*i.e.*, inverse of the slope of linear fitting) at 4.06 K which is also comparable to T_c^{onset}. So, the Arrhenius plot gives the accurate value of U_0 in $V_{0.0015}NbSe_2$.

7.2.3.3. Magnetic field dependence of TAE:

Figure 7. 12 represent the magnetic field dependence of U_0 that has value 266 K at 1 T in $V_{0.0015}NbSe_2$. It can be seen that the U_0 value is decreased significantly in $V_{0.0015}NbSe_2$ as compare to $NbSe_2$ **[41]**. These results suggest that FLL become more entangled due to the point defects and emerges 2D nature in TAFF region of $V_{0.0015}NbSe_2$. This makes the easy movement of flux lines through FLL resulting reduction of U_0 **[42]**. However, another reason behind the reduction of U_0 *(H)* can also be the

weakening of the F_p *(H)*. Liu *et al.* **[43]** reported the reduction in U_0 *(H)* in optimally doped and overdoped $(Ba_{1-x}K_x)Fe_2As_2$ single crystals due to the weak δT_c pinning. In contrast, the underdoped $(Ba_{1-x}K_x)Fe_2As_2$ single crystal shows large U_0 *(H)* value which is associated with strong vortex pinning. Ağil *et al.* **[44]** also reported that the addition of Gd to BSCCO superconductor weakens the link of the grains (*i.e.* reduces the surface pinning) and thus there is a reduction of U_0 compare to pure sample. However, the higher J_c *(0)* value and the high field F_p peak exclude the possibility of reduction of pinning energy of $V_{0.0015}NbSe_2$ compare to pure $NbSe_2$ **[23]**. So it can be concluded that the FLL is in more entangle state in $V_{0.0015}NbSe_2$ due to the presence of point defects resulting lower U_0 *(H)*.

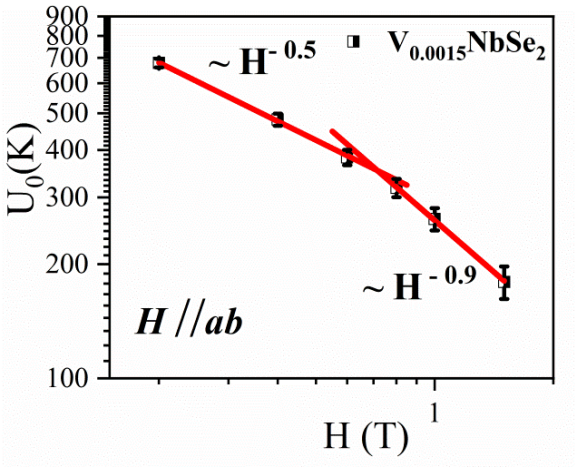

Figure 7.12. *Apparent activation energy (U_0 (K)) of $V_{0.0015}NbSe_2$ is plotted against H on log-log scale. The solid lines represent power-law fitting with U_0 (H) ~ $H^{-\alpha}$.*

In order to examine the field dependence nature of U_0, a log-log graph of U_0 is plotted against the applied magnetic field (Figure 7.12). The U_0 values of $V_{0.0015}NbSe_2$ follow the power law dependence with magnetic field in the form of,

$$U_0 (H) \sim H^{-\alpha} \qquad (7.3)$$

The exponent α has a smaller value 0.5 up to H = ~ 0.7 T and a large value 0.9 over ~ 0.7 T, for H || ab plane. This is the similar mechanism as shown in many iron-based superconductors **[45]**. As mentioned by Choi *et al.* **[42]**, the U_0 *(H)* value of Co doped $NaFe_{1-x}Co_xAs$ (with x = 0.01, 0.03 and 0.07) follows power law relation with lower α value (~ 0.29) below H ~ 2 T and larger α value (~ 0.7) at higher magnetic field for H || ab plane indicating

two different pinning mechanisms. Under the *E-P* crossover model, U_0 should increase with magnetic fields in the elastic creep regime following the relation $U_0 \propto H^{v} J^{\mu}$ with a positive v value. However, according to the plastic-flux-creep-theory, the magnetic field dependence of U_0 should follow the relation $U_0 \sim H^{-0.5}$**[46, 47]**. In this region, the vortices are plastically deformed and entangled due to the point defects in the potential background of weak pinning. In the high magnetic fields, the entangled vortices are cut and disconnected due to the faster motion of vortices so that the $U_0(H)$ follows the relation $U_0 \sim H^{-0.7}$**[48]**. The even faster reduction in U_0 with magnetic fields is obtained due to the entangled vortex liquid behaviour in a state of stronger pinning associated with point defects. From this point of view, it is reasonable to assume that the field dependence of U_0 in $V_{0.0015}NbSe_2$ is governed by weak plastic pinning upto H = 0.7 T and after that it follows stronger entangled state in vortex liquid phase.

7.2.3.4. Vortex phase diagram of $V_{0.0015}NbSe_2$:

In Figure 7.13, the vortex phase diagram plot of $V_{0.0015}NbSe_2$ single crystal has been represented based on magnetization and magneto-transport studies. The characteristic fields like H_{c2}, H_{irr}, H^*, H_g are confirmed from the magneto-transport measurement and the other two fields - H_{SMP} and H_p are confirmed from the magnetization measurement. The $H_{c2}(T)$ and $H_{irr}(T)$ values are estimated from the magnetoresistance measurement using the 90% and 10 % R_n criteria at a constant magnetic field as shown in Figure 7.13. The locations of H^* and H_g are obtained from the deviation of the temperature dependence of resistance from vortex glass critical region (as shown by open and solid squares in Figure 7.13), respectively. However, H_{SMP} and H_p indicate the peaks associated with SMP effect and PE effect which are determined from the anomalous variations of J_c with magnetic field. The H_{c2}-T curve is fitted with the anisotropic Ginzburg-Landau model, $H_{c2}(T) = H_{c2}(0)\left[\left(1-\frac{T}{T_c}\right)^{a}\right]^{b}$ (as indicated by black solid line) associated with the Nb bands at Fermi energy level as we stated earlier **[50]**. The temperature dependence of H_{irr} is fitted with the relation, $H_{irr}(T) = H_{irr}(0)[1-((T/T_c)^2]^{3/2}$ as represented by red solid line in the vortex

phase diagram. This indicates the presence of giant flux creep in $V_{0.0015}NbSe_2$ **[49]**.

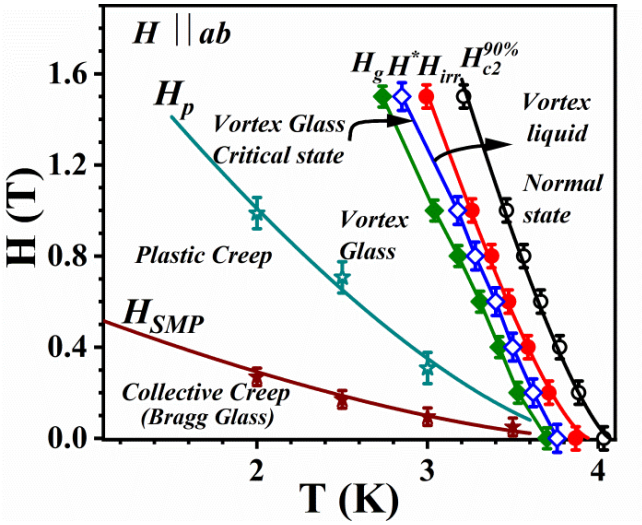

Figure 7.13. *Vortex phase diagram plot of $V_{0.0015}NbSe_2$ shows different phases, i.e., the collective creep region, plastic creep region, vortex glass state, vortex glass critical state, and the vortex liquid state. The solid lines correspond to the fits performed to the $H_{c2}^{90\%} - T$, $H_{irr} - T$, H_{SMP} - T and H_p- T curves.*

As H_{SMP} -T curve don't follow linear behaviour, so it can be predicted to have different origin from those superconductors having linear dependence of H_{SMP} on T. The curve is well fitted with functional relationship having the expressions $H_{SMP}(T) = H_{SMP}(0) \times (1 - \frac{T}{Tc})^{1.5}$ with $H_{SMP}(0)$ = 0.51 T. Sugui *et al.* **[51]** reported similar positive curvature with decreasing temperature for T ≥ 6 K in deoxygenated $YBa_2Cu_3O_{6.65}$ single crystal with the relation $(1 - T/T_c)^m$ with m = 1.5. They refer it to the crossover from plastic pinning that controls creep above H_p to the collective pinning below H_p. In the latter section we demonstrate the difference in the relaxation rate with temperatures for these two pinning mechanisms resulting in the positive curvature of SMP with decreasing temperature. Similar case is observed by Ahmed *et al.* **[32]** in the optimally doped and overdoped $NaFe_{1-x}Co_xAs$ single crystals (with x = 0.03, 0.05 and 0.07) for H//c axis. However, Abulafia *et al.* **[52]** showed the temperature dependence of SMP position with the relation H_p = [1- $(T/T_c)^4$]$^{1.4}$ which supports the origin of the fishtail effect as a crossover from elastic to plastic creep in YBCO crystals. So, the temperature dependence of SMP studies

indicates the H_{SMP}-T line as a transition from collective pinning region to the plastic pinning region. Based on the above analysis, the H-T space of $V_{0.0015}NbSe_2$ (especially the region between H_{SMP} (T) and the H_{c2} (T) curves) has been divided into several vortex phase regions. The regime below H_{SMP} represents the collective creep phase which is also marked as the quasi ordered Bragg glass state. It is avoided here to make the domains of the low field single vortex pinning region of $V_{0.0015}NbSe_2$ as distinct from the collectively pinned state. The region between H_{SMP} and H_p is designated as the plastic creep regime which merges with the disorder dominated vortex glass state at H_p. The transition at H_p might be an indication of the disorder like melting, *i.e*., from the plastically deformed solid to a pinned amorphous state. The region after H_p specifies the dislocation mediated vortex glass phase where FLL shows 2D characteristics. The narrow regime between the $H_g(T)$ and $H^*(T)$ has been noticeable as the vortex glass critical state indicating the initialization of the resistive region of vortex phase diagram. However, the regions above $H^*(T)$ has been named as vortex liquid state. Finally, the state above H_{c2} is referred as normal state suggesting the complete destruction of superconducting state of $V_{0.0015}NbSe_2$.

7.3. Summary

We investigated here the nature of the vortex motion and the corresponding vortex phase diagram in different regions of mixed state of V_xNbSe_2 (with x = 0.0007, 0.001 and 0.0015) using the magnetic and magnetoresistance measurement for H//ab plane. The presence of the V atoms acts as weak point defect centres which result the SMP effect in the M-H curves of all V doped $NbSe_2$. The enhancement of the V concentration boosts the fishtail effect and the corresponding SMP effect, like in $V_{0.0015}NbSe_2$ as compared to $V_{0.0007}NbSe_2$. At the low magnetic field regions, the J_c indicates nearly non-interacting vortex lattice following the single vortex, and small bundle pinning regime. At the intermediate magnetic field, J_c follows 3D collective creep in the form of the large bundle and then enters into the disorder-induced SMP region. At higher temperatures, the SMP moves away from H_{c2} to the lower magnetic field

and finally disappear near transition region. This characteristic of the SMP effect confirms the crossover of flux lattice from interaction dominated collective creep region to the disorder dominated plastic creep region. Moreover, the f_p *vs. h* curve shows zero field peak because of the BL surface barrier effect. In $V_{0.0015}NbSe_2$, the BL zero field peak is highly suppressed by the higher field peak. There is no BL zero-field peak and the higher field peak in $V_{0.001}NbSe_2$ single crystal. However, the prominent peak at the higher magnetic field region (near H_{irr}) indicates 2-dimensional to 3-dimenstional lattice distortion associated with lattice softening in $V_{0.0007}NbSe_2$ and $V_{0.0015}NbSe_2$. Magneto-transport measurements of $V_{0.0015}NbSe_2$ show glassy transition from Bragg-glass to vortex glass region below the TAFF region with 2D like characteristics. The temperature dependence of resistance of $V_{0.0015}NbSe_2$ is analysed in the TAFF region with Arrhenius relation by considering the linear temperature dependence of U_0 (H). The magnetic field dependence of U_0 (H) shows a power law relationship following the relation U_0 (H) ~ $H^{-\alpha}$. The exponent increases from 0.5 to 0.9 at a crossover field of ~ 0.7 T indicating two different pinning mechanisms in $V_{0.0015}NbSe_2$. It suggests that there is a crossover from weak plastic pinning to strong entangled state in the vortex liquid state due to the highly dissipative motion of flux lattice in the presence of weak disorder. Finally, the vortex phase diagram of $V_{0.0015}NbSe_2$ shows collective creep region (*i.e.*, the Bragg Glass state), plastic creep region, vortex glass state, vortex glass critical state and vortex liquid state at different regions of magnetic fields and temperatures.

References

[1] Higgins M. J., Bhattacharya S. (1996), Varieties of dynamics in a disordered flux-line lattice, Physica C, 257, 232-254.

[2] Blatter G., Feigel'man M. V., Geshkenbein V. B., Larkin A. I., Vinokur V. M. (1994), Vortices in high-temperature superconductors, Rev. Mod. Phys., 66, 1125-1388.

[3] Zeldov E., Majer D., Konczykowski M., Vinokur V. M., Shtrikman H. (1995), Thermodynamic observation of first-order vortex-lattice melting transition in $Bi_2Sr_2CaCu_2O_8$, Nature, 375, 373-376.

[4] Schilling A., Fisher R. A., Phillips N. E., Welp U., Dasgupta D., Kwok W. K., Crabtree G. W. (1996), Calorimetric measurement of the latent heat of vortex-lattice melting in untwinned $YBa_2Cu_3O_{7-\delta}$, Nature, 382, 791-793.

[5] Fisher D. S., Fisher M. P. A., Huse D. A. (1991) Thermal fluctuations, quenched disorder, phase transitions, and transport in type-II superconductors, Phys. Rev. B, 43, 130-159.

[6] Daeumling M., Seuntjens J. M., Larbalestier D. C. (1990), Oxygen-defect flux pinning, anomalous magnetization and intra-grain granularity in $YBa_2Cu_3O_{7-\delta}$, Nature, 346, 332-335.

[7] Giamarchi T., Doussal P. L. (1994), Elastic theory of pinned flux lattices, Phys. Rev. Lett., 72, 1530-1533.

[8] Klein L., Yacoby E. R., Yeshurun Y., Erb A., Muller-Vogt G., Breitn V., Wuhl H. (1994), Peak effect and scaling of irreversible properties in untwinned Y-Ba-Cu-O crystals, Phys. Rev. B, 49, 4403-4406.

[9] Yeshurum Y., Bontemps N., Burlachkov L., Kapitulnik A. (1994), Dynamic characteristics of the anomalous second peak in the magnetization curves of Bi-Sr-Ca-Cu-O, Phys. Rev. B, 49, 1548-1551.

[10] Van Der Beek C. J. *et al* (2010), Flux pinning in $PrFeAsO_{0.9}$ and $NdFeAsO_{0.9}F_{0.1}$ superconducting crystals, Phys. Rev. B, 81, 174517.

[11] Senatore C., Flükiger R., Cantoni M., Wu G., Liu R. H., Chen X. H. (2008), Upper critical fields well above 100 T for the superconductor $SmFeAsO_{0.85}F_{0.15}$ with T_c = 46 K, Phys. Rev. B, 78, 054514.

[12] Prozorov R. *et al* (2008), Vortex phase diagram of $Ba(Fe_{0.93}Co_{0.07})_2As_2$ single crystals, Phys. Rev. B, 78, 224506.

[13] Lortz R., Musolino N., Wang Y., Junod A., Toyota N. (2007), Origin of the magnetization peak effect in the Nb_3Sn superconductor, Phys. Rev. B, 75, 094503.

[14] Pissas M., Lee S., Yamamoto A., Tajima S. (2002), Peak effect in single crystal MgB_2 superconductor for H$\|$*c*-axis, Phys. Rev. Lett., 89, 097002.

[15] Kwok W. K., Fendrich J. A., Van der Beck C. J., Crabtree C. W. (1994), Peak effect as a precursor to vortex lattice melting in single crystal $YBa_2Cu_3O_{7-\delta}$, Phys. Rev. Lett., 73, 2614.

[16] Bhattacharya S., Higgins M. J. (1993), Dynamics of a disordered flux line lattice, Phys. Rev. Lett., 70, 2617-2620.

[17] Nishizaki T., Kobayashi N. (2000) Vortex-matter phase diagram in $YBa_2Cu_3O_y$, Supercond. Sci. Technol., 13, 1.

[18] Klein L., Yacoby E. R., Yeshurun Y., Erb A., Müller-Vogt G., Breitn V., Wühl H. (1994), Peak effect and scaling of irreversible properties in untwinned Y-Ba-Cu-O crystals, Phys. Rev. B, 49, 4403-4406.

[19] Yeshurun Y., Bontemps N., Burlachkov L., Kapitulnik A. (1994), Dynamic characteristics of the anomalous second peak in the magnetization curves of Bi-Sr-Ca-Cu-O, Phys. Rev. B, 49, 1548-1551.

[20] Hardy V., Wahl A., Ruyter A., Maignan A., Martin C., Coudrier L., Provost J., Simon Ch. (1994), The fishtail effect in different Tl based single crystals. A possible interplay with the electronic anisotropy, Physica C, 232, 347-358.

[21] Pervin R., Krishnan M., Rana A. K., Arumugam S., Shirage P. M. (2018), Effect of Cr atoms in vortex dynamics of $NbSe_2$ superconductor and study of second magnetization peak effect, Mater. Res. Express., 5, 076001.

[22] Krishnan M., Pervin R., Ganesan K. S., Murugesan K., Lingannan G., Verma A. K., Shirage P. M., Sonachalam A. (2018), Pressure assisted enhancement in superconducting properties of Fe substituted $NbSe_2$ single crystal, Sci. Rep., 8, 1251.

[23] Pervin R., Krishnan M., Rana A. K., Arumugam S., Shirage P. M. (2017), Enhancement of superconducting critical current density by Fe impurity substitution in $NbSe_2$ single crystals and the vortex pinning mechanism, Phys. Chem. Chem. Phys., 19, 11230-11238.

[24] Luo H., Nowak J. S., Li J., Tao J., Klimczuk T., Cava R. J. (2017), S-shaped suppression of the superconducting transition temperature in Cu-intercalated $NbSe_2$, Chem. Mater., 29, 3704-3712.

[25] Chen L., Li C., Tang H., Li H., Liu X., Meng J. (2014), First-principles calculations on structural, electronic properties of V-doped 2H-$NbSe_2$, RSC Adv., 4, 9573-9578.

[26] Werthamer N. R., Helfand E., Hohenberg P. C. (1966), Temperature and purity dependence of the superconducting critical field, H_{c2}. |||. Electron spin and spin-orbit effects, Phys. Rev., 147, 295-302.

[27] Paltiel Y., Fuchs D. T., Zeldov E., Myasoedov Y. N., Shtrikman H., Rappaport M. L., Andrei E. Y. (1998), Surface barrier dominated transport in $NbSe_2$, Phys. Rev. B, 58, R14763-R14766.

[28] Welp U., Kwok W. K., Crabtree G. W., Vandervoot K. G., Liu J. Z. (1990), Magnetization hysteresis and flux pinning in twinned and untwinned $YBa_2Cu_3O_{7-\delta}$, Appl. Phys. Lett., 57, 84-86.

[29] Bean C. P. (1962), Magnetization of hard superconductors, Phys. Rev. Lett., 8, 250-253.

[30] Larkin A. I. (1970), Effect of inhomogeneities on the structure of the mixed state of superconductors, Sov. Phys.-JETP, 31, 784.

[31] Larkin A. I., Ovchinnikov Y. N. (1979), Pinning in type II superconductors, J. Low Temp. Phys., 34, 409-428.

[32] Ahmad D., Choi W. J., Seo Y. I., Jung S. G., Kim Y. C., Sugui S. S., Park T., Kwon Y. S. (2017), Doping dependence of the vortex dynamics in single-crystal superconducting $NaFeCo_xAs$, Supercond. Sci. Technol., 30, 105006.

[33] Banerjee S. S., Ramakrishnan S., Grover A. K., Ravikumar G., Mishra P. K., Sahni V. C., Tomy C. V., Balakrishnan G., Paul D. M., Gammel P. L., Bishop D. J., Bucher E., Higgins M. J., Bhattacharya S. (2000), Peak effect, plateau effect and fishtail anomaly: The re-entrant amorphization of vortex matter in 2H-$NbSe_2$, Phys. Rev. B, 62, 11838-11845.

[34] Nishizaki T., Naito T., Kobayashi N. (1998), Anomalous magnetization and field-driven disordering transition of a vortex lattice in untwinned $YBa_2Cu_3O_y$, Phys. Rev. B, 58, 11169-11172.

[35] Küpfer H., Wolf Th., Lessing C., Zhukov A. A., Lanon X., Hirmer R. M., Schauer W., Wuehl H. (1998), Peak effect and its evolution from oxygen deficiency in $YBa_2Cu_3O_{7-\delta}$ single crystals, Phys. Rev. B, 58, 2886.

[36] Dew-Hughes D. (1974), Flux pinning mechanisms in type II superconductors, Phil. Mag., 30, 293-305.

[37] Koorevaar P., Aarts J., Berghuis P., Kes P. H. (1990), Tilt-modulus enhancement of the vortex lattice in the layered superconductor 2H-$NbSe_2$, Phys. Rev. B, 42, 1004(R).

[38] Koorevaar P., Aarts J., Berghuis P., Kes P. H. (1990), Flux pinning and peak effects in single crystalline 2H-$NbSe_2$, Phys. B, 165-166, 1167-1168.

[39]Pippard A. B. (1969), A possible mechanism for the peak effect in type II superconductors, Philos. Mag., 19, 217-220.

[40] Fisher M. P. A. (1989), Vortex-glass superconductivity: A possible new phase in bulk high-T_c oxides, Phys. Rev. Lett., 62, 1415-1418.

[41] Kaushik S. D., Braccini V., Patnaik S. (2008), Magnetic field dependence of vortex activation energy: A comparison between MgB_2, $NbSe_2$ and $Bi_2Sr_2Ca_2Cu_3O_{10}$ superconductor, Pramana, 71, 1335-1343.

[42] Choi W. J., Seo Y. I., Ahmad D., Kwon Y. S. (2017), Thermal activation energy of 3D vortex matter in $NaFe_{1-x}Co_xAs$ (x = 0.01, 0.03 and 0.07) single crystals, Sci. Rep., 7, 10900.

[43] Liu Y., Zhou L., Sun K., Straszheim W. E., Tanatar M. A., Prozorov R., Lograsso T. A. (2018), Doping evolution of the second magnetization peak and magnetic relaxation in $(Ba_{1-x}K_x)Fe_2As_2$ single crystals, Phys. Rev. B, 97, 054511.

[44] Ağıl H. (2018), Study of microstructure and magneto-transport properties in $Bi_{1.6}Pb_{0.4}Sr_2Ca_3Gd_xCu_4O_\delta$ superconducting systems, J Mater. Sci.: Mater. Electron., 29, 16157-16165.

[45] Wang X. L. *et al.* (2010), Very strong intrinsic flux pinning and vortex avalanches in (Ba, K)Fe_2As_2 superconducting single crystals, Phys. Rev. B, 82, 024525.

[46] Geshkenbein V., Larkin A., Feigel'man M., Vinokur V. (1989), Flux pinning and creep in high-T_c superconductors, Physica C, 16, 2 239-240.

[47] Kierfeld J., Nordborg H., Vinokur V. M. (2000), Theory of plastic vortex creep Phys. Rev. Lett. 85 4948.

[48] Vinokur V. M., Feigel'man M. V., Geshkenbein V. B., Larkin A. I. (1990), Resistivity of high-T_c superconductors in a vortex-liquid state, Phys. Rev. Lett., 65, 259-262.

[49] Qin M. J., Wang X. L., Liu H. K., Dou S. X. (2002), Evidence for vortex pinning induced by fluctuations in the transition temperature of MgB_2 superconductors, Phys. Rev. B, 65, 132508.

[50] Zehetmayer M., Weber H. W. (2010), Experimental evidence for a two-band superconducting state of $NbSe_2$ single crystals, Phys. Rev. B: Condens. Matter Mater. Phys., 82, 014524.

[51] Sugui S. S., Ghivelder L., Friesen M., Moloni K., Veal B., Paulikas P. (1999), Temperature dependence of the second magnetization peak in a deoxygenated $YBa_2Cu_3O_{6.65}$ single crystal, Phys. Rev. B, 60, 102-105.

[52] Abulafia Y., Shaulov A., Wolfus Y., Prozorov R., Burlachkov L., Yeshurun Y., Majer D., Zeldov E., Wühl H., Geshkenbein V. B., Vinokur V. M. (1996), Plastic vortex creep in $YBa_2Cu_3O_{7-x}$ crystals, Phys. Rev. Lett., 77, 1596.

CHAPTER 8

The Conclusions and Scope of Future Work

The core basis of this thesis work is to synthesize large single crystals of $NbSe_2$ with high purity through Iodide vapour transport method for their physical properties characterization to understand the basic mechanism and improve the potential applications. Prominence is provided to study the three fundamental superconducting characteristics (T_c, H_c, and J_c) of $NbSe_2$ in presence of intrinsic and extrinsic defects through magnetic, electronic and magneto-transport measurements. Efforts have been made to understand the vortex dynamics and pinning mechanism of $NbSe_2$ single crystals in presence of foreign atoms like iron (Fe), Cromium (Cr) and Vanadium (V) to realize large, non-dissipative currents in superconductors for various applications.

8.1. Thesis summary

A brief review of different superconducting materials, quasi 2D transition metal dichalcogenides: $NbSe_2$ and diverse physical properties of $NbSe_2$ are discussed in *Chapter 1*.

As stated in the introduction part (*Chapter 1*), there are number of superconducting materials including both low T_c and high T_c superconductors which are discovered for diverse physical properties and various practical applications. However, progressive and excellent research have shown gradual improvement in the physical properties study of different superconductors for better device performance as reported by many scientists. One of the biggest challenges of understanding the fundamental properties of high T_c superconductors is their highly anisotropic and complex crystal structure which involves many atoms. As a result, the discovery of room temperature superconductors is still far from accomplished. Therefore, this thesis took the opportunity to present a comprehensive approach to improve the physical properties of $NbSe_2$ single crystals for understanding the basic physical properties of highly anisotropic, layered superconductors and to realize it for various possible applications.

Chapter 2 describes the different fundamental models that are employed in this research work to analyze the superconducting properties associated with transport and magnetic measurements.

In *Chapter 3*, describes the prime experimental techniques that are employed in this thesis for the growth of materials and characterization.

In *chapter 4*, the effect of Fe doping in $NbSe_2$ single crystals is studied. This study includes the effect of Fe doping on the structural, magnetic and superconducting properties and understanding the physics behind the dissipative vortex motion and the associated pinning mechanism in response to the *dc* magnetic fields. The successful incorporation of Fe atoms is confirmed by XRD analysis and the systematic degradation of T_c value. It enables for further possible characterization of Fe-doped $NbSe_2$. We have studied the effect of Fe impurities on the basis of Larkin-Ovchinnikov (LO) 3D collective pinning model in $NbSe_2$. With

enhancement of the concentration of Fe impurities, the $J_c(0)$ value enhances appreciably compared to pure $NbSe_2$. The random pinning potential that is introduced by the Fe atoms is studied through the interaction between the core region of vortices and the pinning centres. It results a competitive nature between the single vortex, small bundle and the large bundle pinning regions. Furthermore, the field dependence of pinning force density in both pure and Fe doped $NbSe_2$ is investigated through Dew Hughes and Kramer's point pinning and surface pinning model. The normalized pinning force density shows the presence of both point pinning and the surface pinning mechanism with a broadening of the peak in the Fe doped $NbSe_2$. Through studying all the superconducting properties, we conclude that the addition of Fe atom assists the practical applicability of $NbSe_2$.

In *chapter 5*, the effect of Cr doping in $NbSe_2$ single crystals is studied. Basically, in our previous report on Fe_xNbSe_2, our prime focus was to improve J_c *(0)* value and to study the associated pinning mechanism. The addition of Fe atoms in $NbSe_2$ successfully improved the J_c value at low magnetic fields. However, there is a rapid degradation of J_c in the high magnetic field regions. Besides, the presence of the Fe impurities reduces the H_{c2} (T) and T_c values significantly by enhancing the pair breaking phenomena. Therefore, in this chapter, we had focussed to grow Cr_xNbSe_2 single crystals to understand the mechanism to improve the J_c characteristics at high magnetic field. So, we have reported the high-quality single crystal of Cr_xNbSe_2 to study the effect of Cr impurity on $NbSe_2$ superconductor using M - H curves with different relaxation rates. We have observed significant improvement in the field dependence nature of J_c characteristics at low as well as high magnetic field regions with increasing the Cr concentration in $NbSe_2$. The crossover from elastic (E) to plastic (P) creep region is observed which results SMP effect or the fishtail effect at the highest Cr concentration. The interaction between the core region of vortices and pinning centres is investigated based on δl pinning and δT_c pinning. The highest Cr concentration allows both δl pinning and δT_c pinning which enhance the coupling between the vortices. Furthermore, the magnetic field dependence of pinning force density shows diverse features

associated with different pinning mechanism at different magnetic fields. All the Cr concentration result zero field *BL* peak related to the surface barrier effect. Moreover, the appearance of the prominent peak near H_{c2} indicates the lattice softening at higher Cr concentrations (*i.e.*, at $Cr_{0.0009}NbSe_2$ and $Cr_{0.0012}NbSe_2$). These studies not only provide fundamental study of vortex dynamics of Cr_xNbSe_2 but also open the door for further study in high T_c superconductors.

In *chapter 6*, the influence of defects that are created in $NbSe_2$ via intrinsic (*i.e.* Se vacancy) and extrinsic method (*i.e.* Fe incorporation) have been studied effectively through structural, electronic, magnetoresistance and magnetization measurements. Here, we have investigated the coexistence of two antagonistic phenomena (*i.e.*, superconductivity and ferromagnetism) in $NbSe_2$ in presence of these defects through magnetization measurement. The temperature-dependent magnetization measurement gives the signature of coexistence of SC and FM in $NbSe_{1.85}$. Interestingly, there is no such evidence in case of $Fe_{0.0015}NbSe_2$. The temperature-dependent resistance measurements confirm that both Se and Fe defects decrease the superconducting transition temperature due to the presence of disorder as well as enhancement of scattering phenomena of charge barriers. We have also studied the magnetoresistance measurements of $NbSe_{1.85}$ and $Fe_{0.0015}NbSe_2$ to observe the effect of intrinsic and extrinsic defects in the TAFF region of $NbSe_2$. The temperature and magnetic field dependence of TAE is described elaborately in each case. The magnetic field dependence of TAE distinguishes the Fe intercalated $NbSe_2$ from Se deficient $NbSe_2$. The flux lines show 2D characteristics in TAFF region of $NbSe_{1.85}$. Moreover, the first principle calculation is also performed to investigate the variation in band structure and density of state (DOS) in $NbSe_2$, $NbSe_{1.85}$ and $Fe_{0.0015}NbSe_2$. The experimental as well as theoretical calculations will help the communities to understand the effect of defects in FLL of anisotropic superconductors.

In *chapter 7*, the effect of weak point disorder in $NbSe_2$ is studied by incorporation of V atoms through magnetic and magnetoresistance measurement in V_xNbSe_2 single crystal. We observe that the point disorder introduces fishtail effect and the second magnetization peak (SMP) effect in

V doped $NbSe_2$. Unlike the Cr_xNbSe_2 single crystals, V_xNbSe_2 show SMP effect at very low concentration of V atoms. Enhancement of the V atoms boosts the SMP peak. Presence of the 3D collective creep (only large bundle pinning region) of elastic FLL supports the vortex motion below onset of SMP effect. However, the crossover from collective to plastic transformation supports the occurrence of SMP effect in highest V concentration. Magneto transport measurement shows the glassy transition near the zero resistance region. Like Cr_xNbSe_2, the BL zero field peak and the high field peak are observed in the magnetic field dependence of pinning force density of V_xNbSe_2. We have also studied the temperature and magnetic field dependence of TAE in $V_{0.0015}NbSe_2$ which shows similar characteristics to $Fe_{0.0015}NbSe_2$ single crystals as we discussed in the previous chapter. Finally, a vortex phase diagram is constructed demonstrating all the different phases of vortex lattice of $V_{0.0015}NbSe_2$ in *H*-*T* phase space.

Overall, it is concluded that the growth of large single crystals of $NbSe_2$ and its physical properties measurement is very crucial to enhance the practical applications of superconducting materials with stable characteristics. Several key aspects are addressed in the present work. Firstly, the formation of large single crystals of $NbSe_2$ superconductors is discussed in detail by iodine vapour transport method. Secondly, the effect of doping in $NbSe_2$ is highlighted for improving the structural and superconducting properties (*i.e.*, T_c, H_{c2} and J_c). It sheds light on the phase transitions, vortex dynamics and pinning at different kinds of pinning centres, collective creep of vortex lattice, collective motion and dissipative hopping of individual vortices of pure as well as doped $NbSe_2$ in response to an external dc magnetic field.

Thus, the outcomes of the present study are a decent contribution in the FLL of 2D and high T_c anisotropic, layered superconductors. This study also fulfils the main objectives of the thesis and the thesis title is quite well justified.

8.2. Outlook and Future Prospects

Assimilating the benefits from literature and different aspects of the present study, diverse proposals for future work are in line. A few among them are presented briefly:

Niobium diselenide's promising future is dependent on achieving monolayer $NbSe_2$, which is still obstructing and most difficult to grow. This is beneficial to extend its application in the different field of new quantum physics and high-temperature superconductors. As we have shown, $NbSe_2$ stands as a good candidate in providing significantly different properties arising from reduced dimensionality with creating defects. There are also some other observation arising from reduced dimensionality like Ising superconductivity, quantum metallic state, and strong enhancement of charge density wave order. However, there are number of important issues related to its stability and reproducibility that are needed to be addressed by further research to form monolayer $NbSe_2$ for its commercialization.

Besides this, with the help of the efficient exfoliation method, few layers $NbSe_2$ can be extracted which have a significant impact on applications like low noise photon detection, transition edge sensors (TESs), Kinetic inductance detectors (KIDs), and superconducting nanowire single photon detectors (SNSPDs). SNSPDs can be built with > 90% single photon detection efficiency at 1550 nm, and have found applications in quantum optics, quantum key distribution, single photon LIDAR, and infrared astronomy.

As the field of low dimensionality is nurturing, it becomes increasingly necessary to unravel the underlying physics of two-dimensional superconductivity of $NbSe_2$ from both experimental and theoretical aspects.

These are the few points where the future research work is needed and will be focused.